Fatigue Prediction Model of Vibration-Strain Signals with Neuro-Fuzzy Parameters for Durability Assessment

Von der Fakultät für Ingenieurwissenschaften, Abteilung Maschinenbau und Verfahrenstechnik

der

Universität Duisburg-Essen

zur Erlangung des akademischen Grades

eines

Doktors der Ingenieurwissenschaften

Dr.-Ing.

genehmigte Dissertation

von

Chin Chuin Hao
aus
Seremban, Malaysia

Gutachter: Univ.-Prof. Dr.-Ing. Dieter Schramm, Universität Duisburg-Essen (UDE)
Prof. Dr. T. Prakash G. Thamburaja, Universiti Kebangsaan Malaysia (UKM)
Tag der mündlichen Prüfung: 03.11.2022

FATIGUE PREDICTION MODEL OF VIBRATION-STRAIN SIGNALS WITH NEURO-FUZZY PARAMETERS FOR DURABILITY ASSESSMENT

CHIN CHUIN HAO

THESIS SUBMITTED IN FULFILMENT FOR THE DEGREE OF
DOCTOR OF PHILOSOPHY

FACULTY OF ENGINEEERING AND BUILT ENVIRONMENT
UNIVERSITI KEBANGSAAN MALAYSIA
BANGI

2022

MODEL RAMALAN ISYARAT GETRAN-TERIKAN DENGAN PARAMETER NEURO-KABUR UNTUK PENILAIAN KETAHANAN

CHIN CHUIN HAO

TESIS YANG DIKEMUKAKAN UNTUK MEMPEROLEHI
IJAZAH DOKTOR FALSAFAH

FAKULTI KEJURUTERAAN DAN ALAM BINA
UNIVERSITI KEBANGSAAN MALAYSIA
BANGI

2022

DECLARATION

I hereby declare that the work in this thesis is my own except for quotes and summaries which have been duly acknowledged.

22 December 2022

CHIN CHUIN HAO
P90362

ACKNOWLEDGEMENT

I am very fortunate to have Prof. Ir. Dr. Shahrum Abdullah and Prof. Dr.-Ing Dieter Schramm as my main research supervisors. Their constructive guidance is the key of successful of my thesis. Also, I would like to express my high appreciation to my co-supervisors Dr. Salvinder Singh Karam Singh and Prof. Ir. Dr. Ahmad Kamal Ariffin.

Forever, I am grateful to Faculty of Engineering and Built Environment (UKM, Malaysia) and Departmental Chair of Mechatronics (UDE, Germany) for providing research facilities to complete my thesis. I would like to thank all post graduate students of UKM under the supervision of Prof. Shahrum Abdullah and Prof. Dieter Schramm for their help, friendship, and creating a pleasant working environment throughout my years in UKM and UDE.

The support from my family is also the main motivation for me to complete my PhD study. Hence, I am grateful to my parents (Chin Chi Pan and Goh Beng Hong) and siblings (Chin Chuin Siong, Chin Chuin Yew and Chin Si Min) for their continuous encouragement and supports all the time.

Last but not least, I gratefully acknowledge financial support provided by CRIM UKM through Zamalah scholarship scheme and research grant FRGS/1/2019/TK03/UKM/01/3.

ABSTRAK

Kajian ini bertujuan untuk membangunkan model ramalan getaran lesu berdasarkan pencirian isyarat getaran dari pengujaan jalan raya yang berbeza. Kaedah konvensional yang digunakan untuk ramalan ketahanan komponen automotif iaitu kaedah terikan-hayat memerlukan data yang banyak dan membebankan dari segi pengiraaan. Ini menyebabkan analisis ketahanan pegas gegelung menjadi satu proses yang kompleks dan rumit. Oleh itu, kaedah peramalan ketahanan yang diperkenalkan dalam kajian ini yang berasaskan getaran daripada permukaan jalan bertujuan mempercepatkan analisis ketahanan pegas gegelung. Metodologi kajian ini merangkumi pencerapan isyarat, pencirian isyarat getaran jalan, pembangunan model ramalan ketahanan dan penentusahan model. Ujikaji pencerapan isyarat terikan pegas gegelung dan isyarat getaran jalan bawah keadaan jalan yang berlainan telah dijalankan. Seterusnya, pencirian ketahanan berasaskan kepelbagaian bentuk dan tenaga getaran frekuensi rendah dalam isyarat getaran jalan telah dijalankan melalui analisis pelbagaian bentuk dan analisis ketunggalan. Satu model penukaran pecutan-terikan telah dibangunkan berasaskan perkaitan mekanikal antara anjakan pegas dan terikan dalam pegas gegelung. Dengan menggunakan permodelan dinamik pelbagai jasad, tindak balas pegas gegelung dari pengujaan jalan raya telah disimulasi dan ditukar ke isyarat terikan. Hayat lesu seterusnya dikenalpasti daripada isyarat terikan simulasi. Seterusnya, sistem inferansi neuro-kabur penyesuaian (ANFIS) telah digunakan untuk mengenalpasti fungsi keahlian kabur yang optimum berasaskan pencirian getaran jalan. Model peramalan hayat lesu berdasarkan fungsi keahlian kabur yang dioptimumkan telah dibangunkan. Analisis kebolehpercayaan diguna untuk menentukan ciri-ciri kebolehpercayaan model ramalan kebolehpercayaan yang dibangunkan. Analisis frekuensi dengan kepadatan spektrum kuasa telah menunjukkan isyarat getaran mempunyai frekuensi antara 0-50 Hz dan hingar frekuensi tinggi pada 80-100 Hz. Analisis ketunggalan mencirikan isyarat getaran pada frekuensi rendah dan menghapuskan hingar frekuensi tinggi. Seterusnya, model pecutan-terikan yang dibangunkan berupaya menghasilkan isyarat terikan yang tepat. Isyarat terikan yang dihasilkan didapati mempunyai perbezaan di bawah 30% dari segi statistik dengan isyarat terikan ujikaji. Ini menunjukkan kaedah dinamik pelbagai jasad sesuai digunakan dalam kajian ini untuk meramalkan tindak balas pegas gegelung di bawah pengujaan rawak. Model ramalan ketahanan berasaskan neuro-kabur telah memberikan ramalan hayat lesu yang mendekati dengan hayat lesu ujikaji. Analisis peramalan hayat lesu konservatif telah mengesahkan ketepatan model ramalan ketahanan neuro-kabur di mana melebihi 90% hayat lesu yang diramal oleh model tersebut berada di dalam had sempadan penerimaan. Selain itu, hayat lesu yang diramal oleh model ANFIS menunjukkan kolerasi yang bagus dengan data eksperimen di mana nilai r yang melebihi 0.9 telah didapati. Analisis kebolehpercayaan telah megesahkan model ANFIS yang telah dilatih kerana data hayat lesu yang disimulasi menunjukkan kitaran-min-terhadap-kerosakan (McTF) yang amat dekat dengan kebezaan di bawah 10%. Kajian ini telah menyumbang kepada ilmu baru dalam pencirian isyarat getaran jalan raya untuk ramalan hayat lesu pegas gegelung berasaskan fungsi keahlian kabur. Selain itu, model ramalan yang dibangunkan boleh mempercepatkan proses pembangunan pegas gegelung untuk mencapai keperluan ketahanan dalam industri automotif.

ABSTRACT

This study aimed to develop vibration fatigue prediction model based on the features of different vibrational road excitations. Conventional strain-life approaches used for durability predictions requires huge amount of data and heavy computational load. This rendered the durability analysis of coil spring to be a complex and time-consuming process. Therefore, a durability prediction model based on the vibrational excitations from road surfaces is developed in this study to accelerate the durability assessment of coil spring. Methodology of this study include signals acquisition, feature extraction from the road vibrational data, model development and model validation. Road tests were conducted to acquire strain and road vibration signals under various road conditions. Subsequently, multifractality and low-frequency vibrational energy were extracted from the vibration signals with multifractal analysis and singularity analysis, respectively, as the durability-related features. An acceleration-strain conversion model was developed based on the relationship between the spring displacement and strain in coil spring. Through multibody dynamic modelling, spring responses from road excitations were simulated and converted to strain signals. Simulated fatigue lives were then predicted from the generated strain signals. Next, Adaptive Neuro-Fuzzy Inference System (ANFIS) was used to determine the optimal fuzzy membership functions based on the durability features of vibrational road excitations. A vibration-based durability prediction model was developed using the optimised membership functions of road vibration features. Reliability analysis was employed to evaluate the reliability of the developed durability prediction model. The frequency analysis of vibrational road excitations with power spectral density revealed that the signals had frequency range between 0-50 Hz and high frequency noise between 80-100 HZ. Singularity analysis was able to extract low frequency features while eliminate the high frequency noise. In addition, the formulated acceleration-strain conversion model could generate accurate strain signals of coil spring working under random loads. The statistics of the simulated strain signals had deviations below 30% compared to experimental strain signals. This suggested that the use of multibody dynamics model was appropriate to predict the responses of coil spring under random road excitations. The durability prediction model developed based on neuro-fuzzy approach in this study provided accurate prediction of coil spring's fatigue life closed to the experimental results. Fatigue life conservative analysis validated the accuracy of fatigue lives predicted with the ANFIS-based durability prediction model in which above 90% of the predicted fatigue lives were found within the acceptance boundary limits. Furthermore, the simulated fatigue life had good correlation with experimental results with r values above 0.9. The reliability analysis validated the trained ANFIS durability prediction models as the simulated fatigue life data had similar mean-cycle-to-failure (McTF) with the experimental results, with differences less than 10%. This study contributed to characterisation of fatigue-related features of vibrational road excitations based on the fuzzy membership functions for durability prediction of coil spring. The developed durability prediction model in this study can expedite the coil spring development process to meet the durability requirements of automotive industry.

TABLE OF CONTENTS

LIST OF TABLES

LIST OF ILLUSTRATIONS

LIST OF SYMBOLS AND ABBREVIATIONS

AIC	Akaike's Information Criterion
ANFIS	Adaptive neuro-fuzzy inference system
CAL	Constant amplitude loading
CASAS	Chin-Abdullah-Schramm-Ariffin-Singh
CDF	Cumulative density function
CWT	Continuous wavelet transform
C-C	Compression-to-compression
DIC	Digital image correlation
DOF	Degree of freedom
DOG	Derivative of Gaussian
DWT	Discrete wavelet transform
ε-N	Strain-life
FDE	Fatigue data editing
FFT	Fast Fourier transform
HCF	High cycle fatigue
HE	Hölder exponent
LCF	Low cycle fatigue
MBD	Multibody dynamics
McTF	Mean-cycle-to-Failure
MFDFA	Multifractal detrended fluctuation analysis
MF	Membership function
MLE	Maximum Likelihood Estimation
MSE	Mean-square-error
MTTF	Mean-Time-to-Failure
PDE	Partial differential equations
PDF	Probability density function
PSD	Power spectral density

RMS	Root-mean-square
RMSE	Root-mean-square-error
ROI	Radius of influence
SAE	Society of Automotive Engineers
SCM	Substractive clustering method
S-N	Stress-life
STFT	Short-time Fourier transform
TEO	Teager energy operator
T-C	Tension-compression
T-T	Tension-to-tension
VAL	Variable amplitude loading
VHCF	Very high cycle fatigue
WL	Wavelet leaders
WTMM	Wavelet transform modulus maxima
A	Cross section area of coil spring wire
A_s	Signal amplitude
a_j	Approximate coefficient at level j of DWT
b	Fatigue strength exponent
C	Spring index
c	Fatigue durability exponent
c_p	Log-cummulants of scaling exponent $\xi(q)$
c_1	Suspension damping coefficient
d	Coil wire diameter
db2	Daubechies 2
d_i	Detail coefficient at level i of DWT
D	Mean diameter of coil spring
$D(h)$	Multifractal spectrum
D_f	Accumulated fatigue damage

E	Modulus of elasticity
E_{CWT}	CWT energy
E_{PSD}	Energy of PSD
F	Force subjected to spring
F_{max}	Maximum load
F_{mean}	Mean load
F_{min}	Minimum load
F_{amp}	Load amplitude
$F(t)$	Cumulative density function in time t
$F(N_f)$	Cumulative density function in cycle to failure N_f
$f(\alpha)$	Fractal dimension
$f(t)$	Time series
$\hat{f}(\omega)$	Fourier transform of time series
f_n	Natural frequency of sprung mass bouncing
f_d	Damped natural freqeuncy
f_0	Signal frequency
$f_{Normal}(x)$	Normal PDF of fatigue data
$f_{Weibull}(t)$	Weibull PDF
$f_{Lognormal}(t)$	Lognormal PDF
G	Shear modulus of material
$g(t)$	Window function in STFT
$H^r(x(\alpha), \mu(\alpha))$	Hausdorff measurement from fractal subset $x(\alpha)$ with Borel probability measurement
h	Hölder exponent in multifractal spectrum
$h(t)$	Hazard rate function in time
$h(N_f)$	Hazard rate function in cycle to failure N_f
I_{xx}, I_{yy}, I_{zz}	Inertia moments in three directions
J	Polar moment of inertia of a circular cross-section wire

k	Weibull shape parameter
k_1	Spring stiffness
k_2	Tyre stiffness
K_w	Wahl correction factor
L	Length of coil spring wire
L_L	Likelihood function
M_1	Sprung mass
M_2	Unsprung mass
m	Vanishing moment of wavelet function
m_d	Decay parameter of ESD model
P_i	Cluster center in SCM
$P(\omega)$	Power spectral density (PSD)
R	Load ratio
$R(t)$	Reliability function in time
$R(N_f)$	Reliability function in cycle to failure N_f
RR	Ride rates
r	Pearson correlation coefficient
r_a	Radius of neighbourhood in SCM
r_b	Radius of influence (ROI)
S_{cu}	Current opening stress
S_{ss}	Steady state crack opening stress
$S_L(q,j)$	Structure functions of wavelet leaders
s	Scale parameter of wavelet function
T	Torque
T_{ij}	Cauchy stress tensor
u	Shift parameter of wavelet function
W	Displacement of ground
$W_\psi f(s,u)$	Wavelet coefficients obtained from CWT

$W(j,k)$	Wavelet coefficients obtained from DWT
w_m	Firing strength
$\overline{w}_m$	Normalised firing strength
X_1	Displacement of sprung mass
$\dot{X}_1$	Velocity of sprung mass
$\ddot{X}_1$	Acceleration of sprung mass
X_2	Displacement of unsprung mass
$\dot{X}_2$	Velocity of unsprung mass
$\ddot{X}_2$	Acceleration of unsprung mass
x	Spring deflection
$\bar{x}$	Mean of dataset
z	Number of estimated parameters of the fitted distributions
α_s	Material constant for ESD model
β_s	Material constant for ESD model
$\Delta\varepsilon$	Strain range
$\Delta\varepsilon_{eff}$	Net effective strain range
ΔF	Load range
Δh	Multifractality
ΔS_{op}	Crack opening stress differences between adjacent cycles
$\Delta\sigma_0$	Equivalent stress range at zero mean stress
$\Delta\sigma_{\bar{\sigma}}$	Stress range at non-zero mean stress
θ	Phase angle
ε	Strain
ε_i	Intrinsic fatigue limit strain range
ε_{max}	Maximum strain
ε_{op}	Crack opening strain
ε_a^p	Plastic strain amplitude
ε_f'	Durability coefficient

λ	Weibull scale parameter
ξ_s	Damping ratio
$\xi(q)$	Scaling exponentin respect to moment q
σ	Stress
σ_{max}	Maximum stress
σ_{min}	Minimum stress
σ_{SD}	Standard deviation
σ_y	Yield strength
σ_f'	Fatigue strength coefficient
σ_a	Stress amplitude
σ_{UTS}	Ultimate strength of material
$\bar{\sigma}$	Mean stress
σ_{VM}	von Mises stress
τ_F	Transverse shear stress in coil spring
τ_{max}	Maximum shear stress in coil spring
τ_T	Tortional shear stress in coil spring
μ	Lognormal mean parameter
μ_A	Degree of membership of membership function A
μ_B	Degree of membership of membership function B
μ_C	Degree of membership of membership function C
$\mu_{A_i}(x)$	Gaussian membership function
$\psi_{s,u}(t)$	Wavelet function with shift (u) and scale (s) parameters
$\psi_{j,k}(t)$	Discretised wavelet function
ψ^*	Complex conjugate of wavelet function
$\psi(\xi)$	Fourier transform of wavelet function
$2N_f$	Reversal to failure

CHAPTER I

INTRODUCTION

1.1 INTRODUCTION TO FATIGUE LIFE ANALYSIS

Most of the components, such as automotive components, are subjected to vibration loadings with variable amplitude and changing mean stress rather than constant cyclic loadings (Du et al. 2020; Repetto & Torrielli 2017). In 1874, W. Gerber modelled the boundary line for mean stress correction using a parabolic method. O. H. Basquin proposed the log-log relationship of Wöhler's curve in 1910, which later became the basis for the development of strain-life approach (Liu et al. 2016). J. Goodman and C. R. Soderberg imposed the mean stress correction by further modifying Gerber's model (Zhu et al. 2016). Mean stress correction models are stress-based approaches that need to be implemented with the stress-life (*S-N*) analysis. However, *S-N* analysis has limitations in taking the real stress-strain behaviour between monotonic and cyclic loadings into account, which was later explained by J. Bauschinger. The Bauschinger effect highlighted the changing of material elastic limits during repetitive loads, which involved strain hardening and strain softening. This led to the development of the Coffin-Manson strain-life model in 1954. The Coffin-Manson model considered the plastic strain in the assessment of fatigue life. Morrow and Smith-Watson-Topper strain-life models were further established in 1968 and 1970, respectively, to consider the mean stress correction in the strain-life method.

Mechanical failures are inevitable in most mechanical systems and eventually damage and stop the systems from performing tasks. Over the centuries, engineers have invested many efforts in the design of engineering products in order to avoid improper design of the products that could encourage mechanical failures (Kihm, Ferguson & Antoni 2015). A proper engineering design is particularly important in structural

components, such as for aircraft applications (Zhu, Zhang & Xia 2016), automotive (Kaluza et al. 2017), and turbines (Li et al. 2021) as the mechanical failures of such components can be catastrophic and result in the loss of life and properties. There are many types of mechanical failures caused by static or dynamic loads. Fatigue failure is a common type of mechanical failure caused by repetitive cyclic loading, such as mechanical bending, vibrations, or temperature fluctuations (Twomey et al. 2020; Ye, Su & Han 2014). As the components' materials are continuously deteriorated by the cyclic loading, cracking first occurs at some crack initiations, crack propagation, and finally fracture (Branco et al. 2019).

Fatigue failures are found to be responsible for more than half of mechanical failures because most of the mechanical components work under vibrating environment (Ye, Su & Han 2014). Therefore, it is utmost of importance to understand the failure mechanism of fatigue to predict the fatigue life of components. The concept of fatigue failure was first addressed in 1850 by August Wöhler, a German engineer who proposed the *S-N* curve that related the stress amplitude of constant loading to the fatigue life of smooth cylindrical specimens (Liu et al. 2016). In recent years, an important advancement in fatigue analysis is the invention of the strain gauge, which is an electronic-based sensor that can measure the variation in the strain at various sampling frequencies of components subjected to dynamic loading (Iriarte et al. 2021; Urda et al. 2020; Xia & Quail 2016). Strain measurement is important for fatigue analysis in many automotive applications because the strain represents the local plastic deformation that leads to crack initiation.

Apart from fatigue life models, another important aspect of fatigue analysis is the cycle counting algorithm. During testing in laboratory conditions, the loads can be controlled in constant amplitude. However, under field conditions, the load pattern will appear to be far more complex with variable amplitudes. For example, the vibration loads of automotive components are often variable amplitude loading (VAL) time series (Burdzik 2017). For such complex loads, cycle counting is needed to transform the load histories into sets of parameterised fatigue cycles needed by fatigue life models (Twomey et al. 2020). Several cycle counting algorithms have been proposed, including the level-crossing, peak-to-peak, simple-range, and rainflow, specifically for VAL

(Janssens 2020). Rainflow cycle counting proposed by M. Matsuishi and T. Endo in 1968 received a general agreement from researchers as the most robust cycle counting method because it is capable of reducing a complex load spectrum into a simple set of load reversals. Marsh et al. (2016) also remarked that the rainflow counting method demonstrated the best agreement with the fatigue life measured through experiments compared to other cycle counting methods. After cycle counting, the damage accumulation rule is applied to sum the total damage contributed by each cycle. This rainflow cycle counting algorithm and the Palmgren-Miner linear damage rule are widely used in fatigue life assessment because this combination is generally accepted to have high accuracy (Ugras et al. 2019).

Nowadays, fatigue life assessment has become compulsory in most of the design processes of a wide variety of engineering products. The products of some industries, such as automotive (Dong & Dave 2020), aerospace (Zhan & Li 2021), and offshore (Nguyen, Oterkus & Oterkus 2021) industries rely heavily on the fatigue analysis. The importance of fatigue analysis has prompted researchers to develop many theories and fatigue life models to achieve better accuracy in fatigue life predictions. Nevertheless, there remain many challenges in fatigue life assessment due to the complexity of fatigue phenomena in real applications (Mehdizadeh, Haghshenas & Khonsari 2021). For example, fatigue life assessment of structures involving VAL is difficult due to the randomness and uncertainties in the loading signal (Horn, Krokstad & Leira 2019). Furthermore, fatigue life assessment involving VAL is also more complex as it requires cycle counting, and VAL is found to cause more damage to the structure (Idris et al. 2018). Real-life applications are often exposed to VAL, and hence, fatigue analysis that involves VAL is necessary.

1.2 DURABILITY ASSESSMENT

Land vehicles are frequently subjected to vibrations generated by the engine, drivetrain, and road surface (Panda 2016). Vibration induced by the road surface has the most contribution to fatigue damage in automotive components because road excitation is the main vibration source of automotive components (Teixeira, Roberts & Silva 2019). In addition, road vibration also affects the ride quality and control of the vehicle. There is

a necessity to reduce the vibration being transmitted to the car chassis. In order to isolate the body from road excitation, the wheels of the vehicle are mounted on suspension systems. The suspension system generally consists of a spring and a damper to absorb and dissipate the vibration energy received from the road surface and reduce the vibration transmitted to the car chassis. A coil spring is a critical component in a suspension system as it supports the car body while allowing the wheel to move in vertical direction. Hence, it is very crucial to design a durable coil spring that sustains for a reasonable period of service life (Bianco 2019). Under normal conditions, a coil spring is expected to sustain a service period for at most five to six years for the vehicle safety (Huang, Huang & Ho 2017).

As wheels travel across different terrains, the wheels regularly encounter some road surface irregularities, such as bumps, potholes, and rough surface profiles at high speed. These result in instant vertical bouncing movement of the wheels as the wheels hit the surface irregularities. The coil spring in the suspension system reacts interactively to the road excitation by expanding and compressing to absorb the vibration energy (Dong & Dave 2020). During the expansion and compression movements, the circular geometry of the coil spring results in a complex stress state that significantly complicates the fatigue analysis of coil spring under vibration loading. Car manufacturers often perform the fatigue analysis of coil springs using experimental testing machines to understand their fatigue characteristics (Pyttel et al. 2014; Rahul & Rameshkumar 2020). Nevertheless, experimental fatigue tests are always associated with high costs because the tests are destructive and time-consuming, making the tests not cost-effective (McAlorum et al. 2018; Wang et al. 2020a). Besides, most of the fatigue tests in the laboratory are limited to only constant amplitude loading or block cycle loading because VAL is very complex and difficult to replicate by testing machines (Yıldırım, Remes & Nussbaumer 2020). This is due to the randomness and uncertainties in VAL. Therefore, some simulation-based analyses, such as finite-element-based approaches, have started to draw the attention of researchers to reduce the need for experimental fatigue tests, especially in automotive applications (Zhang et al. 2019b).

In the past decades, fatigue life assessment has shifted from laboratory tests to simulations using fatigue models. This is an important transition of paradigm in fatigue life assessment as simulation can greatly reduce the cost and accelerate the duration of product development in different industries. Through durability simulation, engineers can determine the fatigue behaviours of different structural designs without the need for prototyping (Zhang et al. 2019b). Many fatigue models, such as the stress-life and strain-life models, have been introduced for durability analysis. To assess the fatigue life of a component using durability models, knowledge of the structure geometry, material properties, and loading conditions are required (Pejkowski & Skibicki 2019). The use of simulation tools to assist the fatigue analysis of automotive components is commonly increasing. Fatigue simulation tools become very convenient for durability analysis when relevant information including the geometry of component, material properties, and loading histories is available. Using the finite element method, Zhang et al. (2019) successfully simulated the fatigue crack behaviour of stainless steel under tensile overload. In addition, finite element analysis was also found very helpful in the optimisation of the topological design of engineering structures using the von Mises stress as the fail-safe criteria (Wang et al. 2020a). These studies reported high reliability of simulation results in matching real-life operating conditions. Hence, simulation approaches have been extensively utilised in durability analysis in general industry applications (i.e., automotive, aerospace, marine, and building structures).

In addition, multibody dynamics (MBD) simulation is also regularly used in the automotive industry to simulate vehicle responses under road excitation. Different vehicle MBD models, such as full- (Prastiyo & Fiebig 2021), half- (Gandhi, Adarsh & Ramachandran 2017), and quarter car models (Burdzik 2017; Szymański et al. 2015) have been developed to predict vehicle's responses under random loading. Putra et al. (2017) and Kong et al. (2019a) developed a quarter suspension MBD model to simulate strain signals of coil spring under random loading for durability analysis. These simulation-based analyses have been proven to provide accurate results and could significantly reduce the time needed for fatigue analysis. Furthermore, machine learning based approaches such as artificial neuro networks and neuro-fuzzy methods were also extensively used in modelling of durability performances of automotive components. These approaches provided more computational capability to model complicated

fatigue process in automotive applications compared to conventional modelling techniques (Gandhi, Adarsh & Ramachandran 2017; Kong et al. 2019b).

1.3 PROBLEM STATEMENT

To conduct a durability analysis, knowledge of the service load, component geometries, and material properties is necessary. Road tests are usually performed to acquire the load histories of the suspension components through real measurements. However, the load data acquisition through an experimental approach always involves costly instruments. On the other hand, a sufficiently large data size is also required to represent the statistics of real loading conditions and needs a long time for the road test (Ugras et al. 2019). In recent years, strain signals have been utilised as the loading histories in the fatigue analysis of suspension coil springs. Nonetheless, in-situ measurement of real strain data at the suspension coil spring remains a difficult task. The acquired strain signals are often found to be inconsistent because the collected data are easily influenced by some uncertainties in experimental work. Moreover, the acquisition of coil spring strain data is technically difficult, especially under driving conditions, because of the limited workspace and complex geometry of the coil springs.

To reduce the requirement of strain data acquisition, some advanced technologies have been introduced to replace the actual measurement. For example, digital image correlation (DIC) is an emerging technology that can detect strain localisation in a deforming structure without the need for physical sensors, such as strain gauges. DIC was applied in fatigue assessment of different materials (Benabou et al. 2020). However, the technology leads to very high costs and is not practical to capture the strain changes in coil springs under driving conditions. Therefore, Kong et al. (2019a) and Putra et al. (2017a) proposed simulation approaches to generate strain signals from the vibrational excitation of the coil spring. Using MBD simulation, these studies developed conversion models that could transform random vibration signals of a coil spring into strain signals. However, the model of Putra et al. (2017a) was unable to consider the torsional shear stress in the spring under deflection. It was found in the literature that the stress and strain resulting from spring deflection are dominantly torsional. It is hence necessary to consider the effect of torsional shear strain in

generating a realistic strain signal of coil spring. Apart from the torsional stress, spring curvature effect also contributes to a high stress concentration in a helical coil spring. In the model proposed by Kong et al. (2019a), the effect of spring curvature was not considered. In addition, previous models proposed by Putra et al. (2017) and Kong et al. (2019a) were found to have limited accuracy in high fatigue cycle predictions due to a lack of consideration of the MBD effects between the suspension parts. Based on these reasons, there is a need to determine the deflection-strain relationship in a coil spring by considering the torsional shear stress and the spring curvature effect using the MBD method.

Time-domain approaches, especially the strain-life methods, are the most frequently applied durability analysis for coil springs. However, time-domain approaches have been regarded to have low efficiency due to their long computational time. Apart from that, large data samples are needed in time-domain approaches to obtain accurate results and this has led to more complications in data acquisition and processing (Ugras et al. 2019). To accelerate durability analysis, several techniques (e.g., fatigue data editing and frequency domain analysis) have been considered. Some signal processing methods, such as wavelet transform, have also been employed to extract fatigue-related features from the loading signals of coil springs (Rahim et al. 2021). Nevertheless, these techniques mainly emphasised the loading histories without considering the design of the coil spring. The design parameters of the coil spring are related to the ride quality and durability of the spring (Kong et al. 2019c). Nonetheless, the previous models only explained the relationship between the ride comfort and the durability of the coil spring. The automotive industry nowadays is demanding faster and more accurate methods to determine the fatigue life of the suspension coil spring. Therefore, it is necessary to establish a vibration fatigue model for suspension coil springs that includes both design parameters and vibration characteristics of the coil spring to assist the design process of a durable spring.

1.4 RESEARCH OBJECTIVES

This study aims to establish vibration fatigue prediction models based on vibration features of road excitation for suspension coil springs. It can be achieved with the implementation of the three objectives:

1. To generate strain signals from vibration load based on the displacement-strain relationship considering the torsional stress effects using multibody dynamics approaches.

2. To establish vibration fatigue models for durability assessment associated with an adaptive neuro-fuzzy approach based on signal energy, multifractality, and design parameters of coil spring.

3. To validate the established vibration fatigue models with probabilistic and fatigue reliability properties of simulated and experimental fatigue data.

1.5 SCOPES OF RESEARCH

This study focuses on the development of vibration fatigue prediction models based on the vibration loading characteristics and design parameters for the suspension coil spring. The scope of this work is defined according to the three objectives:

(i) An MBD model of the quarter suspension system is developed using MBD software. The relationship to convert the spring deflection into the strain of the coil spring is established. The maximum torsional shear stress and spring curvature effects are considered in the development of the spring deflection-strain relationship. Finite element analysis is also adopted to determine the stress-strain characteristics and the high stress concentration spot of the coil spring. Real measurements of vibration load and strain histories of suspension coil springs are performed through road tests under four road conditions. Spring deflection of coil springs subjected to vibration loading is simulated using MBD analysis. The deflection is subsequently converted to strain signals using the developed deflection-strain relationship. The deflection-strain relationship is

validated by comparing the fatigue life predicted from the simulated strain and the measured strain.

(ii) Multifractal analysis is employed to determine the multifractal properties of vibration loads acquired in road tests. The multifractality characterises the complexity of the loading signal that is closely related to the road surface irregularities. On top of that, singularity analysis of vibration loads is performed to determine the singularities in the vibration signals that contained low-frequency features of the signals. Extracted singularities are then reconstructed into new vibration signals and unnecessary high-frequency noises are eliminated. Power spectral analysis is conducted to determine the energy of the vibration signals under different loading conditions. The fatigue life of the coil spring is calculated from the simulated strain signals using strain-life and effective strain damage models. Next, the adaptive neuro-fuzzy inference system (ANFIS) technique is applied to model the relationship of the vibration features, design parameters, and durability performance of the coil spring. The ANFIS modelling requires three inputs, including the multifractality, vibration energy and spring stiffness, and fatigue life as the output. Optimisation of the ANFIS structure is performed by comparing the mean square error of the output data. The optimised membership function number for each input parameter is determined.

(iii) Validation of the optimised ANFIS model is conducted by fatigue life correlation with the experimental fatigue life. Reliability analysis is subsequently used to determine the fatigue reliability of the coil spring under various loading conditions. In this study, the modified version of mean-time-to-failure has been introduced to represent fatigue reliability. On the other hand, probabilistic approaches are applied to the fatigue lives predicted from the experimental strain signals to estimate the significant characteristics. The probabilistic-reliability characteristics estimated from the ANFIS model and experimental data are compared as a validation to optimise the ANFIS model.

1.6 RESEARCH HYPOTHESIS

According to the three research objectives, the following hypotheses are introduced:

1. If the relationship between the strain and vibration of coil spring is correlated, then the strain can be simulated by the MBD method.

2. If multifractality and energy of vibration fatigue responses are correlated with the intelligent data analysis, then fatigue life can be predicted using machine learning data modelling.

3. If the simulated fatigue data using machine learning data modelling have similar probabilistic and reliability characteristics with the experimentally measured strain data, then the proposed machine learning models are validated.

1.7 IMPORTANCES OF RESEARCH

This study contributes to the establishment of the deflection-strain relationship of coil springs by integrating MBD simulation. The relationship allows the generation of realistic strain signals from the vibration signals. Therefore, this approach can reduce the need for the real measurement of strain histories of coil springs, which often requires long and expensive road tests. The effects of spring curvature on the stress concentration of torsional shear stress and MBD interactions in the suspension systems are considered. Such modifications allow more explicit consideration of the dynamic responses of coil springs under vibration loading and significantly improve the accuracy of the generated strain signals for durability prediction.

In addition, this study also fills the gap in the relationship of the load multifractality, load vibration energy, and fatigue life of the suspension coil spring using artificial intelligent method. The prediction of coil spring's fatigue life based on the multifractality and energy of vibration load is unprecedently reported and thus, this study contributes to novel knowledge. For suspension system development, the optimised ANFIS durability model can accurately predict the durability prediction for coil springs with different designs. This can significantly reduce the time and cost needed for coil spring design as no simulation or prototype is needed. Therefore, the development of vibration fatigue prediction models for coil springs that can provide good accuracy of fatigue life assessment is the main contribution of this study.

CHAPTER II

LITERATURE REVIEW

2.1 INTRODUCTION

This chapter addresses on the theoretical background and research trend related to the current research scope of the three objectives. The mechanisms of different types of suspension systems are reviewed by focusing on the coil spring design and multibody dynamics (MDB) characteristics of a passive suspension system. In the current study, coil spring failure due to fatigue damage is the main concern, and therefore, trend analysis on coil spring failure is provided. In addition, the theoretical background and recent research trends related to the durability analysis of coil springs including the loading signals, cycle counting methods, fatigue life prediction, and damage cumulative rule are also discussed. The fatigue life prediction with the consideration of load sequence effects and available fatigue model are also discussed.

This study also involves signal processing to extract fatigue-related features from loading signals, with the implementation of signal processing techniques that are classified into time-domain, frequency-domain, and time-frequency-domain methods. The signal processing methods are discussed with their theoretical background and some recent applications in automotive durability. Another important element of current research is the modelling of vibrational features to establish the relationship with the fatigue performance of coil springs. Therefore, a research trend of data analysis techniques is discussed and an appropriate technique for durability modelling is suggested. Furthermore, a systematic literature review on the validation methods for the established fatigue models is also discussed.

2.2 AUTOMOTIVE WHEEL SUSPENSION SYSTEMS

A suspension system is one of the most important systems in vehicles to separate the sprung mass of the vehicle from road excitation, ensuring a comfortable ride and good handling of the steering (Reddy et al. 2016). There are three types of suspension systems, namely passive, semi-active, and active suspension systems. An active system is capable of adjusting the energy dissipation of the spring and damper system according to external stimulation through an electronic controller, while a semi-active system has variable damping characteristics with fixed spring stiffness (Yang et al. 2021; Zhang & Jing 2021). A passive suspension system with fixed spring constant and damping coefficient is the most widely used system in ground vehicles due to its cost-effectiveness and simplicity (Rizvi et al. 2018). Coil springs are the main components in suspension systems and are vital to determine the dynamic behaviour of the systems. Hence, coil springs are carefully designed to meet the desired characteristics. Suspension system simulation using modelling techniques is widely utilised today to facilitate the development process of suspension systems.

2.2.1 Passive Suspension Systems

A passive suspension system can be further classified into dependent and independent systems (Reddy et al. 2016). In a dependent suspension system, two opposite wheels on the opposite sides of a vehicle are linked by a rigid lateral axle, and their movements are influenced by each other. Typical examples of dependent suspension systems are the beam axle suspension system and the trailing twisted beam axle suspension system. Unlike a dependent suspension system, an independent suspension system allows each wheel to respond without affecting the motion of other wheels. This provides extra movement flexibility and improves the ride comfort. Besides, an independent system also offers benefits in packaging as it requires less space and adjustable camber angle for better tyre contact. Therefore, an independent suspension system is more appropriate for passenger cars.

Figure 1 illustrates various types of independent suspension system that are commonly used. Among many types of independent suspension systems, the

MacPherson suspension system is the most widely used suspension system in passenger cars due to its lighter weight than a beam suspension (Theunissen et al. 2021). This suspension system is commonly used when weight optimisation is implemented in the design of a ground vehicle to achieve better fuel efficiency. The upper part of a MacPherson suspension, known as the strut, contains a coaxially mounted coil spring and a damper. The strut is connected to the body chassis at the top mounting with a bearing. It is designed to support the applied loads and rotates with the wheel during steering manoeuvres. The unique strut orientation of MacPherson suspension that incorporates the spring and damper in a concentric package reduces the space required for the mounting and suspension weight (Shinde, Maheshwari & Kumar 2018). Moreover, another advantage of MacPherson suspension is that it provides more space in the car chassis for engine mounting; therefore, it is a very suitable choice for passenger cars with a front engine (Balkwill 2018).

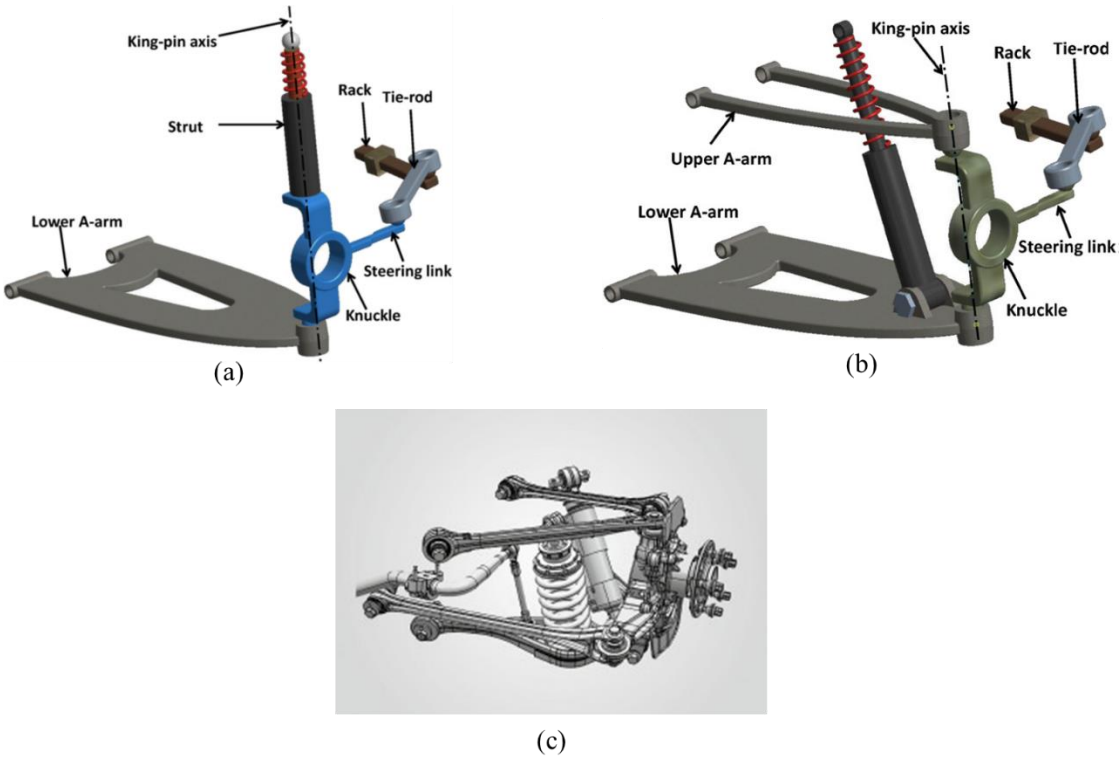

Figure 2.1 Independent suspension systems: (a) MacPherson suspension, (b) Double wishbone suspension, (c) Multi-link suspension

Source: Reddy et al. 2016

In addition to the MacPherson suspension, double wishbone suspension, better known as double A-arm suspension and multi-link suspension, is also commonly used

the suspension in passenger cars (Balkwill 2018). These suspensions have better suspension performance compared to the MacPherson suspension. The double wishbone suspension system possesses two lateral control arms connected between the wheel knuckle and the car chassis. In the multi-link suspension, four or more independent connection links are connected between the wheel carrier and the car chassis by means of movable joints. These designs provide a good camber control, and thus, have improved kinetic characteristics of the suspension system compared to the MacPherson suspension system (Reddy et al. 2016). These advantages make the suspension systems more applicable in racing cars that require excellent handling (Prastiyo & Fiebig 2021). However, double wishbone and multi-link suspension systems are much less seen in passenger cars considering their large space requirement and expensive costs. Table 2.1 lists the advantages and disadvantages of the MacPherson, double wishbone, and multi-link suspension systems.

Table 2.1 Differences between MacPherson, double wishbone and multi-link suspension systems

Type of suspension	Advantages	Disadvantages
MacPherson	- Low building cost - Low space requirements - Less unsprung masses - Suitable for drive	- Camber change during tyre rolling reduce less tyre contact. - Large design height.
Double wishbone	- Flexible design of spatial wheel kinematics - No camber change during tyre rolling - Good tyre contact	- Large space requirements - Complex structure - Expensive cost
Multi-link	- No camber change during tyre rolling - Good tyre contact	- Large space requirements - Complex structure - Require many joints - Expensive cost

2.2.2 Coil Spring Design and Characteristics

Coil springs are usually made of steel material that exhibits good resistance to failure and high reliability (Hoeltgebaum et al. 2012). Spring is one of the essential elements in the suspension system of a vehicle to restore the original position after the work done by a given load and absorb the strain energy to perform the work (Rahul & Rameshkumar 2020). Different types of springs have been utilised in suspension systems, such as coil spring, leaf spring, and torsion spring. In the suspension system of passenger cars, helical compression coil springs are most widely used because coil

springs provide good ride comfort and steering handling (Kushwah, Parekh & Mangrola 2020; Sun, Thompson & Zhou 2019).

Coil springs are designed to achieve the target spring stiffness or spring constant so that they can sustain the weight of the car and the external load (Pawar & Desale 2018). Before a coil spring is designed, it is important to know the working load, available car space, the ride height, and the spring rate to determine the required material and geometry. Some important geometrical parameters related to the spring stiffness in coil spring design include the number of active coils, mean coil diameter, wire diameter, length of the coil spring, and the distance of the pitch. Engineers need to evaluate the loading condition of the spring to determine the suitable spring rate to meet the suspension specifications and define the total spring length that matches the available space in the car chassis.

To start with coil spring design, it is important to understand the mechanism of coil spring under loading conditions. Helical compression coil springs used in suspension systems are usually designated to sustain compression load. Given a helical coil spring subjected to an axial load F along the spring axis as schematically illustrated in Figure 2.2, a torsional shear force or torque $T = FD/2$ acts on the spring wire surface (Pattar, Sanjay & Math 2014). As the spring is deformed under the uniaxial load, this torque is transmitted throughout the spring wire. Meanwhile, a transverse shear force (F) with the same magnitude but in an opposite direction to the applied axial load can also be found at the cross-section of the wire (Kato & Suzuki 2021). The torque (T) and transverse shear force (F) will result in combined shear stress in the spring with a higher value on the inner surface.

The torsional shear stress resulting from the torque T is given by:

$$\tau_T = \frac{TD}{2J} \qquad \ldots(2.1)$$

where J is the polar moment of inertia of a circular cross-section wire, $J = \pi d^4/32$.

Thus, the torsional stress is expanded to:

$$\tau_T = \frac{8FD}{\pi d^3} \qquad \ldots(2.2)$$

The transverse shear stress due to the transverse force at the cross-section of the spring wire is:

$$\tau_F = \frac{F}{A} = \frac{4F}{\pi d^2} \qquad \ldots(2.3)$$

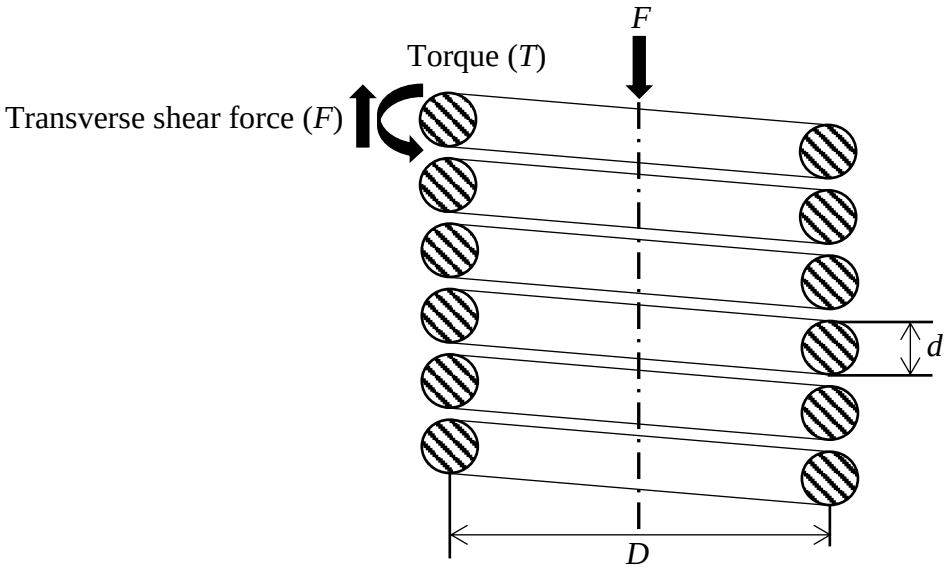

Figure 2.2 Cross-section schematic diagram of a helical spring under axial loading

Assuming a linear elastic response between the torsional and transverse shear force, combining the torsional and transverse shear stress obtained the maximum shear stress in the spring as follows (Pattar, Sanjay & Math 2014):

$$\tau_{max} = \tau_T + \tau_F = \frac{8FD}{\pi d^3} + \frac{4F}{\pi d^2} = \frac{8FD}{\pi d^3}\left(1 + \frac{1}{2C}\right) \qquad \ldots(2.4)$$

where C denotes the spring index and $C = D/d$. For a helical coil spring, the value of C must not be less than 6 or higher than 12 (Hoeltgebaum et al. 2012). In many stress

calculations of coil spring, the transverse shear stress is often neglected due to its minimal contribution to the maximum stress; thus, the shear stress in a coil spring is dominantly torsional (Champion & Champion 2011). Another important factor to be considered in spring design is the curvature of the spring. Spring curvature can cause significant stress concentration on the spring surface facing the spring axis (Čakmak et al. 2019; Dragoni & Bagaria 2011). The stress concentration effect can be considered with the curvature stress concentration factor (K_w), better known as the Wahl correction factor. K_w is defined in the equation (Pöllänen & Martikka 2010):

$$K_w = \frac{4C-1}{4C-4} + \frac{0.615}{C} \quad \ldots(2.5)$$

K_w becomes higher with a smaller spring index C. Therefore, it is important to consider the stress concentration due to spring curvature effects, especially for spring design with a small value of spring index.

The stress concentration due to the spring curvature effect is taken into consideration, and the expression of the maximum shear stress in the coil spring becomes:

$$\tau_{max} = K_w \frac{8FD}{\pi d^3} \quad \ldots(2.6)$$

By implementing Hooke's law as the fundamental theory in spring mechanics, the relationship between the applied force (F) and spring stiffness (k) can be related to the spring deflection (x) in the elastic region (Pöllänen & Martikka 2010):

$$F = kx \quad \ldots(2.7)$$

with the spring stiffness (k):

$$k = \frac{Gd^4}{8D^3N} \quad \ldots(2.8)$$

and the shear modulus *G*. Hooke's law is also applied to the stress-strain relationship of material. Under elastic conditions, the stress-strain relationship of material is expressed by:

$$\sigma = E\varepsilon \qquad \ldots(2.9)$$

where σ denotes the stress, ε is the strain, and E is the modulus of elasticity.

The state of stress distribution plays an important role in engineering design to determine if a component will fail under certain loading conditions. The von Mises stress failure criteria are one of the commonly used criteria to determine the failure state of ductile material in engineering design, especially under complex loading conditions (Liu et al. 2020; Mansor, Abdullah & Ariffin 2019). The von Mises equivalent stress can be defined as follows (Juvinall & Marshek 2017; Mises 1913):

$$\sigma_{VM} = \sqrt{\frac{(T_{11}-T_{22})^2+(T_{22}-T_{33})^2+(T_{33}-T_{11})^2+6(T_{12}^2+T_{23}^2+T_{31}^2)}{2}} \qquad \ldots(2.10)$$

The tensor consists of nine stress components that fully represent the state of stress of a point inside a material (Sadd 2019), such that:

$$T_{ij} = \begin{bmatrix} T_{11} & T_{12} & T_{13} \\ T_{21} & T_{22} & T_{23} \\ T_{31} & T_{32} & T_{33} \end{bmatrix} \qquad \ldots(2.11)$$

where T_{ij} is the Cauchy stress tensor, named after Augustin-Louis Cauchy, T_{11}, T_{22}, and T_{23} are referred to as the normal stresses, while T_{13}, T_{12}, T_{21}, T_{23}, T_{31}, and T_{32} are known as the shear stresses. Figure 2.3 shows the stress components as represented by the Cauchy stress tensor. In a balance of angular momentum, the stress tensor becomes symmetric matrices since the pairs of shear stress in opposite direction are equal. Hence, Equation 2.11 can be rewritten as:

$$T_{ij} = \begin{bmatrix} T_{11} & T_{12} & T_{13} \\ T_{12} & T_{22} & T_{23} \\ T_{13} & T_{23} & T_{33} \end{bmatrix} \quad \ldots(2.12)$$

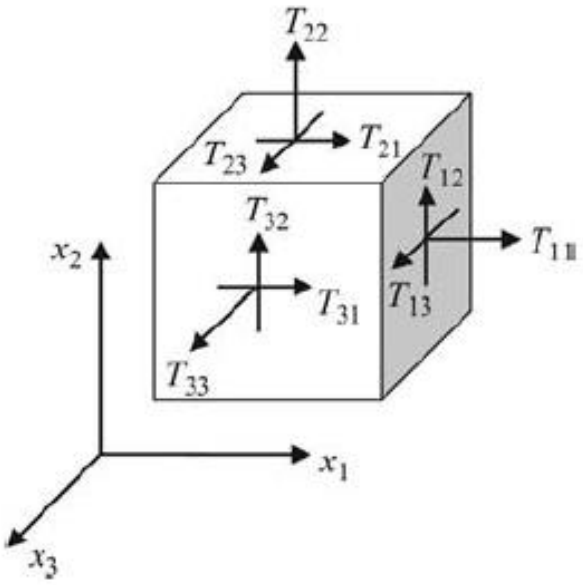

Figure 2.3 Stress components of material represented by the Cauchy stress tensor

Source: Sadd 2019

The von Mises failure criteria have been applied in engineering component design for failure analysis, including automotive applications, due to the accuracy of von Mises equivalent stress in representing the stress state of a material. For example, Kaoua et al. (2011) evaluated the von Mises stress distribution in a twin helical spring for design optimisation. Wang et al. (2020) defined the topological fail-safe criteria of engineering structures by evaluating the von Mises stress. A component fails if the stress exceeds its ultimate tensile strength and this type of failure is known as static failure. However, investigations showed that the failures of suspension coil springs are rarely caused by static failure, but primarily owing to the repeated cyclic loading (Zhu, Wang & Huang 2014; Kong et al. 2018a; Pastorcic, Vukelic & Bozic 2019). Figure 2.4 shows the fatigue of suspension coil spring due to fatigue damage of metallic material accumulated over time. Therefore, it is of utmost importance to perform durability analysis during the design stage of suspension coil springs to predict the fatigue life and avoid early failure of the coil springs.

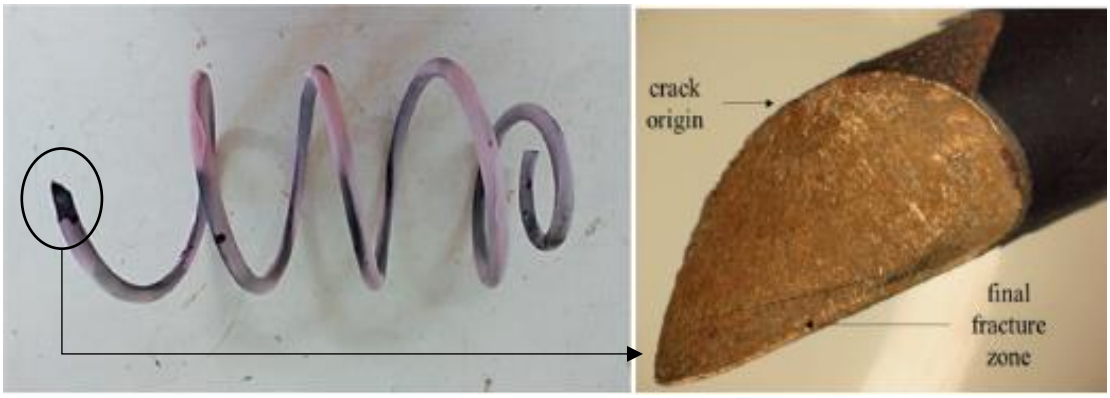

(a) (b)

Figure 2.4 Fatigue failure of suspension coil spring: (a) fractured coil spring, (b) fracture surface

Source: Pastorcic, Vukelic & Bozic 2019

2.2.3 Modelling of Suspension Systems

Simulation-based analyses have been increasingly important in the development of vehicle suspension systems. This is because the simulation provides an accurate prediction of suspension response or motion at much lower cost and time compared to prototypes. In automobile applications, vehicle suspension modelling is often used in the design of a car steering system to predict the car body motion, such as the rolling and pitching angle of the car under road excitation and steering manoeuvres (Schramm, Hiller & Bardini 2014). Furthermore, suspension modelling also plays an essential role in the evaluation ride quality of the passenger (Banerjee, Balamurugan & Krishnakumar 2016).

Suspension models can be classified into different types, including a quarter-car model, half-car model, and full-car model, as shown in Figure 2.5. A quarter-car suspension model focuses on a frontal suspension system with an assumption that the suspension systems in a car are isolated and work independently. A quarter-car suspension model is the simplest model that provides fast prediction of suspension with appropriate accuracy. Many studies (Kashyzadeh, Ghorabi & Arghavan 2014; Reddy et al. 2016; Zhang et al. 2020) adopted the quarter-car suspension model in their analyses for different purposes, especially for durability prediction. For example, a quarter-car model was used by Putra et al. (2017a) and Kong et al. (2019b) to simulate coil spring

response under random vibration loading for durability analysis. These studies successfully generated strain signals from the vibration signals with similar fatigue behaviours using the quarter-car models. A half-car suspension model considers a frontal and rear suspension system while a full-car suspension model takes all the four suspension systems into account. Both half- and full-car models give more accurate prediction but the computational complexity increases significantly. Zhang et al. (2020) developed quarter-, half-, and full-car suspension models to predict the suspension responses integrated with regenerative shock absorbers. The study commented that the quarter-car model offers good computational efficiency compared to half-car and full-car models. Besides, the development of half-car and full-car models also requires the instalment of extra sensors that would inevitably increase the experimental cost.

In suspension modelling, a vehicle is modelled as a single-degree-of-freedom (DOF) system with the road surface irregularities as the input, as shown in Figure 2.6. A quarter-car model consists of a sprung mass that represents the car body weight and is supported by the suspension elements composed of spring with a spring constant *k* and a damper with a damping coefficient *c*. Some important dynamic characteristics, such as pitching, rolling, yawing, and bouncing of the model are affected by the ride rates (RR), such that:

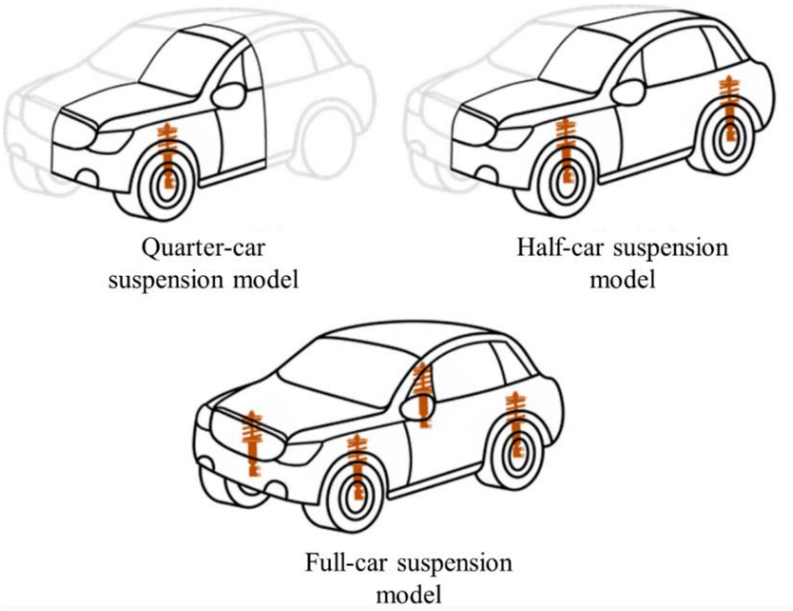

Figure 2.5 Illustrations of quarter-car, half-car and full-car suspension models

Source: Zhang et al. 2020

$$RR = \frac{k_1 k_2}{k_1 + k_2} \qquad \ldots(2.13)$$

where k_1 is the spring stiffness and k_2 is the tyre stiffness. The natural frequency of the bouncing of sprung mass is an important factor to be considered in the design of a suspension model in order to maintain good ride quality. Without taking the damping into account, the natural frequency of the suspension system can be expressed as:

$$f_n = \frac{1}{2\pi}\sqrt{\frac{k_1}{M_1}} \qquad \ldots(2.14)$$

where f_n is the natural frequency of the sprung mass bouncing and M_1 is the sprung mass of the vehicle.

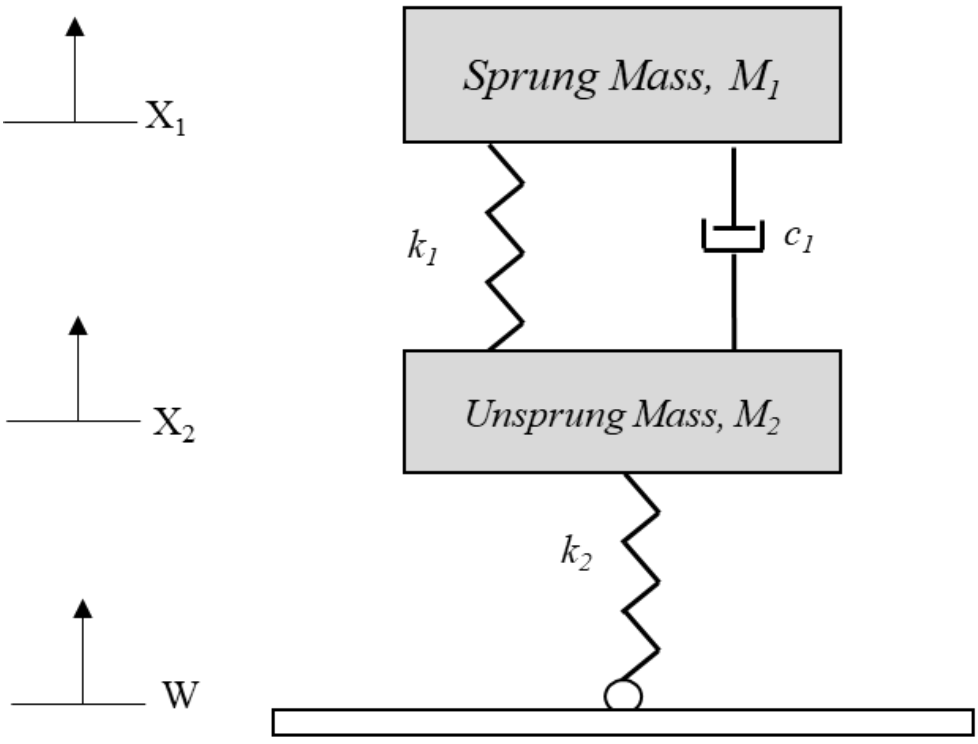

Figure 2.6 A schematic quarter-car suspension model with 2 DOF

Source: Szymański et al. 2015

When damping is considered, the damped natural frequency (f_d) of the suspension system becomes:

$$f_d = f_n\sqrt{1-(\xi_s)^2} \quad \ldots(2.15)$$

with ξ_s as the damping ratio expressed as follows:

$$\xi_s = \frac{c_1}{\sqrt{4k_1M_1}} \quad \ldots(2.16)$$

where c_1 is the suspension damping coefficient. Nabagło, Jurkiewicz & Kowal (2021) remarked that the frequency of a vehicle is kept around 1 Hz to maintain good comfort and the acceptable range is within 1.0–1.5 Hz.

In a quarter-car suspension modelled into a 2-DOF as in Figure 2.6, the tyre is modelled as a single spring with spring stiffness, and the damping is often neglected (Schramm, Hiller & Bardini 2014). The unsprung mass that represents the suspension weight is connected between the tyre and the suspension spring and damper. The kinematics of sprung and unsprung masses can be described by the equations of motion by considering the kinetic relationship between both masses (Szymański et al. 2015):

$$M_1\ddot{X}_1 = -k_1(X_1-X_2)-c_1(\dot{X}_1-\dot{X}_2) \quad \ldots(2.17)$$

$$M_2\ddot{X}_2 = -k_2(X_2-W)+k_1(X_1-X_2)+c_1(\dot{X}_1-\dot{X}_2) \quad \ldots(2.18)$$

where $\dot{X}$ represents the first derivative and $\ddot{X}$ represents the second derivative; W, X_1, and X_2 denote the ground, sprung, and unsprung masses displacement, respectively; M_1 is the sprung mass; M_2 is the unsprung mass; k_1 is the suspension spring constant; k_2 is the tyre spring constant; and c_1 is the damping coefficient of the suspension damper. The 2-DOF suspension quarter-car model is the most often used model in multibody dynamics (MBD) analysis of car suspension due to its simplicity and computational efficiency (Abdelkareem et al. 2018). For example, Lafarge et al. (2016) investigated the dynamics of suspension systems using a 2-DOF quarter-car model to determine the energy quantity for recovering. In addition, the 2-DOF suspension model was also applied in the road profile simulation of the suspension system under random profile

input (Alhasan, White & De Brabanterb 2016). For durability analysis of coil springs, previous studies (Kong et al. 2019c; Putra et al. 2017a) adopted a 2-DOF quarter-car model to determine the spring response under random loading for strain generation. The results of these studies showed a good accuracy above 80% provided by the 2-DOF suspension model as the simulated strain achieved similar fatigue properties with the experimental results. Therefore, MBD modelling of suspension systems has been proven to be a useful tool to facilitate the fatigue analysis of suspension components.

2.3 FATIGUE LIFE ASSESSMENT

Durability analysis is important in aerospace and automotive fields because many accidents are caused by fatigue failure of critical components. In ground vehicles, suspension components (e.g., coil springs) are highly susceptible to fatigue failure because the components are continuously exposed to vibrational excitation (Pastorcic, Vukelic & Bozic 2019). Failure of suspension components can result in the loss of vehicle control and lead to catastrophic accidents. Therefore, durability analysis is compulsory in the design of critical suspension components, especially the coil springs to ensure the safety of the passenger.

The importance of durability analysis in engineering design is to estimate the fatigue life of a structure design under a specific load. Durability analysis becomes increasingly important in the automotive industry when weight optimisation is implemented in automotive design (Paraforos, Griepentrog & Vougioukas 2016). Weight reduction in automotive components to achieve better fuel efficiency renders the components weaker and more susceptible to fatigue failure. Therefore, accurate prediction of the components' fatigue life is essential to ensure good performance of the components during the designated service period. In addition, understanding of the fatigue life of components can facilitate design optimisation to avoid unnecessary waste of materials and reduce maintenance costs (Chauhan, Sah & Kaushal 2021).

Loading condition is the main element in a durability analysis because there are many types of loading in real-life applications. Different fatigue assessment methods are proposed to determine the fatigue life of components under different loading

conditions. For example, rainflow cycle counting determines the fatigue cycle in variable amplitude loading (VAL). Stress-based and strain-based fatigue analyses determine the fatigue life of different components under various loading conditions.

2.3.1 Importance of Durability Analysis

In order to perform a durability analysis, it is required to understand the geometry, material, and loading conditions of the component. Figure 2.7 shows the basic requirements of durability analysis or also known as the "Five-Box Trick". The geometry is required to understand the stress concentration spot in the component where the fatigue crack is more likely to initiate. Computer-aided engineering (CAE) software has been extensively used to perform durability analysis. The material properties refer to some basic mechanical properties, such as tensile strength, modulus of elasticity, yield strength, and others, as well as the fatigue properties of the material that are represented by the stress-life or strain-life curves. The load history (in the form of force, acceleration, stress, or strain) of the component is necessary as it provides essential information, including the number of fatigue cycles, mean stress, and amplitude range for fatigue life prediction.

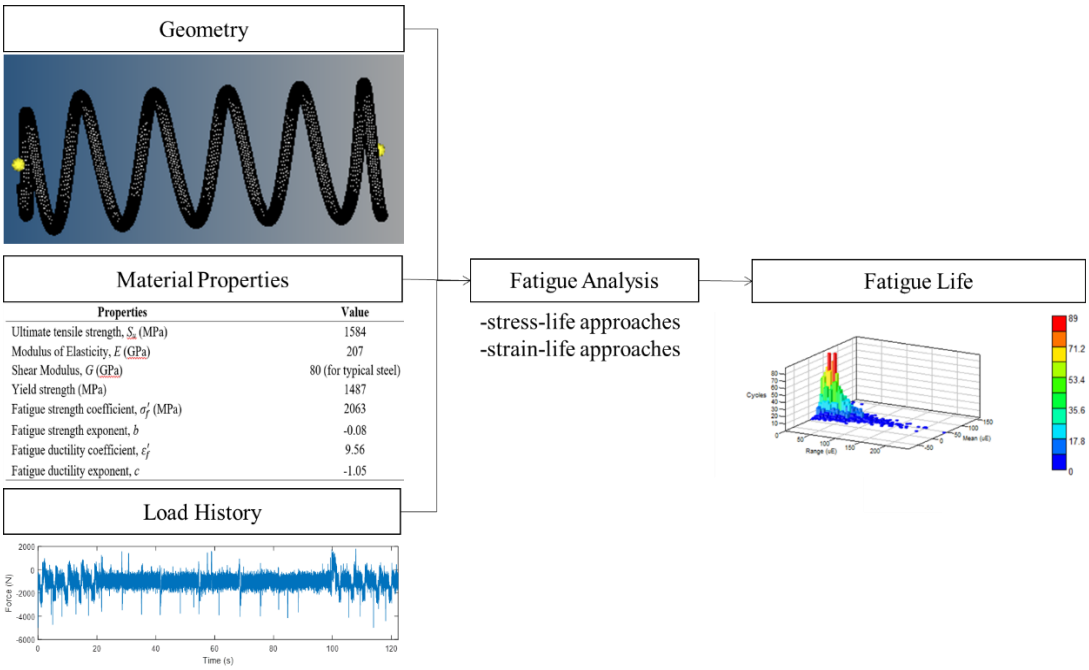

Figure 2.7 "Five-Box-Trick" of durability analysis

Source: Karthik, Chaitanya & Sasanka 2012

After decades of research as shown in Table 2.2, durability analysis has been widely applied to determine the fatigue life of automotive components. Early studies (Abdullah et al. 2006; Qian & Fatemi 1995) of durability analysis mainly focused on the material characterisation and failure analysis to understand the material fatigue properties and fracture mechanism of fatigue failure. Then, studies of durability focused on some engineering applications, such as manufacturing (Prawoto et al. 2008), automotive (Scuracchio, de Lima & Schön 2013; Mayer et al. 2016), and other sectors. In recent development, durability analysis in the automotive industry gradually shifted from laboratory tests to model development for fatigue life prediction (Gan, Wu & Zhong 2021; Nguyen, Oterkus & Oterkus 2021), finite-element-based approaches (Kadhim, Abdullah & Ariffin 2012; Zhang et al. 2019b), and loading signal processing (Putra, Abdullah & Schramm 2020) in order to predict fatigue life under complex loading conditions.

Table 2.2 Research development of durability analysis in automotive industry

Authors	Year	Contribution
Qian & Fatemi	1995	Investigate the influence of ion-nitriding process on the durability performance of SAE 1045 steel at room temperature.
Heyes	1998	Systematic case studies on the failure of automotive components including suspension components. Fatigue failure had been concluded as the main cause of component failure in automotive
Nakano et al.	2001	Developed high-strength suspension coil springs with enhanced corrosion fatigue strength.
Abdullah et al.	2006	Wavelet-based bumps extraction algorithm from strain loading histories of suspension coil spring considering load sequence effect for accelerated durability analysis.
Akiniwa et al.	2008	Investigate the fatigue strength of an oil-tempered spring steel under axial and torsional loading condition up to high cycle regime.
Kaiser, Pyttel & Berger	2011	Report on the fatigue behaviour of shot peened helical compression springs in very high fatigue cycle regime. Fatigue behaviours of difference materials were also studied.
Scuracchio, de Lima & Schön	2013	Investigate the effect of residual stress to the fatigue behaviour of leaf springs.
Pyttel et al.	2014	Comparison of the fatigue properties of helical spring with various dimension, materials and shot peening conditions in the VHCF-region.
Mayer et al.	2016	Investigate the very high cycle fatigue properties of shot-peened spring steel using the ultrasonic fatigue testing technique.
Kong et al.	2018	Applied vibration fatigue model for durability prediction of coil spring based on vibration signals.
Nasir et al.	2020	Risk-based fatigue reliability analysis for suspension coil spring to evaluate the risk level of component exposed to fatigue failure.
Singh, Abdullah & Ariffin	2020	Fatigue reliability assessment of automotive crankshaft considering probabilistic characteristics of randomly induced stress-based fatigue data.

2.3.2 Classification of Loading Signals

Load history is one of the important elements in durability analysis. Fatigue load is a cyclic load that can be represented in different forms, such as force, stress, strain, and acceleration. To understand the characteristics of the signals, the statistical properties of the signals must be determined. Figure 2.8 displays the categories of loading signals based on the statistical characteristics with two main types of deterministic and non-deterministic signals. A deterministic signal can be represented by a specific mathematical function of time and does not vary over time. For example, a sine function as expressed in Equation 2.19 can be categorised as a deterministic signal.

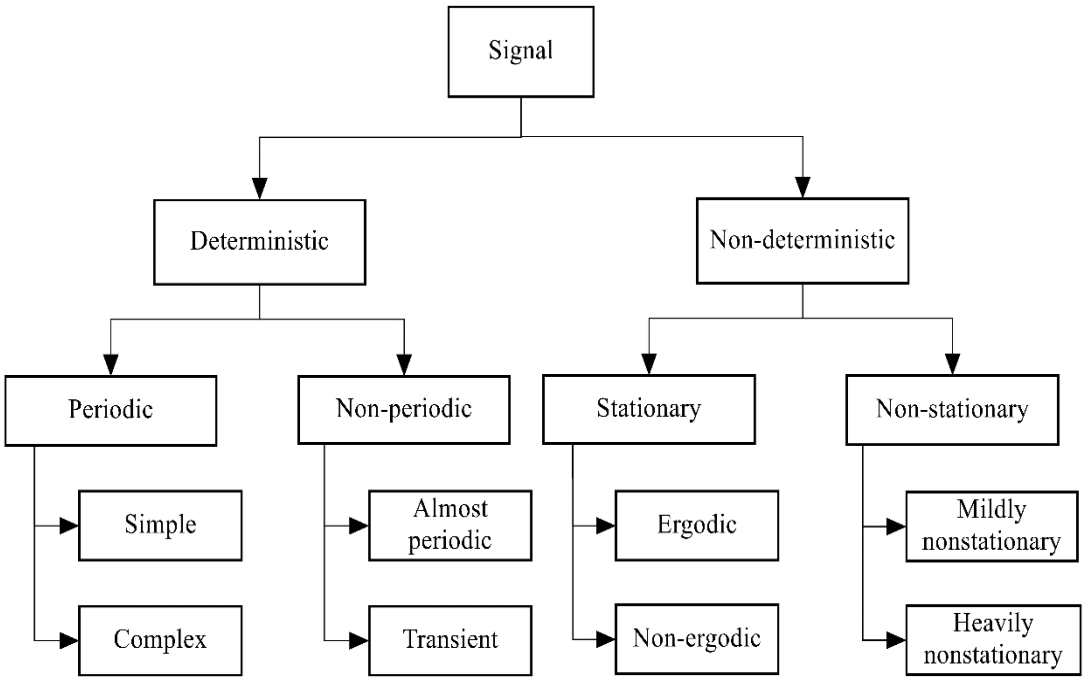

Figure 2.8 Classification of loading signals

Source: Bendat & Piersol 2010

$$f(t) = A_s sin(2\pi f_0 t + \theta) \quad \ldots(2.19)$$

where A_s is the signal amplitude, f_0 is the frequency, and θ is the phase angle. Furthermore, deterministic signals can be divided into periodic and non-periodic. Periodic signals show repeated patterns after a specific time frame while non-periodic signals do not repeat. Simple periodic signals are expressed with only one frequency

and complex periodic signals have multiple frequencies. Non-periodic signals can be almost periodic or quasi-periodic in which the signals show repeating patterns in an infinitely long time frame. Meanwhile, transient signals are patterns with sudden changes within a very short time period.

For non-deterministic signals, the signals can be divided into stationary and non-stationary. A stationary signal has statistics independent of the number of samples in which its statistical properties remain unchanged with time (Altamura & Straub 2014). In contrast, a non-stationary signal refers to the changing statistical characteristics with time (Kihm, Ferguson & Antoni 2015). Mao et al. (2015) mentioned that many vibration signals involving vehicle dynamics are random and non-stationary. Given the complex statistical properties of non-stationary signals, longer simulation time is needed to simulate non-stationary signals compared to stationary signals using finite element approaches (Wolfsteiner 2017). This limits the durability analysis of applications involving non-stationary signals, especially when analysing structures with complex geometries. For stationary signals, an ergodic property means that the signal's statistics are deductible from a realisation of the process (Yaich & El Hami 2019). Non-stationary signals can be further divided into mildly and heavily non-stationary.

2.3.3 Constant Amplitude Loading and Variable Amplitude Loading

In general, the loading of components can be classified into two types, namely constant amplitude loading (CAL) and VAL. A CAL signal fluctuates in amplitude with a constant range. CAL can be characterised by some parameters, such as mean load (F_{mean}), load amplitude (F_{amp}), load range (ΔF), maximum load (F_{max}), minimum load (F_{min}), and load ratio (R), as illustrated in Figure 2.9 (Sarfaraz 2015). It should be noted that the maximum and minimum load, the load range, as well as the load ratio, are technically equivalent. In reality, the mean load and load amplitude are often used to represent CAL. Meanwhile, the load ratio represents the condition of loading, where $0 < R < 1$ indicates tension-to-tension (T-T) loading, $1 < R < +\infty$ shows compression-to-compression (C-C) loading, and $-\infty < R < 0$ expresses a mixed tension-compression (T-C) loading. Mathematically, the mean load, maximum, and minimum load of load cycles are expressed as:

$$F_{mean} = \frac{F_{max}+F_{min}}{2} \quad \ldots(2.20)$$

$$F_{mean} = \frac{F_{max}+F_{min}}{2} \quad \ldots(2.21)$$

$$F_{max} = F_{mean}\text{-}F_{amp} \quad \ldots(2.22)$$

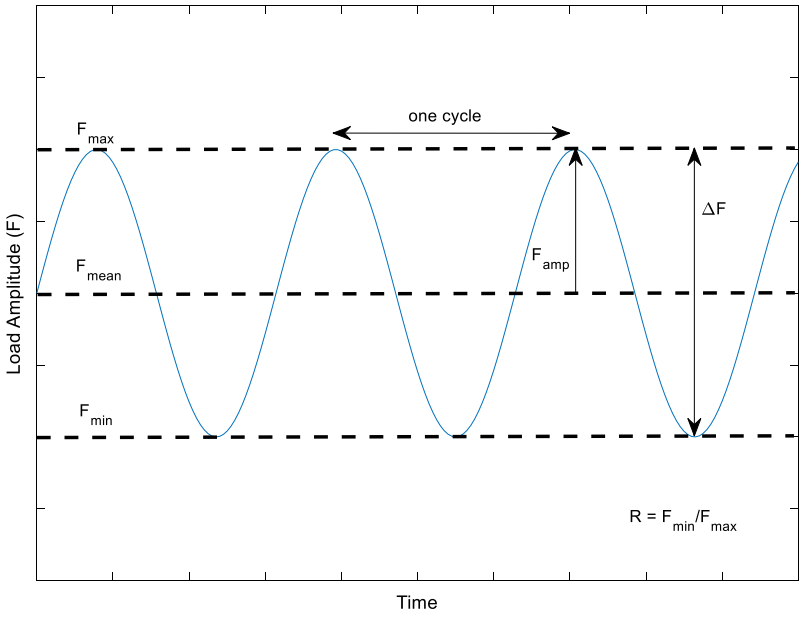

Figure 2.9 Characterisation of a constant amplitude load history

In durability analysis, time series are converted into peak-valley series to extract the necessary information for fatigue life prediction, such as the number of cycles and amplitude range. The peaks and valleys are the turning points of the load amplitude when it reaches maximum and minimum, respectively. Peak-valley series of loading histories are essential in counting the fatigue cycles in the histories. In the case of CAL, fatigue cycle counting is relatively simple and straightforward as all the load cycles in CAL are identical. The fatigue cycle in the CAL signal can be determined between a point and the next point at an equivalent position after a peak and a valley. CAL is often used in laboratory tests for material characterisation, especially fatigue behaviour. For example, Yıldırım, Remes & Nussbaumer (2020) examined the fatigue properties of welded steel joints under the effects of CAL and VAL. Liao et al. (2019) also studied the effects of temperature on the fatigue properties of welded steel joints under CAL.

CAL is used in many applications as the reference for characterising the fatigue properties of materials because the loading pattern is controllable as an important parameter in fatigue tests.

As for VAL, the load history appears to be more complex with alternating load amplitude at different ranges. In some cases, VAL histories are also referred to as random loading when the excitations are random. In many engineering applications, such as automotive, the components are exposed to random loading conditions with variable amplitude ranges (Kong et al. 2018b; Rahim et al. 2020). Unlike CAL histories with simple harmonic cycles, the fatigue cycle extraction process of VAL is more complicated given the complex patterns of VAL histories. Numerous cycle counting methods have been introduced, including range-pair counting, level-crossing counting, reservoir counting, and rainflow counting (Marsh et al. 2016). Among the counting methods, the rainflow cycle counting method is the most widely accepted method as the experimental tests demonstrated good agreement with the measured fatigue cycles (Marsh et al. 2016; Ugras et al. 2019).

2.3.4 Rainflow Cycle Counting in Assessing Fatigue Life

The rainflow cycle counting algorithm was first proposed by Mitsuishi and Endo in 1968 to determine fatigue cycles in uniaxial load time histories (Lee & Tjhung 2012; Mršnik, Slavič & Boltežar 2013). It was given the name because this process identifies the fatigue cycles by linking to the path of rain flowing down at the edge of the pagoda's roof (Marsh et al. 2016). In this algorithm, a full cycle is defined as a stress range of two adjacent points of higher and lower magnitude (Marsh et al. 2016). For a full cycle, the stress path returns to the first turning point and forms a closed stress-strain hysteresis loop. However, there are also some cases where the stress points do not return to the original turning point and form an open hysteresis curve. The stress range is counted as a half-cycle. Given a stress load history, the rainflow algorithm first converts the time series into peak-valley series. Subsequently, the fatigue cycle identification process starts with some small fatigue cycles with closed hysteresis loops, as illustrated in Figure 2.10(a–c). In this process, the identified small cycles are erased from the load history to determine the next fatigue cycle. The remaining large cycles with diverging

hysteresis loops are eventually counted as the half-cycles. The results of rainflow cycle counting are summarised by a histogram with the information on cycle stress/strain range, mean stress/strain, and the number of cycles. Figure 2.11 shows an example of a rainflow histogram determined from a strain load history using a rainflow cycle counting algorithm. The histogram shows the number of fatigue cycles counted with different mean stress and amplitude range values. This enables the calculation of fatigue damage from each fatigue cycle at different mean stress and stress amplitude range using stress-life or strain-life approaches.

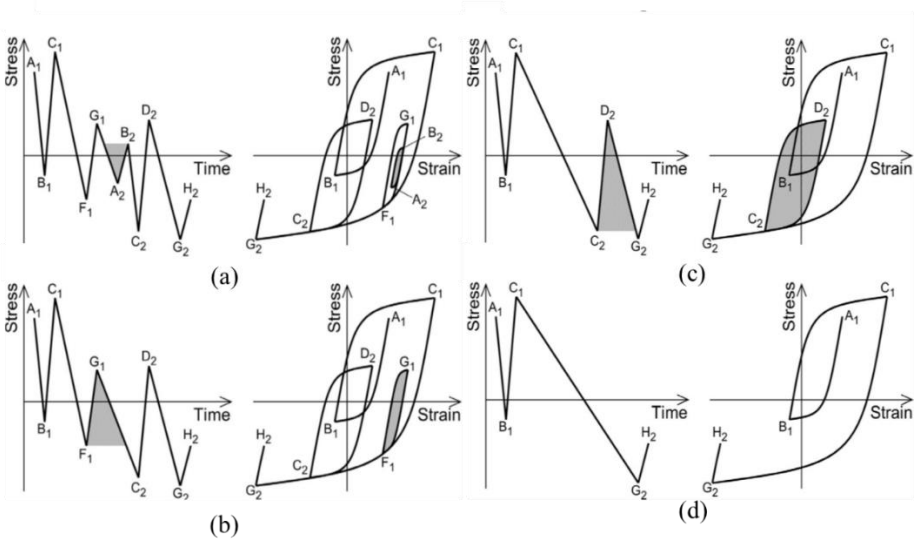

Figure 2.10 Procedures of rainflow cycle counting algorithm in extracting fatigue cycles from a load history: (a) small full cycle, (b) medium full cycle, (c) large full cycle, (d) half-cycles

Source: Marsh et al. 2016

2.3.5 Fatigue Life Prediction using Stress-Life Approaches

Fatigue life prediction of components subjected to cyclic loading is based on the "safe-life" approaches (Santecchia et al. 2016). Fatigue life is the number of load cycles in which a component can sustain before failure under specific loading conditions (Chetan, Khushbu & Nauman 2012). Fatigue life assessment can be generally categorised into two, namely the high cycle fatigue (HCF) regime and the low cycle fatigue (LCF) regime. The HCF regime refers to fatigue failure that occurs above the fatigue life of 1×10^4 cycles, while the LCF regime takes place below 1×10^4 cycles (Mansor et al.

2014). For fatigue failure occurring in the region up to 1×10^7 cycles, the failure is classified as very high cycle fatigue (VHCF) (Mayer et al. 2016).

Many components with large structures, such as rotating turbine blades and building structures, are designed with HCF because the components are expected to sustain a large number of fatigue cycles (Fu et al. 2020; Pratumnopharat, Leung & Court 2014). In the HCF regime close to the endurance limit in which the material behaves elastically, the stress in the component that contributes to fatigue damage is dominantly elastic stress and the presence of plastic stress is hardly detected. Therefore, stress-life (*S-N*) approaches that consider elastic stress are appropriate for HCF applications (Roostaei et al. 2019). *S-N* approaches consider the fatigue life caused by the initiation and propagation of crack until failure happens. The concept of *S-N* approaches was first introduced by a German engineer, August Wöhler in 1867 by assuming that the nominal elastic stress has a power relationship with the fatigue life (Karthik, Chaitanya & Sasanka 2012). Mathematically, the *S-N* power relationship (also known as *S-N* curve) can be expressed as follows:

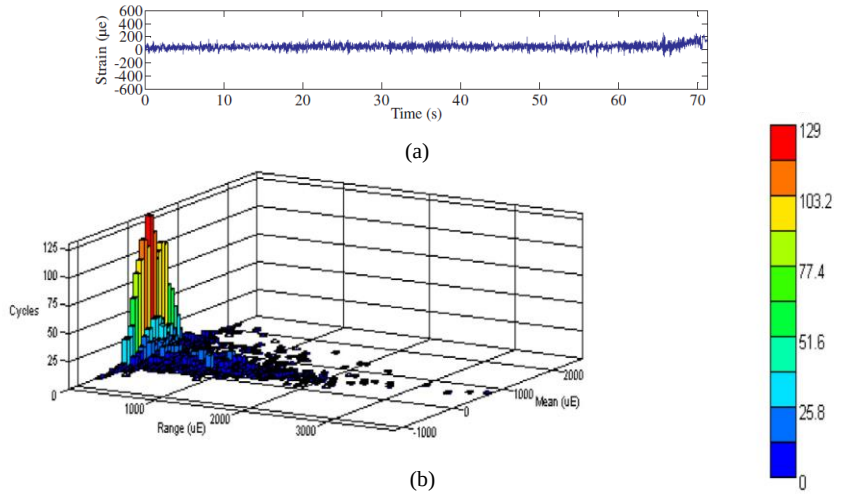

Figure 2.11 Rainflow analysis of a strain load history: (a) strain histories, (b) rainflow histogram

Source: Putra, Abdullah & Schramm 2020

$$\sigma_a = \sigma_f'(2N_f)^b \qquad \ldots(2.23)$$

where σ_a is the stress amplitude, $2N_f$ is the reversal to failure, σ_f' is the fatigue strength coefficient, and b is the fatigue strength exponent. Figure 2.12 shows the *S-N* curve of steel material with the fatigue life regime of LCF, HCF, and VHCF.

An *S-N* curve is typically obtained from a controlled test with zero mean stress. Positive mean stress indicates a tensile load while a compressive load has negative mean stress. However, it was found that tensile load brings more fatigue damage to the structure compared to compressive load, and this phenomenon is known as the mean stress effect (Marsh et al. 2016; Niesłony & Böhm 2013). This is because tensile load is likely to contribute to crack opening stress compared to compressive load. To consider the influence of non-zero mean stress on fatigue damage, several mean stress correction models, including the Soderberg, Goodman, and Gerber models were proposed to determine the equivalent stress under non-zero mean stress conditions prior to the fatigue damage calculation (Chen 2014). Equation 2.24 shows the universal representation of the Soderberg, Goodman, and Gerber models (Marsh et al. 2016):

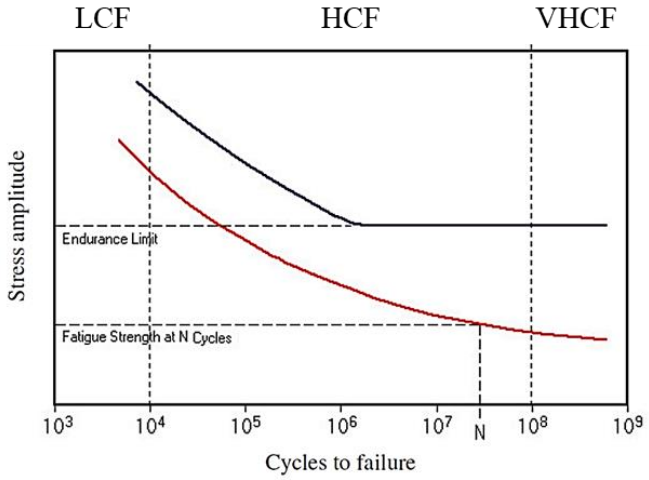

Figure 2.12 *S-N* curve of steel material showing the fatigue life regime of LCF, HCF and VHCF

Source: Niesłony & Böhm 2013

$$\Delta\sigma_{\bar{\sigma}} = \Delta\sigma_0 \left(1 - \left[\frac{\bar{\sigma}}{\sigma_{UTS}} \right]^Z \right) \qquad \ldots(2.24)$$

where $\Delta\sigma_{\bar{\sigma}}$ is the stress range at non-zero mean stress, $\Delta\sigma_0$ is the equivalent stress range at zero mean stress, $\bar{\sigma}$ is the mean stress, and σ_{UTS} is the ultimate strength of the

material. The value of Z is 1 and 2 for the Goodman and Gerber mean stress correction relations, respectively. For the Soderberg mean stress correction, the ultimate strength is replaced with the yield strength of the material and the Z value is 1. Equations 2.25, 2.26, and 2.27 give the Goodman, Gerber, and Soderberg mean stress correction, respectively:

$$\Delta\sigma_{\bar{\sigma}} = \Delta\sigma_0 \left(1 - \left[\frac{\bar{\sigma}}{\sigma_{UTS}}\right]\right) \quad \ldots(2.25)$$

$$\Delta\sigma_{\bar{\sigma}} = \Delta\sigma_0 \left(1 - \left[\frac{\bar{\sigma}}{\sigma_{UTS}}\right]^2\right) \quad \ldots(2.26)$$

$$\Delta\sigma_{\bar{\sigma}} = \Delta\sigma_0 \left(1 - \left[\frac{\bar{\sigma}}{\sigma_y}\right]\right) \quad \ldots(2.27)$$

The mean stress correction models are only applicable in tensile loading conditions. Therefore, under compression loading conditions, it is assumed that:

$$\Delta\sigma_{\bar{\sigma}} = \Delta\sigma_0 \quad \ldots(2.28)$$

The mean stress correction models are insufficient as they only provide an accurate prediction of fatigue life under tensile loading. Dowling (2004) investigated the fatigue properties of steel and aluminium specimens with *S-N* approaches and found that fatigue life prediction with ultimate tensile strength was highly inaccurate. In addition, *S-N* approaches only emphasise on the nominal stress of the specimens and do not consider the cyclic hardening and softening of the material during deformation. Therefore, a model that can predict the fatigue life by considering the cyclic hardening effects is needed. This has led to the development of strain-life (ε-*N*) approaches for durability analysis.

2.3.6 Fatigue Life Prediction using Strain-Life Approaches

The strain-life (ε-*N*) approach provides greater accuracy of fatigue life prediction in a low fatigue cycle regime below 1×10^4 cycles (Mansor et al. 2014). This approach

considers the local strain that includes both elastic and plastic strain. In 1910, O. H. Basquin proposed a linear elastic stress-strain relationship for *ε-N* approaches, as mentioned by Santecchia et al. (2016). The Basquin stress-strain relationship is derived from the *S-N* relationship in Equation 2.29, such that:

$$\sigma_a = \frac{E.\Delta\varepsilon}{2} = \sigma_f^{'}(2N_f)^b \quad \ldots(2.29)$$

where $\Delta\varepsilon$ is the strain range in the elastic region and E is the modulus of elasticity. In 1954, S. S. Manson expressed the relationship of plastic strain with fatigue life as follows:

$$\varepsilon_a^p = \varepsilon_f^{'}(2N_f)^c \quad \ldots(2.30)$$

with ε_a^p, $\varepsilon_f^{'}$ and c correspond to plastic strain amplitude, fatigue durability coefficient, and fatigue durability exponent, respectively. Combining Equations 2.29 and 2.30 becomes the widely used Coffin-Manson strain-life relationship that determines the fatigue life in both elastic and plastic strain ranges. The Coffin-Manson strain-life relationship is written as (Kong et al. 2019a):

$$\varepsilon = \varepsilon_a^e + \varepsilon_a^p = \frac{\sigma_f^{'}}{E}(2N_f)^b + \varepsilon_f^{'}(2N_f)^c \quad \ldots(2.31)$$

where ε is the total strain amplitude and ε_a^e is the elastic strain amplitude.

The Coffin-Manson relationship was applied for the durability of many automotive suspension components, such as coil springs (Nasir et al. 2020), leaf springs (Loganathan, Vinoth Kumar & Madhu 2020), and lower suspension arms (Yuan-Chun 2019), and good accuracy in fatigue life prediction was reported. Karthik, Chaitanya & Sasanka (2012) reported that the Coffin-Manson relationship showed higher sensitivity of fatigue life prediction, especially in the low fatigue cycle regime compared to *S-N* approaches. However, one major limitation of the Coffin-Manson relationship is that it

does not consider the mean stress effects and gives over-conservative fatigue life prediction when the load is non-zero mean stress (Dowling 2004).

Morrow introduced the mean stress into the Coffin-Manson model as a mean stress correction factor, such that:

$$\varepsilon = \frac{\sigma_f^{'}-\sigma_m}{E}(2N_f)^b+\varepsilon_f^{'}(2N_f)^c \quad \ldots(2.32)$$

where σ_m denotes the mean stress, which is positive in tension and negative in compression. In addition, K. N. Smith, P. Watson, and T. H. Topper proposed another mean stress correction for the ε-N curve in 1970. This model is known as Smith-Watson-Topper (SWT) model. For the SWT model, the maximum stress of the hysteresis cycles is taken as the mean stress correction parameter. The SWT model is expressed as:

$$\sigma_{max}\varepsilon = \frac{\left(\sigma_f^{'}\right)^2}{E}(2N_f)^{2b}+\sigma_f^{'}\varepsilon_f^{'}(2N_f)^{b+c} \quad \ldots(2.33)$$

with the maximum stress, $\sigma_{max} = \sigma_m+\sigma_a$. The SWT model was proven to be more robust compared to the Morrow model with better accuracy in fatigue life prediction and applicable for a wide variety of materials (Ince & Glinka 2011). Karthik, Chaitanya & Sasanka (2012) also agreed that the Morrow model is more conservative than the SWT model in durability prediction under tensile loading.

Finally, the fatigue damage contributed by each fatigue cycle needs to be calculated to determine the fatigue life. The most commonly used fatigue damage rule is the Palmgren-Miner linear damage rule, which expresses the accumulated fatigue damage as (Gates & Fatemi 2018):

$$D_f = \sum \frac{n_i}{N_{fi}} \quad \ldots(2.34)$$

where n_i is the number of fatigue cycles at specific stress counted from the loading block. A zero D_f value indicates no fatigue damage, while fatigue failure is predicted to happen at D_f = 1. The Palmgren-Miner rule has limitations in considering the load sequence effect between loading blocks with variable amplitudes (Wang, Serra & Argoul 2019). Several fatigue damage models, such as the modified Palmgren-Miner rule, Marko-Starker relationship and the Morrow approach that consider the non-linear relation between fatigue cycles have been proposed (Mansor et al. 2014). These non-linear models have shown better performance in the fatigue life assessment of VAL considering the effect of cycle sequence. However, the non-linear damage rules often need material parameters, which significantly increase the complexity of durability analysis. Regardless of the incapability of the Palmgren-Miner rule in considering the load sequence effect, the linear damage rule is still used in many designs, mainly due to its simplicity and low computational effort (Xia et al. 2020).

2.3.7 Loading Sequence Effect and Effective Strain Damage Approach

As the simple linear damage summation rule is applied in the *S-N* and ε-*N* approaches mentioned earlier, it is also important to note that these approaches exclude the effect of loading sequence in the fatigue life assessment (Wang, Serra & Argoul 2019). This is because the summation of fatigue damage using the Palmgren-Miner rule is cumulative and there is no concern about the sequence of cycles' occurrence (Santecchia et al. 2016). However, VAL with large fluctuations of mean stress often has a significant influence on the fatigue crack growth behaviour, and thus, affecting the final fatigue life.

Fiedler & Vormwald (2016) remarked that the load sequence effect in components can be due to local plastic deformation. Tensile stress often causes higher damage compared to compressive stress (Marsh et al. 2016). This shows that after local plastic deformation owing to overloading, the mean stress is changed and the fatigue properties are also affected. Therefore, the consideration of the load sequence effect is necessary for fatigue analysis. Several models have been proposed to consider the effect of cycle sequence under VAL. For example, Fiedler & Vormwald (2016) proposed a local strain approach for the consideration of the load sequence effect. Furthermore,

several non-linear damage rules were also proposed as an alternative to replace the Palmgren-Miner linear damage rule that could not evaluate the load sequence effect (Zhu, Liu & Huang 2017; Zhu et al. 2019b; Xia et al. 2020). Mansor, Abdullah & Ariffin (2019) also proposed a fatigue life predictive model of crack growth under load sequences through modification of the Walker crack closure model. Although the proposed models showed better improvement in durability prediction, many of these approaches have limitations for practical use due to the complex computational procedures and requirement of complete material information (Calderon-Uriszar-Aldaca & Biezma 2017). Therefore, an acceptable durability prediction approach that can evaluate the load sequence effect for general use is needed by the industry.

The strain-life fatigue model was proposed by DuQuesnay et al. (1992) and Topper & Lam (1997) using the concept of effective strain range that was successfully applied to various alloy and loading histories. The effective strain range model was modified from the *S-N* relationship by determining the effective strain range in a closed hysteresis loop. The model is suitable for various materials, loads, geometries, and also the mean-stress effect. This model assumes the effective strain range as the fatigue damage parameter, as defined in the following equation:

$$E.\Delta\varepsilon_{eff} = A(N_f)^B \qquad \ldots(2.35)$$

where $\Delta\varepsilon_{eff}$ is the net effective strain range in a closed hysteresis loop, N_f is the fatigue cycle to failure, and A and B are material constants. The effective strain range of each cycle depends on the current crack opening stress that changes with the overload. Therefore, the cycle sequences and the mean stress are important in the evaluation of the effective strain range. Figure 2.13 shows the determination of effective strain range from different rainflow cycles under a constant crack opening stress level.

From Equation 2.35, $E.\Delta\varepsilon_{eff}$ is a function of crack opening stress (S_{op}) and can be defined as:

$$E.\Delta\varepsilon_{eff} = E(\varepsilon_{max}-\varepsilon_{op})-E\varepsilon_i \qquad \ldots(2.36)$$

where ε_{max} and ε_{op} are the maximum and crack opening strains of a particular cycle, respectively. For a hysteresis loop, if ε_{op} is smaller than the minimum strain (ε_{min}), then ε_{op} is equal to ε_{min}. ε_i is the intrinsic fatigue limit strain range of the material.

The steady-state crack opening stress is a function of the maximum stress, such that (El-Zeghayar, Topper & Bonnen 2013):

$$S_{ss} = \alpha_s \sigma_{max} \left(1 - \left(\frac{\sigma_{max}}{\sigma_y} \right)^2 \right) + \beta_s \sigma_{min} \quad \ldots(2.37)$$

where α_s and β_s are material constants obtained by a curve fitting of the experimentally measured crack opening stress versus the maximum stress (σ_{max}), σ_{min} is the minimum stress, and σ_y is the yield strength of the material. A large overload cycle and a partially open cycle have minimum stress below the crack opening stress ($S_{op} > S_{min}$) and the effective strain is determined from the portion of the hysteresis loop above the baseline of the crack opening stress, as shown in Figure 2.13(a–b). For a fully closed cycle with minimum stress above the crack opening stress as in Figure 2.13(c), the entire strain range of the loop is taken as the effective strain range. One major drawback of the effective strain range model developed by DuQuesnay et al. (1992) is the assumption of a constant crack opening stress level for the entire load histories during the fatigue damage calculation. The crack opening stress is a changing variable that depends on the previous cycles. This can introduce significant error in the fatigue analysis results, especially when the cycles in the load histories have large changes in mean stress that could lead to a large margin in the crack opening stress.

To determine the effect of load interaction, Abdullah et al. (2006) proposed the effective strain damage (ESD) model by modifying the effective strain range model based on the integration of crack growth and crack closure. In the ESD model, the crack opening stress differences between adjacent cycles are expressed by a decay parameter m_d, such that (Khalil & Topper 2003):

$$\Delta S_{op} = m_d (S_{ss} - S_{cu}) \quad \ldots(2.38)$$

where S_{cu} is the current opening stress and S_{ss} is the steady-state opening stress as expressed in Equation 2.37. The crack opening stress decay parameter, m_d represents the rate of the decay of the crack opening stress after an overload, followed by underload cycles. Based on Equation 2.38, the value of m_d is experimentally determined from a series of fatigue damage tests (El-Zeghayar, Topper & Bonnen 2013). The m_d parameter measured directly from the crack opening stress after an underload is applied until the crack opening stress level return to a steady-state condition. Based on the work done by El-Zeghayar, Topper & Soudki (2011), the test was conducted using different values of frequencies to form the underload conditions. The changes in fatigue life values were obtained in terms of damage per block. These change values were used to determine the m parameter. Several studies (El-Zeghayar, Topper & Bonnen 2013; El-Zeghayar, Topper & Soudki 2011; Khalil & Topper 2003) performed crack opening stress measurements over three steel materials (i.e., DP 590, SAE 1045, and AISI 8822) to determine the crack closure parameter m_d of the materials. There are also studies that adopted m_d parameter from the literature for fatigue life prediction using the ESD model. Table 2.3 shows the values of m_d reported in the studies.

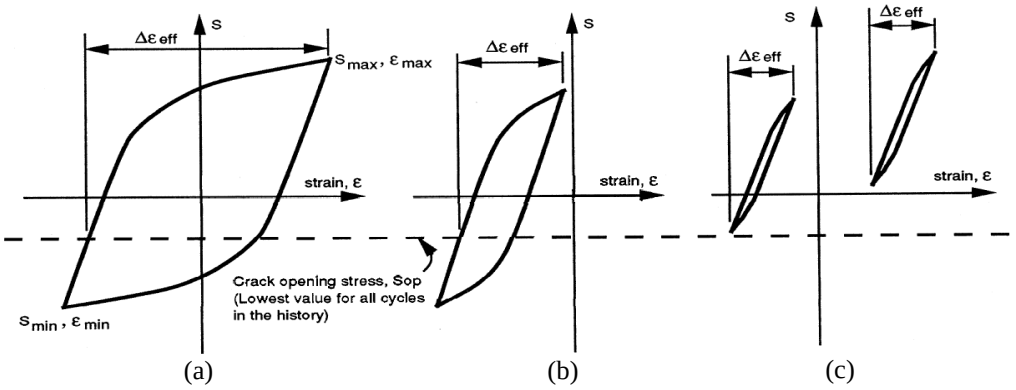

Figure 2.13 Determination of effective strain range from various type of rainflow cycle: (a) overload with large plasticity, (b) partially open cycle, $S_{op} > S_{min}$, (c) fully open cycle, $S_{op} < S_{min}$

Source: DuQuesnay, Pompetzki & Topper (1993)

Based on the ΔS_{op} , crack-opening stress (S_{op}) of a cycle is given as:

$$S_{op} = E\varepsilon_{op} = S_{cu}\text{-}\Delta S_{op} \quad \ldots(2.39)$$

with S_{cu} as the current crack opening stress, which is the S_{op} of the previous cycle. Subsequently, the fatigue life (N_f) is calculated from Equations 2.35 and 2.36. Prior to the fatigue life calculation using the ESD model, it is essential to note that the rainflow cycles in strain histories have to be rearranged according to their cycle sequences in the loading histories (Abdullah et al. 2006; Kadhim, Abdullah & Ariffin 2012). This is because the cycle sequences have a significant effect on the calculation of the crack opening stress level and affect the fatigue life assessment process using the ESD model.

Table 2.3 Values of m_d parameters determined in previous studies over different materials

Authors	Year	m_d parameter of steel material		
		DP 590	SAE 1045	AISI 8822
El-Zeghayar, Topper & Bonnen	2013	0.023	0.008	0.0009
Kadhim, Abdullah & Ariffin	2012	-	0.002	-
El-Zeghayar, Topper & Soudki	2011	0.023	0.008	0.0009
Abdullah et al.	2006	-	0.002	-
Khalil & Topper	2003	-	0.002	-

Abdullah et al. (2006) introduced the ESD model for the fatigue life prediction of coil spring under VAL and performed bump extraction from the load histories whilst preserving the load sequence effect. It was reported that the ESD model was a suitable approach for fatigue life assessment considering the load sequence effect compared to conventional strain-life approaches. Apart from that, Kadhim, Abdullah & Ariffin (2012) also adopted the ESD model in the durability analysis of the suspension lower control arm using finite element analysis (FEA). From their work, it was reported that the ESD model demonstrated better prediction of fatigue life based on the FEA model and proved the capability of the ESD model in accounting for the load sequence and mean stress effects.

2.4 SIGNAL ANALYSIS

The loading histories of mechanical systems or structures often contain important information related to the behaviours of the systems. Therefore, signal processing is increasingly important in engineering applications to characterise and extract the desired information hidden in the signals. For example, fatigue failures that happened in various engineering structures are closely related to the loads subjected to the components. Hence, analyses to characterise the signal patterns are vital to determine

the durability of the components and estimate the remaining fatigue life. In automotive applications, signal acquisition is the first step to assess the performance of the systems or detect any system fault.

Durability analysis of automotive is to achieve the desired specifications and strength capacity of the designed components or systems by relating to the load conditions under a real operating environment (Burger, Dreßler & Speckert 2021). The characterisation of the load distribution, especially for automotive applications, is a great challenge due to the complex loading conditions in real life applications. Many loading conditions are completely random and stochastic, which add more difficulty to the modelling of the loads. For durability analysis, the loading histories are one of the important elements as they represent the loading conditions of the component and are essential for fatigue damage characterisation. Loading histories are often obtained as time series, and signal processing methods are applied to extract valuable information.

2.4.1 Signal Processing in Time Domain

Loading signals are used to determine the fatigue damage using time-domain approaches, such as *S-N* or ε-*N* approaches. Fatigue cycles are determined from time load histories with rainflow cycle counting and fatigue damage is subsequently calculated with fatigue models (Marsh et al. 2016; Singh, Abdullah & Ariffin 2020). Later, studies have focused on the statistical modelling of the loading distribution to investigate the influence of loading statistical parameters on the durability performance (Kihm, Ferguson & Antoni 2015; Cianetti et al. 2017; Palmieri et al. 2017). For example, the loading behaviour can be generally classified based on stationarity or Gaussianity and observed based on the kurtosis of the loading distribution (Palmieri et al. 2017). Kihm, Ferguson & Antoni (2015) demonstrated that non-stationary load distribution with kurtosis larger than three contributed to more severe damage to the structure. Statistical modelling of loading distribution is absolutely beneficial for simulating the loading environment, rather than depending on the time loading signals, which often involve high experimental costs and time for data sampling (Burger, Dreßler & Speckert 2021; Kong et al. 2018a). The time loading histories provide valuable information for durability analysis, and it is also necessary to determine the

signal behaviours in the frequency domain as the components have different responses under various loading frequencies. Therefore, frequency domain signal processing methods were introduced to investigate the signal properties in frequency domain.

2.4.2 Signal Processing in Frequency Domain

When traditional time-domain approaches, such as *S-N* and *ε-N* approaches are proven to be too computational heavy for durability analysis, especially for components with complex geometries and loading conditions, frequency-domain approaches start to receive considerable research attention (Mršnik, Slavič & Boltežar 2018). This is because time-domain approaches often need very long loading histories to sufficiently represent the statistics of the loading condition of real-life applications (Wang, Burger & Aloe 2017). The frequency-domain approaches offer a much lighter computational load with acceptable fatigue life prediction because frequency-domain approaches do not require a long-time signal to represent the load (Capponi et al. 2017; Mršnik, Slavič & Boltežar 2013). Several vibration fatigue models, such as narrow-band approximation, Dirlik, Tovo-Benasciutti, and Tovo's $\alpha_{0.75}$ methods have been introduced for fatigue life assessment using vibration signals in the frequency domain (Ugras et al. 2019). For vibration fatigue analysis in the frequency domain, the vibrational time signal is converted into the frequency domain using Fourier transform.

In 1822, a French mathematician, Joseph Fourier, showed that all time functions could be written as an infinite sum of harmonics with different frequencies. Mathematically, the Fourier transform of a time function $f(t)$ is expressed as an inner product with a sinusoidal wave $e^{j\omega t}$, such that (Zhu, Wong & Hong 2009):

$$\hat{f}(\omega) = \langle f(t), e^{j\omega t} \rangle = \int_{-\infty}^{\infty} f(t) e^{j\omega t} dt \qquad \ldots(2.40)$$

with $\hat{f}(\omega)$ as the Fourier transform and ω denotes the frequency. The Fourier transform converts the time signal from the time domain into the frequency domain and becomes the basis of signal processing in the frequency domain. Later, the introduction of Fast Fourier transform (FFT) further accelerated the calculation of the frequency spectrum

and became a standard for signal processing in the frequency domain (Szymański et al. 2015). The Fourier transform has limitation of overshooting when there is discontinuity in the time series and could result in non-convergence of the Fourier series. In many studies (Luo, Huang & Zhou 2018; Ugras et al. 2019) that investigated the signals in the frequency domain, the signals are represented in the form of power spectral density (PSD). The PSD of the signal contains some essential characteristics of the signal, such as the energy content of the signal within a frequency band (Chen, Fan & Zhang 2013). PSD can be expressed as the mean square value in a unit of frequency band within a Fourier transform series length *N*, such that (Dai et al. 2018):

$$P(\omega) = \frac{1}{N}\left|\hat{f}(\omega)\right|^2 \qquad \ldots(2.41)$$

Both time- and frequency-domain methods have the limitation of revealing the signal characteristics in the time and frequency domain simultaneously. To solve this problem, the time-frequency domain signal processing methods are introduced.

2.4.3 Signal Processing in Time-Frequency Domain

The frequency components in the entire signal can be revealed using Fourier transform. However, Fourier transform has a critical limitation as this method is unable to analyse any local frequency properties of the time signal (Manhertz & Bereczky 2021; Mao et al. 2015). This is because the Fourier transform is the integration of time function for all times. Thus, it only reveals the global properties of frequencies in the time function. Therefore, the Fourier transform is not suitable for the processing of non-stationary signals because it cannot detect some time-localised features, such as impulses. To overcome this deficiency, Dennis Gabor adopted a windowing technique on Fourier transform and the new technique was named short-time Fourier transform (STFT) (Pratumnopharat, Leung & Court 2013). In STFT, a sliding window function *g(t)* is introduced into Fourier transform to obtain the localised time-frequency properties, such that (Zhu, Wong & Hong 2009):

$$STFT\,(t,\omega)=\int_{-\infty}^{\infty} f(t)g(t-u)e^{j\omega t}dt \qquad \ldots(2.42)$$

where u is the time position of the window. Frequency spectral of each localised windowed segment that reveals the time-frequency properties of the signal is obtained. Nevertheless, STFT also has its own limitation in time-frequency resolution. According to the Heisenberg uncertainty principle, a high resolution in time and frequency cannot be attained simultaneously. This is because STFT is still limited by the single triangular basis of Fourier transform, in which Fourier transform can detect harmonic features but is less effective in detecting impulse features in non-stationary signals (Chen et al. 2016). For fatigue signals, sudden changes often occur at high frequencies, which need a smaller window to detect the changes (Putra et al. 2017b). Hence, STFT is less favourable for the processing of fatigue signals owing to its limitation in time-frequency resolution. As a solution to the insufficient time-frequency resolution of STFT, wavelet transform was introduced by Morlet in 1982 (Li & Chen 2014). The wavelet transform can be categorised into continuous wavelet transform (CWT) and discrete wavelet transform (DWT). Table 2.4 summarises significant research works that applied time-frequency analysis for fatigue data editing (FDE) since the year 2001.

2.4.4 Continuous Wavelet Transform (CWT)

CWT was designed to meet the demand for an adaptive time-frequency analysis, which was not seen in Fourier analysis (Alhasan, White & De Brabanterb 2016). Unlike STFT which adopts harmonic function as the basis function, CWT uses families of wavelets as its basis function that better matches the transient features that are usually seen in non-stationary signals (ALTobi et al. 2019). The wavelet refers to a function with compact support in which the function is non-zero only within a finite interval. CWT can convert a time signal into a representation with simultaneous localised information in time and frequency domains, known as wavelet coefficients (Amin et al. 2013). The sets of wavelet coefficients are often presented in the form of a scalogram, a two-dimensional contour plot in which one axis represents the time (translation) while another axis represents the scale or frequency at different levels of resolution, as illustrated in Figure 2.14 (Li & Chen 2014). At the lowest resolution level, the

coefficients describe the low-frequency features of the data, while the highest level projects the highly localised high-frequency features (Cruz, Mendes & Magalhães 2001).

Table 2.4 Summary of research works related to fatigue data editing using time-frequency analysis since 2001

Author(s)	Year	Time-frequency analysis	Contribution
Oh	2001	DWT	First work to apply wavelet theory for FDE application
Steinwolf, Giacomin & Staszewski	2002	DWT	Apply orthogonal wavelet decomposition filtering method for bumps identification in vibration signals of automobiles.
Abdullah et al.	2006	DWT	Developed wavelet-based bumps extraction algorithm whilst preserving load sequence effect of loading histories.
Abdullah, Nizwan & Nuawi	2009	STFT	Applied STFT together with the distribution of Accumulative Power Spectral Density for FDE of strain time histories and successfully removed low amplitude cycles.
Pratumnopharat, Leung & Court	2013	STFT	Applied STFT for FDE of stress time histories of wind turbine blades and achieved signal reduction of 15.38%.
Pratumnopharat, Leung & Court	2014	CWT	Applied CWT for FDE of stress time histories of wind turbine blades and achieved signal reduction of 20.77%.
Putra et al.	2017	CWT	Characterise signal energy with Morlet wavelet for extraction of high damaging section in strain loading histories of coil spring.
Shangguan et al.	2020	DWT	Proposed a modified down-sampling algorithm and a wavelet transform-based spectrum editing method that effectively accelerated the durability analysis of mechanical components.

The apparent advantages of CWT in time-frequency resolution over traditional STFT have attracted extensive research attention in applying CWT to solve problems involving partial differential equations in the 1990s (Canuto, Tabacco & Urban 1999, 2000; Chen & Wu 1995; Cruz, Mendes & Magalhães 2001). The introduction of CWT has been a paradigm shift in mathematics and engineering fields, which shed a light on the solution of problems involving singularities and steep changes, such as stress concentration, elastoplasticity, shock wave, and crack (Hariharan & Kannan 2014; Li & Chen 2014). CWT provides possible solutions to process the signals with many transient events, especially the fatigue loading data. Many researchers (Pratumnopharat,

Leung & Court 2014; Putra et al. 2017b; Shangguan et al. 2020) sought solutions for fatigue damage and durability analyses in engineering structures through CWT.

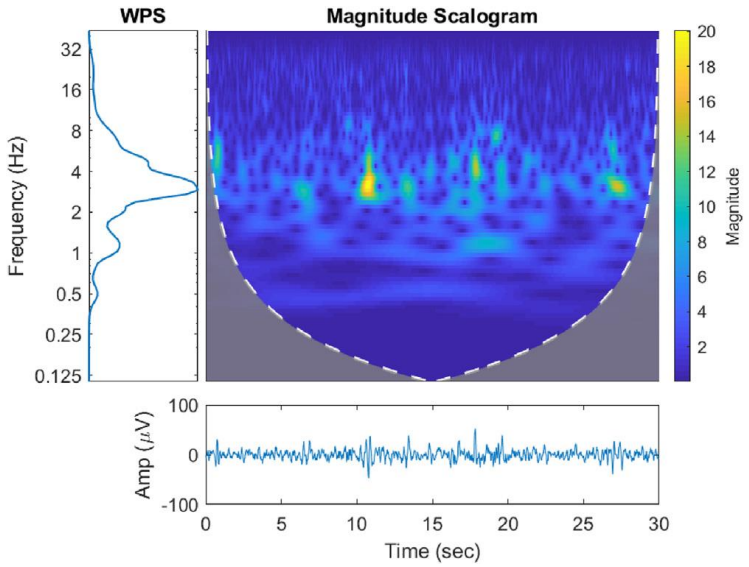

Figure 2.14 A scalogram of obtained by CWT to visualise the time-frequency properties.

Source: ALTobi et al. 2019

CWT originates from the idea of dilation and translation of the wavelet functions to adapt the non-stationary features in the signal (Chen et al. 2016). Unlike STFT with a fixed size window, CWT uses a window function with variable size, where the window size becomes larger at a lower frequency and vice versa. The variable window size at different scales gives adaptive time-frequency resolution in CWT compared to STFT. CWT is an analysis of breaking the time function into shifted and scaled version of the mother wavelet $\psi_{s,u}(t)$ as given below (Jadhav et al. 2020):

$$\psi_{s,u}(t) = \frac{1}{\sqrt{s}}\psi\left(\frac{t-u}{s}\right) \qquad \ldots(2.43)$$

where s is the scaling parameter and u is the shift parameter. The mother wavelet must fulfil the following admissive conditions (Zhu, Wong & Hong 2009):

$$\int_{-\infty}^{\infty}\psi(t)\,dt = 0\,,\ \int_{-\infty}^{\infty}\psi^2(t)\,dt = 1 \qquad \ldots(2.44)$$

The CWT wavelet coefficients of a signal $f(t)$ are mathematically expressed as the inner product of the mother wavelet function and the time signal, such that (ALTobi et al. 2019):

$$W_{\psi}f(s,u) = \left\langle f(t) , \psi_{s,u}(t) \right\rangle = \frac{1}{\sqrt{s}} \int_{-\infty}^{\infty} f(t) \psi^{*}(\frac{t-u}{s})\, dt \qquad \ldots(2.45)$$

where ψ^{*} represents complex conjugate of the mother wavelet function.

The original signal can be reconstructed using the inverse wavelet transform as expressed in Equation 2.46:

$$f(t) = \frac{1}{C_{\psi}} \int_{-\infty}^{+\infty} \int_{-\infty}^{+\infty} |s|^{-1/2} \psi \left(\frac{t-u}{s} \right) W_{\psi}f(s,u) \frac{dsdu}{s^2} \qquad \ldots(2.46)$$

where

$$C_{\psi} = 2\pi \int_{-\infty}^{+\infty} \frac{|\psi(\xi)|^2}{|\xi|} d\xi \qquad \ldots(2.47)$$

and $\psi(\xi)$ is the Fourier transform of the wavelet function.

The CWT coefficients are defined as the total of the multiplication between the time signal with the shifted and scaled version of the mother wavelet function over the entire sampling period of time. Nonetheless, CWT is found to be too computational heavy because CWT supplies a huge amount of data (Barelli et al. 2012). In many cases, the information provided by CWT is over-detailed, and this results in unnecessary waste of computational time. To improve the computational efficiency of CWT, DWT was developed. DWT is implemented by filtering the signal in two channels using a low-pass filter and a high-pass filter, followed by down-sampling the outputs by a factor of two (Rabi, Balusamy & Raj Jawahar 2019). This process is known as signal decomposition as the signal is decomposed into different levels with various frequency ranges. In engineering applications, DWT is implemented with the Mallat pyramidal

algorithm (also known as a two-channel sub-band filter) with repeating filtering and down-sampling procedure to the low-pass channel output of the preceding level to obtain different decomposition levels of the signal (Wang et al. 2020b). In each decomposition at level i, the high-pass filter generates the detail coefficients (d_i) of the signal and the low-pass filter provides the approximate coefficients (a_i) (Brancati, Rocca & Savino 2015).

2.4.5 Discrete Wavelet Transform (DWT)

In DWT, the mother wavelet is discretised into different sizes using a scale parameter, 2^j and shifted with a shift parameter, $2^j k$. The discretised mother wavelet function is modified from Equation 2.43 and rewritten as (Rabi, Balusamy & Raj Jawahar 2019):

$$\psi_{j,k}(t) = \frac{1}{\sqrt{2^j}} \psi\left(\frac{t-2^j k}{2^j}\right) \quad \ldots(2.48)$$

for all $j,k \in Z$. The DWT of a time function $f(t)$ at scale j is then given as (Bajric et al. 2016):

$$W(j,k) = \int_{-\infty}^{\infty} f(t) \frac{1}{\sqrt{2^j}} \psi^*\left(\frac{t-2^j k}{2^j}\right) dt \quad \ldots(2.49)$$

The original signal can be reconstructed from the decomposed approximate and detail coefficients by the following equation (Wang et al. 2017):

$$f(t) = a_j + \sum_{i=1}^{j} d_i \quad \ldots(2.50)$$

where $f(t)$ represents the original signal, a_j is the approximate coefficient at level j, and d_i is the detail coefficient at level i.

Automotive components, especially the suspension system, are often subjected to random excitation from the road surface. In the past two decades, wavelet transform

was applied as an important signal processing tool to accelerate the durability assessment. Conventional fatigue tests often require a long time duration and high experimental costs due to the requirement of huge loading data size (Putra et al. 2017b). Given the fact that the low amplitude cycles in the loading histories do not significantly contribute to fatigue damage, these cycles can be removed, and thus, shorten the loading signals. One technique to obtain shorter loading signals by editing the loading histories is known as FDE (Duraffourg et al. 2015). Both CWT and DWT are favourable in FDE as they offer a smaller window at high frequencies and better capability in detecting small amplitude changes than a fixed-window analysis like STFT (Putra et al. 2017b).

Different studies (Pratumnopharat, Leung & Court 2013, 2014) applied CWT and STFT to edit the stress-time histories of a wind turbine and reported a total signal length reduction of 20.8% and 15.5% using CWT and STFT techniques, respectively, while retaining the original fatigue damage per repetition of signal block. It was found that the CWT showed better performance in FDE due to its adaptive time-frequency localisation as compared to the STFT. This allowed the wavelet function window to better match the transients in loading histories and detect the high damaging segments (Chen et al. 2016). Furthermore, Putra et al. (2017b) applied Morlet wavelet in CWT analysis to identify high damaging segments in the strain loading histories of a suspension coil spring. The signal energy was computed from the CWT wavelet coefficients of loading histories and an energy gate value was applied to identify high energy segments in the loading histories that significantly contributed to fatigue damage. A signal reduction of up to 41.4% was reported after the extraction of high damage sections from the load histories.

For DWT-based theory, several studies (Oh 2001; Steinwolf, Giacomin & Staszewski 2002) proposed the use of DWT in fatigue data editing of load histories in the early 2000s. Abdullah et al. (2006) used 12^{th} order Daubechies wavelets to determine “bumps” from VAL histories of a suspension coil spring. The bumps with large amplitude events in the loading histories that contributed to high fatigue damage were determined from wavelet levels. Furthermore, a recent study (Shangguan et al. 2020) proposed a new multi-axis load spectrum editing method based on the DWT theory. A time duration reduction of as high as 68% was reported using the edited load

spectrum obtained from the proposed DWT method, which achieved good agreement in retained damage with the time-domain editing method that showed 75% of time reduction.

2.4.6 Singularity Analysis using Continuous Wavelet Transform

Processing non-stationary signals is a challenging task given the random and highly transient properties of such signals. CWT has been regarded as a signal processing tool with exceptional capability in analysing non-stationary signals (Chen et al. 2016). Singularities are some unusual points in time series that are often characterised with discontinuity or abrupt changes. In many applications, singularities in time series contain valuable information about the system performance (Yang, Hull & Seymour 2006). Therefore, CWT is found to be especially useful in characterising singularities in many non-stationary signals. Singularity analysis using CWT has been successfully applied in many engineering applications, especially fault detection in mechanical systems. For example, Barbieri et al. (2019) proposed a new gearbox fault assessment method by analysing vibration signals of a gearbox with CWT. The study verified different gearbox faults from the mathematical morphology and entropy of the wavelet coefficients. This technique becomes a new diagnostic and damage control system to assess the damaged gearbox components.

Next, CWT has also been used to detect singularity in signals for damage evaluation in mechanical components. The mode shape of the damaged structure is analysed with CWT to detect the damage location and its severity. A recent study by Zhu et al. (2019a) proposed a CWT-based damage index for crack identification in the beams made of functionally graded materials. The damage index was successfully defined based on the position of the wavelet transform modulus maxima, which represented the singular points. Moreover, Cao et al. (2014) combined the CWT with the Teager energy operator and effectively detected multiple cracks in beams, even though under a noisy environment.

In singularity analysis, Hölder exponent (HE) is a commonly used notion to quantify the local regularity of a time function (Venkatakrishnan et al. 2014). It should

be noted that there are other notions being used to describe local regularity, for example, the Hurst exponent (Luo & Huang 2018; Nishawala & Ostoja-Starzewski 2017). A time function *f(t)* is said to have fulfilled a Hölder continuity at $t = x_0$ if and only if the following inequality is followed:

$$|f(x)-P(x-x_0)| \leq C|x-x_0|^{\alpha} \quad \ldots(2.51)$$

with the constant $C > 0$ and a polynomial P with degree $m < \alpha$. The pointwise HE is defined as the supremum of α, which fulfils the Hölder continuity condition as defined above.

Singularities in a time series can be estimated from the CWT. Being a time-frequency signal processing tool, CWT is capable of projecting the irregular behaviour of a time series at a particular point in wavelet coefficients as some large changes (Zhang et al. 2016). Large changes in the wavelet coefficient magnitude can be shown via the wavelet transform modulus maxima (WTMM) determined by the maxima lines of the wavelet coefficients. To estimate the maxima line along the scale *s* at position *u*, the partial differential of wavelet coefficients $W_{\psi}f(s,u)$ with respect to *u* is equal to zero, as expressed in the following equation:

$$\frac{\partial W_{\psi}f(s,u)}{\partial u} = 0 \quad \ldots(2.52)$$

At different scale *s* along a WTMM line, the wavelet coefficients $W_{\psi}f(s,u)$ can be related to the pointwise HE (α) as follows (Zhou et al. 2020):

$$W_{\psi}f(s,u) \leq As^{\alpha+1/2} \quad \ldots(2.53)$$

By introducing natural logarithm on both sides of Equation 2.53, it can then be rewritten as:

$$log_2|W_\psi f(s,u)| \leq log_2 A + \left(\alpha + \frac{1}{2}\right) log_2 s \quad \ldots(2.54)$$

From Equation 2.54, it can be seen that the pointwise HE of a time series at time $t = v$ can be estimated from the maximum gradient of a log-log plot between the $W_\psi f(s,u)$ and s of each maxima line converging to v.

Recently, Zhou et al. (2020) analysed singularities in vibrational signals of milling tools to monitor the tool conditions and proposed the second derivative of Gaussian wavelet with two vanishing moments as the most effective wavelet function to discover singular points in vibration signals of the milling tools. It was also found that the mean value of HEs and the number of singularities in the vibration signals are the most relevant to the wear states of the milling tools. Furthermore, Venkatakrishnan et al. (2014) applied a similar approach to identify singular points in the vibration signal of a gear box for damage assessment and tracking of the gear box. Zhang et al. (2016) also employed wavelet-based singularity analysis for detecting the rotating stall inception of a spike-type compressor. In the study, the Morlet wavelet was compared with the derivative of Gaussian (DOG) wavelet in detecting singularities in the wall pressure signals of a spike-type compressor. It was concluded that using the DOG wavelet with low vanishing moments could effectively determine the singularities with HE values of 0.5.

2.4.7 Multifractal Analysis

The fractal or multifractal theory introduced by Benoit Mandelbrot has opened a new window towards the understanding of stochastic events in nature. The word “Fractal” describes sets of data or patterns that exhibit self-similarity or scale-invariance properties. Complex fractals, also known as multifractals, are usually observed naturally in many systems, while simple, self-similar objects are only an idealisation of real phenomena (Pavlov & Anishchenko 2007). The theory of multifractals is introduced to measure the complexity and reveal the scaling properties of a signal or time series (Salat, Murcio & Arcaute 2017). In most cases, time series obtained from a

natural system exhibit multifractal properties, which need to be accounted for by more than one scaling exponent.

In the past decade, multifractal analysis was widely utilised in the analyses of non-stationary time signals in the automotive industry. For example, Quan et al. (2013) performed a multifractal analysis on a road surface profile and concluded that the road profile with high roughness possessed obvious multifractal properties, which are closely related to the surface irregularities. Moreover, a previous study (Puchalski et al. 2018) found that the multifractality of the in-use speed profile of automobiles could be effectively used for the evaluation of the non-linear and non-stationary movement of a car under different road conditions. Xiong et al. (2018) also established a fault detection algorithm for fatigue failure detection of axle box bearings by evaluating the multifractal properties of the vibration signals. Puchalski & Komorska (2017) characterised the noise level in a diesel engine under low and idle speed through the determination of the multifractal properties of acoustic signals. Nowadays, various multifractal theories have been developed and practically applied in the processing of signals with irregular, scale-invariant, and non-stationary properties (Xiong et al. 2016).

In the multifractal analysis of non-stationary time series, the multifractal properties of signals are usually described by a multifractal spectrum, also known as a singularity spectrum. The singularity spectrum consists of two parts: the Holder exponents that quantify the local regularity of the signal and the fractal dimensions that characterise the multifractality of the signal (Xiong et al. 2016). Hausdorff measurement was proven to be more accurate due to its general technical definition (Fernández-Martínez & Sánchez-Granero 2015). As for the Hausdorff measurement, x is a set of data with topology dimension d, and μ is the Borel probability measurement of x. After (x,μ) is iteratively decomposed based on the Hölder exponent α for n steps, subsets with the same measure $\mu(\alpha)$ structure the subsets $x(n,\alpha)$. If $lim_{n\to\infty} x(n,\alpha) = x(\alpha)$ is a fractal set, then $x(\alpha)$ is the fractal subset of (x,μ). Therefore, x is a union set of all fractal subsets $x(\alpha)$ with specific dimensions. For any subsets $x(\alpha)$, note that a δ-cover of $x(\alpha)$ is a countable family of subsets $\{U_i : i \in N\}$ with $0 < diam(U_i) < \delta$ and the following definition is introduced (Fernández-Martínez & Sánchez-Granero 2015):

$$H_{\delta}^{r}(x(\alpha),\mu(\alpha))=inf\left\{\sum_{i=1}^{\infty} diam(U_i)^r : x(\alpha)\subset\bigcup_{i=1}^{\infty} U_i\right\} \quad \ldots(2.55)$$

According to the definition of Hausdorff measurement, under the limit of δ close to zero, the r-dimensional Hausdorff measure about μ is given as:

$$H^{r}(x(\alpha),\mu(\alpha))=\lim_{\delta\to 0} H_{\delta}^{r}(x(\alpha),\mu(\alpha)) \quad \ldots(2.56)$$

The Hausdorff dimension of $x(\alpha)$ is described as the critical value of r, where $H^{r}(x(\alpha),\mu(\alpha))$ experiences a sudden transition from zero to infinity, such that (Xiong, Yu & Zhang 2015):

$$H^{r}(x(\alpha),\mu(\alpha))=\begin{cases}0 & r>f(\alpha)\\ A & r=f(\alpha)\\ \infty & r<f(\alpha)\end{cases} \quad \ldots(2.57)$$

with A is a constant positive value. Therefore, $f(\alpha)$ is the fractal dimension or Hausdorff dimension of $x(\alpha)$ and also the multifractal spectrum of $x(\alpha)$ with varying α. Equivalently, $f(\alpha)$ can also be mathematically expressed as the infimum of r, where $H^{r}(x(\alpha),\mu(\alpha))$ equals zero or supremum of r, where $H^{r}(x(\alpha),\mu(\alpha))$ becomes infinity:

$$\begin{aligned} f(\alpha) &= inf\left\{r : H^{r}\left(x(\alpha),\mu(\alpha)\right)=0\right\}\\ f(\alpha) &= sup\{r : H^{r}(x(\alpha),\mu(\alpha))=\infty\}\end{aligned} \quad \ldots(2.58)$$

Analytical computation of multifractal spectrum using Hausdorff measurement has been used in practical applications (Fernández-Martínez & Sánchez-Granero 2015). Therefore, many numerical approaches for the estimation of multifractal spectrum, also known as multifractal formalism, are proposed. Some early multifractal formalism approaches developed in the mid-1980s include the moment method and histogram method (Salat, Murcio & Arcaute 2017). Later, multifractal detrended fluctuation analysis (MFDFA), WTMM method, and wavelet leaders (WL) method are originally

designed for non-stationary time series. MFDFA is a generalised detrended fluctuation analysis and has been successfully adopted to solve engineering problems (Kantelhardt et al. 2002; Márton et al. 2014; Xiong et al. 2018).

The simple implementation of MFDFA is a great advantage that allows its application to higher dimension time series. For wavelet-based multifractal formalism, the WTMM method is well suited for higher dimension time series compared to MFDFA. This is mainly because the WTMM method is applicable to non-conservative and continuous phenomena (Salat, Murcio & Arcaute 2017). Nonetheless, some researchers found that the WTMM method is computationally heavy as it is intrinsically continuous and also presents some difficulties in the processing of signals with oscillating singularities (Mintzelas, Sarlis & Christopoulos 2018).

A new formulation in terms of local suprema of wavelet coefficients called wavelet leaders (WL) was introduced by Lashermes, Jaffard & Abry (2005). Unlike the WTMM method, the WL method takes low computational efforts because the WL are computed using DWT (Pnevmatikos et al. 2020). Serrano & Figliola (2009) also stated that the WL method has more significant computational effectiveness than MFDFA. Furthermore, the WL method provides a good characterisation of the multifractal properties on a full domain and it is well supported by a complete mathematical theoretical framework (Du et al. 2014).

WL-based multifractal formalism is one of the most recently introduced methods to estimate the multifractal spectrum of a time series. Given the apparent advantages of the WL method against other multifractal formalisms, this method has received considerable research interest. The WL method has been employed in various engineering applications, including real-time fault diagnosis (Du et al. 2014) and structural health monitoring (Pnevmatikos et al. 2020). To compute the multifractal spectrum using the WL method, suppose a function $\psi(t)$ with a compact time support and vanishing moment $m \geq 1$, for all $k = 0, 1, 2, \ldots, m-1$, fulfilling the following conditions:

$$\int t^k \psi(t)dt \equiv 0\,,\ \int t^m \psi(t)dt \neq 0 \qquad \ldots(2.59)$$

then $\psi(t)$ can be selected as a mother wavelet function. $\psi(t)$ can be dilated to scale 2^j and translated to time position $2^j k$, forming an orthogonal basis of $L^2(R)$, such that:

$$\psi_{j,k}(t) = 2^{\frac{-j}{2}}\psi\left(2^{-j}t-k\right),\ j \in Z,\ k \in Z \qquad \ldots(2.60)$$

The wavelet coefficients for a signal $X(t)$ obtained from DWT are expressed as:

$$d_X(j,k) = \int X(t)2^{-j}\psi(2^{-j}t-k)dt \qquad \ldots(2.61)$$

Let the dyadic interval $\lambda = \lambda_{j,k} = \left[k.2^j,(k+1).2^j\right]$ and 3λ denotes the union of its two adjacent dyadic intervals: $3\lambda_{j,k} = \lambda_{j,k-1} \cup \lambda_{j,k} \cup \lambda_{j,k+1}$. Then, the wavelet leader is taken as the local supremum of wavelet coefficients calculated within a spatial neighbourhood at all finer scales (Du et al. 2014). The wavelet leader is thus mathematically expressed as follows:

$$L_x(j,k) \equiv L_\lambda = sup_{\lambda' \subset 3\lambda}\left|d_{X,\lambda'}\right| \qquad \ldots(2.62)$$

There is a direct relationship between the wavelet leader and the pointwise Hölder exponent (α). Let $\lambda(x_0)$ be the unique dyadic interval with point x_0 in the interval and $L_j(x_0)$ be the corresponding wavelet leader. If the Hölder continuity $f \in C^\alpha(x_0)$ is fulfilled at x_0, then, for all $j > 0$ (Serrano & Figliola 2009):

$$\left|L_j(x_0)\right| \leq C2^{-j\alpha} \qquad \ldots(2.63)$$

for some constant $C > 0$. Thus, structure functions $S_L(q,j)$ can be expressed as follows:

$$S_L(q,j) = \frac{1}{n_j}\sum_{k=1}^{n_j}|L_x(j,k)|^q \cong j^{\xi(q)} \quad \ldots(2.64)$$

where j is the scale, q is the moment, $L_x(j,k)$ is the wavelet leaders by scale, n_j is the number of wavelet leaders at each scale, and $\xi(q)$ is the scaling exponent. $\xi(q)$ is defined as:

$$\xi(q)=\lim_{j\to 0} inf\left(\frac{log_2 S_L(q,j)}{j}\right) \quad \ldots(2.65)$$

From Equation 2.65, it can be seen that $\xi(q)$ can be estimated from the graph of j versus $log_2 S_L(q, j)$. Through the Legendre transform of $\xi(q)$, the multifractal spectrum $D(h)$ can be obtained as the fractal dimension $f(\alpha)$, such that:

$$D(h) = f(\alpha) = \inf_{q\neq 0}(1+q\alpha-\xi(q)) \quad \ldots(2.66)$$

Additionally, $\xi(q)$ can be expanded to a polynomial as:

$$\xi(q)=\sum_{p=1}^{\infty} c_p \frac{q^p}{p!} \quad \ldots(2.67)$$

where c_p is the log-cumulants. The log-cumulants contain important information of the multifractal spectrum: c_1 characterises the location of maximum $f(\alpha)$, c_2 defines the spectrum width, and c_3 corresponds to the spectrum symmetry (Du et al. 2014).

2.5 DATA ANALYSIS

Durability prediction of suspension components, such as coil springs, often obtains fatigue life results with large variations because the fatigue process is highly random and consists of large uncertainties (Manouchehrynia, Abdullah & Singh 2020). Therefore, a better interpretation of fatigue life results requires data analysis so that the

fatigue life results are statistically valid. In many cases of durability analysis for automotive components, loading histories with a large sample size are required to sufficiently represent the statistics of the loading conditions. The sample size of the acquired signal usually depends on the sampling rate. To analyse signals with a large sample size, statistical analysis is performed because a single point of data is meaningless in characterising the fatigue life.

2.5.1 Introduction to Data Analysis

Eigenvalues of a data set that characterise the statistical nature of data can be categorised into two types: (a) central position and (b) dispersion of data. The mean of the data set is a classical representation of data centroid. In durability analysis, these eigenvalues of loading histories also provide valuable information about the loading behaviours, which are closely related to the fatigue life. For a set of data with sample number n, the data mean ($\bar{x}$) is given as (Gu et al. 2012):

$$\bar{x} = \frac{1}{n}\sum_{i=1}^{n} x_i \qquad \ldots(2.68)$$

For durability analysis, the mean value of the loading history represents the tensile or compressive nature of the loading. A positive value of mean indicates tensile loading and vice versa for compressive load. To determine data dispersion, the standard deviation (σ_{SD}) shows the scattering of data points about the data centroid. A greater σ_{SD} shows a larger dispersion of data. The σ_{SD} of a data set with a sample size less than 30 can be expressed as:

$$\sigma_{SD} = \sqrt{\frac{\sum_{i=1}^{n}(x_i - \bar{x})^2}{n-1}} \qquad \ldots(2.69)$$

For a set of data with sample size larger than 30, the σ_{SD} is expressed as:

$$\sigma_{SD} = \sqrt{\frac{\sum_{i=1}^{n} (x_i - \bar{x})^2}{n}} \quad \ldots(2.70)$$

In addition, the root-mean-square (RMS) also characterises the dispersion of a data set, such that (Gu et al. 2012):

$$RMS = \sqrt{\frac{1}{n}\sum_{i=1}^{n} (x_i)^2} \quad \ldots(2.71)$$

Palmieri et al. (2017) proposed the use of RMS in signal processing for durability analysis as the RMS can be a good indication of signal energy.

Apart from data central and dispersion, the skewness of data (*S*) and kurtosis (*K*) are the third and fourth moments of statistical eigenvalues that measure the asymmetry and "tailedness" of data probability distribution, respectively (Cianetti et al. 2018). The skewness, together with kurtosis, interpret the extreme values in a data set that are not shown in the average. The skewness of a data set can be obtained by (Cain, Zhang & Yuan 2017):

$$Skewness = \frac{\sum_{i=1}^{n} (x_i - \bar{x})^3}{n(RMS)^3} \quad \ldots(2.72)$$

A perfectly symmetric data distribution has zero skewness, and positive skewness shows that the distribution is skewed to the right, while a negative value indicates a left-skewed distribution (Cain, Zhang & Yuan 2017).

The kurtosis determines if a data distribution is heavily tailed or lightly tailed to a normal distribution. Given a set of data with *n* samples, the kurtosis of the data set is expressed as:

$$Kurtosis = \frac{\sum_{i=1}^{n}(x_i - \bar{x})^4}{n(RMS)^4} \quad \ldots(2.73)$$

Studies (Cianetti et al. 2017; Palmieri et al. 2017) have remarked that loading signals with high kurtosis values are likely to bring more fatigue damage. Signals with kurtosis higher than three are known as leptokurtic; they are otherwise known as platykurtic (Palmieri et al. 2017). Apart from that, a non-stationary signal with varying statistical properties with time also has a kurtosis value higher than three (Kihm, Ferguson & Antoni 2015). A normal distribution has zero skewness and a kurtosis value of three. Data distribution with high kurtosis shows a sharper peak compared to a normal distribution.

2.5.2 Machine Learning Approach for Fatigue Life Modelling

Despite significant advancements in the research of durability analysis, the prediction of fatigue life under complex loading conditions with conventional mathematical techniques, such as multiple linear regression, remains a difficult challenge. Many available fatigue life prediction models, such as *S*-*N* and ε-*N* approaches produced using the regression method, work better with CAL rather than VAL (Vassilopoulos & Bedi 2008). This is mainly because fatigue processes under complex loads are highly non-linear, uncertain, and controlled by various mechanisms (Mohanty et al. 2011). Recently, soft-computing techniques, such as artificial neural network (ANN), fuzzy logic, genetic algorithm (GA), and adaptive neuro-fuzzy inference system (ANFIS) have been extensively applied in durability analysis involving complex loading problems as the soft-computing methods which offer good tolerance of imprecision, uncertainty, and partial truth.

W. McCulloch and W. Pitts proposed the ANN method in 1943 that became a popular machine learning approach resembling the vast network of neurons in the human brain (McCulloch & Pitts 1943). The network is composed of multiple layers of nodes (also known as the neurons) that are interconnected through sets of weights and biases (Aljarah, Faris & Mirjalili 2018). A hidden layer exists between the input and output layers. A single layer ANN consists of only a hidden layer, while multi-layer

ANN can have more than one hidden layer. Nowadays, ANN is extensively applied in durability analysis of different materials because of its outstanding capability in modelling non-linear relationships. For example, Khatir et al. (2020) developed an ANN model for crack identification of plates that could accurately predict the scenario and length of cracks. ANN has been proven as a powerful tool in the modelling of complex systems due to its excellent capability in adapting and learning. Nonetheless, ANN also has a negative attribute of being a "black-box" process that brings difficulty for the users in understanding the system behaviours (de Campos Souza 2020).

2.5.3 Development of Neuro-Fuzzy in Durability Assessment

Apart from ANN, another frequently used soft computing technique is the fuzzy inference system. The fuzzy set theory was introduced by L. Zadeh in 1965 to provide a qualitative explanation of parameters with uncertainties (de Campos Souza 2020; Zadeh 1965). Unlike classical sets with crisp boundaries, the fuzzy sets are classified as smooth sets where the transition at the set boundary happens gradually rather than abruptly. The transition at fuzzy set's boundary is expressed by membership functions with values ranging between zero (does not belong to the set) and one (belongs to the set) (Zuo et al. 2014). A fuzzy inference system models a complex system based on a set of sample data and "if-then" fuzzy rules. Hence, a fuzzy model provides good reasoning ability on the sample data based on qualitative aspects of human knowledge without involving quantitative analysis (Shihabudheen & Pillai 2018). However, many fuzzy models rely heavily on expertise and knowledge to develop the fuzzy sets for analysing complex systems (Chen et al. 2021).

Researchers proposed hybrid systems of neural networks and fuzzy systems known as neuro-fuzzy systems. The systems inherit the advantages of ANN and fuzzy logic without having any of the disadvantages (Das et al. 2016). Among many neuro-fuzzy systems, the adaptive neuro-fuzzy inference system (ANFIS) is the most commonly applied system. ANFIS is a type of ANN based on the Takagi-Sugeno fuzzy inference system that consists of five layers of interconnected nodes (Saikia & Sarma 2015). The nodes are characterised by node functions with fixed or variable parameters. Figure 2.15 depicts the five-layer structure of an ANFIS model with multiple inputs and

a single output. During the training process using available data, the network "learns" by adjusting the parameter functions of the nodes to fit the data (de Campos Souza 2020).

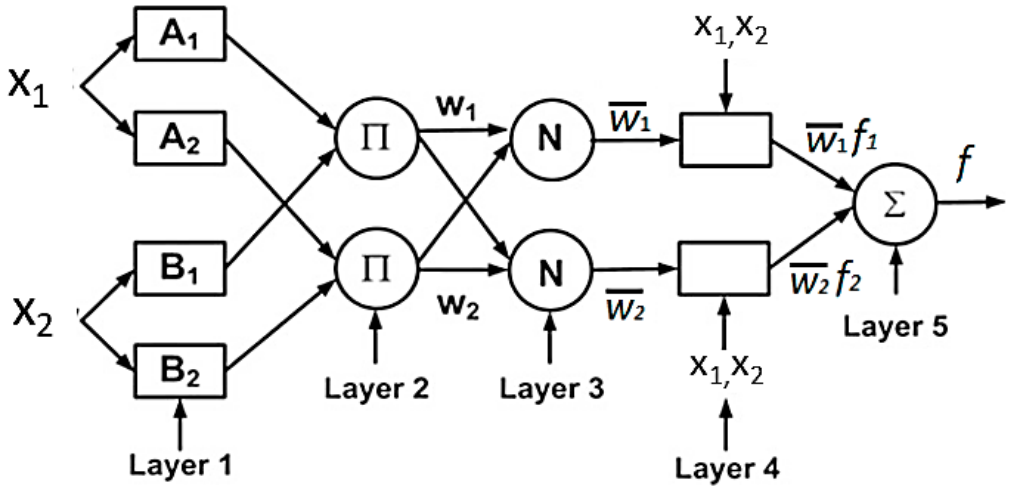

Figure 2.15 Architecture structure of ANFIS model

Source: Gandhi, Adarsh & Ramachandran 2017

Each layer in the ANFIS structure carries out different functions. The first layer in the structure is the fuzzy layer with nodes consisting of membership functions for every input variable. Layer 1 is also known as the fuzzification layer where the crisp inputs are converted into fuzzy memberships. Given an ANFIS model with N input variables, the membership function (MF) of input variables (x_i) with $i = 1, \dots, N$ can be written as:

$$O_{1,j} = \mu_{A_j}(x_1) \qquad j=1,\dots,N_1$$

$$O_{1,k} = \mu_{B_k}(x_2) \qquad k=1,\dots,N_2 \qquad \dots(2.74)$$

$$O_{1,l} = \mu_{C_l}(x_3) \qquad l=1,\dots,N_3$$

where μ_A, μ_B, and μ_C represent the degree of membership of membership functions A, B, and C, respectively. The membership function in this layer can be expressed in parameterised membership functions, such as triangular, trapezoidal, Gaussian, or

Gumbell (de Campos Souza 2020). Layer 2 consists of nodes with fixed values obtained from the products of all membership functions, such that:

$$O_{2,m} = \mu_{A_j}(x_1)\mu_{B_k}(x_2)\mu_{C_l}(x_3) = w_m \quad \ldots(2.75)$$

The *Π* symbol in Layer 2 indicating a multiplying operation. The output of Layer 2 w_m is the firing strength of the fuzzy rule. It represents the degree of fulfilment of the fuzzy rules of which the input data are satisfied. Layer 3 consists of a node function that normalises the firing strength:

$$O_{3,m} = \overline{w}_m = \frac{w_m}{\sum_{L=1}^{N_1,N_2,N_3} w_L} \quad \ldots(2.76)$$

with $\overline{w}_m$ as the normalised firing strength. The *N* symbol in the Layer 3 representing a normalisation operation. Layer 4 calculates a parameter function known as the consequent function, such that:

$$O_{4,m} = \overline{w}_m f_m \quad \ldots(2.77)$$

The summation process is also known as the defuzzification process to convert the fuzzy number back into a crisp number. Finally, Layer 5 summarises the overall output by summing all defuzzification neurons, such that:

$$O_{5,m} = \sum \overline{w}_m f_m \quad \ldots(2.78)$$

ANFIS inherits the learning capability from neural networks. The hybrid learning algorithm of ANFIS can adapt the membership function nodes in the first layer. The parameters in the first layer are also known as premise or antecedent parameters, while the fourth layer's parameters are referred to as consequent parameters (Zhang et al. 2019a). During the training process, the ANFIS model is able to adapt itself to fit into the input data and provide accurate output. The adapting process is achieved by the backpropagation algorithm and least square error estimation in order to optimise the

membership function parameters in the first layer. Similar to ANN, ANFIS learning algorithm can be classified into forward pass and backward pass. In the forward pass of the hybrid learning algorithm, the consequent parameters in Layer 4 are identified by the least square error optimisation. Meanwhile, in the backward pass, backpropagation algorithm is popularly used in ANN for the training process (de Campos Souza 2020). The computed errors in Layer 4 are propagated backward to the first layer after each epoch of training and the premise parameters in the first layer are adjusted accordingly based on the gradient-descent method to achieve a minimum average error (Tran-Ngoc et al. 2019). The feedforward-backpropagation algorithm allows the ANFIS model to have self-learning properties and adapt effectively to the input data (Nwobi-Okoye, Ochieze & Okiy 2019).

ANFIS modelling requires a clustering method to determine the number of fuzzy rules. Subtractive clustering method (SCM) is one of the popular fuzzy clustering methods for estimating the cluster centres and their locations in a given set of data (Fattahi et al. 2013). In ANFIS modelling, fuzzy clustering methods are employed to determine the MFs by partitioning the data samples into different clusters in which the data in a cluster share similar behaviours (Keshavarzi et al. 2017). In the beginning, the SCM assumes that each data point is a potential cluster centre. Next, a new cluster is identified by calculating the probability of each data point becoming a new centre based on the density of the surrounding data points. The cluster centre P_i at a data point x_i in the clustering of SCM is defined as (Fattahi et al. 2013):

$$P_i = \sum_{j=1}^{l} exp\left(-\frac{\|x_i - x_j\|^2}{(r_a/2)^2} \right) \quad \ldots(2.79)$$

where l is the total number of data points in N-dimensional with data points x_i and x_j, r_a is the radius of neighbourhood, and $\|.\|$ represents the Euclidean distance. The first cluster is selected as c_1 point with the highest probability or potential value, P_{c_1}. The second cluster centre is obtained after subtracting the first cluster centre from the dataset and recalculating the new density value, such that:

$$P_i = P_i - P_{c_1} exp\left(- \frac{\|x_i - x_{c_1}\|^2}{(r_b/2)^2} \right) \quad \ldots(2.80)$$

$$r_b = \eta r_a \quad \ldots(2.81)$$

where $\eta > 1$ is a constant to prevent cluster centre from being too closely estimated. After subtraction of the first cluster centre, the potential measurement will be reduced by the data points around the vicinity of the first cluster centre c_1. Then, a new cluster centre c_2 is based on the recalculated largest potential. The potential of k^{th} cluster centre with location c_k after k times of cluster subtraction becomes:

$$P_i = P_i - P_k \, exp\left(- \frac{\|x_i - x_k\|^2}{(r_b/2)^2} \right) \quad \ldots(2.82)$$

where P_k is the largest potential density value. The cluster centres are chosen iteratively until the stopping criteria are achieved. In the SCM algorithm, the radius of influence (ROI), r_b is the control parameter that determines the number of cluster centres.

ANFIS has been successfully applied in the durability analysis of different engineering applications and materials. For example, ANFIS was adopted in the modelling of the complex fatigue behaviours of multidirectional composite laminates and very high accuracy was reported (Vassilopoulos & Bedi 2008). Furthermore, ANFIS was also very effective in predicting the fatigue crack growth in alloys, as demonstrated in several studies by Mohanty et al. (2010, 2011). Das et al. (2016) also proposed a condition monitoring model of a cantilever shaft based on robust damage using the ANFIS method and reported satisfactory accuracy. According to the previous studies (Das et al. 2016; Mohanty 2016), ANFIS was proven as an effective tool for the modelling of fatigue life in different engineering components.

2.5.4 Fatigue Reliability Analysis

Many established durability prediction models focus on the deterministic analysis of the fatigue process. Nonetheless, the fatigue process of most of the engineering components

under real-life loading conditions is stochastic in nature (Zhu, Liu & Huang 2017). Apart from the load histories, the fatigue process of engineering structures is a complex process that depends on material properties, manufacturing process, working environments, global and local geometry, and other factors (Altamura & Straub 2014; Dong, Garbatov & Soares 2021). These factors contribute to considerable uncertainties during fatigue life assessment of structures. In addition, there are also many assumptions and hypotheses employed in fatigue life assessment that could result in a large error margin (Abdullah et al. 2021). Traditional approaches of fatigue analysis, such as *S*-*N* or *ε*-*N* approaches are found to have limited assessment of variability and uncertainty in the stochastic loads. Owing to the lacking of uncertainty analysis of testing data, it remains a difficult task to accurately predict the probability distribution of fatigue life under random loading conditions (Wang et al. 2019).

Fatigue reliability analysis is the computation of the probability of fatigue failure under specific loading conditions and can provide a quantitative assessment of the safety level of the component (Xu & Kong 2019). To account for the stochastic behaviours of the fatigue process, the fatigue reliability assessment must be performed with probabilistic approaches. In a fatigue reliability analysis, sufficient fatigue life data are required to characterise the probability density function (PDF). Researchers remarked that the fatigue behaviour of many mechanical components is non-Gaussian and follows the Weibull or Lognormal distributions (Chen et al. 2021; Jin et al. 2020). Equations 2.83 and 2.84 give the PDF of the Weibull and Lognormal distributions of a set of fatigue failure data in time (*t*), respectively:

$$f_{Weibull}(t)=\frac{k}{\lambda}\left(\frac{t}{\lambda}\right)^{k-1} e^{-\left(\frac{t}{\lambda}\right)^{k}} \qquad \ldots(2.83)$$

where k is the shape parameter, and λ is the scale parameter.

$$f_{Lognormal}(t)=\frac{1}{t\sigma_{SD}\sqrt{2\pi}} e^{-\frac{(\ln t-\mu)^2}{2\sigma_{SD}^2}} \qquad \ldots(2.84)$$

where μ is the mean, and σ_{SD} is the standard deviation. In the context of durability analysis, the fatigue life is often expressed in cycles (N_f) rather than time because the fatigue process is a time-independent process (Nasir et al. 2020). However, cycles can be converted into time scale when the sampling frequency of the loading histories is known.

The maximum likelihood estimation (MLE) method can be employed to determine the optimum parameters of probability distributions (Cai et al. 2018). For a given set of data, the MLE method estimates the optimal parameters of the probability distribution by maximising the likelihood function, so that the observed data are most probable (Kirkby et al. 2022; Mekonnen, Aburbu & Sarwat 2018). For a probability distribution with two parameters and a set of data with n samples, the likelihood function (L_L) can be expressed as follows (Langat, Kumar & Koech 2019):

$$L_L = \prod_{x=i}^{n} F(x_i;a,b) \qquad \ldots(2.85)$$

where $F(x)$ is the CDF of the probability distribution, and a and b are the parameters of the distribution.

The Akaike's information criterion (AIC) is extensively used for the selection of the appropriate probability model that fits the fatigue life data (Portet 2020). The AIC can be calculated according to the following equation (Cavanaugh & Neath 2019):

$$AIC = 2z\text{-}2ln(L_L) \qquad \ldots(2.86)$$

where L_L is the likelihood function computed through the MLE method, and z is the number of estimated parameters of the fitted distributions. A lower AIC index value indicates better data fitting with the distribution.

The cumulative density function (CDF) can be expressed as the integral of the PDF, such that:

$$F(t)=\int_{-\infty}^{x} f(t)dx \qquad \ldots(2.87)$$

also, the reliability function is the reverse of CDF:

$$R(t) = 1\text{-}F(t) \qquad \ldots(2.88)$$

The hazard rate is expressed as:

$$h(t)=\frac{f(t)}{R(t)} \qquad \ldots(2.89)$$

In reliability analysis, the mean-time-to-failure (MTTF) is an essential parameter to evaluate fatigue reliability. MTTF must be used because small components like coil springs are not repairable items after failure (Mekonnen, Aburbu & Sarwat 2018). With the PDF determined, the MTTF based on the failure time data can be expressed as:

$$MTTF = \int_{0}^{\infty} t.f(t)\,dt \qquad \ldots(2.90)$$

MTTF represents the service time duration until the first failure is expected to occur (Singh, Abdullah & Ariffin 2020). MTTF gives a reasonable estimation of the service life of components. Through probabilistic approaches, the MTTF obtained in this study can provide a more reliable expected service life of a coil spring under various loading conditions.

Nowadays, fatigue reliability analysis has been extensively adopted in many engineering applications, such as automotive (Abdullah et al. 2021; Manouchehrynia, Abdullah & Singh 2020), marine and offshore structures (Dong, Garbatov & Guedes Soares 2021), and turbines (Li et al. 2021) to estimate the service life of the components under complex loading conditions. Singh et al. (2020) recently proposed the generation of random stress histories of automotive crankshafts using stochastic method. The

induced stress load was employed to determine the hazard rate-reliability of the crankshaft and reasonable service life of the component. Furthermore, Gao & Liu (2021) introduced a novel non-linear time-varying reliability analysis that could determine fatigue life with better accuracy than conventional fatigue life assessment methods and also considered the load sequence effects. Fatigue reliability analysis has been proven to be a necessary process in fatigue life assessment due to the ability to account for the uncertainties in the fatigue process.

2.5.5 Validation Approaches for Durability Analysis

The predicted fatigue life using developed fatigue life predictive models must be validated with experimental results to evaluate the performance of the developed models. One conventional method to assess the validity of the predicted fatigue life is through fatigue life conservative analysis. The predicted fatigue life by a predictive model is compared to the fatigue life obtained by an experimental approach within a boundary of factor two (Zhang et al. 2019a). The predicted and experimental fatigue lives are compared within a logarithm scale and plotted in 1:1 correlation. For data scattering, there are upper and lower bounds that represent 1:2 and 2:1 correlation, respectively, to determine if the predicted fatigue lives are conservative or non-conservative compared to the experimental results. If the predicted fatigue life correlated with the experimental results beyond the 2:1 correlation boundary, this indicates that the predictive model provides non-conservative fatigue life prediction and vice versa for fatigue life prediction below the 1:2 correlation boundary (Branco et al. 2019). The fatigue life conservative analysis can be classified as a kind of data survivability analysis. It is important to determine the rate of fatigue data survival within the acceptable boundary to justify the acceptability of the established models. Furthermore, the fatigue life conservative analysis provides good visual inspection of the performance of a developed fatigue life predictive model. However, this analysis is still lacking statistical validation on the model outputs.

To assess the accuracy of a fatigue life prediction model quantitatively and statistically, the root-mean-square error (RMSE) of the predicted values can be evaluated by:

$$RMSE=\sqrt{\frac{\sum_{i=1}^{N}(x_i-\hat{x}_i)^2}{N}} \quad \ldots(2.91)$$

where x_i is the predicted value, $\hat{x}_i$ is the actual value, and N is the total number of data. The RMSE value is a good index that reflects the accuracy of durability model in predicting fatigue life through comparison between the predicted data and the experimental data. Low RMSE values indicate a small deviation between the predicted and actual values, and thus, the model has high accuracy. RMSE has been applied in different applications, such as durability modelling (Kong et al. 2019b; Sivák & Ostertagová 2012) and tool monitoring (Mohanraj et al. 2020) to statistically evaluate the accuracy of established models.

2.6 SUMMARY

This chapter discusses some theoretical frameworks and previous works related to fatigue analysis of automotive components. The main focus of this chapter is the development of durability analysis for automotive applications. A recent research trend in durability analysis has shown an increasing role of simulation methods and signal processing techniques, such as MBD simulation and time-frequency domain methods in durability analysis. Besides, machine learning-based approaches, including ANN and neuro-fuzzy methods have replaced traditional regression methods in modelling the fatigue properties of complex, non-linear systems. Machine learning-based methods have shown significant improvement in the accuracy of fatigue life prediction compared to regression methods.

Through detailed literature review on recent developments in durability analysis of automotive applications, it can be determined that the MBD simulation can be used to improve accuracy in strain generation for coil springs. Given the outstanding capability of wavelet transform in analysing non-stationary signals, this study also adopted wavelet-based technique for fatigue-related feature extraction from vibration signals. Machine learning approaches have extraordinary accuracy in the modelling of non-linear fatigue data. Therefore, the neuro-fuzzy method was applied to establish the

durability prediction model. For the validation of durability prediction model, the reliability method was employed because this method considered uncertainties in random fatigue data. In Chapter III, details of the methodology adopted in this study will be discussed. A comprehensive explanation of the methodology to achieve the novelty of this study is presented.

CHAPTER III

METHODOLOGY

3.1 INTRODUCTION

This section explains the methodology of the study to achieve the research objectives, in which the vital aim is to establish a durability predictive model using a neuro-fuzzy approach with vibration characteristics and design parameters of the coil spring. Figure 3.1 illustrates the methodology flow of this study, divided into three sections corresponding to each objective.

In order to achieve the first objective, the vibration and strain signals of the coil spring were acquired via road tests under various road conditions. A new displacement-strain relationship for the coil spring was derived to enable the conversion of vibration signals to strain signals in the coil spring. Multibody-dynamics (MBD) simulation was also adopted to simulate the spring responses under vibration loading. The accuracy of the developed acceleration-strain conversion model was then confirmed by comparing the fatigue life of simulated strain signals with the experimentally measured strain signals.

The second objective of this study was the establishment of a vibration fatigue prediction model based on vibration features. This involves the extraction of fatigue-related features from the vibration signals for prediction of the coil spring's durability. The characterisation of the vibration signals was performed using a wavelet transform which is a popular time-frequency domain signal processing technique. With the wavelet coefficients obtained through wavelet transform, Hölder singularity analysis was conducted to extract singularities that represent the low frequency features of the vibration signals. Power spectral analysis was then applied to determine the signal

energy in the singularity signals. Subsequently, using wavelet-leaders of multifractal formalism, the multifractal properties of vibration signals collected from various road conditions were evaluated. Multifractal spectrums were computed to determine the multifractality of the vibration signals. With the extracted features of vibration signals, adaptive neuro-fuzzy inference system (ANFIS) was applied to establish fatigue life prediction model based on the vibration features.

For the third objective, the trained ANFIS durability model was validated using probabilistic-reliability approaches. A probabilistic distribution was fitted using the Maximum Likelihood Estimation (MLE) technique based on the experimental vibration data. Several standard probabilistic distributions, such as Normal, Lognormal, and Weibull distributions, were applied to determine the appropriate distribution for the dataset. Probabilistic analysis was performed to determine the reliability function and Mean-cycle-to-Failure (McTF) based on the simulated fatigue data. In addition, experimental data were also used to obtain the reliability function and McTF with the same procedure. Lastly, the ANFIS model was validated by comparing the reliability properties of simulated and experimental data.

3.2 STRAIN GENERATION USING MULTIBODY DYNAMICS APPROACHES

This section discusses the methodology for strain generation from vibration signals using MBD approaches. This section includes the finite element analysis, MBD modelling of suspension system, and strain generation from vibration signals.

3.2.1 Finite Element Analysis of a Coil Spring

A frontal coil spring of a 1,300 cc Malaysian made sedan car with a passive MacPherson strut suspension system was tested. The suspension system had spring stiffness and damping coefficients of 16,806 N/m and 15,564 Ns/m, respectively (Putra et al. 2015). The material of the suspension coil spring was SAE5160 carbon steel, a common material used in automobile coil spring production (Murakami, Kanezaki & Sofronis 2013; Putra et al. 2017a). The material properties of SAE5160 carbon steel such as the elastic modulus, yield strength, as well as fatigue parameters, are shown in Table 3.1.

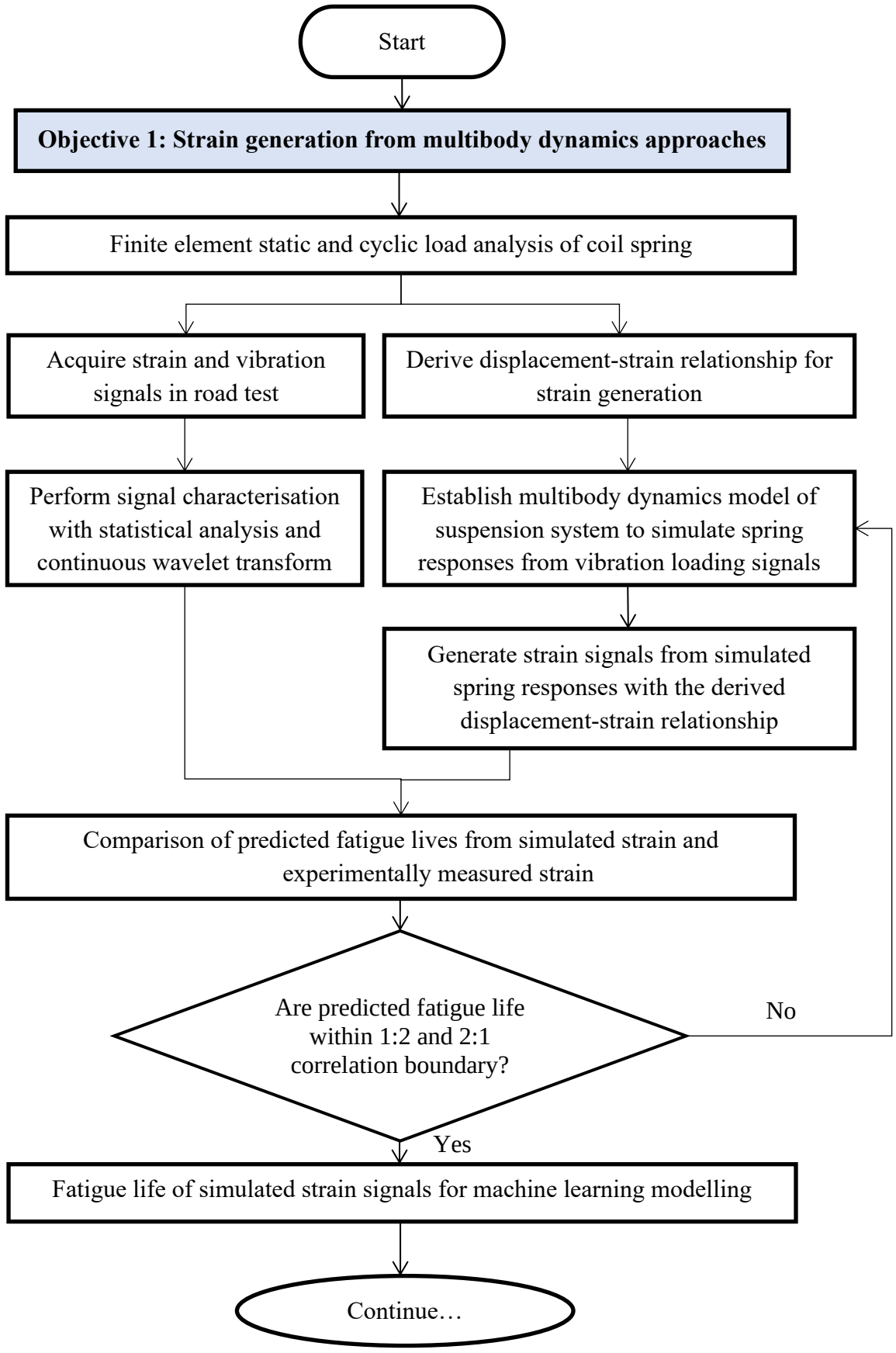
Start
Objective 1: Strain generation from multibody dynamics approaches
Finite element static and cyclic load analysis of coil spring
Acquire strain and vibration signals in road test
Derive displacement-strain relationship for strain generation
Perform signal characterisation with statistical analysis and continuous wavelet transform
Establish multibody dynamics model of suspension system to simulate spring responses from vibration loading signals
Generate strain signals from simulated spring responses with the derived displacement-strain relationship
Comparison of predicted fatigue lives from simulated strain and experimentally measured strain
Are predicted fatigue life within 1:2 and 2:1 correlation boundary?
No
Yes
Fatigue life of simulated strain signals for machine learning modelling
Continue…

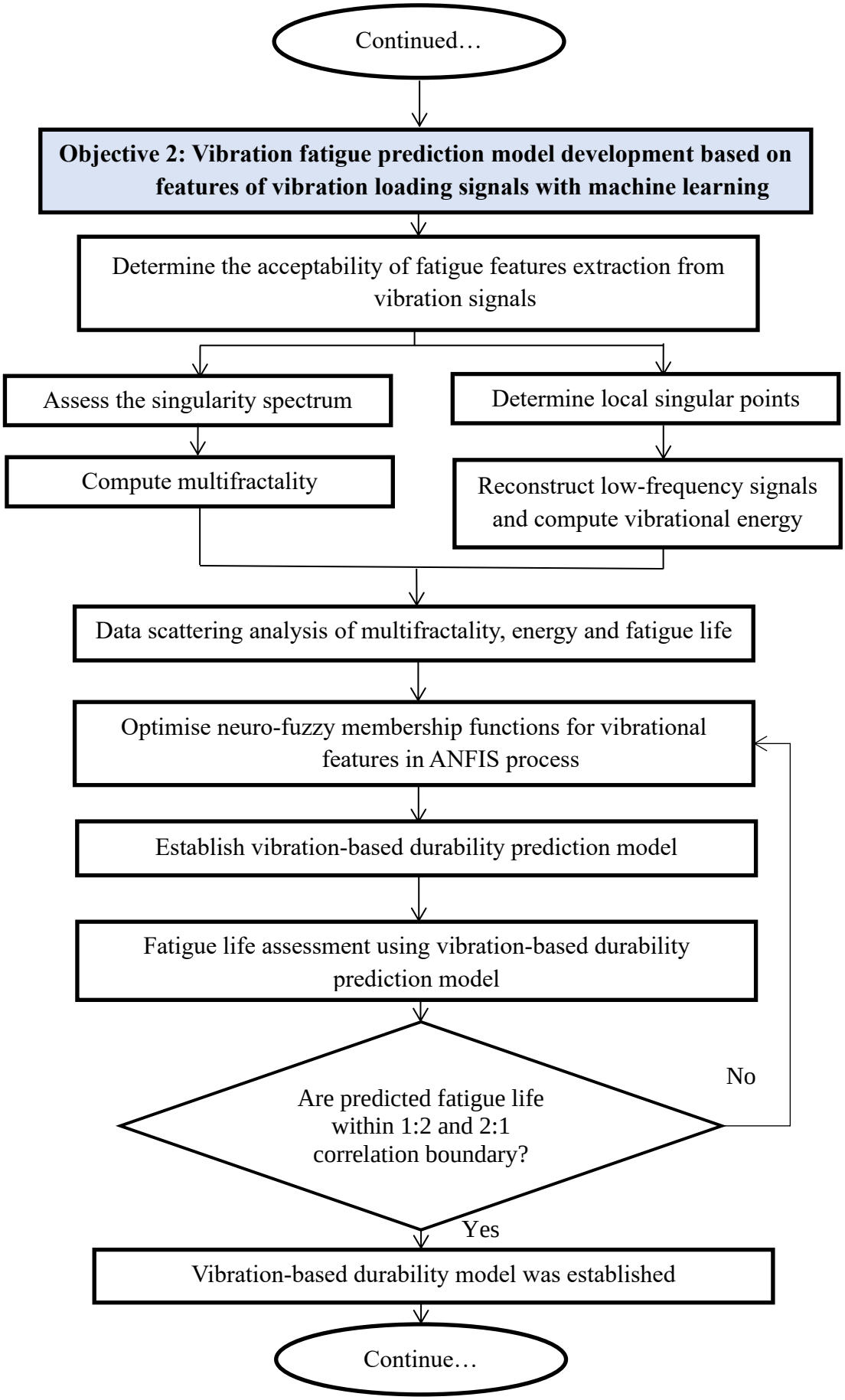
Continued…
Objective 2: Vibration fatigue prediction model development based on features of vibration loading signals with machine learning
Determine the acceptability of fatigue features extraction from vibration signals
Assess the singularity spectrum
Compute multifractality
Determine local singular points
Reconstruct low-frequency signals and compute vibrational energy
Data scattering analysis of multifractality, energy and fatigue life
Optimise neuro-fuzzy membership functions for vibrational features in ANFIS process
Establish vibration-based durability prediction model
Fatigue life assessment using vibration-based durability prediction model
Are predicted fatigue life within 1:2 and 2:1 correlation boundary?
No
Yes
Vibration-based durability model was established
Continue…

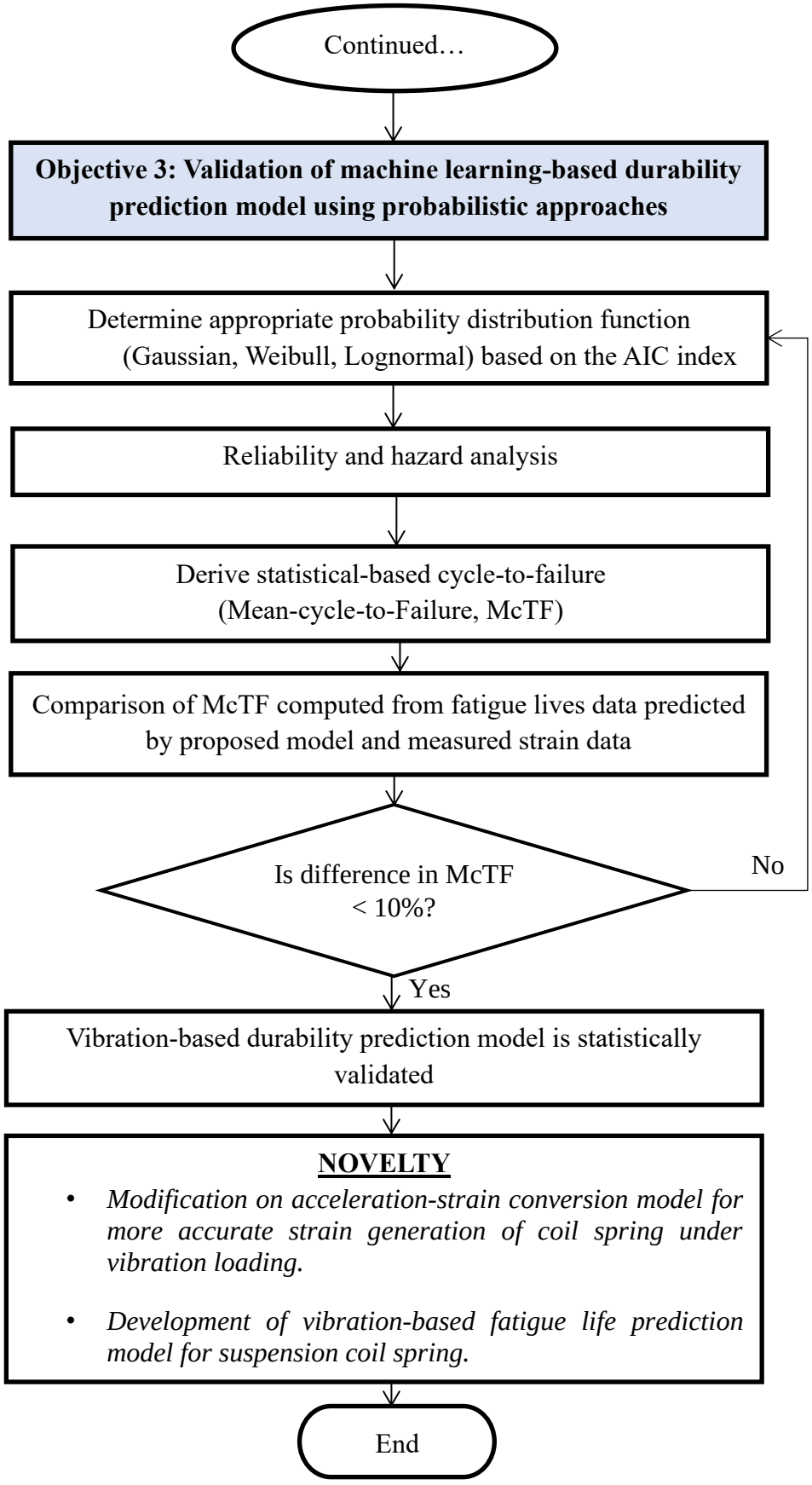

Figure 3.1 Methodology flowchart of vibration fatigue model establishment

Table 3.1 Material properties of SAE5160 carbon steel (Gonçalves et al. 2016)

Properties	Value
Ultimate tensile strength, S_u (MPa)	1584
Modulus of Elasticity, E (GPa)	207
Shear Modulus, G (GPa)	80 (for typical steel)
Yield strength (MPa)	1487
Fatigue strength coefficient, σ_f' (MPa)	2063
Fatigue strength exponent, b	-0.08
Fatigue ductility coefficient, ε_f'	9.56
Fatigue ductility exponent, c	-1.05

A static load analysis was performed on the coil spring using finite element analysis with an ANSYS solver before the road tests to determine the location of the highest stress in the coil spring. This procedure is crucial to determine the position of the strain gauge to capture the maximum strain because the critical spot is where the fatigue failure is most likely to happen (Putra, Abdullah & Schramm 2020).

For a quarter-car suspension model, the total load was assumed to be evenly supported by the four suspension springs and therefore the total load is divided by four (He, Wang & Gao 2010). In the analysis, a static load of 3,384 N was imposed on the coil spring from the bottom coil, considering a total car weight of 1,060 kg and four passengers carrying a load of 320 kg (assuming 80 kg each) (Rahul & Rameshkumar 2020). Meanwhile, the upper coil spring was fixed as a boundary condition. The boundary conditions of the coil spring for the static load analysis are also illustrated in Figure 3.2. A geometry model of the coil spring with the exact geometry as the tested coil spring was produced and meshed into three-dimensional hexahedral elements with an element size of 2 mm as shown in Figure 3.2. The hexahedral meshing was used because it provided uniform meshing of the coil spring and avoided unnecessary stress concentration between the elements (Čakmak et al. 2019). Reduced integration meshing technique was also used to provide good computational efficiency. The optimum mesh size was determined through a mesh convergence analysis in a mesh size ranging between 1 mm and 3 mm (Nasir et al. 2020). The meshed coil spring geometry model is shown in Figure 3.2. It has a total of 41,954 elements and 53,794 nodes. Besides static load analysis, a dynamic load analysis was also performed by imposing a time dependent load on the spring. The load increased from 0 N to 3384 N in 1 s and hold for 2 s before returned to 0 N at the same rate of load increment. The time step of the load was 0.1 s.

A vibration fatigue analysis was also performed on the meshed geometry model using the nCode DesignLife software to determine the fatigue damage contour of the coil spring under cyclic loading. The software provided effective calculation considering the vibration load and geometry of the components using strain-life approaches. The purpose of the analysis was to determine the high fatigue damage region of the coil spring under the amplitude loading variable. In this analysis, vibration loading data of the suspension system acquired by the International Society of Automotive Engineers (SAE) was used as the input load. The SAE vibration data was a typical example of the vibration load of a car suspension system and was extensively used for automotive research (El-Zeghayar, Topper & Bonnen 2013; Putra et al. 2017b). Figure 3.3 shows the SAE vibration signal employed for cyclic load analysis. The location with the highest fatigue damage was recorded and compared to the hotspot in the static load analysis. Figure 3.4 shows the cyclic load analysis of the coil spring performed to determine the high fatigue damage spot. A computer equipped with 32G RAM was used to complete the finite element analysis.

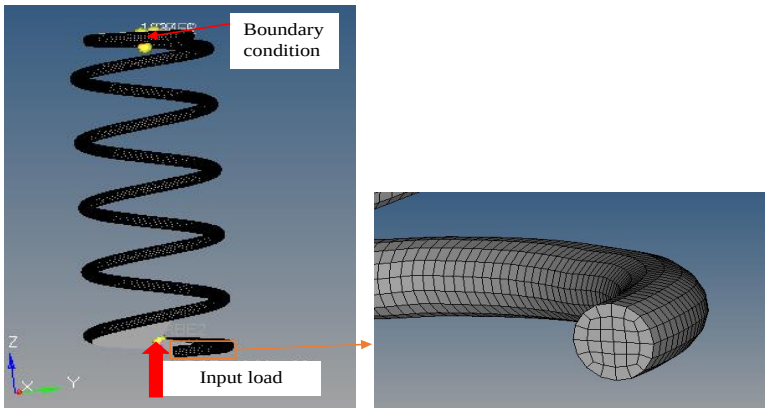

Figure 3.2 Geometrical model of coil spring for finite element analysis based on static and cyclic loads: (a) boundary conditions, (b) meshing of solid elements

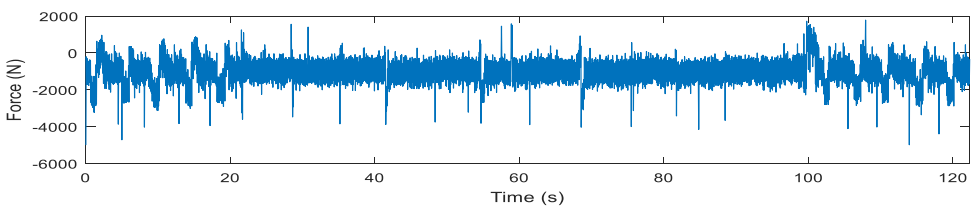

Figure 3.3 SAE vibration load data for cyclic load analysis of coil spring

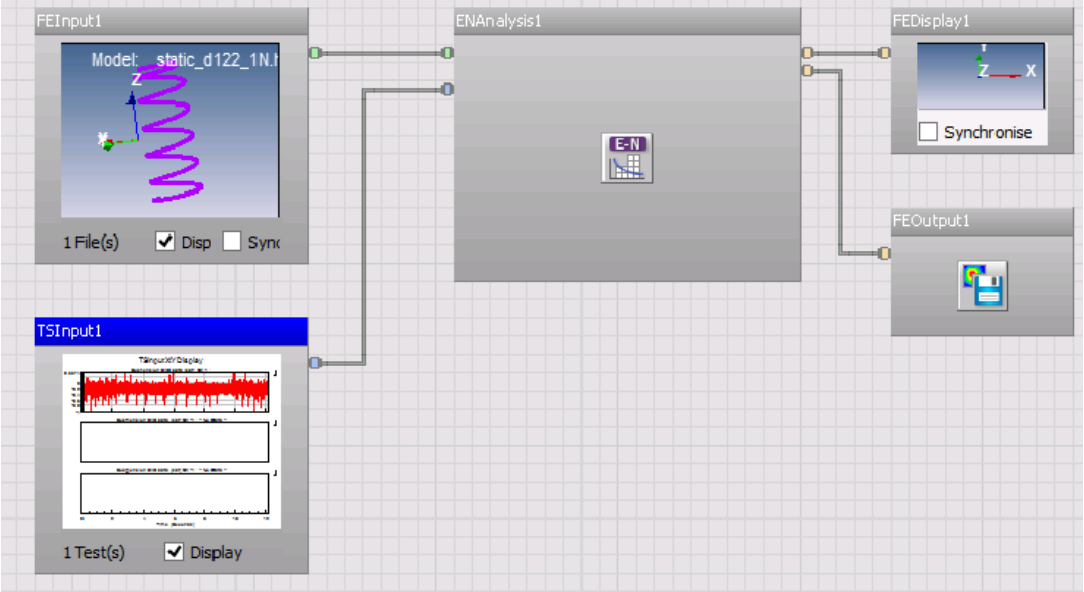

Figure 3.4 Cyclic load analysis of coil spring using nCode DesignLife

3.2.2 Acquisition of Acceleration and Strain Signals

To acquire the vibration and strain signals of the coil spring, road tests on four types of road conditions, including rural area road, industrial area road, university campus road, and highway, were performed. These were some road terrains which are often encountered by ground vehicles in Malaysia. Figure 3.5 illustrates the route and road surface conditions in which the signals were acquired. The car was driven at a speed of 30–40 km/h on the rural road, university campus road, and industrial road, while the car speed was 70–80 km/h on the highway. The rural area road had a very rough surface filled with marbles and sand which continuously gave strong excitations to the suspension system as the car was driven on the road. Due to the uneven road surface during data measurement in the current research, the author reported that the frequency of high amplitude excitations from the rural road surface was the largest. In contrast, the highway road had the smoothest road profile with the least excitation to the car body. The road surface in the industrial area and university campus had some speed bumps or road curbs which would give strong excitations to the car wheels. It is essential to collect the vibration and strain signals from several types of road profile that could statistically represent random road excitations in Malaysia.

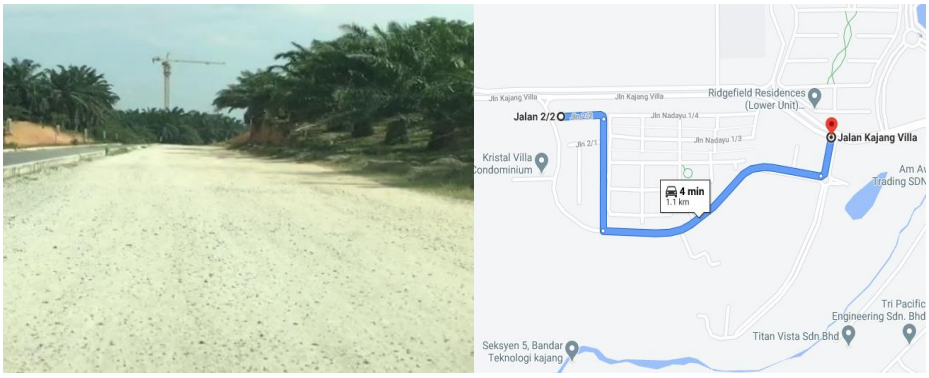

(a)

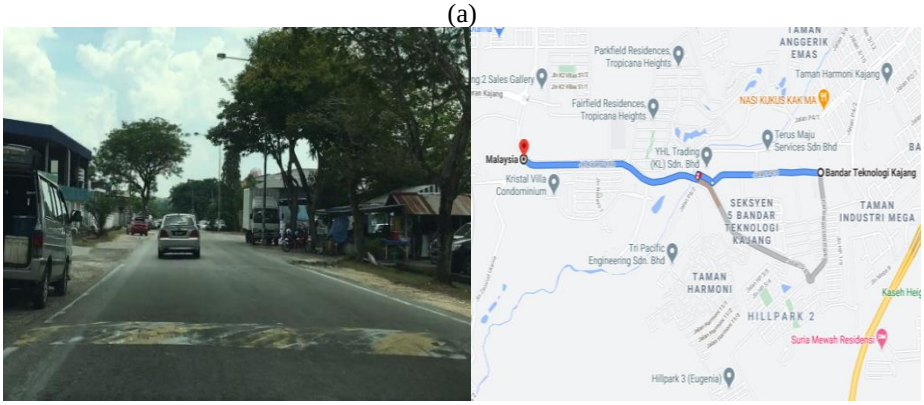

(b)

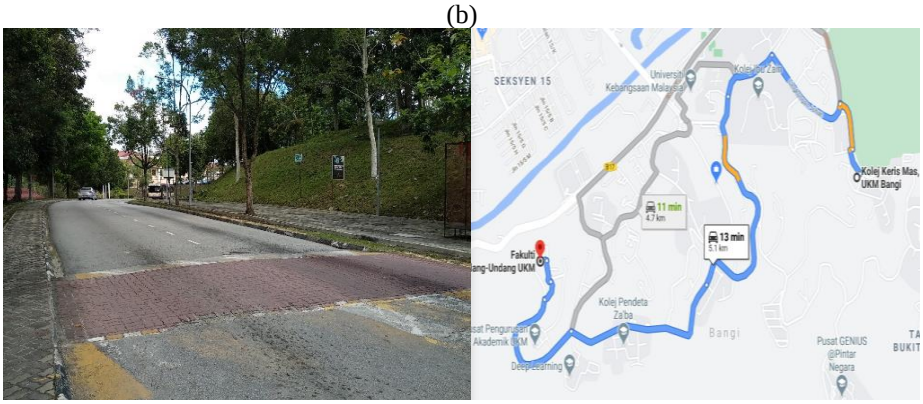

(c)

(d)

Figure 3.5 Road surface conditions and routes of road tests for signal acquisition: (a) Rural area road, (b) Industrial area road, (c) University campus road, (d) Highway road

The suspension system of a Malaysian made 1,300 cc sedan car was used as a test subject. The vibration and strain signals were acquired with the aid of the Dewesoft Sirius data acquisition instrument system. The surface of the coil spring where the strain gauge was placed was first cleaned with sandpaper with a grade of 400 grits to minimise the interference of dirt on the signal acquisition process. Subsequently, strain gauge (Kyowa KFGX-1-120-C1-11L-1M2R) with gauge length of 5 mm was firmly adhered with adhesive glue at the coil spring to record the strain histories under driving condition. The strain gauge was placed as near as possible to the critical spot determined through the FEA-based static and vibrational load analysis, as discussed in Section 3.2.1. This was to ensure that the strain histories captured in the road tests were the maximum strain which caused fatigue failure to the coil spring.

Figure 3.6 depicts the experimental setup for the road tests including the tested car, the sensors used for signal acquisition and the data acquisition instrument used. A uniaxial accelerometer manufactured by PCB Piezotronics® with a sensitivity of 10.07 mV/ms^{-2} was placed at the lower suspension arm of the suspension system to measure the vertical acceleration of the car wheel under excitations from the road surface. The accelerometer was placed as near as possible to the lower ball joint of the lower suspension arm to measure vertical acceleration of the wheel. Figure 3.7 illustrates the accelerometer and strain gauge used for vibration and strain data measurement, respectively. The accelerometer used in the road test had been calibrated by the manufacturer over a range of sampling frequency (1-20k Hz) to ensure accurate reading. The vertical acceleration of the car wheel represented the vibrational excitation from the road surface as the wheel bounced vertically as it hit some road surface irregularities (Suzuki et al. 2021). Previous studies by Manouchehrynia, Abdullah & Singh (2020) and Rahim et al. (2020) remarked that the loading signals of the suspension system needed to be acquired with a frequency higher than 400 Hz to avoid the loss of signal information due to under-sampling. Therefore, a sampling frequency of 500 Hz was set for signal acquisition (Shangguan et al. 2020). Vibration signals and strain histories were simultaneously and repeatedly recorded using the data acquisition instrument. The road tests were repeated under the same road terrains to sufficiently capture long loading signals of the suspension system. Subsequently, 80 s loading signals were selected from the recorded loading signal of each road condition to represent different loading

conditions for further analysis. These short loading signals were sufficient to represent the random road excitations based on the statistical behaviours (Shangguan et al. 2020).

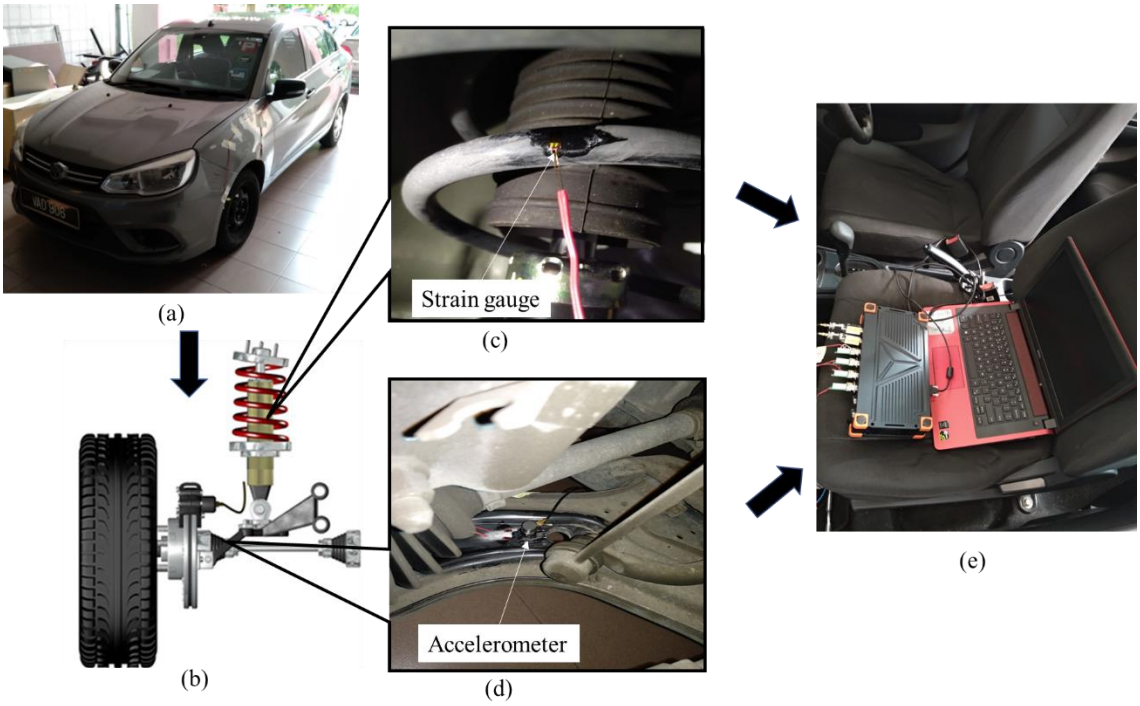

Figure 3.6 Experimental setup for road tests: (a) tested car, (b) location of sensors for signal acquisition in suspension system, (c) strain gauge at coil spring, (d) accelerometer at lower suspension arm, (e) data acquisition instrument

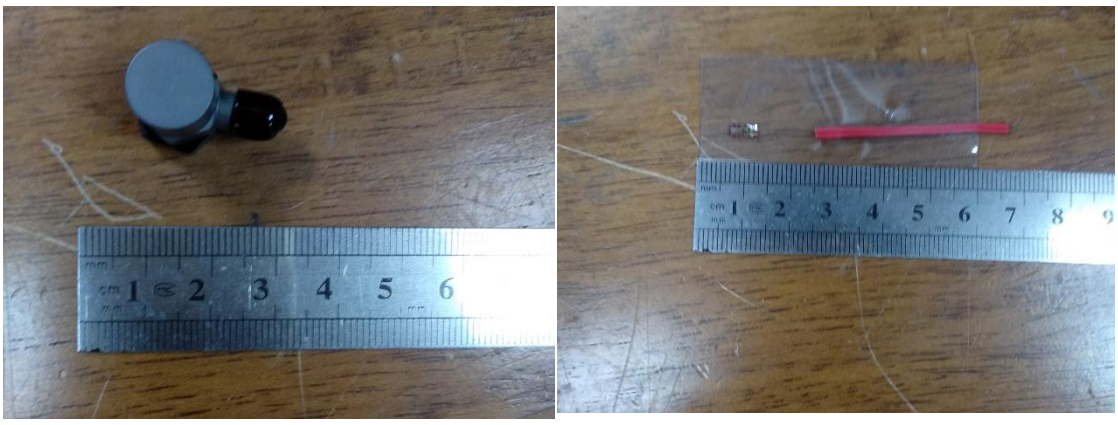

Figure 3.7 Sensors used for loading data measurement: (a) accelerometer, (b) strain gauge

Statistical parameters, including mean, RMS, skewness, and kurtosis of the loading signals, were computed to determine the signal behaviours. The mean and RMS measured the distribution of data while the skewness and kurtosis quantified the amount of extreme data. CWT analysis, as expressed in Equation 2.45, was also used to reveal the time-frequency properties of the loading signals. The CWT energy (E_{CWT}) was determined from the CWT coefficients, such that:

$$E_{CWT} = \left| \sum_{s=1}^{n} W_{\psi} f(s,u) \right|^2 \quad \ldots(3.1)$$

The CWT energy revealed the high energy sections in the loading signals which were closely related to the fatigue damage (Pratumnopharat, Leung & Court 2014). A Morlet wavelet, as expressed in Equation 3.2, was selected as the mother wavelet function for the CWT analysis because the Morlet wavelet can effectively detect the transient event in the signals since the time-frequency structure of the Morlet wavelet could match the transient events (Liu et al. 2014; Zhang et al. 2016):

$$\psi(t) = exp\left(\frac{-\beta_m{}^2 t^2}{2}\right) cos(\pi t) \quad \ldots(3.2)$$

where β_m is the shape parameter which controls the dilation of the function.

3.2.3 Multibody Dynamics Model of Quarter-Car Suspension System

A quarter-car suspension model was used as the multibody dynamics (MBD) representation of the car suspension system (Szymański et al. 2015). Even though half-car and full-car models provide a more accurate prediction of suspension responses (Sharma et al. 2016), these models involve a massive computational load and also have high difficulty to obtain the experimental data that involve multiple suspension systems. In contrast, the quarter-car model provides reasonable accuracy with relatively lower computational load and hence widely used in many studies involving ground vehicle suspension (Nagarkar, Patil & Patil 2016; Suzuki et al. 2021).

The quarter-car model was composed of two bodies, namely a sprung mass (car chassis mass, M_1) and an unsprung mass (suspension components and wheel masses, M_2). The sprung and the unsprung masses were linked by a spring with stiffness k_1 and a damper with damping coefficient c_1. The tyre was modelled as another spring with a tyre stiffness k_2. Equations 2.17 and 2.18 describe the motion of the sprung and unsprung masses in a 2 DOF mass-spring-damper suspension system. Equations 2.17 and 2.18 only explain the kinetic (forces) relationship between the unsprung and sprung masses but reveal no kinematics information (displacement, velocity, and acceleration) of the suspension components subjected to external forces. To accurately predict the spring responses, the kinematics interaction between suspension components must be known.

The quarter car model was built into an MBD model as shown in Figure 3.8, facilitated with a commercial MBD software, AdamsView®, to simulate the suspension components' motions and the spring responses under vibrational loading. This MBD model of car suspension is considered more than just the forces interactions between components alone. The joint connections between components and the moments of inertia of bodies are also taken into account. These considerations could provide a more accurate prediction of the motions of suspension components and the spring responses under random excitations. A detailed information of the suspension components' hard points, masses and moments of inertia is shown in Table 3.2 and Table 3.3. In the MBD simulation, the car body mass (M_1) was set as 345 kg considering a quarter weight of the tested car. The hard points of the suspension systems were important to define the component and joint positions that represented the linkage of the components in the suspension system (Vdovin & Chichekin 2016). For example, the hard point coordinates of the lower control arm, including the bushing, were essential to determine the locations of the joints in the MBD simulation. Apart from that, inertia moments in three directions (I_{xx}, I_{yy} and I_{zz}) were also essential in the MBD simulation as they represented the inertial properties of the components, and this information was needed to predict the dynamic responses of the components (Prastiyo & Fiebig 2021). The mass and inertial moments of the lower control arms played an important role to determine the unsprung mass acceleration in respond to the vertical road excitations.

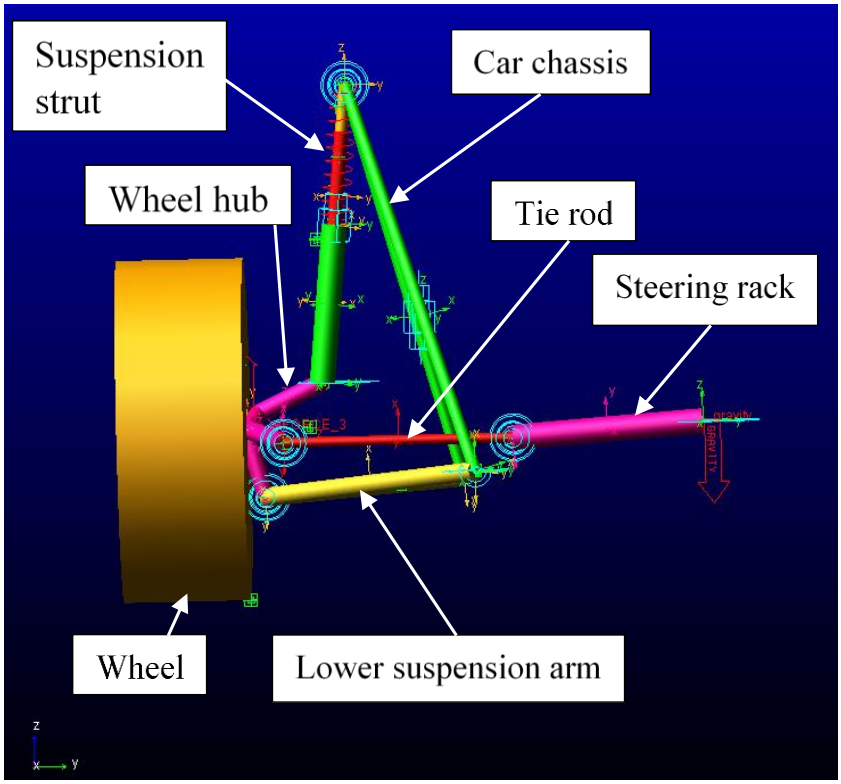

Figure 3.8 Quarter-car suspension model simulation to estimate the spring responses under random road excitations

The quarter-car suspension system consisted of a suspension strut composed of a strut tube and a strut rod, connected with each other with a translation joint which allowed them to slide through each other along their axes. The lower end of the suspension strut was connected between the wheel hub with a fixed joint to transmit the vibration from the tyre and the other end connected to the car chassis with a ball joint. The suspension strut had a massless spring with stiffness, k_1, of 16,806 N/m and a massless damper with damping coefficient, c_1, of 15,564 Ns/m (Kong et al. 2018b). The values of the spring stiffness and damping coefficient were obtained from the specifications of the tested suspension system. At the lower part of the suspension system, the wheel hub was also linked to a lower control arm through a lower ball joint to the car chassis. The control arm had two bushings connected to the car chassis with rotational joints. The control arm allowed the tyre to move vertically without being detached from the car body. A tie rod that controls the steering movement of the tyre was connected to the steering rack and wheel hub with ball joints. The steering rack was fixed as the information of steering degree during the road tests was not available. Vertical acceleration signals of the tyre captured via the road test was used in the MBD

simulation to represent the road excitation and the spring responses were simulated (Risaliti et al. 2019).

Table 3.2 Hard points and coordinates in suspension system

Hard point of suspension component	Coordinates (mm)		
	x	***y***	***z***
Wheel centre	-35.00	-723.00	0.00
Spindle	-35.00	-623.00	0.00
Knuckle	-89.53	-703.40	22.80
Lower ball joint	-38.61	-695.00	-108.06
Outer tie rod ball joint	95.19	-661.93	-19.04
Lower control arm centre of gravity	76.29	-481.53	-89.00
Lower control arm front bushing	-31.05	-382.25	-83.48
Lower control arm rear bushing	276.11	-356.99	-64.82
Upper damper rod	-0.19	-554.00	540.28
Lower damper tube	-30.38	-601.79	71.06
Upper spring	-2.29	-559.43	50572
Lower spring	-15.28	-604.12	296.76
Tyre patch	-35.00	-723.00	-270.00
Strut road lower joint	-14.69	-576.59	314.91
Upper strut tube	-14.41	-576.51	319.27

Source: Kong et al. 2019b

Table 3.3 Inertia moments (*I*) of suspension components

Components	Mass (kg)	***Ixx***	I_{yy}	I_{zz}
Knuckle	10.26	7,422.19	36,256.26	36,765.55
Lower control arm	3.57	235,543.81	81,500.94	244,206.35
Wheel	10.00	1,768,682.22	3,001,113.30	1,767,569.89
Wheel hub	27.00	120,411.99	103,005.90	117,438.71
Strut rod	0.84	116,061.30	147,381.99	20,590.32
Strut tube	1.65	83,896.67	57,144.03	27,914.09
Tie rod	1.00	84,291.56	47,767.64	70,608.18

Source: Kong et al. 2019b

3.2.4 Derivation of New Displacement-Strain Relationship for Strain Generation

In this study, a new relationship between the strain in the coil spring and the spring displacement had been derived to generate strain signals based on road vibration data. The idea of strain simulation using FEA-based approaches had been extensively investigated (Deshmukh, Venkatachalam & Saraf 2019; Henkel, Weijtjens & Devriendt 2019; Reu 2015). This study aimed to improve the accuracy of generated strain signals by considering the spring curvature and MBD effects. By considering the mechanism of a helical compression coil spring and the spring curvature effect, the maximum shear stress in the coil spring can be obtained from the combination of the torsional and

transverse shear stresses. Equation 2.4 shows the contribution of transverse shear stress to maximum shear stress in the spring, depending on the spring index.

The geometry parameters of the tested suspension spring are shown in Table 3.4. The mean coil diameter represented the overall size of the coil spring and a smaller mean coil diameter resulted in higher stiffness. The spring wire diameter was the size of the coil wire, and this parameter was directly proportional to the stiffness. The active coils were the coils involved in spring deflection. The spring geometry of the tested spring resulted in a spring index of 10.66. This indicated that the transverse shear stress had a minimal contribution of only 4.7% to the maximum stress. Therefore, the effect of transverse shear stress can be neglected in this study and only the torsional shear stress was taken into consideration as defined in Equation 2.2 (Champion & Champion 2011).

Table 3.4 Geometry parameters of suspension spring

Spring geometry parameter	**Value**
Mean coil diameter, *D* (mm)	130
Spring wire diameter, *d* (mm)	12.2
Number of active coils, *N*	6

The curvature of the spring can cause a significant stress concentration on the spring surface and thus it is necessary to be considered in strain generation (Čakmak et al. 2019). The stress concentration effect due to spring curvature is considered with the curvature stress concentration factor, K_w (also known as Wahl correction factor) as defined in Equation 2.5. Given the spring geometry parameters, the spring index of the spring in this study resulted in a K_w of 1.135. This indicates that the curvature effect in the spring magnified the maximum shear stress in the spring by 13.5 %. Therefore, the stress concentration due to spring curvature effect was taken into consideration given its significant effect and Equation 2.6 expresses the maximum torsional shear stress by considering the K_w. Equation 2.8 shows the dependence of the spring stiffness (k_1) on the geometry parameters and material properties. By substituting Equation 2.8 into Equation 2.6, the maximum tortional shear stress of the coil spring under loading can be rewritten as follows (Pöllänen & Martikka 2010):

$$\tau = K_w \frac{1}{\pi} \frac{Gd}{D^2 N} x \quad \ldots(3.3)$$

The torsional shear stress in the spring wire results in the deformation of the wire and produces strain energy in the wire. The strain energy due to torsional shear stress in the spring is given by (Singh 2021):

$$U_s = \frac{\tau^2}{4G} \times AL \quad \ldots(3.4)$$

where A is the cross-section area of spring wire and L is the total length of spring wire. Hence, the Equation 3.4 can be rewritten as:

$$U_s = \frac{K_w{}^2 Gd^2 x^2}{4\pi^2 N^2 D^4} \times AL \quad \ldots(3.5)$$

In general, the potential strain energy stored in an elastic body with volume, $V=AL$, due to the deformation of the body can be expressed as follows (Kong et al. 2019a):

$$U_p = \frac{1}{2} E\varepsilon^2 \times AL \quad \ldots(3.6)$$

By assuming there is no internal energy dissipation in elastic deformation, the strain energy caused by spring deflection and the potential strain energy stored in the spring while deflected were equal ($U_s=U_p$), the relationship between the spring deflection and the strain in the spring can be established as:

$$\varepsilon = \sqrt{\frac{K_w{}^2 Gd^2}{2\pi^2 D^4 N^2 E}} \times x \quad \ldots(3.7)$$

Equation 3.6 provides the relationship between spring deflection due to axial force and the maximum strain in spring by considering the torsional strain energy and spring

curvature effect. The displacement-strain conversion model is known as the Chin-Abdullah-Schramm-Ariffin-Singh (CASAS) model afterwards. Since the $X_1 - X_2$ in Equation 2.17 represents the spring deflection, by substituting Equation 3.7 into Equation 2.17, a new acceleration-strain conversion model can be obtained, and further analysis can be proposed in this research:

$$\varepsilon = \frac{M_1\ddot{X}_1 + c_1(\int \ddot{X}_1\,dt - \int \ddot{X}_2\,dt)}{-k_1} \times \sqrt{\frac{K_w{}^2 G d^2}{2\pi^2 D^4 N^2 E}} \quad \ldots(3.8)$$

Equation 3.8 is a mathematical model that represents the conversion of unsprung mass vibration signals in acceleration form ($\ddot{X}_1$) into strain signals for durability analysis of the coil spring. The sprung mass acceleration ($\ddot{X}_2$) can be obtained by solving the differential equation with its initial condition being set to zero (Mitra et al. 2016). This model integrates the typical kinetics equation of a passive suspension system with the derived displacement-strain relationship, enabling a direct conversion between vibration and strain signals. This provides less computational effort for strain simulation compared to FEA-based approaches. However, this model does not consider the MBD effects between the suspension components and therefore MBD simulation is used in this study to predict the spring displacement before the strain conversion.

3.2.5 Strain Generation with Acceleration-Strain Conversion Model

With the newly derived acceleration-strain conversion model as shown in Equation 3.8, the vibration signals collected via road tests were used as input of the MBD simulation to estimate the coil spring responses under random road excitations. The quarter-car suspension MBD model as shown in Figure 3.8 was used in the simulation. The vibration signals were used as the vertical movement of the wheel in the MBD simulation to reconstruct the road excitations under real-life conditions (Suzuki et al. 2021). Vibration signals collected under different road conditions, such as university campus, industrial area, rural area, and highway, were employed in the MBD simulation. The coil spring displacements during road excitations were recorded at the frequency of 500 Hz as the strain histories were also collected at the same sampling

frequency. Shangguan et al. (2020) also reported that a sampling rate of 500 Hz was sufficient to retain the fatigue damage in the loading histories of suspension system.

After the spring displacement was estimated from the MBD simulation, the estimated spring displacement was subsequently converted into strain signals of coil spring using the displacement-strain relationship by considering the torsional shear stress and spring curvature effect. The simulated strain signals were then filtered using a high-pass filter at 0.5 Hz to remove ultra-low frequencies in the simulated strain signals. The filter frequency was determined by comparing the CWT mapping of the simulated and experimental strain. Minaker &Yao (2017) reported that the frequency range between 0.5 and 2 Hz in vehicles' loading histories was due to large chassis motion while 8–12 Hz resulted from the wheel motion. Therefore, frequency components below 0.5 Hz in the simulated strain signals were likely the results of undesired amplitude fluctuations. As a comparison, strain signals were also generated using an acceleration-strain conversion model proposed by Kong et al. (2019a), later known as the Kong-Abdullah model. The Kong-Abdullah model assumed a relative displacement between the sprung and unsprung masses as the complete working place of spring without considering the MBD relationship between the suspension components. The strain-displacement relationship proposed in the Kong-Abdullah model is given in the following equation Kong et al. (2019a):

$$\varepsilon = \sqrt{\frac{Gd^4}{8ND^3EAL}} \times x \qquad \ldots(3.9)$$

The Kong-Abdullah model required the measurement of vertical acceleration of both unsprung and sprung masses to determine the spring responses. However, the vertical sprung mass acceleration was not measured in this study because the sprung mass acceleration was simulated by MBD simulation. Therefore, the Kong-Abdullah model was reproduced using a simulation based on the kinetic equations of the suspension quarter-car model as expressed in Equations 2.17 and 2.18 with MATLAB Simulink®. Kong et al. (2019a) reported an acceptable accuracy of Kong-Abdullah model in fatigue

life prediction with R^2 values above 0.8. However, a limitation in predicting high cycle fatigue above 10^7 cycles was also observed.

After the strain signal simulations, the statistical properties, such as mean, RMS, skewness, and kurtosis, of the simulated strain signals were computed and compared to the strain histories experimentally collected in the road tests. Comparison of statistical properties of strain signals are important to determine if the simulated strain signals exhibited similar behaviours to the experimental collected strain signals. The mean values of the strain histories indicated if the nature of loading was tensile or compressive. A tensile loading is known to have more detrimental effects than a compressive loading (Zhang et al. 2019b). The RMS is a good indication of signal energy and is related to the fatigue damage in the strain loading (Palmieri et al. 2017). The skewness measures the symmetricity of the data distribution, and a symmetric distribution has zero skewness. The kurtosis of a signal reveals the "peakedness" of the distribution that is related to the extreme values in the signals (Cianetti et al. 2018). A perfect Gaussian loading signal should have a zero skewness and kurtosis of about 3 (Ugras et al. 2019). Several studies (Capponi et al. 2017; Kihm, Ferguson & Antoni 2015) remarked that the non-Gaussian loading histories with higher kurtosis values are likely to inflict more fatigue damage to structures due to the existence of high amplitude events.

Subsequently, fatigue life was also predicted from the simulated strain signals using strain-life approaches and effective-strain-damage (ESD) model. Strain-life models, such as Coffin-Manson, Morrow, and Smith-Watson-Topper (SWT) models, are represented by Equations 2.31, 2.32, and 2.33, respectively and widely use durability prediction models in automotive industry because of the acceptable accuracy and simplicity (Niederwanger et al. 2019; Yang, Yang & Wang 2020). In addition, the strain-life approaches are more appropriate for automotive components with small geometry, such as coil spring, because the plastic strain is dominant and contributes to high fatigue damage (Kahoul et al. 2019). A plasticity check was performed on the coil spring using finite element method to confirm that the spring experience plastic deformation under an extreme load, as shown in Appendix A. The coil spring was found to experience plastic deformation under a load of 4990 N, the highest load in the SAE

vibration load data. Hence, strain-life approaches were applied to consider the plastic strain in fatigue life assessment (Putra et al. 2017a). Morrow and SWT models consider the mean-stress effect in the loading while Coffin-Manson predicts the fatigue life at zero mean stress. The rainflow cycle counting algorithm was employed to determine the fatigue cycle in the strain signals because the rainflow cycle count is the most accepted cycle counting method with good accuracy and robustness (Marsh et al. 2016). The procedures of the rainflow cycle counting are discussed in Section 2.3.4.

Regardless of the widely accepted accuracy of strain-life approaches, the strain-life models are unable to evaluate the load sequence effect which can bring significant effects in VAL applications (Wang, Serra & Argoul 2019). Hence, the ESD model was adopted in this study to assess the fatigue life of coil spring under the consideration of load sequence effect. The ESD model is explained in detail in Section 2.3.7. It is also important to note that the rainflow fatigue cycles determined in the strain histories must be rearranged according to the original cycle sequence in the strain histories before the fatigue damage calculation using ESD model (Kadhim, Abdullah & Ariffin 2012). This was an important procedure to ensure that the load sequence effect was considered during the fatigue damage calculation. The estimation of fatigue damage using ESD model required some information of fatigue parameters of the material, especially the crack closure parameter (m_d). Due to the lack of the experimental information of SAE5160 carbon steel regarding the parameter, m_d, the fatigue parameters were obtained from previous research (El-Zeghayar, Topper & Bonnen 2013; El-Zeghayar, Topper & Soudki 2011) that had conducted the crack opening experiments on several materials including DP509, SAE1045, and AISI8822 steels. The SAE1045 carbon steel was found to have the nearest mechanical properties with SAE5160 carbon steel compared to other materials as shown in Table 3.5. As reported by El-Zeghayar, Topper & Bonnen (2013), the m_d parameter of SAE1045 steel was 0.08 and this value was utilised in this study.

Table 3.5 Mechanical properties of SAE1045, DP509, AISI8822 and SAE5160 steels.

Mechanical properties	**SAE1045**	**DP509**	**AISI8822**	**SAE5160**
Author (year)	**El-Zeghayar, Topper &Bonnen (2013)**			**Putra et al. (2017a)**
Ultimate tensile strength, S_u (MPa)	1271	623	1480	1584
Modulus of Elasticity, E (GPa)	205	209	209	207
Yield strength (MPa)	1200	349	-	1487
Fatigue strength coefficient, σ_f' (MPa)	1813	806	2234	2063
Fatigue strength exponent, b	-0.094	-0.083	-0.109	-0.08
Fatigue ductility coefficient, ε_f'	0.577	0.351	-	9.56
Fatigue ductility exponent, c	-0.6	-0.5	-	-1.05

Source: El-Zeghayar, Topper &Bonnen 2013; Putra et al. 2017a

Lastly, the cumulative fatigue damage was computed using the Palmgren-Miner linear damage rule, as expressed in Equation 2.34. The Palmgren-Miner rule is still extensively used in industrial practices because of its simplicity and acceptable accuracy (Ugras et al. 2019). The total fatigue life (N) can then be determined from the inverse of D_f, such that:

$$N = \frac{1}{D_f} \qquad \ldots(3.10)$$

After the determination of fatigue life, fatigue life conservative analysis was conducted to evaluate if the proposed model gave conservative fatigue life predictions. Apart from that, the root-mean-square-errors (RMSE) between the predicted fatigue lives from simulated and experimental strains were computed to determine the accuracy of the simulated strain signals (Mahmud et al. 2018). The RMSE values were also compared between the proposed model in this study and the Kong-Abdullah model to determine the enhancement of the proposed model in simulating strain signals of coil spring compared to the previous model.

3.3 MACHINE LEARNING APPROACH FOR PREDICTING THE VIBRATION-BASED DURABILITY

The vibration signals collected at the lower suspension arm during road tests represent the excitations from road surface (Suzuki et al. 2021). Fatigue-related feature extraction from the loading signals often speeds up durability assessment of engineering components. For example, Marciniak et al. (2019) characterised the strain energy for

fatigue life prediction of structural material. The low amplitude cycles can be eliminated in strain histories of coil spring through determination of signal energy (Pratumnopharat, Leung & Court 2014; Shangguan et al. 2020). Multifractal properties, representing the complexity of loading histories, were also characterised as a fatigue prediction parameter.

3.3.1 Determining Low-Frequency Vibration Energy via Hölder Singularities

The energy of loading signal had been related in several studies with the high fatigue damage events in the loading histories (Liao & Zhu 2019; Putra, Abdullah & Schramm 2020). Kong et al. (2017) supported that fatigue damage of coil spring due to road excitations occurred at low frequency signal below 50 Hz. The road surface roughness often gives low-frequency excitations to the wheel (Minaker & Yao 2017). However, high frequency noises due to environmental or instrumental factors often exist in the acquired signals (Panda 2016). The high frequency noises may result in some errors during the estimation of the signal energy. A denoising processing is therefore necessary to mitigate the effects of high frequency noises. Singularities in the vibration signals were characterised with Hölder Exponents (HE) and then the signal was reconstructed to eliminate high frequency noises.

To obtain the low-frequency energy of vibration signals, the singularities in the time series must be first determined. Figure 3.9 illustrates the process flow of the determination of Hölder singularities in the vibration signals. CWT, as expressed in Equation 2.45, was performed on the vibration signals collected in road tests. CWT was used for singularities determination because CWT provided more detailed information of the local properties in time-frequency domain compared to discrete wavelet transform (DWT) (Zhang et al. 2016; Zhou et al. 2020). In this study, the singularities were characterised with HE, which is a commonly used notion to measure local regularity, as expressed in Equation 2.51. After the wavelet coefficients were obtained through CWT, maxima lines were estimated from the wavelet coefficients. The localised maxima of the wavelet coefficients were the coefficients with the largest magnitude among neighbouring coefficients. These lines, also known as the wavelet

transform maxima modulus (WTMM), indicated the convergence at the finest scale and the location was the location of the singularity.

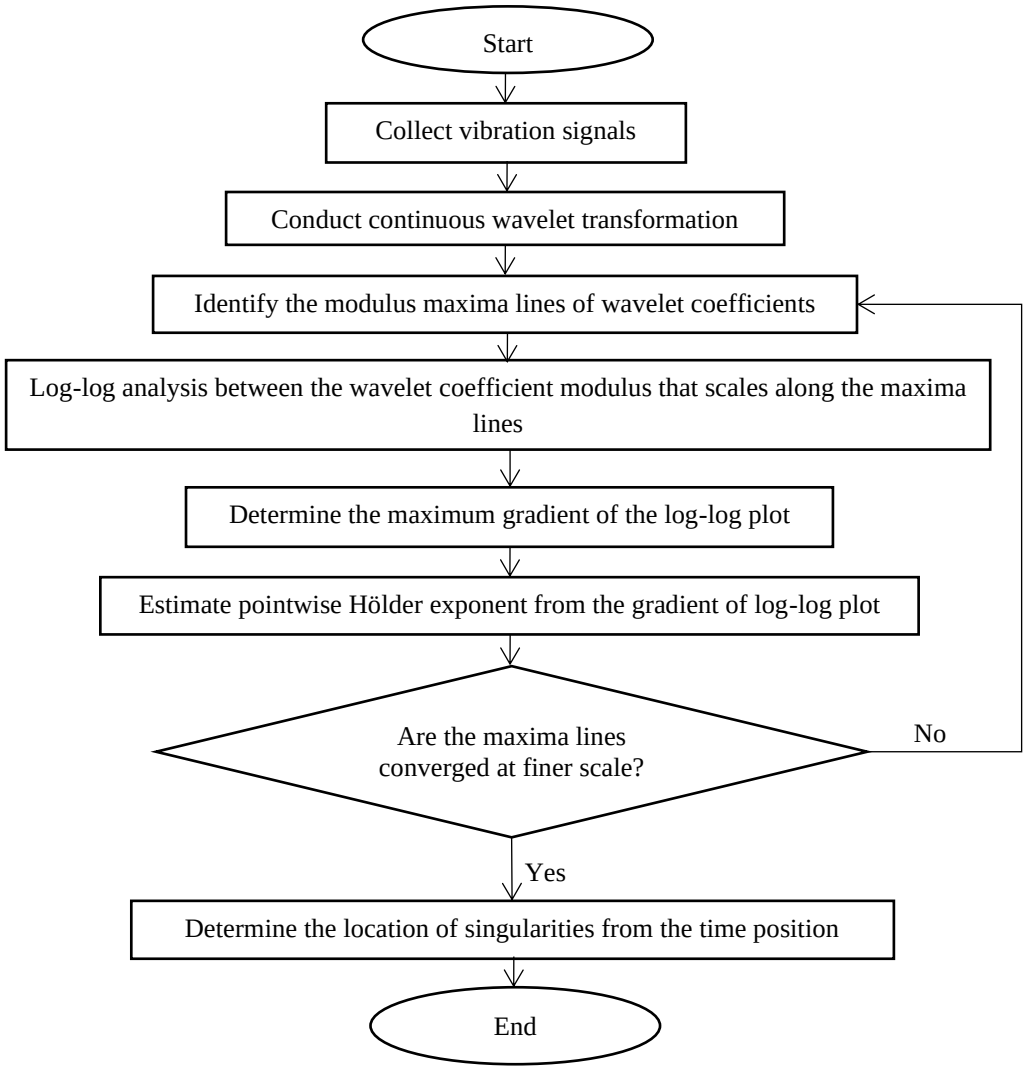

Figure 3.9 Flowchart of singularities determination from vibration signals

In the singularity analysis, the choice of wavelet function played an important role. Previous studies (Zhang et al. 2016; Zhou et al. 2020) recommended the derivative of Gaussian (DOG) wavelet to be applied in singularity analysis due to its well-defined vanishing moments corresponding to its order of derivative. Furthermore, Zhang et al. (2016) also made comparison using the DOG and complex Morlet wavelets to determine the singularities of the pressure changes during stall inception of a spike-type compressor. The study remarked that DOG wavelet with low vanishing moments was effective in identifying singularities with HE below 0.5 because low vanishing moment

of DOG wavelet had better match with the low-frequency singularities of signals. Therefore, the DOG wavelet with *m* order of derivative, as shown in Equation 3.11, was employed for the CWT in the singularity analysis (Venkatakrishnan et al. 2014):

$$\psi^{(m)}(t) = \frac{(-1)^{m+1}}{\sqrt{\Gamma(m+\frac{1}{2})}} \frac{d^m}{dt^m}\left(e^{-\frac{t^2}{2}}\right) \quad \ldots(3.11)$$

The suitable vanishing moment of DOG wavelet for the singularity analysis was optimised by comparing the second, fourth, and sixth orders of DOG wavelet functions with 2, 4, and 6 vanishing moments, respectively. An appropriate vanishing moment is important in a singularity analysis as the vanishing moment of the wavelet function determines the highest HE of the singularities to be estimated (Régis, Doncescu & Desachy 2008). Too high vanishing moment may result in estimation of redundant singularities with high HE values and include high-frequency features in the signal. The statistical parameters (RMS and kurtosis) of resulted singularity signals were then compared to determine the appropriate number of vanishing moments with the least difference of signal behaviour with the original signals (Sinha & Das 2020). This minimised the information loss during singularity extraction and preserve the fatigue properties of the signals.

The vibration signals were then reconstructed using the extracted singularities. The signal reconstructed process was performed by maintaining the sampling frequency at 500 Hz. The missing data between singular points were estimated using the linear interpolation method:

$$\frac{y-y_0}{t-t_0} = \frac{y_1-y_0}{t_1-t_0} \quad \ldots(3.12)$$

where *y* is the predicted data point, *t* denotes the time location, and the subscripts 0 and 1 indicate the points before and after the predicted point, respectively. The power spectral density (PSD) of the signal was then estimated using Equation 2.38. The PSDs were estimated using a Hanning window with the size of 1028 and a buffer overlapping

of 67 with the nCode GlyphWork® software (Kallel et al. 2012). To validate the effectiveness of the proposed singularity method in extracting low-frequency features, the vibration signals were also filtered using conventional lowpass filter at 50 Hz and the PSDs were also estimated. Hence, the vibration signal energy was calculated by estimating the area under the PSD graph:

$$E_{PSD} = \int_0^{\infty} P(\omega)\, d\omega \qquad \ldots(3.13)$$

where E_{PSD} is the energy of vibration signal and $P(\omega)$ is the PSD.

3.3.2 Wavelet Function for Multifractality of Vibration Signals

In this study, multifractal analysis plays an important role to extract one of the fatigue-related features from the vibrational loading signals of coil spring under various road conditions. Wavelet leaders (WL) multifractal formalism had been chosen to reveal the multifractal properties of vibration signals. This is because WL method is exceptional in handling non-stationary signals with low computational cost compared to other numerical multifractal formalisms, such as the WTMM and MFDFA methods (Pnevmatikos et al. 2020; Serrano & Figliola 2009). In addition, WL method also offers a full-domain multifractal characterisation in time series supported by a complete mathematical theoretical framework (Du et al. 2014). Komorska & Puchalski (2021) determined the multifractal properties of vibration signals obtained from rotating machines using WL method to diagnose the fatigue damage. Details of the theoretical framework of WL methods can be found in Section 2.4.7.

Figure 3.10 summarises the estimation process of multifractal spectrum of vibration signals using WL methods. First, DWT was conducted on the vibration signals to reveal the time-frequency properties of the signals as given in Equation 2.49. The WL method is a DWT-based multifractal formalism and it is less computational heavy compared to CWT-based techniques (Pnevmatikos et al. 2020). In multifractal analysis, the mother wavelet function must be carefully selected so that the vanishing moments (m) of the wavelet function are larger than the largest singularity exponent in the data

to achieve stable structure functions and suppress the potential superimposed smooth trend (Du et al. 2014; Xiong et al. 2016). However, too high vanishing moment could result in undesired border effects and it is reasonable to limit the vanishing moment of the wavelet function below 2 (Zhou et al. 2020). Based on this reason, the Daubechies 2 (*db2*) wavelet with two vanishing moments was employed for DWT in the current work.

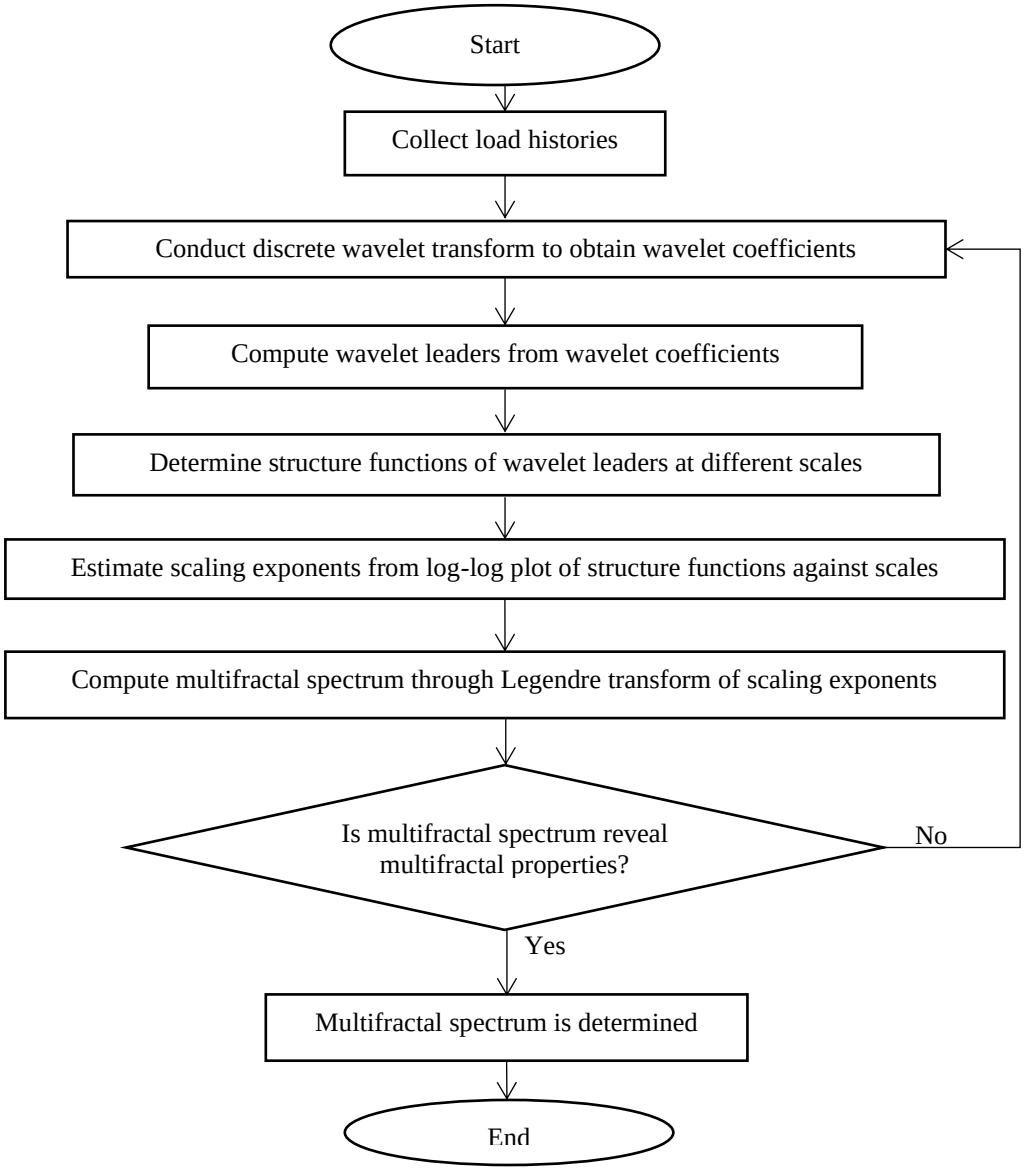

Figure 3.10 Estimation of multifractal spectrum of vibration signals using WL method

The range of the statistical moment, q, is another important parameter in WL multifractal formalism. The range of moment, q, must be selected to present the

linearisation during the scaling exponent estimation from the log-log plot of structure function against scales (Du et al. 2014). The moment, q, must cover both positive and negative ranges to obtain the multifractal spectrum $D(h)$ by the Legendre transform of scaling exponents. On the other hand, the range of q must also be selected to ensure that the resulting singularity spectrum maintains above zero ($D(h) > 0$). This was important for a fair comparison of multifractality between different vibration signals and determined the influences of loading multifractality to the durability performance of coil spring. Therefore, a range of moment, q, between -8 and 10 was used in this study.

The multifractality of the vibrational signal is determined from the width of the multifractal spectrum ($\Delta h = h_{max} - h_{min}$) as shown in Figure 3.11 (Du et al. 2014; Krzyszczak et al. 2019). Theoretically, the spectrum of a pure monofractal signal should appear as a single dot with $\Delta h = 0$ since a monofractal signal is accounted for by a single exponent. According to Makowiec & Fulinski (2010), a signal can be regarded as monofractal if its spectrum width is less than 0.05. This is because the small spectrum width below 0.05 is mainly due to uncertainties in the numerical methods. Hence, it is important for the baseline of the monofractal spectrum width to be known in order to determine if the loading signals for having multifractal characteristics. Apart from the spectrum width which represents the multifractality, the type of events in the studied process can be investigated by the HEs. The h_{min} represents the most extreme event while h_{max} shows the smoothest event in the signal. The h_0 indicates that the spectrum achieves its maximum point and provides valuable information about the structure of the studied signal. A signal with a high h_0 value is less correlated and shows a fine structure. In contrast, a low h_0 value is obtained in a highly correlated signal. A signal with many high amplitude events is highly correlated and exhibits lower h_0 value.

3.3.3 Structure of Three-Inputs One-Output ANFIS Model

Two fatigue-related features including the multifractality and signal energy had been characterised from the vibration signals collected at the road tests. The multifractality quantified the signal complexity related to the road surface condition. High road surface roughness can result in higher road multifractality (Quan et al. 2013). The signal energy is dependent on the high amplitude events in the loading signal. Through singularity

analysis followed by energy analysis, the total energy of low-frequency features in the vibration signals were quantified.

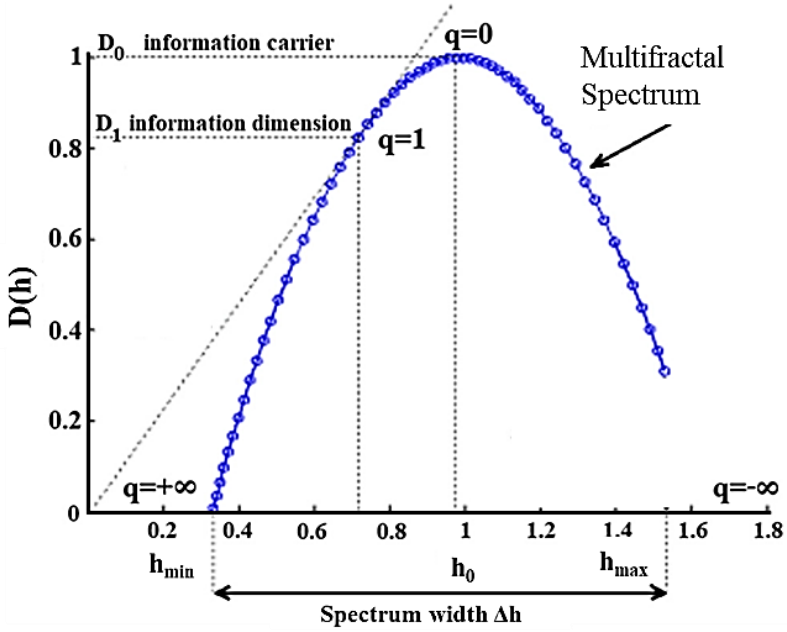

Figure 3.11 Determination of multifractality from the width of a multifractal spectrum

Source: Krzyszczak et al. 2019

Distinctive design of the coil spring also affects the durability performance of the coil spring significantly (Kong et al. 2019b). It was also necessary to add a spring design parameter as a predictive variable so that the developed durability prediction model was applicable to different spring designs. Therefore, this study also considered different coil spring designs for durability prediction. The main property of a spring that would affect the suspension performance was the spring stiffness. According to Equation 2.8, the stiffness of a helical coil spring, also known as spring constant (k_1), depends on the shear modulus of material (G) and geometry parameters, such as spring diameter (D), number of active coil (N), and coil wire diameter (d).

Different coil wire diameters were investigated to determine the influences of spring stiffness to durability performance of a coil spring. This is because the change of the coil spring wire diameter had the least impact on the original design of the suspension while achieving different spring stiffness (Kong et al. 2019d). Changing of material was not practical because most coil springs are made of spring steel and other

materials are not commercially available (Abidin et al. 2013). Based on actual measurement, the tested coil spring had a coil diameter of 12.2 mm. Hence, the tested suspension system in the road tests had a spring stiffness of 16,806 N/m and damping coefficient of 15,564 Ns/m. The theoretical natural frequency of the suspension system is around 1.25 Hz according to Equation 2.15. Therefore, different spring designs with spring stiffness between 11,000 and 22,000 N/m had been used in this study to achieve the designated natural frequency range. According to Nabagło, Jurkiewicz & Kowal (2021), the natural frequency of a suspension system should be kept between 1.0 and 1.5 Hz to optimise the ride comfort. Table 3.6 shows the spring stiffness and theoretical natural frequency of suspension system with different coil spring designs. The natural frequencies of suspension system were the theoretical values calculated from Equation 2.15. These values were depending on the fixed value of damping coefficient and changing spring stiffness values from different coil wire diameters.

Table 3.6 Spring stiffness and suspension natural frequency of various spring designs with different coil wire diameters

Coil wire diameter, d (mm)	**Spring stiffness, k_1 (N/m)**	**Suspension system natural frequency, f_d (Hz)**
11.0	11,107	1.01
11.5	13,268	1.11
12.0	15,731	1.21
12.2	16,806	1.25
12.5	18,521	1.31
13.0	21,667	1.42

To predict the coil spring's durability based on the extracted fatigue parameters of the vibration signal, the relationship between the parameters and the fatigue life of the coil spring must be investigated. Machine learning approaches, especially ANFIS and ANN, are well-known to have better performance in modelling non-linear relationship compared to regression modelling methods (Škrjanc et al. 2019). ANFIS method was employed to establish the relationship because fatigue process is often highly non-linear and random (Mohanty et al. 2011). ANFIS is a machine learning technique integrated from artificial neural networks (ANN) and fuzzy logic (Pramod & Pillai 2021). ANFIS inherits the superior computational ability of ANN and good reasoning capability of fuzzy logic (Saikia & Sarma 2015). In addition, multifractality and low-frequency energy of the vibration signals had been characterised and used as

the predictive parameters of the model. Moreover, the spring constant was also added as a predictive parameter of the ANFIS modelling to determine the effect of different coil spring design to the coil spring durability. The three-inputs and one-output ANFIS model, as shown in Figure 3.12, was developed for durability prediction of coil spring based on vibrational features. Takagi-Sugeno type ANFIS modelling had been used to develop the fatigue life predictive model because the structure of Takagi-Sugeno ANFIS is one of the most robust and widely used models in ANFIS modelling (Mohanty et al. 2011; Shihabudheen & Pillai 2018). The ANFIS structure consisted of five layers and each layer carried out specific functions, as discussed in Section 2.5.3. The five-layer ANFIS structure was found suitable for durability modelling of different structures and materials (Muc 2020; Zhang et al. 2019a).

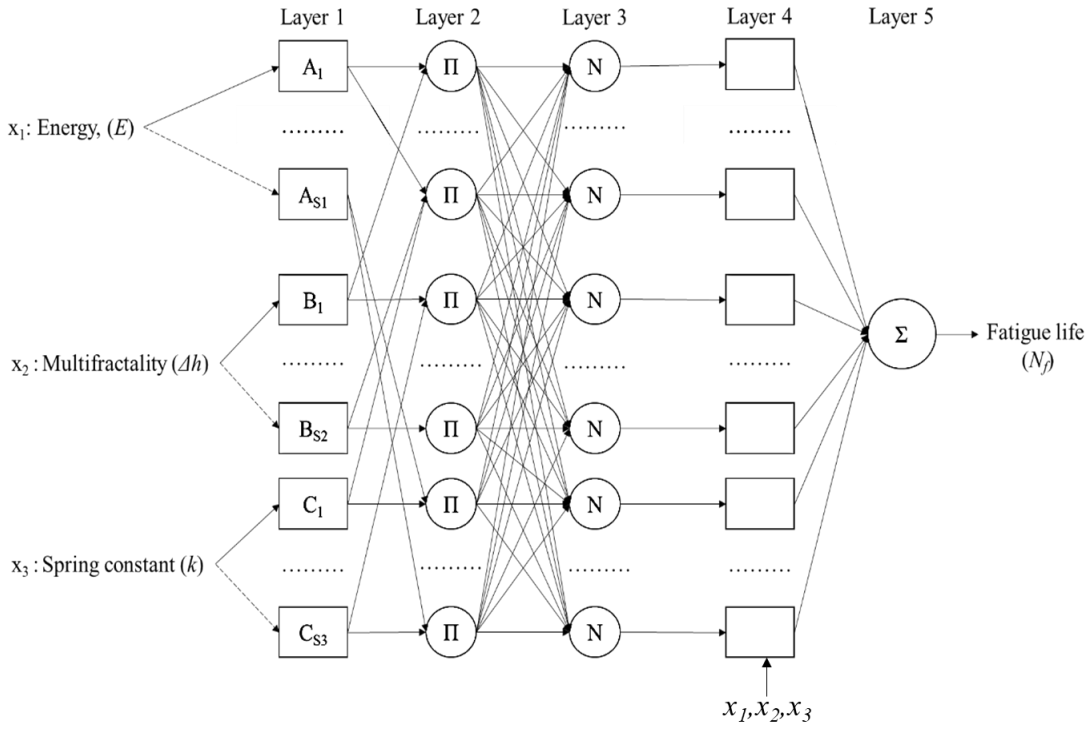

Figure 3.12 Fatigue life predictive ANFIS model with three inputs

A typical three-inputs and one-output ANFIS model can be expressed in the form of fuzzy if-then rule (Mohanty et al. 2010):

$$IF \qquad x_1=A_j \quad j=1, \ldots, S_1 \qquad \ldots(3.14)$$

$$x_2 = B_k \quad k = 1, \ldots, S_2 \qquad \ldots(3.15)$$

$$AND \qquad x_3 = C_m \quad m = 1, \ldots, S_3 \qquad \ldots(3.16)$$

$$THEN \qquad f_i = o_i x_1 + p_i x_2 + q_i x_3 + r_i \quad i = 1, \ldots, S_1 \times S_2 \times S_3 \qquad \ldots(3.17)$$

where *A*, *B*, and *C* are the fuzzy membership sets of the input variables x_1, x_2, and x_3, respectively; S_1, S_2, and S_3 are the number of membership functions (MFs); *f* is the linear consequence function; *o*, *p*, *q*, and *r* are the linear coefficients referred as the consequence parameters. In the proposed ANFIS structure, the input variables x_1, x_2, and x_3 had a total of S_1, S_2, and S_3 number of membership functions, respectively. Therefore, the input space was partitioned into $S_1 \times S_2 \times S_3$ fuzzy subspace and each subspace was governed by a series of fuzzy if-then rules. The first layer of the structure, also known as the premise layer, defines the fuzzy subspace and output was defined by the consequent layer, i.e., layer 4.

3.3.4 Training Process towards the Development of Fatigue Life Prediction Model

In order to obtain adequate training data for ANFIS modelling, road tests in different road conditions, including rural area, university campus, industrial area, and highway roads, were repeated to acquire more vibration and strain signals. Appendices B and C show the vibration and strain signals obtained from the repeated road tests, respectively. Next, strain histories resulting from different spring designs were simulated using the established quarter-car suspension MBD model and the displacement-strain conversion model, as given in Equation 3.7. Different spring stiffness values that represented various spring designs, as given in Table 3.6, had been used in the MBD simulation to estimate the spring responses of different spring designs. The fatigue lives of simulated strain histories were then determined using strain-life and ESD models. It shall be noted that the fatigue lives had been converted into base-10 logarithm scale to avoid significant differences between data points and obtain a better fitting using ANFIS modelling (Zhang et al. 2019a). A dataset consisting of 220 data that included the three inputs, such as the signal energy, multifractality and spring constants, and the fatigue life as the output, were prepared for ANFIS modelling as shown in Appendix D. To

optimise the durability model using machine learning methods, a sample size above 100 samples was recommended so that the samples are statistically represent the real loading condition (Kong et al. 2019b; Zhang et al. 2019a).

The purpose of ANFIS modelling was to determine the relationship between the three input parameters, including the vibration loading features and spring design, with the fatigue life of coil spring. The ANFIS training process was aided by MATLAB® neuro-fuzzy designer toolbox. Before the training, subtractive clustering method (SCM) was used to determine the membership functions (MFs) of input data. Zhang et al. (2019a) demonstrated that SCM is an effective method to determine the optimal MFs for complex fatigue data. An MF is a curve that maps a data point to its corresponding membership function value or degree of membership function between 0 and 1. The MFs played a significant role in the fuzzy set theory in quantifying the uncertainties of the input parameters. A Gaussian parameterised MF was selected because it has the characteristics of smoothness compared to triangular and trapezoidal (Mohanty et al. 2010), as it is the most widely used MF in ANFIS as reported by Shihabudheen & Pillai (2018). Furthermore, Das et al. (2016) demonstrated that Gaussian MF yielded better results with relative error below 0.0012 compared to other MFs in ANFIS modelling of fatigue crack. The Gaussian MF is defined as (Mohanty et al. 2010):

$$\mu_{A_i}(x) = exp\left(\frac{-(x-\mu)^2}{2\sigma_{SD}{}^2}\right) \qquad \ldots(3.18)$$

where μ is the mean and σ_{SD} is the standard deviation of the membership function.

Upon completing the training or learning process, a training dataset that includes the multifractality, signal energy, spring constant, and fatigue life was prepared. A number of 10% of the total data points was excluded from the training dataset and used as the testing data (Vassilopoulos & Bedi 2008; Zhang et al. 2019a). In ANFIS modelling, testing data is a dataset that is not involved in the training process for validation purpose to prevent overfitting of the model (Mohanty et al. 2011). Overfitting is a common phenomenon in machine learning process in which a trained model is too influenced by the patterns in training data and eventually results in extremely high errors

when the model is fitted to a fresh dataset (de Campos Souza 2020). Overfitting happens when the model becomes better fitting not only to the data trend, but also the noises due to increased complexity of model (Zhang et al. 2019a). There is a necessity to optimise the number of MFs or fuzzy rules in the ANFIS model to obtain the most optimum structure for fatigue life prediction. This is because an increased number of MFs results in more fuzzy rules that complicate the structure networks. This can lead to increased computational efforts and overfitting of the model (Škrjanc et al. 2019). The optimisation of the fuzzy rule number was performed by adjusting the predefined ROI during SCM to obtain different fuzzy rule number between 2 and 7. The training process was repeated with various fuzzy rule numbers.

During the learning process, a hybrid learning algorithm that combined the gradient decent method and least square estimation methods was employed (Zhang et al. 2019a). The conventional gradient method had the risk of being trapped in a local minimal. The hybrid learning algorithm was an improved version of the back-propagation algorithm which adapted the premise and consequent parameters for optimisation of the network (Mohanty et al. 2010). In forward pass, the error in the consequent parameters was calculated in Layer 4 using the least square estimation. The error rates were backpropagated to the premise layer (Layer 1) and the premise parameters were then adjusted accordingly. The training process was terminated when either the conditions was achieved: 1) the mean-square error (MSE) between the training data points and the predicted values reached a pre-specified threshold, 2) after a predefined number of iterations of training known as epochs is completed (Gandhi, Adarsh & Ramachandran 2017; Vassilopoulos & Bedi 2008). The number of epochs was set at 50 because the dataset size was not big. The MSE of training data and testing data is expressed as:

$$MSE = \frac{1}{n}\sum_{i=1}^{n}(f_i\text{-}y_i)^2 \qquad \ldots(3.19)$$

where n is the total sample number, f_i is the predicted value, and y_i is the observed value. The optimal fuzzy rule number was selected based on the testing error before the error started to rise which was an indication of overfitting (Zhang et al. 2019a). Figure 3.13

shows the optimisation process of fuzzy rule number of the ANFIS model. The radius of influence (ROI) in the SCM process was adjusted to obtain different clusters of data with each cluster represented by a fuzzy rule. A range of fuzzy rule number between 2 and 7 was tested since serious overfitting was observed in ANFIS model with fuzzy rule number higher than 7. Subsequently, a linear defuzzification method was used to obtain the final output value as expressed in Equation 3.17 (Zhang et al. 2019a). The MSE was then computed from each predicted value of fatigue life. The optimum fuzzy rule number was selected from the model with the lowest testing error.

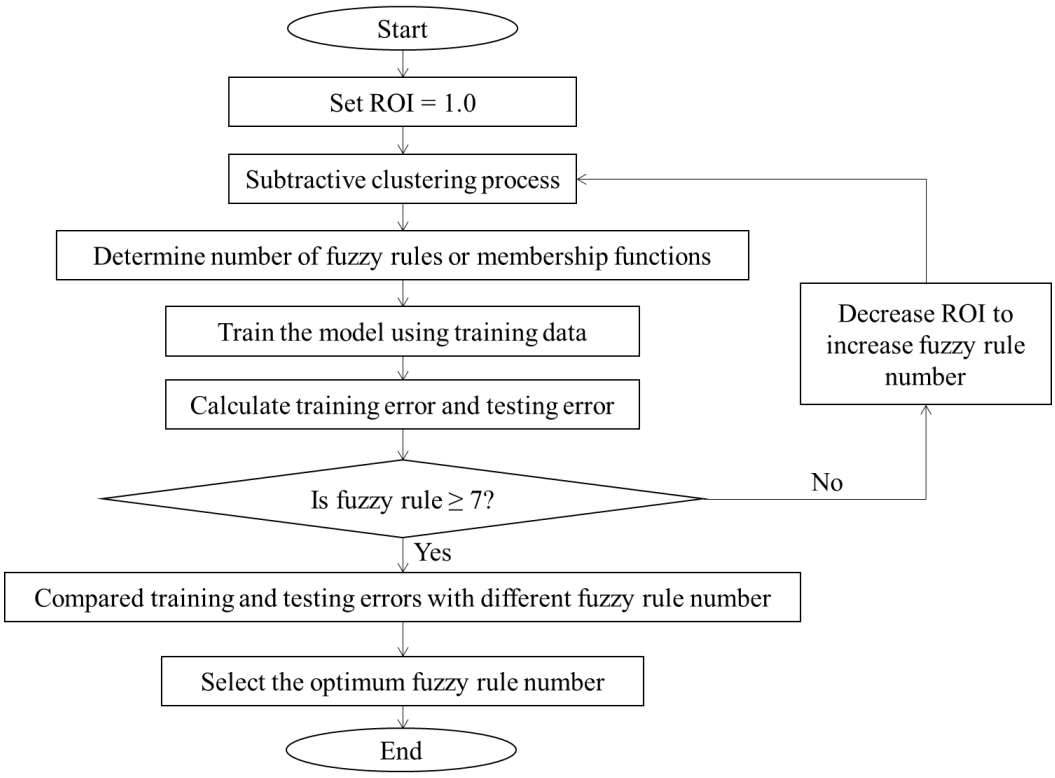

Figure 3.13 Optimisation of fuzzy rule number of ANFIS model

After the vibration-based predictive models were developed through ANFIS modelling, the models were validated by comparing the predicted fatigue lives with the fatigue lives estimated from the measured strain data. This was performed through fatigue life conservative analysis to determine the conservative of predicted fatigue lives by the ANFIS models within the boundary of 1:2 and 2:1 (Zhang et al. 2019b). The accuracy in fatigue life prediction of the models was estimated by computing the Pearson correlation coefficients (r) between the fatigue life predicted by ANFIS model and measured strain data, such that (Feng et al. 2016):

$$r = \frac{L_{XY}}{\sqrt{L_{XX}L_{YY}}} \quad \ldots(3.20)$$

with $L_{XX} = \sum_{i=1}^{n}(X_i - \bar{X})^2$, $L_{YY} = \sum_{i=1}^{n}(Y_i - \bar{Y})^2$ and $L_{XY} = \sum_{i=1}^{n}(X_i - \bar{X})(Y_i - \bar{Y})$. $\bar{X}$ and $\bar{Y}$ denote the mean values of the ANFIS predicted and measured strain fatigue lives, respectively. The r value close to one indicates a higher linearity between the fatigue life predicted by the ANFIS models and strain data.

In order to account for the uncertainties in the predicted fatigue life, a fatigue data survival analysis within a 95% confidence interval was also conducted. The confidence interval was an estimated range from the statistics of the observed data such that the estimated interval contained the true value of the parameter at a given confidence level. This analysis helped to determine the accuracy of the ANFIS models in predicting the fatigue life of coil spring from a statistical aspect. The survival rate of the fatigue life correlation between ANFIS and strain measurement predicted fatigue lives within 95% confidence interval was computed.

3.4 VALIDATION OF MACHINE LEARNING FATIGUE LIFE PREDICTION MODELS

The validation of established machine-learning-based models was conducted using probabilistic-reliability methods. This includes the determination of appropriate probability distribution for fatigue data, reliability analysis, and determination of the modified MTTF to compare the difference between experimental and simulated fatigue data.

3.4.1 Determine the Probability Distribution Function

In order to validate the predicted fatigue lives from the ANFIS modelling, probabilistic approach was used in the current study to validate the accuracy of the ANFIS model. The fatigue lives predicted by ANFIS models and strain measurement were fitted into standard distributions including the Gaussian, Weibull, and Lognormal distributions to determine the probability of fatigue failure under random loading. The Weibull and

Lognormal distributions had been expressed in Equations 2.83 and 2.84, respectively. Researchers remarked that both distributions were appropriate to represent fatigue behaviour in steel components (Altamura & Straub 2014). The Gaussian or normal distribution was used as a reference to observe if the fatigue data showed normality. The normal distribution is given as:

$$f_{Normal}(x) = \frac{1}{\sqrt{2\pi\sigma_{SD}{}^2}} e^{-\frac{(x-\mu)^2}{2\sigma_{SD}{}^2}} \quad \ldots(3.21)$$

where μ and σ_{SD} denote the mean and standard deviation of the data, respectively. Maximum likelihood method, as expressed in Equation 2.85, was utilised to determine the optimum distribution parameters by fitting the fatigue life data into the distributions. The appropriate probability model that fit the fatigue life data was then selected by computing the AIC indices of each fitted distribution from the Equation 2.86. Accordingly, the Normal, Weibull, and Lognormal distributions were compared to determine the most appropriate distribution. The appropriate probability distribution was selected from the lowest AIC index value (Portet 2020).

3.4.2 Reliability and Hazard Analysis

When the appropriate distribution for fatigue data was determined, the fatigue reliability properties of the fatigue data were investigated. The cumulative distribution functions (CDFs), reliability functions and hazard rate functions, as expressed in Equations 2.87, 2.88, and 2.89, respectively, were computed. However, the failure time in this study was measured in cycles rather than time since the fatigue failure is a cycle-dependent phenomenon. Therefore, Equations 2.87, 2.88, and 2.89 can be rewritten as Equations 3.22, 3.23, 3.24, respectively:

$$F(N_f) = \int_{-\infty}^{x} f(N_f) dN_f \quad \ldots(3.22)$$

$$R(N_f) = 1\text{-}F(N_f) \quad \ldots(3.33)$$

$$h(N_f) = \frac{f(N_f)}{R(N_f)} \quad \ldots(3.24)$$

The CDF reveals the cumulative failure probability of the coil spring under random road excitations at a given specific service cycles. The reliability is the inverse of CDF to show the remaining life the component can sustain. Hazard rate function determines the rate of failure of the coil spring or the likelihood of survival at a given life cycle based on the probability of survival to an earlier time (Almalki & Nadarajah 2014).

3.4.3 Derivation of Statistical-Based Cycle to Failure

One of the important parameters that indicates the reliability of a component in reliability engineering is the mean-time-to-failure (MTTF), as represented in Equation 2.90. MTTF is applicable to non-repairable components, and it gives an approximation of reasonable service time of the components before large scale failures are expected to occur (Mekonnen, Aburbu & Sarwat 2018). Research concerning the fatigue reliability of the structures under cyclic loading measured the fatigue failure data in time scale (Qiu et al. 2021; Smith et al. 2022). However, the fatigue process of coil spring is a time-independent process in which the fatigue life is measured in cycles to failure. Therefore, it is more appropriate to determine the MTTF in the scale of cycles rather than time scale (Nasir et al. 2020). Therefore, this study proposed the Mean-Cycle-to-Failure (McTF) as a representation of the fatigue reliability properties, such that:

$$McTF = \int_0^\infty x.f(N_f)dN_f \quad \ldots(3.25)$$

McTF can also represent the expected life cycles of the coil spring until the fatigue failure occurs. This provides essential information to determine the optimal service life of coil spring under random loading conditions. To validate the accuracy of predicted fatigue lives by the ANFIS models by considering the uncertainties in random loading, McTFs were obtained from fatigue life data predicted by trained ANFIS

models and strain measurement. The McTFs between the simulated and experimental fatigue life datasets were then compared. The percentage of difference between the McTFs was calculated by:

$$Percentage\ of\ difference = \left|\frac{McTF_{predicted} - McTF_{strain}}{McTF_{strain}}\right| \times 100\% \quad \ldots(3.26)$$

where the subscripts "predicted" and "strain" indicate that the McTF was computed from fatigue life data predicted by the ANFIS model and strain measurement, respectively. The ANFIS model can be statistically validated to give an accurate durability prediction if the difference in McTF is less than 10%, as it is a generally accepted tolerance of differences in fatigue data (Putra, Abdullah & Schramm 2020).

3.5 SUMMARY

Chapter III discusses the details of methodology to achieve the three objectives of this study. This study aims to characterise the fatigue-related features from the vibration signals of coil spring and develop vibration fatigue prediction models. Using the ANFIS modelling technique, the parameter of the ANFIS models has been optimised to achieve an accurate prediction of fatigue life. Fatigue reliability approaches using statistical and probabilistic theory are employed to validate the fatigue data predicted by the developed models with the fatigue data of strain measurement.

In the next chapter, the research findings of the methodology that reflect the objectives in this study are presented. The results will be presented in the sequence of the objectives including the strain generation of coil spring using developed displacement-strain conversion model, establishment of ANFIS-based fatigue life predictive model, and validation of the established models using reliability analysis. The discussion of the results will be focusing on providing justifications and achievement of the novelty of this study.

CHAPTER IV

RESULTS AND DISCUSSION

4.1 INTRODUCTION

This chapter presents the research findings to achieve the three research objectives. The first objective was to determine the displacement-strain relationship of suspension coil spring by considering the spring curvature and torsional stress effects using MBD approaches. The main purpose of the displacement-strain relationship was to generate more realistic and accurate strain signals of a coil spring subjected to variable amplitude loading for durability analysis. To achieve this objective, an MBD model of a quarter-car suspension system was developed to simulate the spring responses under random road excitation. A new displacement-strain relationship for coil springs was introduced by modifying previous acceleration-strain conversion models proposed by Putra et al. (2017a) and Kong et al. (2019a). The proposed acceleration-strain conversion model was expected to generate more accurate strain signals. It led to the contribution of accelerating the durability analysis without depending on time-consuming experimental measurement of strain signals. This model also provided an alternative approach for durability prediction of coil spring using vibration signals as input.

The second objective was to establish durability predictive models using adaptive neuro-fuzzy inference systems based on vibration characteristics and design parameters of coil spring. It involved the characterisation of the vibration signals of coil springs with energy analysis and multifractal analysis. The energy and multifractality of loading signals were proven to have significant impacts on the durability properties of coil spring. The nonlinear relationship between the signal energy, multifractality with various spring designs (spring constant) with the fatigue life of coil spring were modelled with ANFIS modelling technique. The optimisation of the ANFIS network

structure was performed to determine the optimal fuzzy rule number to achieve accurate predictions of the fatigue life. The accuracy of the fatigue life prediction was determined by fatigue life conservative analysis and fatigue life correlation analysis. The main contribution of the study was to establish a vibration-based durability prediction model for an accelerated and accurate durability analysis of coil springs. It significantly reduced the necessity of strain measurements in normal time-consuming practices of coil spring fatigue analysis.

The third objective was to validate the established ANFIS models using probabilistic approaches. The fatigue life data estimated using ANFIS models were compared to the fatigue life data predicted from strain data measurement with fatigue reliability approach. Mean-Cycle-to-Failure (McTF), which was translated from conventional MTTF, was estimated from each dataset and compared. Similar McTF between two sets of fatigue data proved that the fatigue life data predicted by the established ANFIS models had similar probabilistic properties with the experimental data. Therefore, the ANFIS models can be suggested to have accurate predictions of fatigue life. The findings stand as a strong evident based on the statistics analysis that supported the validity of the established vibration-based durability prediction model.

4.2 ACCELERATION-STRAIN CONVERSION MODEL FOR GENERATING STRAIN LOAD

This section discussed the findings of finite element analysis of the coil spring, loading signals characteristics that affect the durability performances, and the strain generation for durability analysis through MBD method. The findings in this section completed the first objective of the current research.

4.2.1 Finite Element Analysis of Coil Spring

Static analysis was conducted on the coil spring using finite element approach to determine the stress distribution of coil spring under a static load of 3,384 N. A cyclic load analysis was also conducted to determine the spot with the highest fatigue damage in the coil spring. Prior to the finite element analysis, a mesh sensitivity analysis was conducted to determine the optimised element mesh size with mesh convergence

method. Table 4.1 shows the maximum stress level and the duration of analysis and maximum displacement of spring at various mesh sizes. The maximum stress level represents the von Mises stress at the hotspot where stress concentration was the largest. The total number of elements in the geometry model at different mesh size was also shown to represent the complexity of the analysis. The duration of analysis indicated the computational load required for the analysis. Figure 4.1 shows the convergence of maximum von Mises stress in the coil spring and the duration of analysis with different mesh sizes. It was found that the maximum von Mises stress decreased with increasing mesh size and this was in agreement with the findings by Nasir et al. (2020). The maximum stress started to converge at 1,132 MPa with mesh size of 2 mm as the mesh size decreased. Meanwhile, the duration of analysis was also recorded to evaluate the computational load. The computational duration is always proportional to the number of elements, as smaller mesh size could provide better accuracy but it could drastically increase the computation time (Rahul & Rameshkumar 2020). It was shown that the computation time increased to 420 s and 1,500 s at mesh sizes of 1.5 mm and 1.0 mm, respectively. This was due to the significant increase of number of elements at smaller mesh size. Considering the stress convergence and computational duration, a mesh size of 2 mm was appropriate for the finite element analysis of coil spring.

Figure 4.2 illustrates the stress distribution of the coil spring under static loading, dynamic loading and the spot of the highest fatigue damage under variable amplitude cyclic loading. A hotspot with the highest stress level of 1,132 MPa was observed in the coil spring under a static load. The hotspots were located at the inner surface of the second coils at the bottom of the element 15,517. This finding corresponded to the previous works (Kong et al. 2019d; Putra et al. 2017a) where the hotspots were also found at the inner coil surfaces. The higher stress level in the inner surface of the coil spring was mainly due to the combined effect of torsional and transverse shear stress in the coil spring under deflection (Arshad, Nazir & Jeng 2022). In many compressive helical coil springs, the transverse shear stress had very limited contribution to the overall stress and was negligible in many applications. The spring curvature effect also significantly contributed to the stress concentration in the inner surface since the inner surface had the smallest spring curvature that resulted in larger stress concentration effect (Bergh et al. 2021). Under a dynamic load, the hotspot was

found at the same location with the static load analysis associated a slightly increase of the maximum stress to 1,135 MPa. This strongly indicates that the dynamic load effect was minimal in the coil spring. The location of the highest fatigue damage found in coil springs under cyclic loading condition corresponded to the location of the highest stress level in static load analysis. This indicated that the hotspot with the highest stress level had contributed to the highest fatigue damage in the coil spring (Kong et al. 2019c).

Table 4.1 Maximum stress, displacement and duration of analysis of static load analysis of coil spring geometry

Mesh size (mm)	Number of elements	Maximum von Mises stress (MPa)	Duration of analysis (s)	Maximum displacement (mm)
1.0	534890	1145	1500	198.9
1.5	160910	1134	420	197.7
2.0	41954	1132	56	196.4
2.5	33570	1060	37	193.1
3.0	27970	929	7	191.8

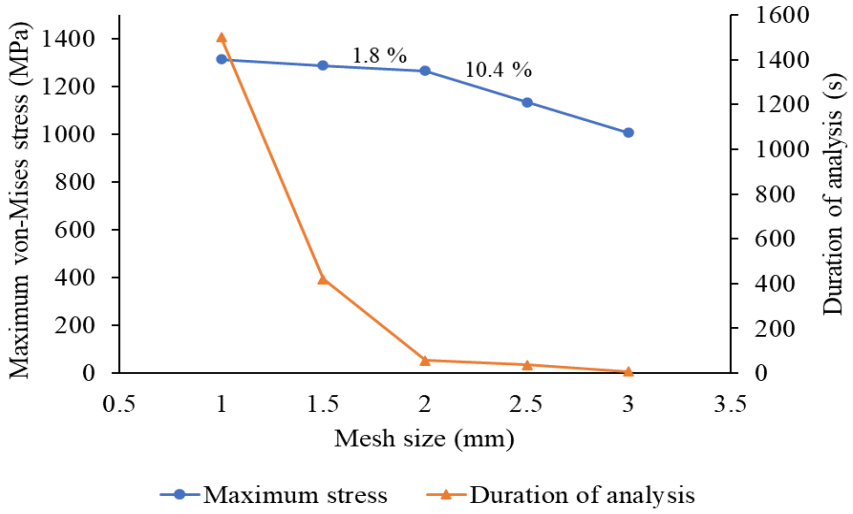

Figure 4.1 Mesh convergence assessment for finite element analysis of coil spring geometry

In a specific scenario, the deflection in coil spring became large and the local strain at the hotspot was dominantly plastic due to the curvature effect (Kato & Suzuki 2021). For this reason, strain-life approaches that consider both elastic and plastic strain were appropriate for the durability prediction of coil spring and thus strain measurements were necessary (Kahoul et al. 2019). Strain varied at different locations of the component. The location of the hotspot was essential to determine the location of

the strain gauge during the strain signal acquisition because the highest stress concentration spot had the highest probability of fatigue failure. Therefore, the strain signals must be acquired at the hotspot.

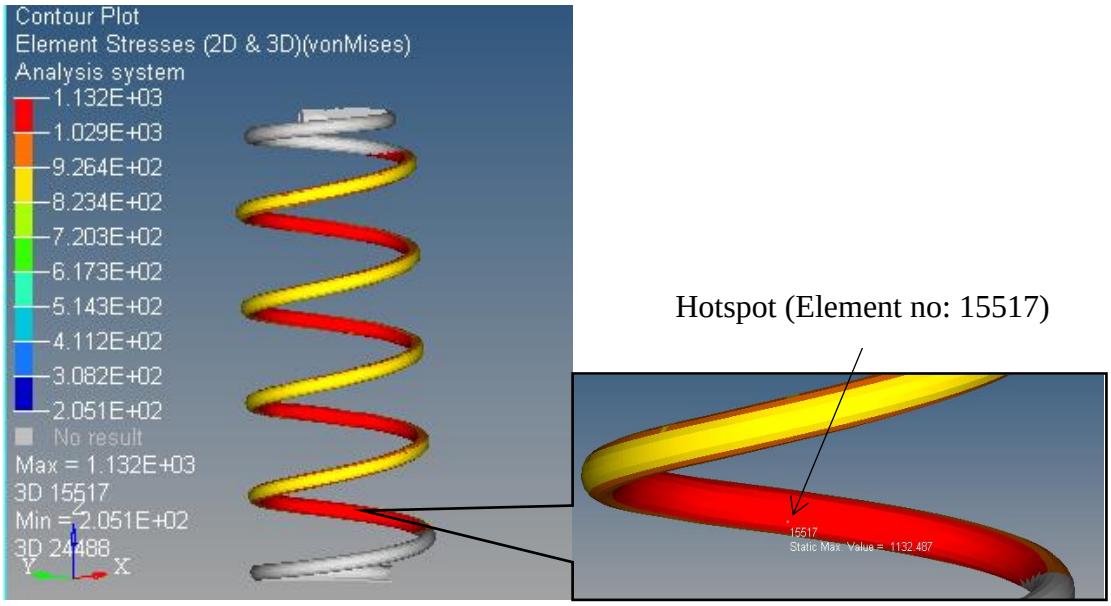

(a)

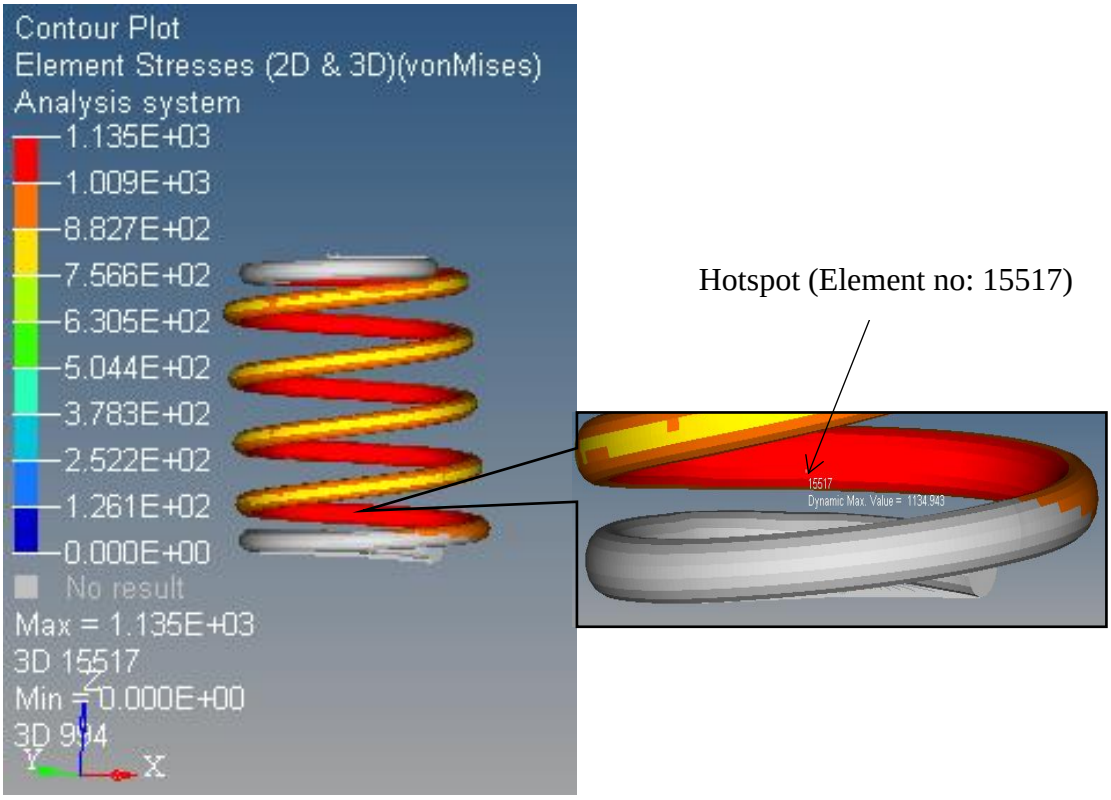

(b)

Continue…

…continued

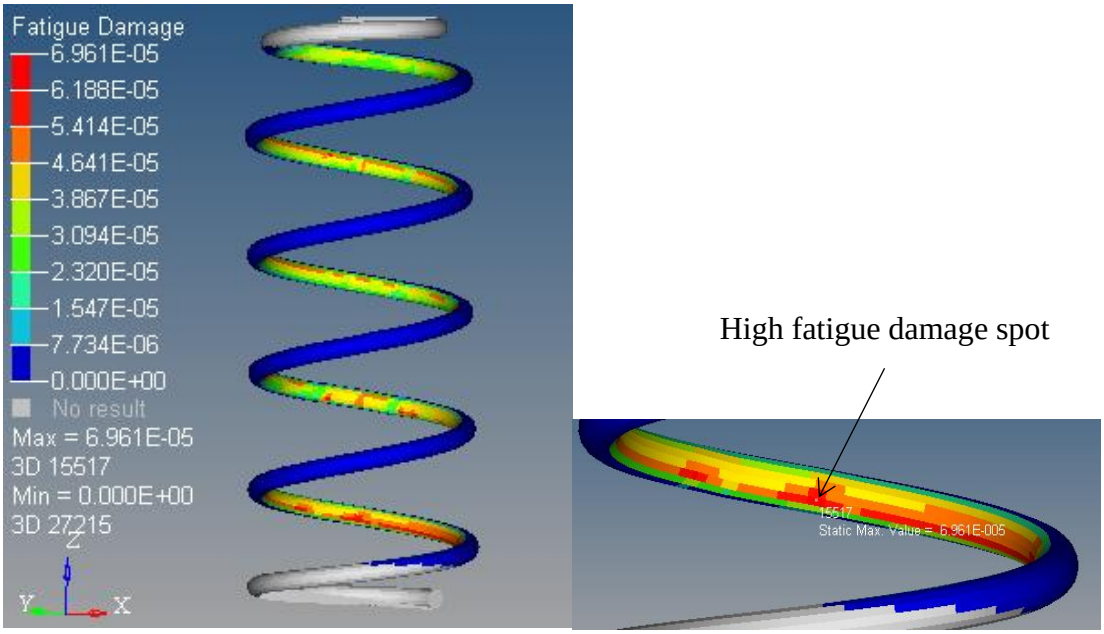

(c)

Figure 4.2 Finite element analysis of coil spring: (a) stress distribution under static load, (b) stress distribution under dynamic load (c) fatigue damage contour under cyclic load

4.2.2 Characterisation of Vibration Signals

As the tested car was driven across various road terrains, strain loading histories of the coil spring and vibration signals due to road excitations were acquired simultaneously with the corresponding sensors. The vibration loading signals were recorded in the form of the unsprung mass acceleration signals since the vertical movement of unsprung mass, particularly the wheel, which represented the direct excitation from the road surfaces to the suspension system (Suzuki et al. 2021). Figures 4.3–4.6 show the acquired vibration signals from various road conditions and signals selection for further analysis. The window selection of the signals was based on the occurrence of high amplitude events that represented the road conditions. The rural signals contained large amplitude spikes resulting from the uneven road surface. In contrast, the highway signals had smoother profile with lower amplitude spikes. For the campus and industrial signals, high amplitude spikes occurred occasionally due to some speed bumps on the roads.

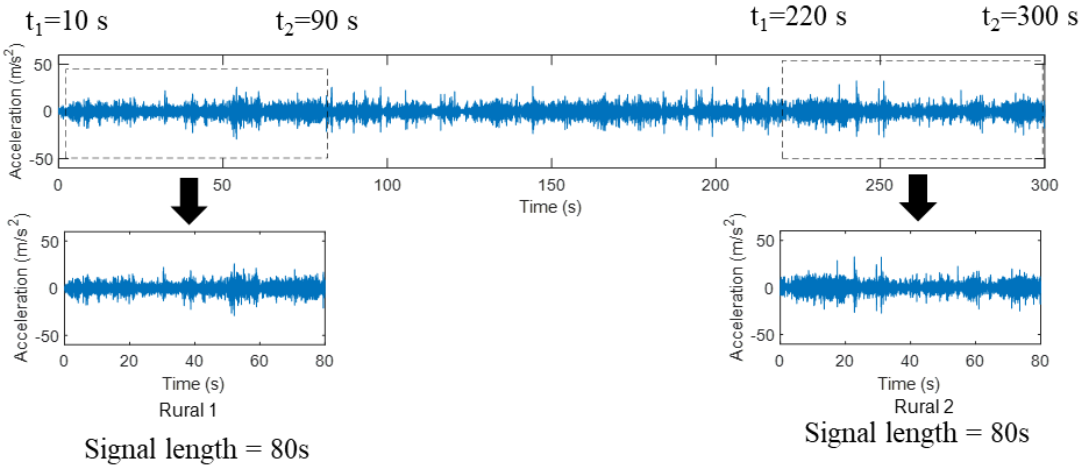

Figure 4.3 Vibration signals acquisition in rural area and extraction of signals from raw data

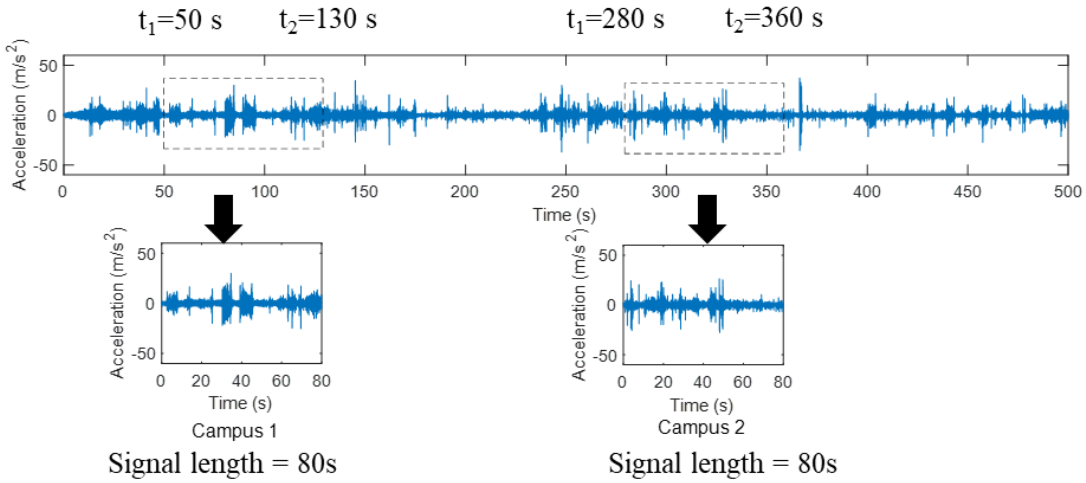

Figure 4.4 Vibration signals acquisition in university campus and extraction of signals from raw data

The statistical properties of the vibration signals including the root-mean square (RMS), skewness, and kurtosis were computed as given in Table 4.2. The vibration signals had zero-mean properties due to the characteristics of the accelerometer used in data acquisition. The RMS of a signal is an amplitude-related statistical parameter that quantifies the dispersion of data. In durability analysis, the RMS was also applied to represent the energy content in a signal (Shangguan et al. 2020). The vibration signals of the rural area exhibited the highest RMS value in range of 3.77–4.12 m/s^2, indicating the highest energy content due to the high surface roughness. The skewness of the data was related to the symmetry of the data distribution. It was found that the vibration data

of various road conditions showed skewness within a range of -0.43 to 0.11, which was close to zero. This showed that the vibration data had symmetrical data distributions. Meanwhile, the kurtosis was an important measurement of the peak sharpness and the width of the probability distribution of a signal (Palmieri et al. 2017). The kurtosis also characterised the stationarity of the signals in which a signal with kurtosis value larger than three can be regarded as a non-stationary signal (Kihm, Ferguson & Antoni 2015). The signals had kurtosis values in the range of 5.32–30.83. Therefore, the signals were found to be non-Gaussian and non-stationary as all kurtosis values were larger than three. A non-stationary signal can also be characterised with its constantly varying statistical properties, such as the mean and variance in time (Benasciutti & Tovo 2018). Previous studies by Cianetti et al. (2018) and Palmieri et al. (2017) related higher kurtosis values of a loading signal to high fatigue damage caused by the signal. This can be attributed to the high amplitude events in the signals, which eventually resulted in high kurtosis value (Kihm, Ferguson & Antoni 2015).

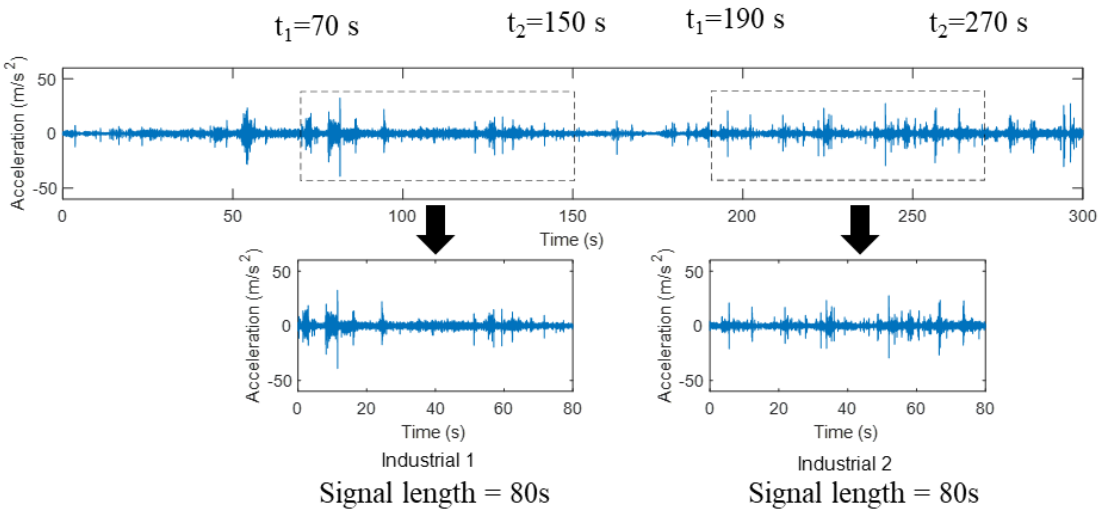

Figure 4.5 Vibration signals acquisition in industrial area and extraction of signals from raw data

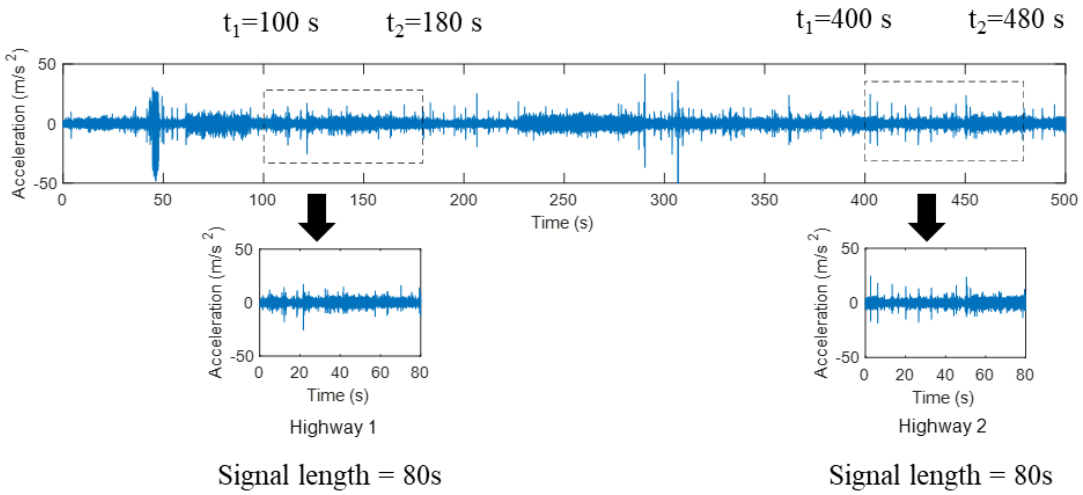

Figure 4.6 Vibration signals acquisition in highway and extraction of signals from raw data

Table 4.2 Statistical parameters of vibration signals obtained from different road conditions

Road condition	RMS (m/s^2)	Skewness	Kurtosis
Rural 1	3.77	-0.02	5.76
Rural 2	4.12	-0.01	5.32
Campus 1	2.70	-0.07	13.88
Campus 2	2.62	-0.17	20.03
Industrial 1	2.24	-0.43	30.83
Industrial 2	2.28	0.05	21.32
Highway 1	2.15	-0.20	8.09
Highway 2	2.22	0.11	8.63

Figures 4.3–4.6 indicate many spike-like features in the vibration signals associated with sudden amplitude fluctuations, such as sudden spikes, observed when the wheel encountered some road surface irregularities, i.e., bumps and potholes. These transient features rendered the vibration signals to behave non-stationary (Mao et al. 2015). The transient events in loading signals were pointed out as the high amplitude cycles which had significant contribution to high fatigue damage. The intensity of vibration load from road excitations was the highest in the rural area as large amplitude spikes were observed in the Rural 1 and Rural 2 signals. This was mainly due to the untarred road surface with many irregularities, such as the potholes. Statistically, the vibration signals acquired in the rural area recorded the highest RMS among other signals as shown in Table 4.2. In contrast, the highway vibration signals showed less high-amplitude cycles since the highway road had a smoother road profile. The lowest

RMS values recorded in the highway vibration signals confirmed the low-amplitude properties of the road. The industrial road signals have low RMS values with kurtosis values between 20.03 and 30.83. This is because the high amplitude events in Industrial 1 and 2 were due to the bumps on the road surface and led to high kurtosis. The loading signals in university campus also showed medium RMS and high kurtosis on the same reason as the industrial road signals.

The vibration was also characterised in time-frequency domain using CWT analysis. The CWT energy of the signals were computed to detect high-energy sections in the signals. Figures 4.7–4.10 show the CWT mapping of the vibration signals in time-frequency domain and the CWT energy mapping of the corresponding signals. It can be observed that the CWT can effectively reveal the time-frequency properties of vibration signals especially the high amplitude events in the signals. High amplitude events are spike-like features in the loading signals with large and sudden amplitude changes. These events are mainly due to the road surface irregularities, such as speed bumps and potholes (Kong et al. 2017). The high amplitude events appeared as high magnitude CWT coefficients, representing the energy level in the loading signals as shown in Figures 4.7–4.10. It was found that high amplitude events could be characterised as the high energy sections through CWT energy mapping. Compared to other signals, the rural road signals exhibited high energy level throughout the entire signal because high amplitude events took place very frequently. The high CWT energy sections were associated with high amplitude events in the vibration signals, as pointed out in Figures 4.7–4.10. For example, high amplitude events between 50 s and 60 s in Rural 1 signal contributed to significantly high magnitude of wavelet coefficients and thus high CWT energy. For Campus 1, a series of speed bump events within 30–48 s apparently resulted in high energy sections. The highest CWT energy of 6.2×10^4 $(m/s^2)^2$ was recorded in the vibration signal of Industrial 1, resulting from a large amplitude event with an amplitude range of around 80 m/s^2. Due to the smooth surface profile of the highway road, CWT analysis revealed the lowest energy in the highway signals compared to other signals. Hence, it can be concluded that CWT was effective to identify high amplitude cycles in the loading histories.

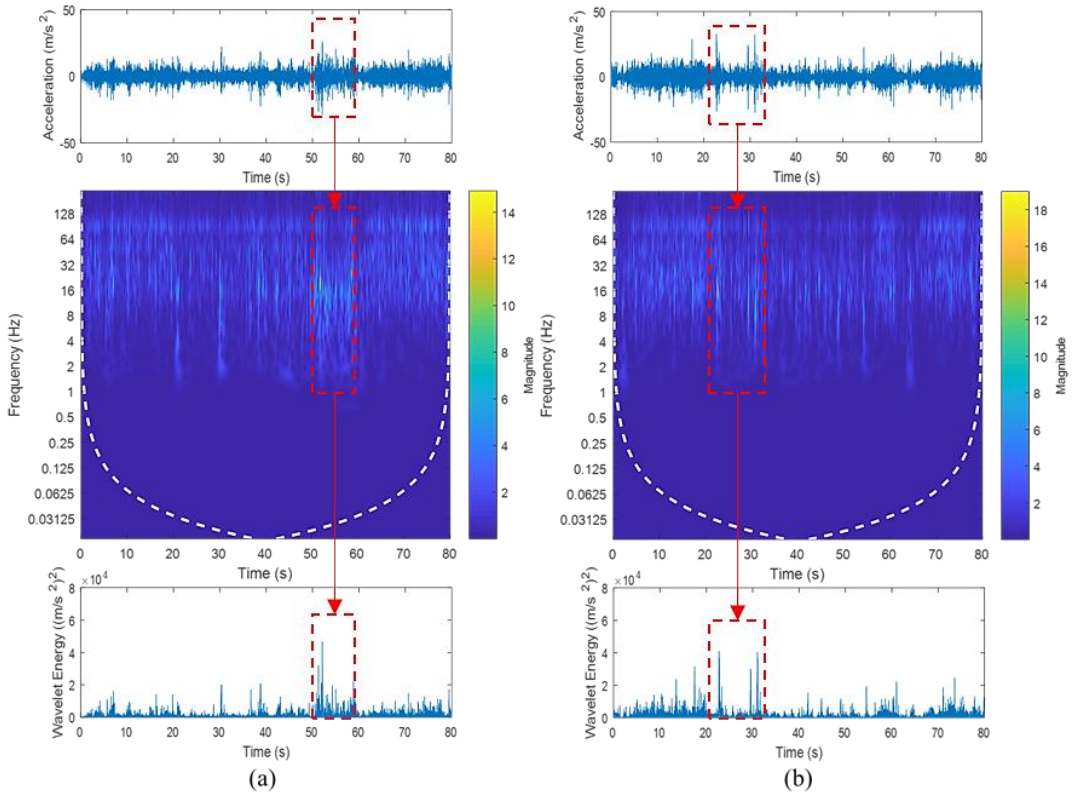

Figure 4.7 CWT analysis and CWT energy mapping of vibration signals obtained in rural area: (a) Rural 1, (b) Rural 2

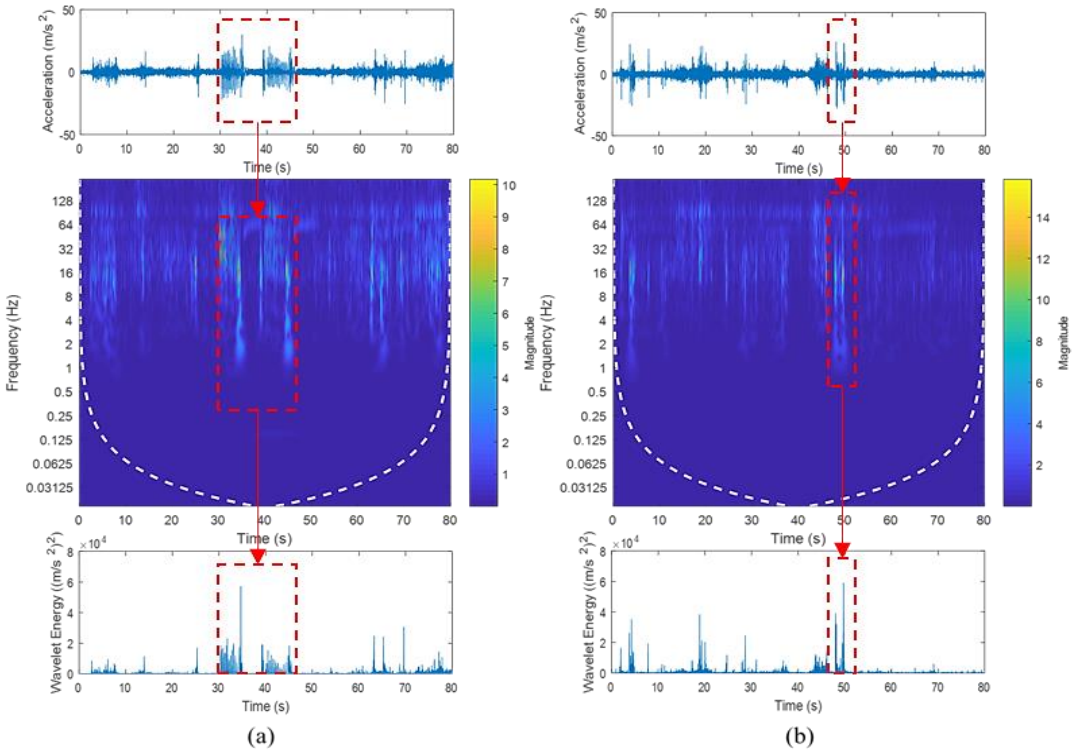

Figure 4.8 CWT analysis and CWT energy mapping of vibration signals obtained in university campus: (a) Campus 1, (b) Campus 2

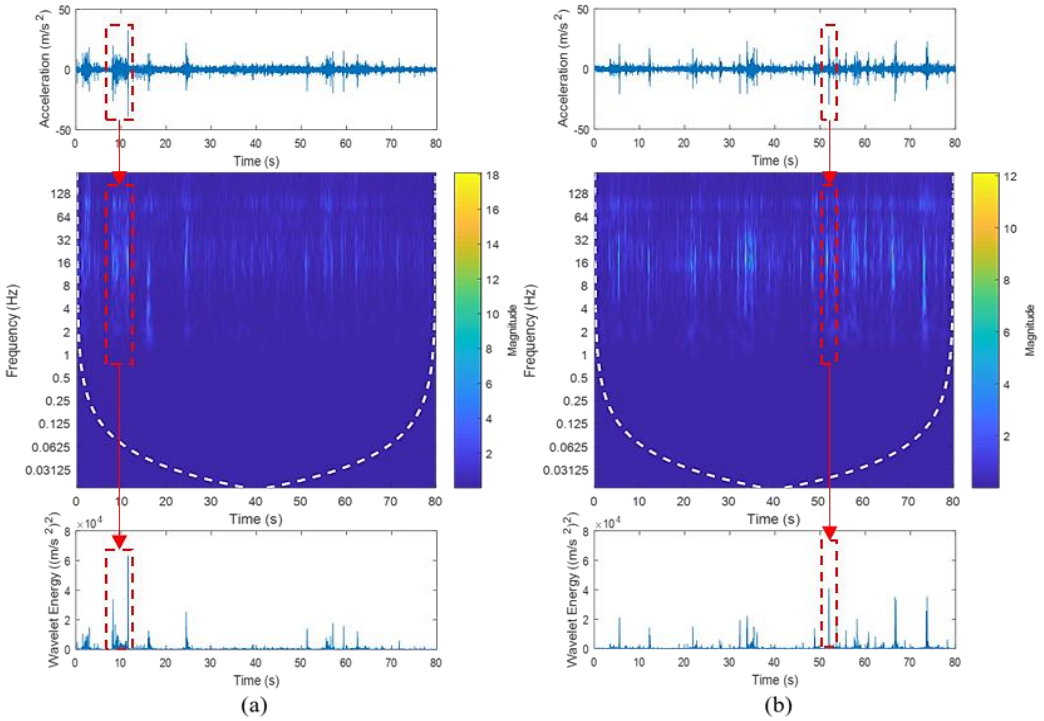

Figure 4.9 CWT analysis and CWT energy mapping of vibration signals obtained in industrial area: (a) Industrial 1, (b) Industrial 2

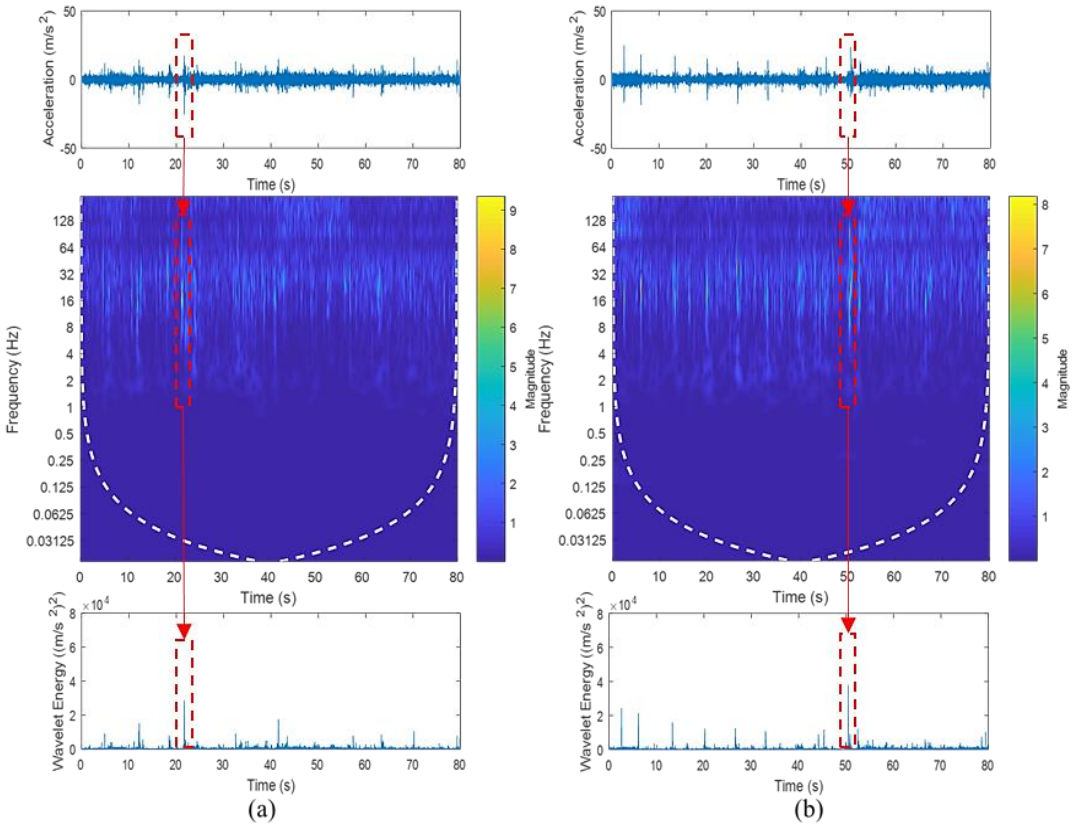

Figure 4.10 CWT analysis and CWT energy mapping of vibration signals obtained in highway: (a) Highway 1, (b) Highway 2

Studies by Pratumnopharat, Leung & Court (2014) and Putra et al. (2017b) had utilised CWT analysis to relate the high energy sections in loading signals with high fatigue damage. In further analysis, CWT was used to determine the singularities in the vibration signals, which are important to characterise the energy that mainly contributed to fatigue damage. Furthermore, the frequencies during the occurrences of high amplitude event can also be observed via CWT analysis. Most high amplitude events were found within the frequency range of 2–16 Hz. This indicates that the vibration excitations due to road surfaces are classified as low frequency range. This finding was in agreement with Minaker & Yao (2017) which remarked that the car body vibration due to wheel motion occurred in the frequency range of 0.5–12 Hz.

4.2.3 Characterisation of Strain Loading Histories

Strain histories were the response of the coil spring under vibrational excitation from the road surfaces. The strain histories represented the load condition and were necessary elements for durability assessment of the coil spring. The strain histories under various road conditions were acquired simultaneously with the vibration signals and shown in Figures 4.11–4.14. The mean values were removed from strain histories because the unsprung mass acceleration signals were intrinsically zero mean over time, as discussed in the previous section. As a result, the strain signals generated from the vibration signals also inherited the zero-mean properties. Normalisation of the experimental strain signals with removed mean was therefore necessary to ensure an acceptable comparison between the generated and measured strain signals.

Similar to the vibration signals, statistical analysis was also conducted on the strain loading histories to determine the behaviour of the strain histories. Table 4.3 illustrates the statistical parameters of the strain histories. The campus road and highway strain signals were found to have negative mean values, indicating compressive loading condition. Meanwhile, Rurals 1 and 2 had positive means of 48.96 με and 45.28 με, respectively, showing that the loads were tensile. Industrial strain loading showed zero mean loading with approximately zero mean value. Tensile loading is well-known to be detrimental to the durability performance of structures (Zhang et al. 2019b). The highest RMS value of 52.55 με was recorded in the strain loading of Rural 1. This was related

to the high excitations of rural road surface, which can contribute to high fatigue damage. In contrast, Highway 2 recorded the lowest RMS value of 14.50 με, indicating that the signal had limited high amplitude cycles and contributed to limited fatigue damage.

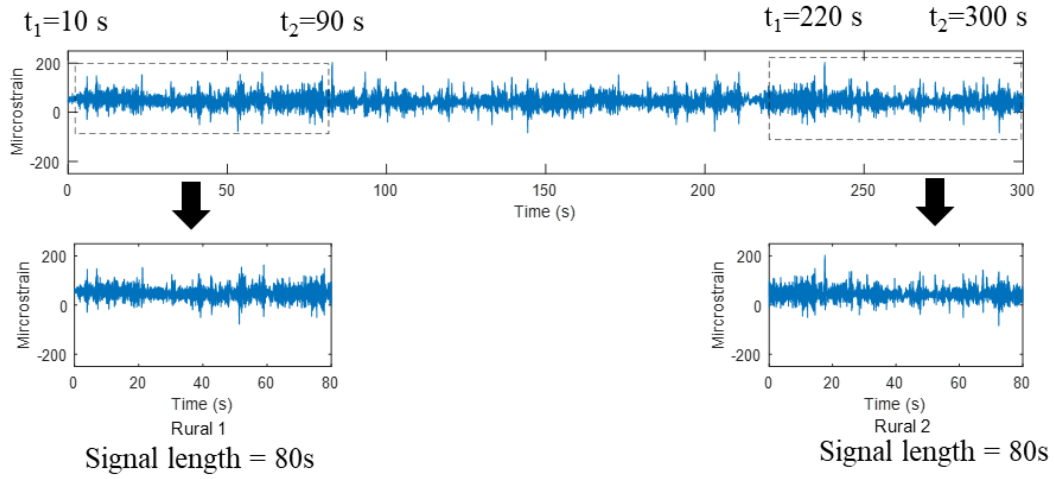

Figure 4.11 Strain histories acquisition in rural area and extraction of signals from raw data

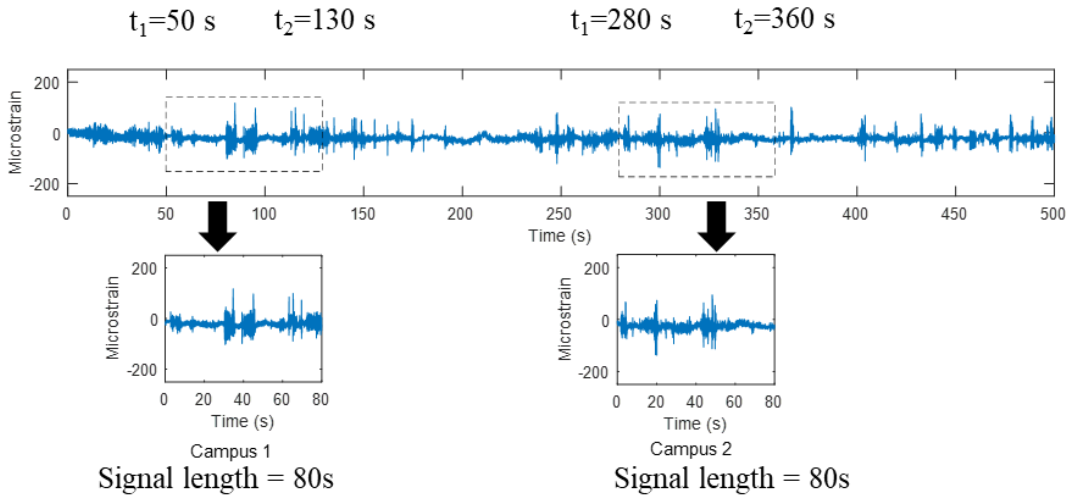

Figure 4.12 Strain histories acquisition in university campus and extraction of signals from raw data

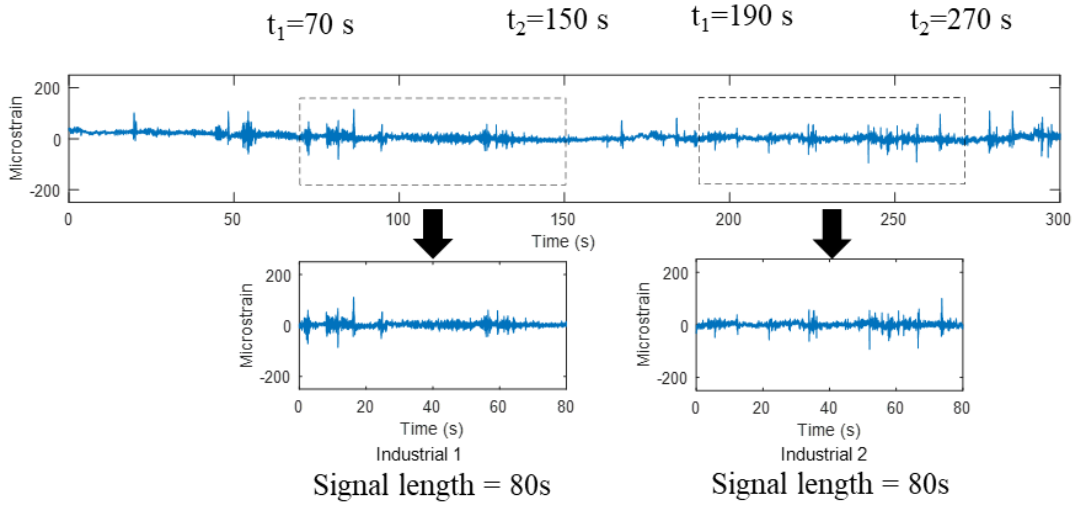

Figure 4.13 Strain histories acquisition in industrial area and extraction of signals from raw data

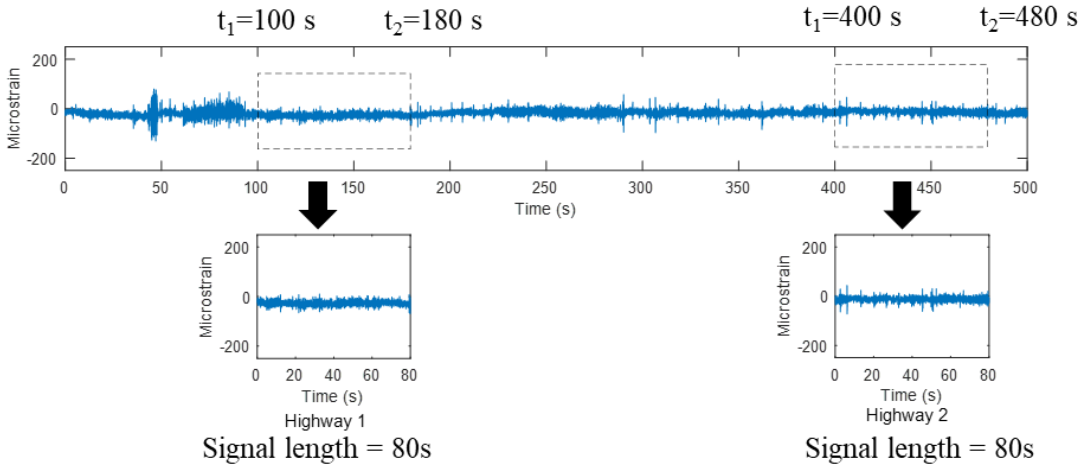

Figure 4.14 Strain histories acquisition in highway and extraction of signals from raw data

Table 4.3 Statistical parameters of strain loading histories obtained from different road conditions

Road condition	Mean (με)	RMS (με)	Skewness	Kurtosis
Rural 1	48.96	52.55	0.29	6.41
Rural 2	45.28	49.18	0.74	7.18
Campus 1	-19.81	24.08	1.67	24.34
Campus 2	-24.31	27.30	1.72	20.69
Industrial 1	2.77	19.87	0.85	12.49
Industrial 2	0.77	18.65	0.23	10.77
Highway 1	-26.87	17.90	0.11	3.64
Highway 2	-12.37	14.50	0.14	3.32

The skewness values of the signals showed that most strain histories were nearly symmetrical given their skewness values close to zero (0.11–0.85) (Cain, Zhang & Yuan 2017), except Campuses 1 and 2. Both signals had higher skewness values of 1.67 and 1.72 , respectively, indicating that their data distributions were not symmetric and skewed to right. Most data points in the strain loading signals concentrated to the left side of the distribution and had a long right tail. Kurtosis values of the strain loading also confirmed that the strain signals were non-stationary as the vibration signals given that the kurtosis values were larger than 3.0 (Kihm, Ferguson & Antoni 2015). Non-stationary loading, with varying statistical properties in time, were found to bring more fatigue damage to structures than stationary loading (Cianetti et al. 2017). The highest kurtosis value of 24.34 was recorded in Campus 1 as a result of the high amplitude events due to the speed bumps on the road. Highway 2 had the lowest kurtosis of 3.32 given the smooth profile of the strain signal.

The CWT was also performed on the strain loading signals to reveal the time-frequency properties of the signals followed by energy mapping. The fatigue damage of strain histories was characterised to obtain the distribution of fatigue damage in time (also known as running damage). Figures 4.15–4.18 depict the time-frequency CWT mapping of strain signals, CWT energy mapping, and the running damage of strain signals under different road conditions. The CWT wavelet coefficients showed that the high damage sections in strain histories were closely related to the high amplitude events with high energy. The rural strain signals had high energy level and the highest fatigue damage of above 1×10^{-5} throughout the entire signal in time. The strain loading histories under rural area contained many large amplitude cycles due to the road surface irregularities. In contrast, the lowest fatigue damage (below 1×10^{-8}) was observed in highway signals with limited occurrences of large amplitude events. Some bump events on the university campus and industrial roads had also resulted in high damaging sections in the strain responses of the coil spring. Given the close relationship between the high amplitude cycles and the high damaging sections in the loading signals, it was essential to identify and extract the high amplitude cycles from the vibration loads as the fatigue-feature for durability prediction.

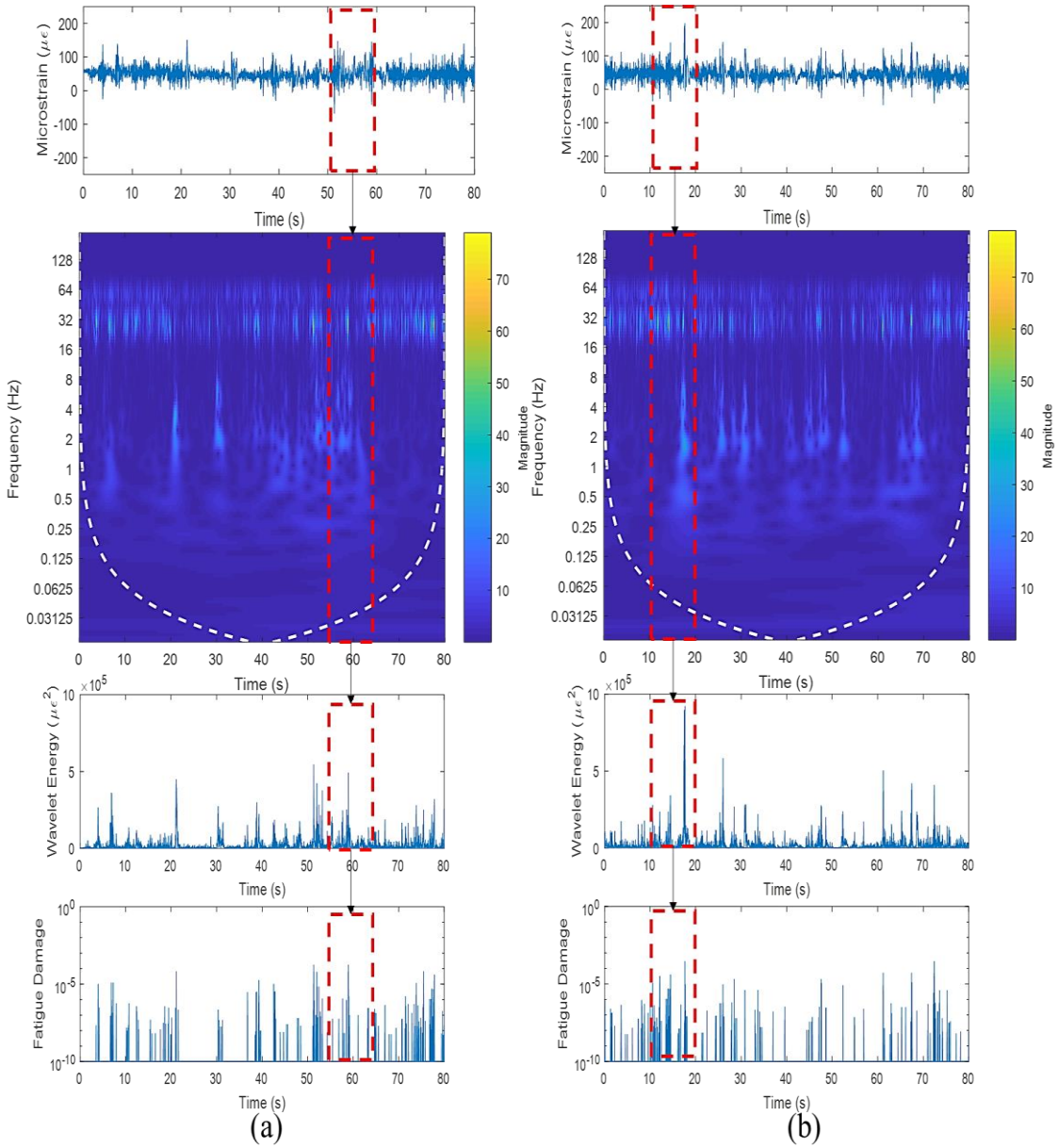

Figure 4.15 Time-frequency analysis, CWT energy mapping and running damage of strain loading signals acquired from rural road: (a) Rural 1, (b) Rural 2

The CWT is an extensively used time-frequency domain signal processing technique by researchers to determine high damaging sections in fatigue loads (Pratumnopharat, Leung & Court 2014; Zhou & Abdel Wahab 2017). Through CWT analysis, the high amplitude events in the strain histories could be pointed out as high magnitude wavelet coefficients in time-frequency domain. The rural area loading signal had the high magnitude of wavelet coefficients while the highway signal recorded the lowest magnitude. In addition, the high amplitude cycles in the strain histories appeared

as high energy segments and contributed to significant fatigue damage. The high amplitude events were found at a frequency range below 16 Hz, which were similar to the vibration loading. For example, the series of high amplitude cycles in Campus 1 signal resulted in high energy segments, which had brought high fatigue damage.

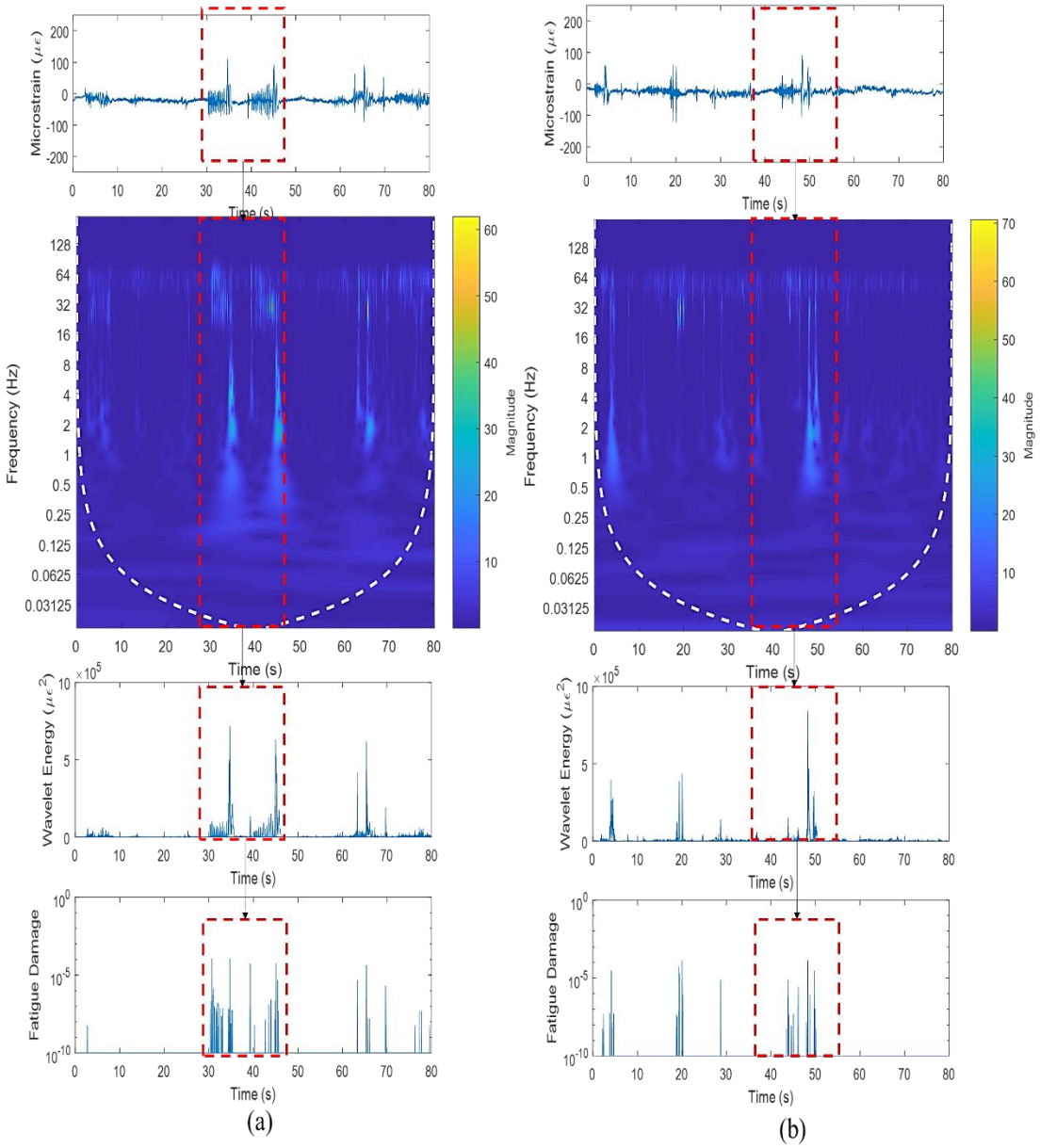

Figure 4.16 Time-frequency analysis, CWT energy mapping and running damage of strain loading signals acquired from university campus: (a) Campus 1, (b) Campus 2

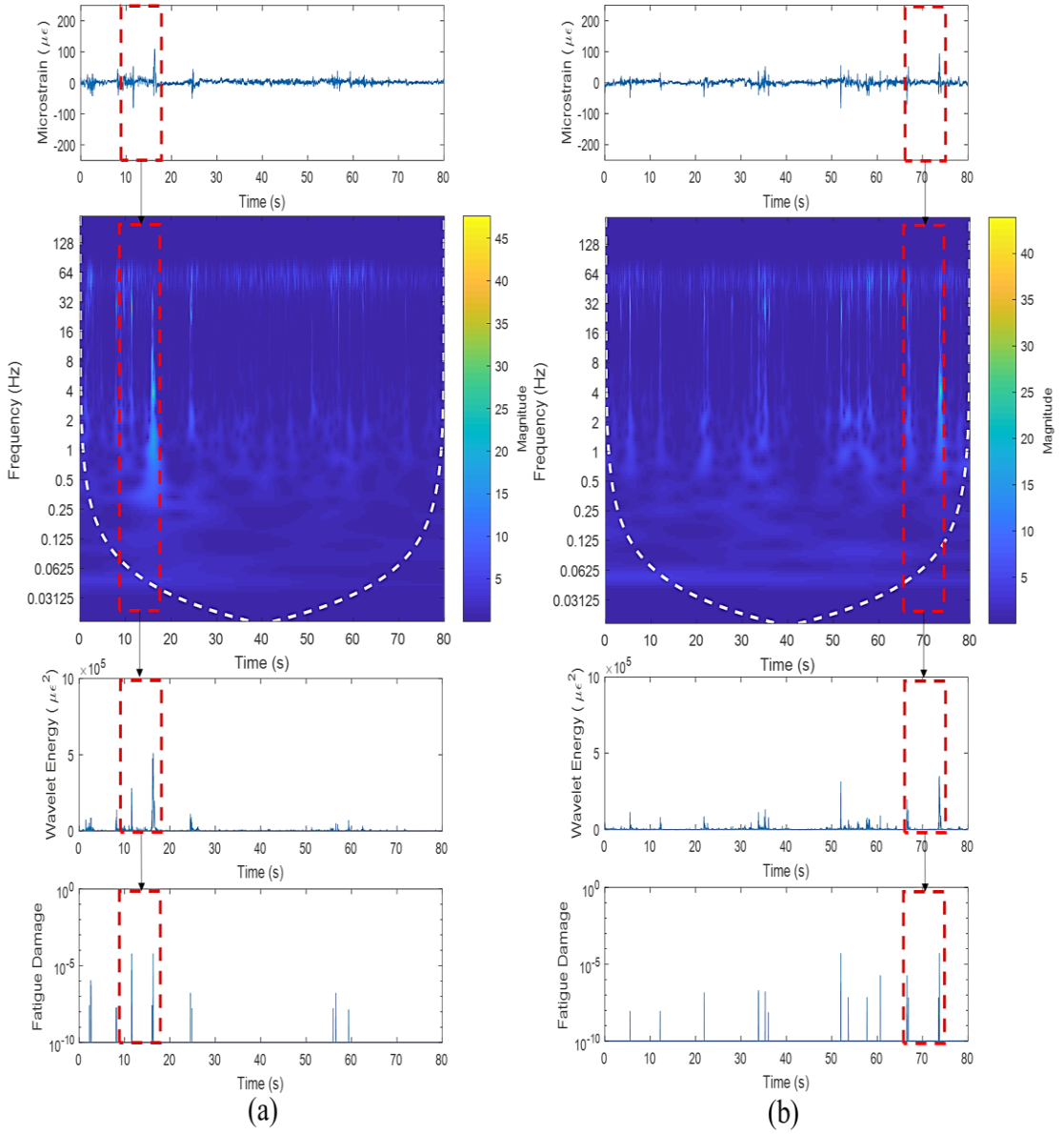

Figure 4.17 Time-frequency analysis, CWT energy mapping and running damage of strain loading signals acquired from industrial area: (a) Industrial 1, (b) Industrial 2

High frequency noises above 50 Hz were also observed in the strain signals and the noises were low amplitude cycles in the loadings that had minimal contribution to the fatigue damage. These noises can be due to the instrumental or environmental factors during data acquisition process. Hence, there is a necessity to remove the high frequency noises from the vibration loading signals before further processing to obtain accurate results (Panda 2016). Several techniques, such as wavelet denoising (Bi, Ma & Wang 2019) and empirical mode decomposition (Li & Wang 2019), are available to

reduce the noises. A new singularity noise reduction method based on CWT was proposed in this study and the results of the denoising process are discussed in the following section.

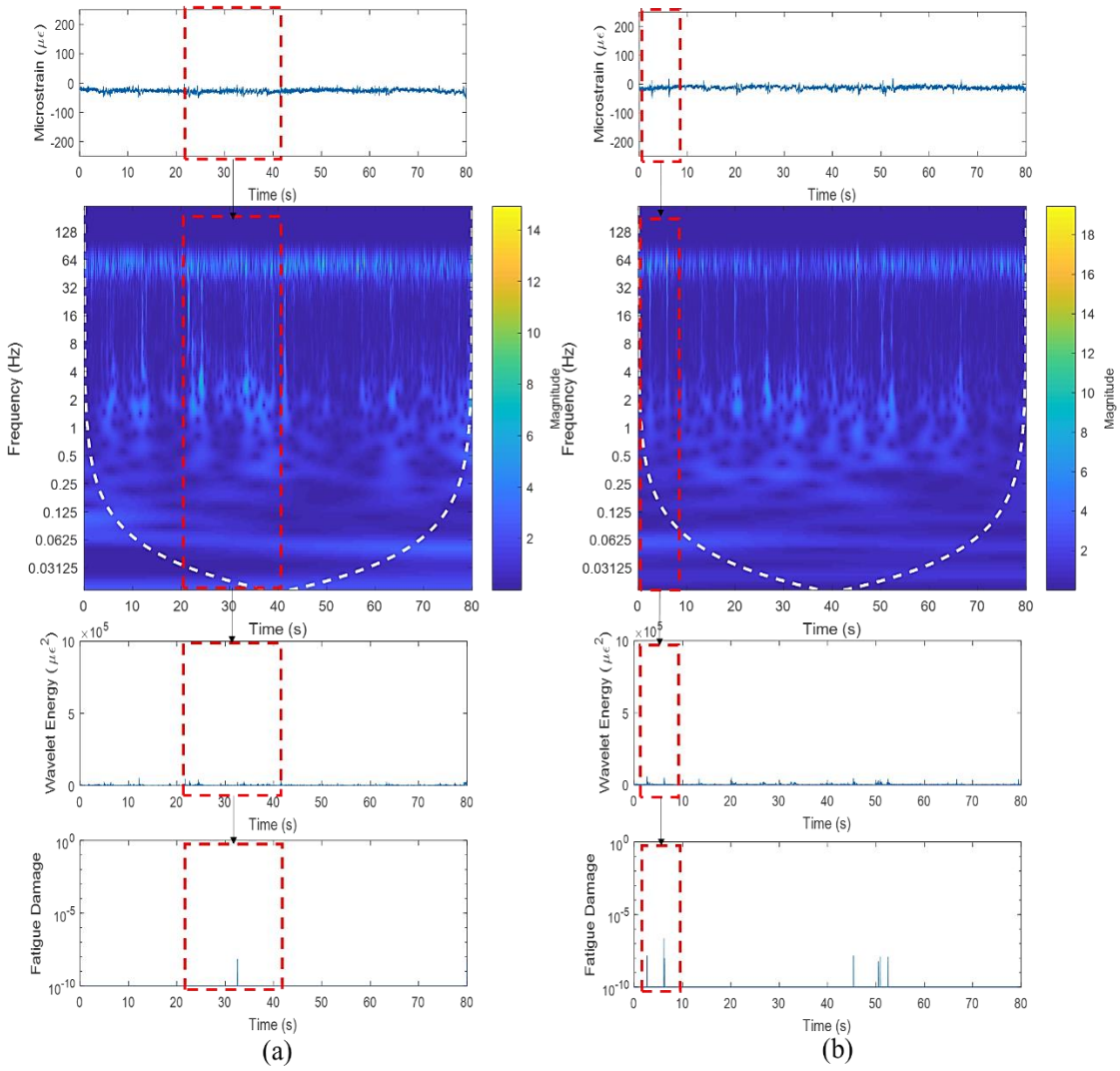

Figure 4.18 Time-frequency analysis, CWT energy mapping and running damage of strain loading signals acquired from highway road: (a) Highway 1, (b) Highway 2

4.2.4 Strain Signal Generation based on Multibody Dynamics Simulation from Vibration Signals

Multibody dynamics (MBD) model of quarter-car suspension system was built to simulate the spring displacement of coil spring under vibration loading. The simulated spring displacement was then converted into strain signal via the derived displacement-

strain relationship, i.e., the CASAS model. After the conversion, the generated strain signals were filtered with a conventional high-pass filter at 0.5 Hz to remove the low frequencies in simulated strain signals caused by signal drifting during MBD simulation. This was because Minaker & Yao (2017) reported that vibrations in vehicles due to the motion of chassis and wheels should fall within the frequency range of 0.5–12 Hz. Thus, frequency below 0.5 Hz needed to be removed. Furthermore, CWT analysis was also employed to determine the high-pass frequency gate value by revealing the time-frequency properties of ultra-low frequency caused by the signal drifts.

Figures 4.19–4.26 illustrate the simulated strain signals of coil springs of various road conditions before and after applying the high-pass filtering. In addition, the corresponding time-frequency mapping of each signal was also illustrated. By comparing the simulated strain signals with corresponding experimental strain signals, some high amplitude cycles were observed in the simulated strain signals while not found in the corresponding experimental strain signals. For example, large fluctuations of strain amplitude could be seen at the beginning of the simulated strain signals of Industrial 2. This can be attributed to the signal drifting of the input vibration loading signals in the MBD simulation. Signal drifting is a common signal processing problem of complex time series in which the signal amplitude constantly changes with time at a specific rate (Kopel et al. 2019). In the MBD simulation, signal drifting happened because of the integration process to convert the input vibration load in acceleration into displacement (Kong et al. 2019a). This will eventually result in low-frequency signal drifts and lead to high amplitude cycles in the simulated strain signals. Hence, further signal processing using high-pass filtering was needed to mitigate the effect of signal drifting in the simulated strain signals.

For simulated strain signals before high-pass filtering, CWT revealed the existence of ultra-low frequencies below 0.5 Hz, which were caused by the strain amplitude fluctuations. Furthermore, the CWT mapping also showed that the high amplitude cycles in the signals occurred at frequencies between 1 and 16 Hz. This was in agreement with the study by Minaker & Yao (2017), which reported that vibration loading in vehicles was within the frequency range of 0.5–12 Hz. Hence, the simulated

strain signals were high-pass filtered at a frequency of 0.5 Hz. A significant signal drifting which led to large amplitude fluctuations in the simulated strain signals was also found in Putra et al. (2015). Although the signal drifting effect can be minimised by detrending the vibration loading signal before the MBD simulation, signal drifting was still inevitable in MBD simulation. Therefore, it is necessary to remove the ultra-low frequencies in the simulated strain because these ultra-low frequencies can cause serious error in fatigue life predictions, especially when the load sequence effect is taken into consideration (Fiedler & Vormwald 2016). It was found that the simulated strain signals after high-pass filtering had the amplitude fluctuations due to signal drifting removed and matched with their corresponding experimental strain signals. The differences between simulated strain signals after high-pass filtering with the experimental strain signals were determined by comparing their statistical behaviours which will be discussed later.

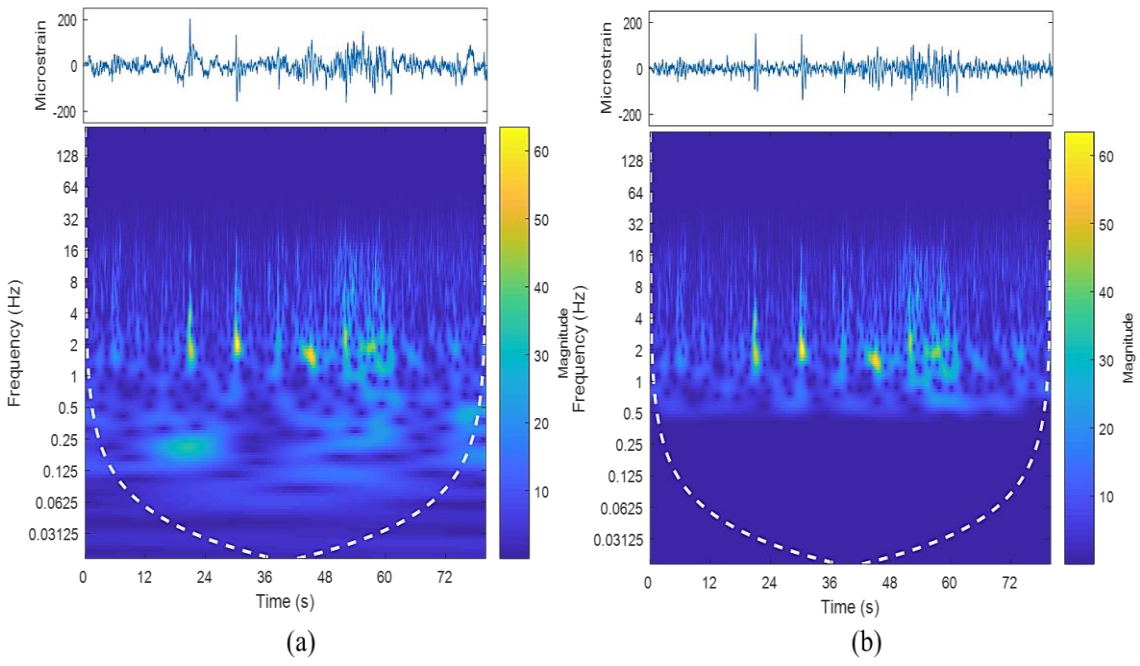

Figure 4.19 Simulated strain loading histories of Rural 1: (a) before high-pass filtering, (b) after high-pass filtering

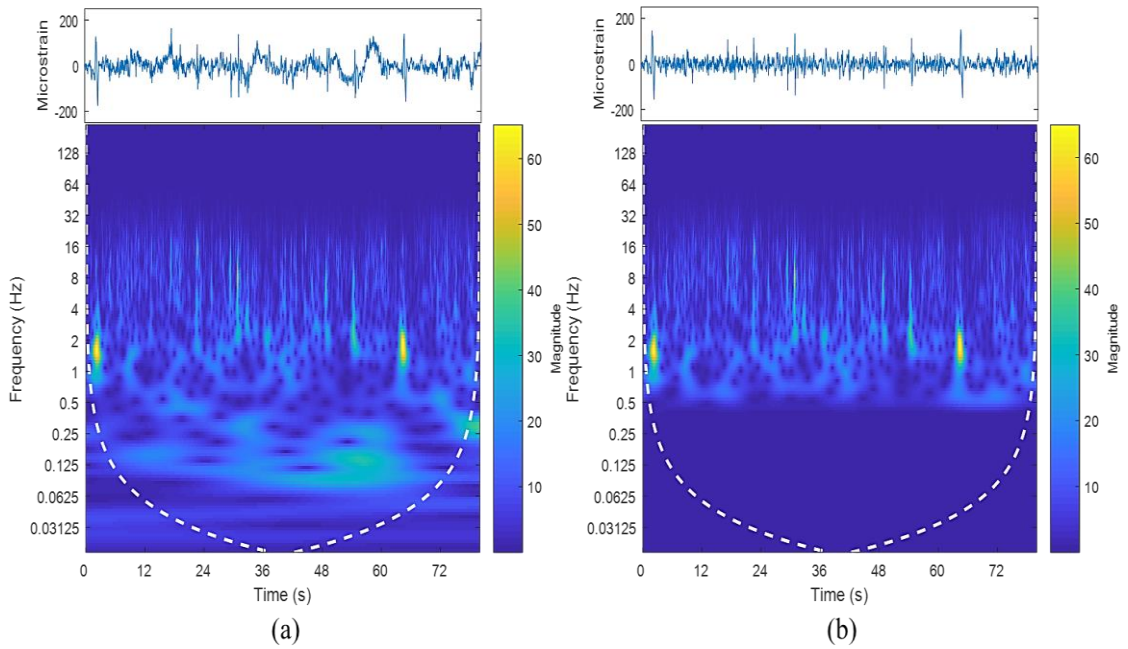

Figure 4.20 Simulated strain loading histories of Rural 2: (a) before high-pass filtering, (b) after high-pass filtering

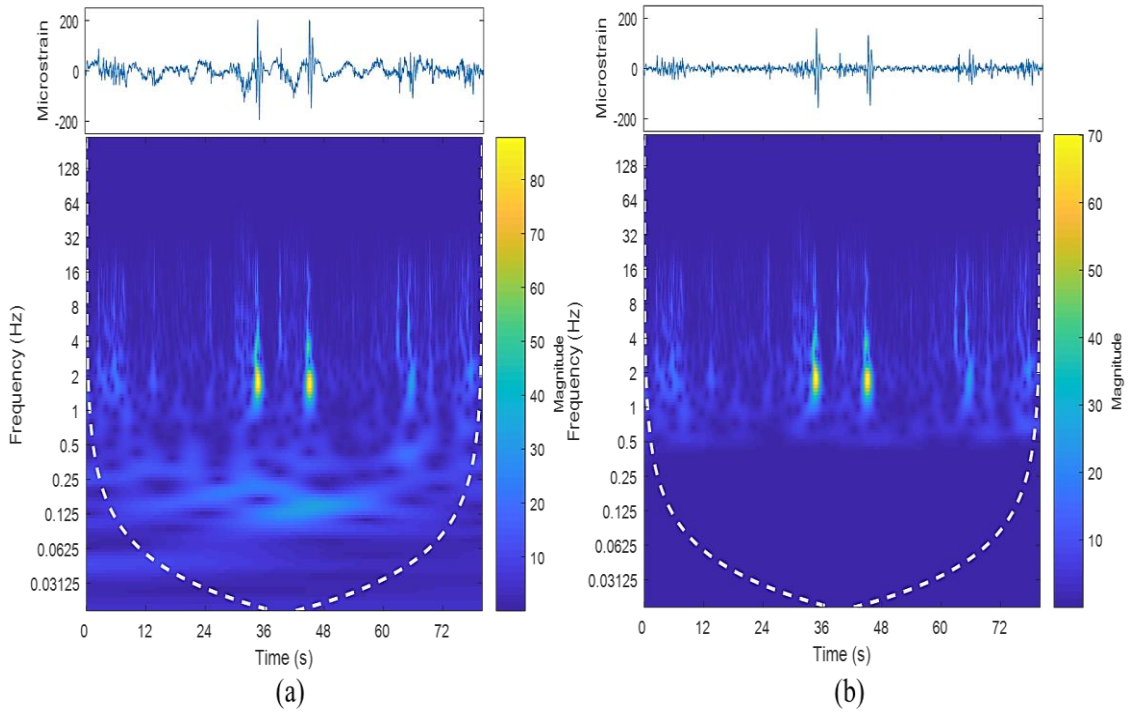

Figure 4.21 Simulated strain loading histories of Campus 1: (a) before high-pass filtering, (b) after high-pass filtering

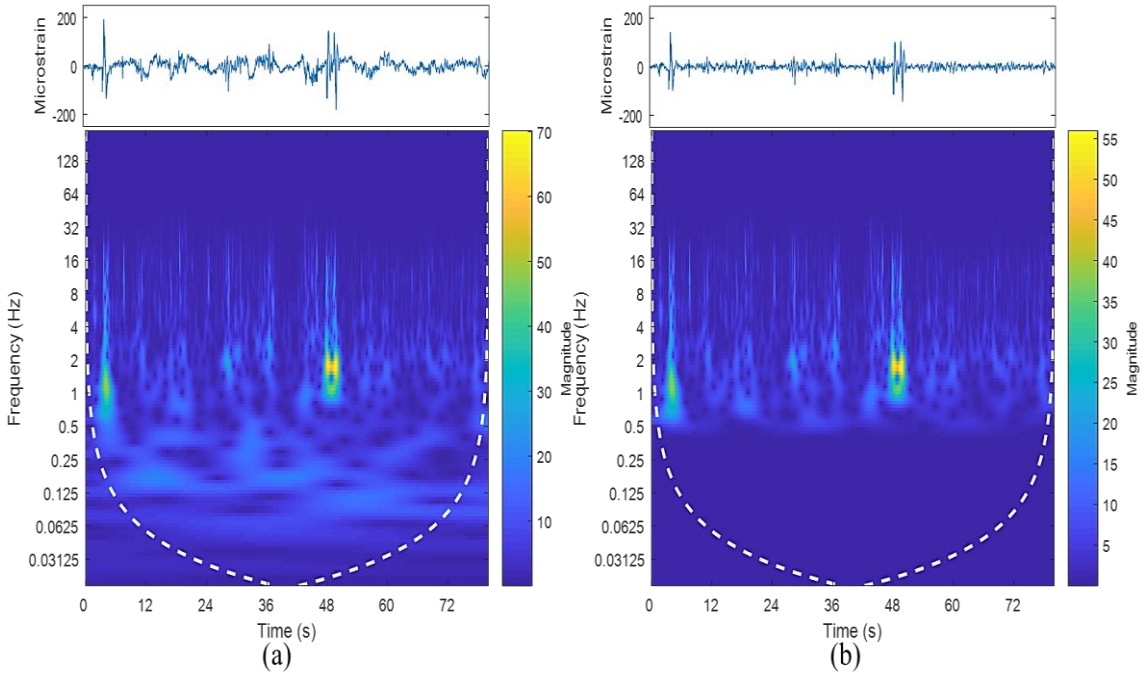

Figure 4.22 Simulated strain loading histories of Campus 2: (a) before high-pass filtering, (b) after high-pass filtering

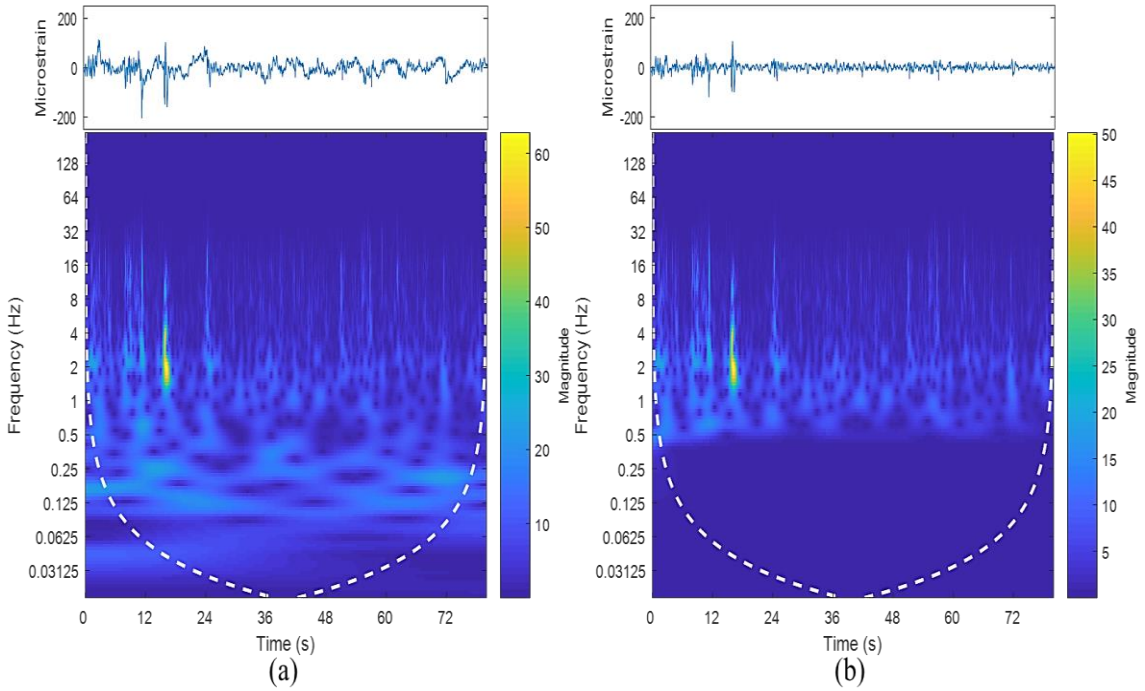

Figure 4.23 Simulated strain loading histories of Industrial 1: (a) before high-pass filtering, (b) after high-pass filtering

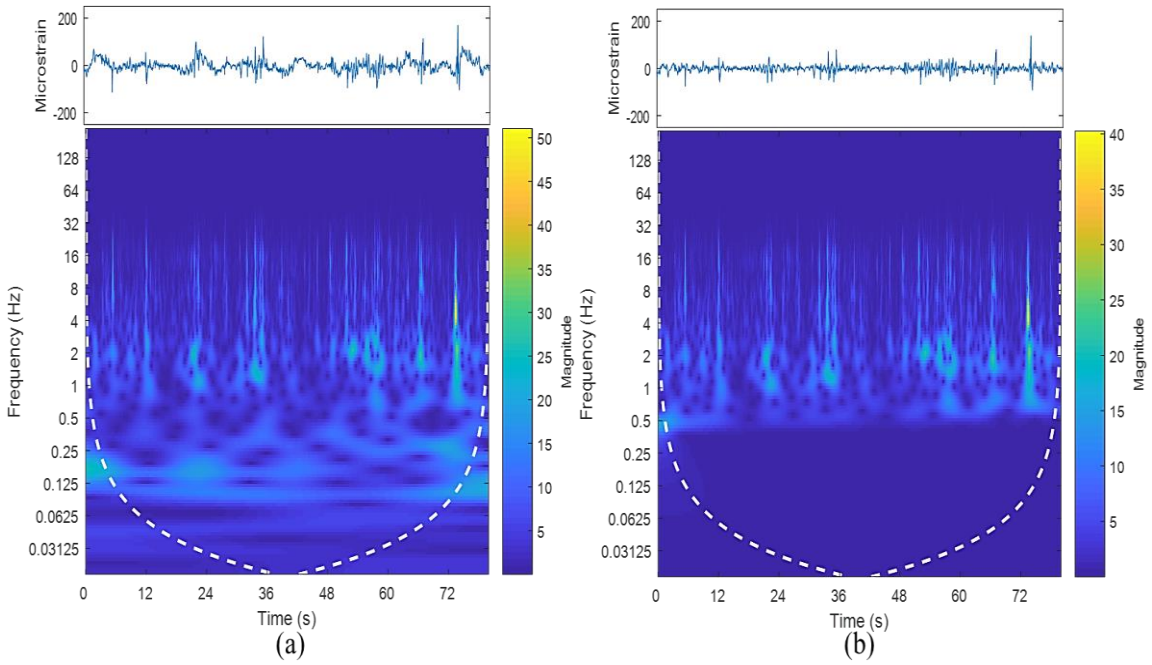

Figure 4.24 Simulated strain loading histories of Industrial 2: (a) before high-pass filtering, (b) after high-pass filtering

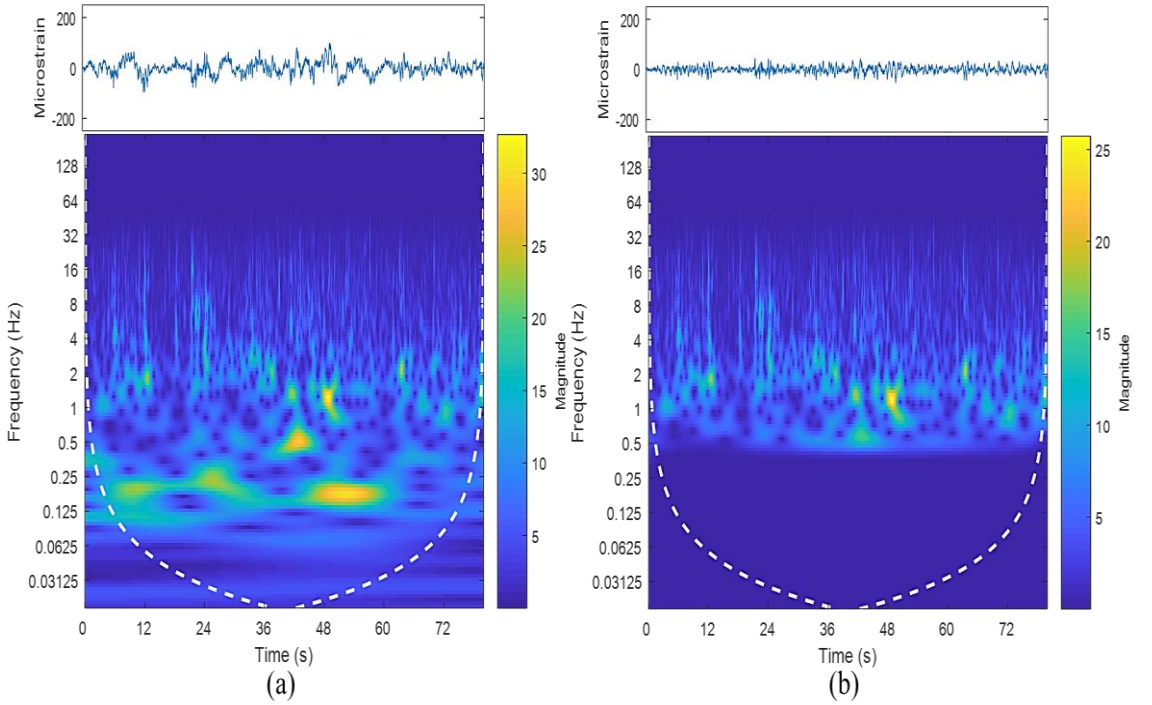

Figure 4.25 Simulated strain loading histories of Highway 1: (a) before high-pass filtering, (b) after high-pass filtering

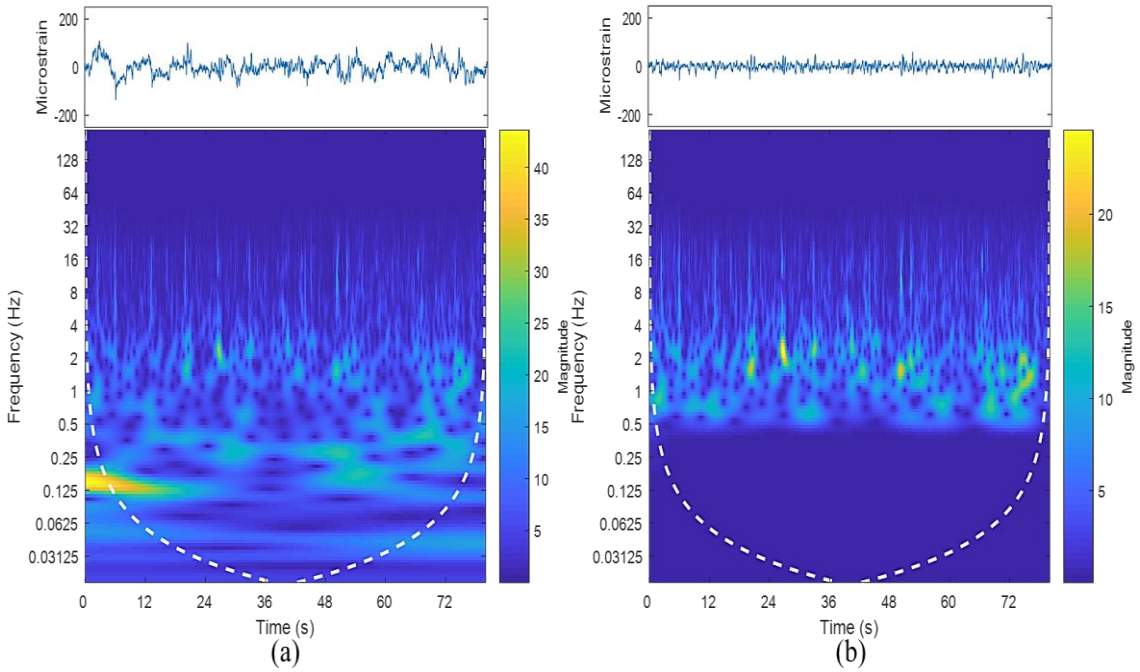

Figure 4.26 Simulated strain loading histories of Highway 2: (a) before high-pass filtering, (b) after high-pass filtering

The statistical properties of the simulated strain signals were determined and compared to the experimental measured strain signals. Table 4.4 shows the statistical parameters of the simulated strain signals. It was noted that the simulated strain inherited the zero mean properties from the vibration signals and thus the mean values of the simulated strain signals were not compared. Figures 4.27– 4.29 show the differences in the statistical parameters with the experimental strain signals. The highest deviation in RMS of 25.5% was observed in Highway 1 signal. Meanwhile, the Industrial 2 had the largest difference of kurtosis up to 24.9%. The highest deviation of skewness at 24.0 % was observed in Campus 1. Some large amplitude cycles in the simulated signals were the main reason that caused higher RMS and kurtosis values in the simulated signals. This can be attributed to the signal drifting of the input vibration loading signals in the MBD simulation. Overall, majority of the simulated strain signals had differences in the statical parameters under 20% and this can be accepted (Putra et al. 2015). The simulated strain signals had shown similar statistical properties with the experimental strain and therefore the simulated strain could be used for durability analysis.

Table 4.4 Statistical behaviours of simulated strain signals and the differences with experimental strain signals

Road condition	Difference in RMS (%)	Difference in skewness (%)	Difference in kurtosis (%)
Rural 1	9.1	10.3	14.2
Rural 2	11.2	9.5	16.6
Campus 1	3.8	24.0	12.7
Campus 2	4.9	20.3	7.1
Industrial 1	16.4	14.1	8.3
Industrial 2	14.9	13.0	24.9
Highway 1	25.5	18.2	1.1
Highway 2	17.1	14.3	18.4

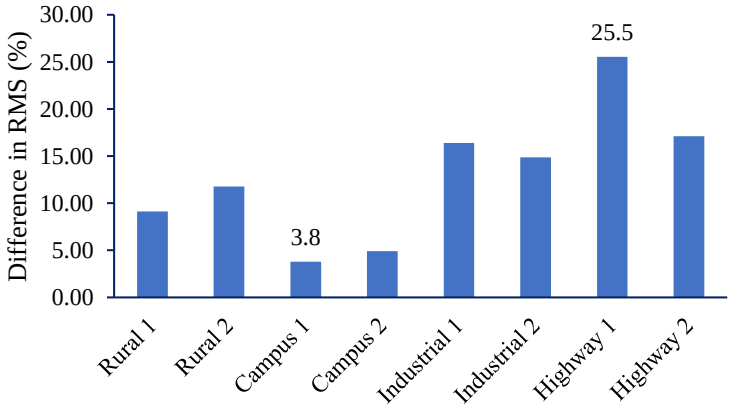

Figure 4.27 Difference in RMS between simulated and experimental strain signals

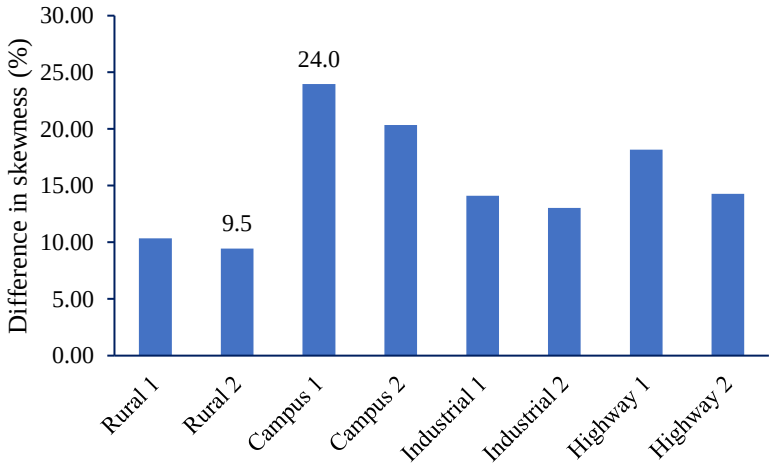

Figure 4.28 Difference in skewness between simulated and experimental strain signals

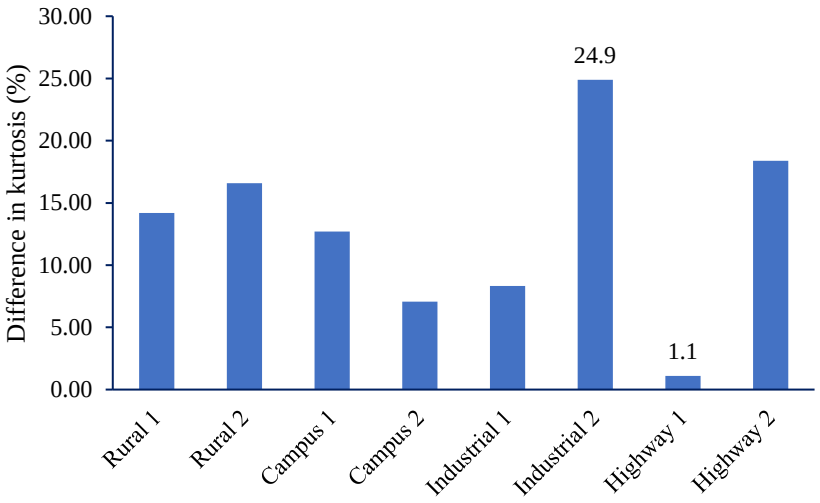

Figure 4.29 Difference in kurtosis between simulated and experimental strain signals

A correlation study between simulated strain signals using CASAS model and measured experimental strain signals was conducted. Various strain histories from different road conditions, including Rural 1, Campus 1, Industrial 1 and Highway 1, were chosen. This was to confirm that CASAS model generated strain signals with 1:1 correlation with the experimental strain. Figure 4.30 shows that correlation scatter plot between that data points of the simulated and measured strain signals. Correlation factors were calculated from the ratio of simulated strain data points to the measured strain data points. The mean values of the correlation factors were obtained to determine the correlation between different signals. From Figure 4.30, it can be observed that the simulated strain signals using CASAS model had good correlation of 1:1 relationship with the measured strain data, within an acceptance boundary determined by the data range of the measured strain signals. Furthermore, the mean correlation factors in the range of 1.054-1.182 supported that simulated strain data had good correlation but with slightly higher amplitude compared to the experimental strain data. This can be attributed to some high amplitude cycles found in the simulated strain signals, especially in bumpy road surfaces. Therefore, it can be remarked that the simulated strain signals exhibited good point-to-point correlation with the measured strain, with correlation factors closed to one.

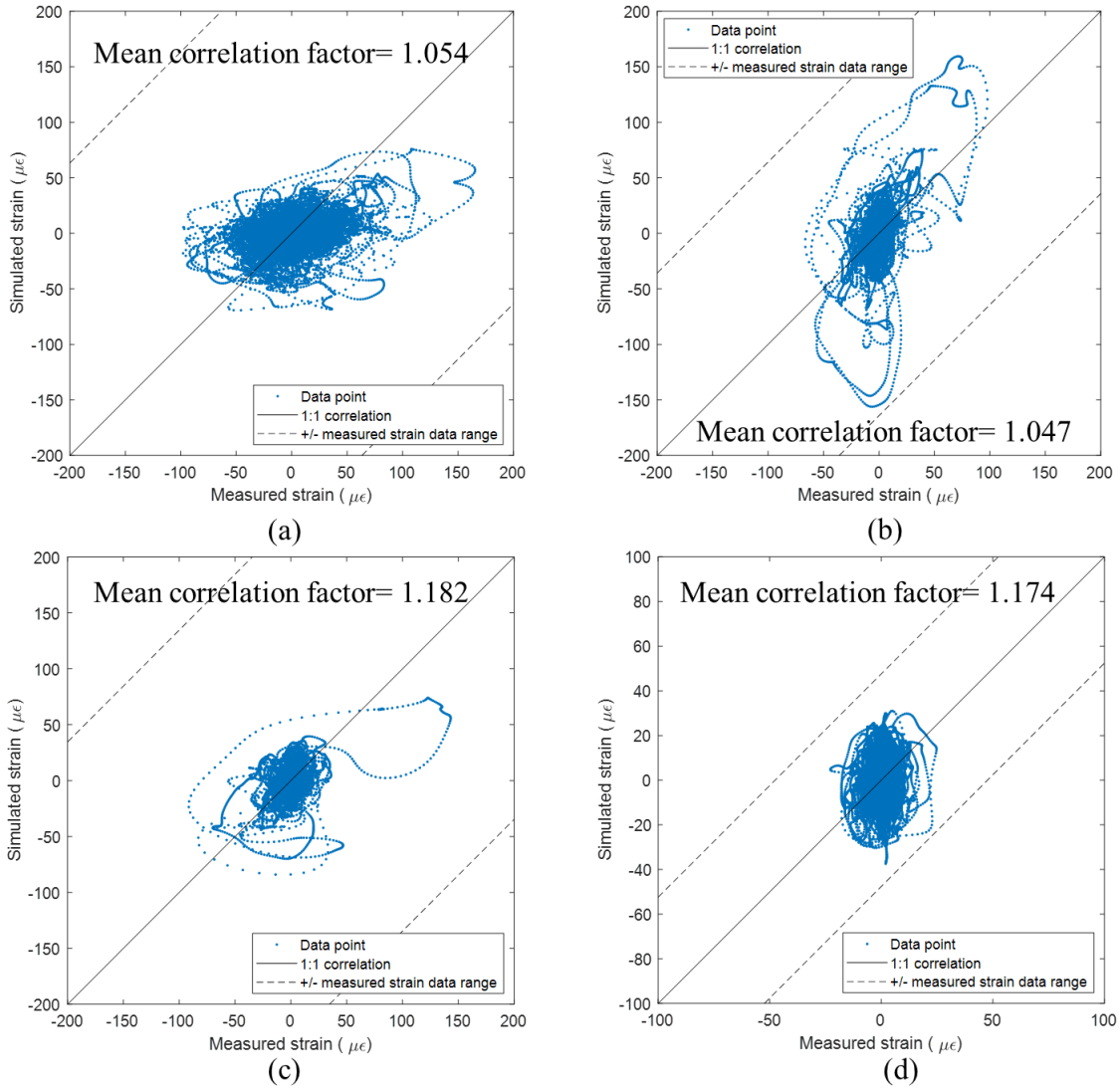

Figure 4.30 Point-to-point correlation analysis between simulated and measured strain data under (a) Rural 1, (b) Campus 1, (c) Industrial 1, (d) Highway 1

The power spectral density (PSD) of the strain signals were also computed as shown in Figure 4.31 as the PSD energy can be calculated based on the area under the PSD graph. The differences of PSD energy between simulated and experimental strain signals were then determined. Table 4.5 shows the PSD energy of strain signals and the percentage of differences between the experimental and simulated signals. The PSDs revealed the power distribution of the simulated strain signals in frequency domain. It was important to ensure that the simulated strain signals also exhibited similar characteristics with experimental strain signals in frequency domain. In the frequency domain, both the experimental and simulated strain signals under different loading conditions had shown a low frequency range of 0–10 Hz with the highest amplitude

peaks between 1 and 2 Hz. These findings were in agreement with previous study (Kong et al. 2017), which also discovered low-frequency range in the loading histories of coil springs and reported PSD peaks at 1.0–1.1 Hz. This result suggested that the simulated strain signals through MBD simulation highly resembled the experimental strain signals in the frequency domain. The highest PSD energy was recorded in experimental strain of Rural 1 and Rural 2 with PSD energy values of 625.54 $\mu\varepsilon^2$ and 636.48 $\mu\varepsilon^2$, respectively. This was due to the highest amplitude in rural signals as observed in the PSDs of rural area. In contrast, highway signals exhibited the lowest strain PSD energy below 60 $\mu\varepsilon^2$ given the smooth surface profile of highway road. This can also be related to their low RMS values which indicated that the highway road gave the lowest excitations to the suspension coil spring.

Table 4.5 Strain PSD energy and differences in PSD energy of various road conditions

Road Condition	Strain PSD energy ($\mu\varepsilon^2$)		PSD energy differences (%)
	Experimental strain	Simulated strain	
Rural 1	625.54	570.31	8.8
Rural 2	636.48	510.45	19.8
Campus 1	319.27	287.02	10.1
Campus 2	243.58	257.38	5.7
Industrial 1	139.86	173.43	24.0
Industrial 2	121.05	154.09	27.3
Highway 1	35.63	40.33	13.2
Highway 2	48.81	57.41	17.6

Figure 4.32 shows the differences in PSD energy between simulated and experimental strain signals. PSD energy differences as high as 27% were observed in the simulated strain signals of Industrial 2. This might be due to the removal of ultra-low frequency below 0.5 Hz using high-pass filtering method and resulting in the loss of some PSD energy. Overall, the differences in PSD energy for the simulated strain were below 30% and were acceptable. Putra, Abdullah & Schramm (2020) edited the strain signal based on the signal energy using wavelet method and found that the edited signal contributed to similar fatigue damage of the original if the energy difference was within 30%. It can be confirmed that the simulated strain signals had similar PSD characteristics with the experimental strain signals. Therefore, the simulated strain

signals also exhibited similar durability properties based on the fatigue life parameters with the experimental strain signals.

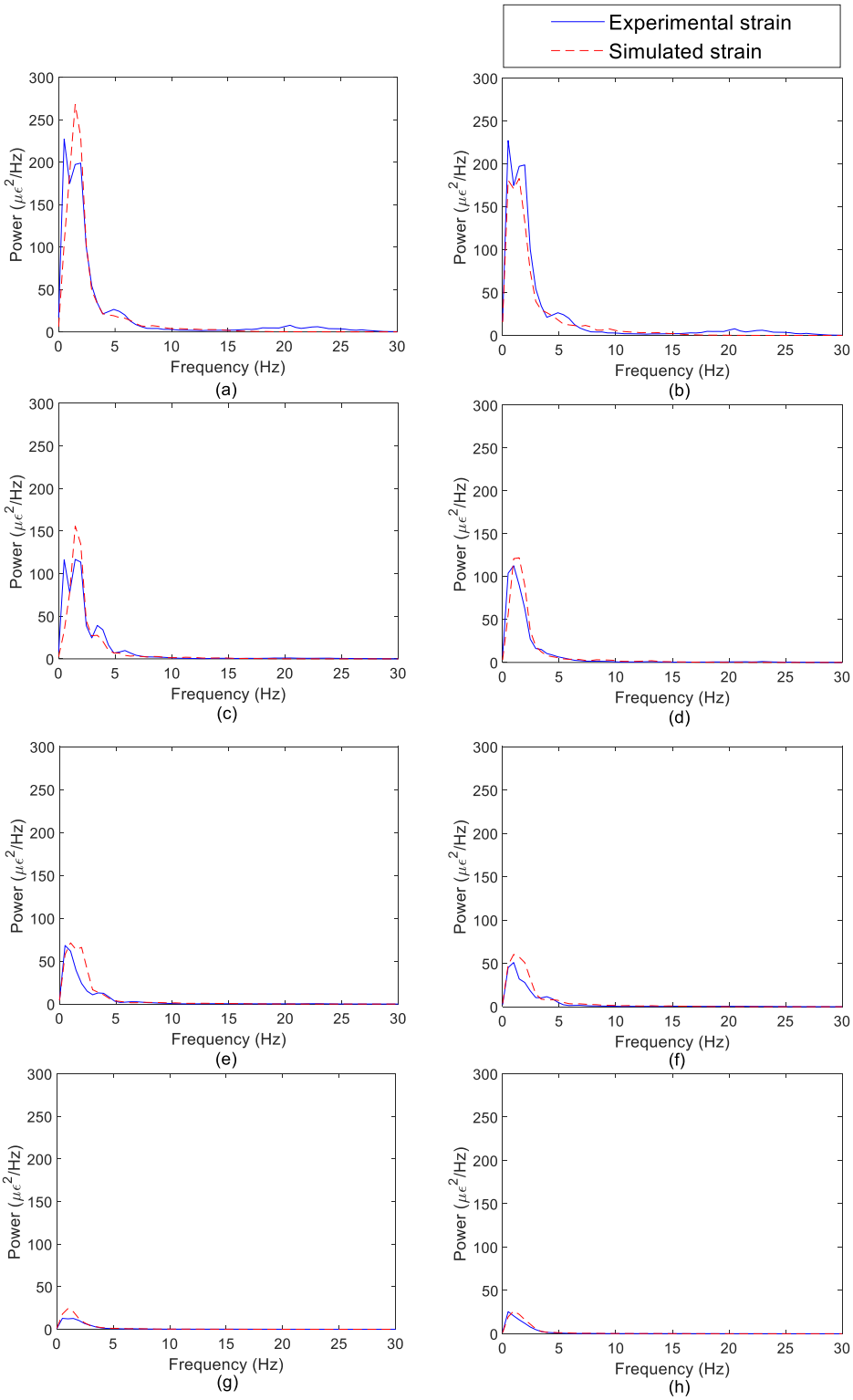

Figure 4.31 Power spectral densities of the measured and simulated loading histories under different road conditions: (a) Rural 1, (b) Rural 2, (c) Campus 1, (d) Campus 2, (e) Industrial 1, (f) Industrial 2, (g) Highway 1, (h) Highway 2

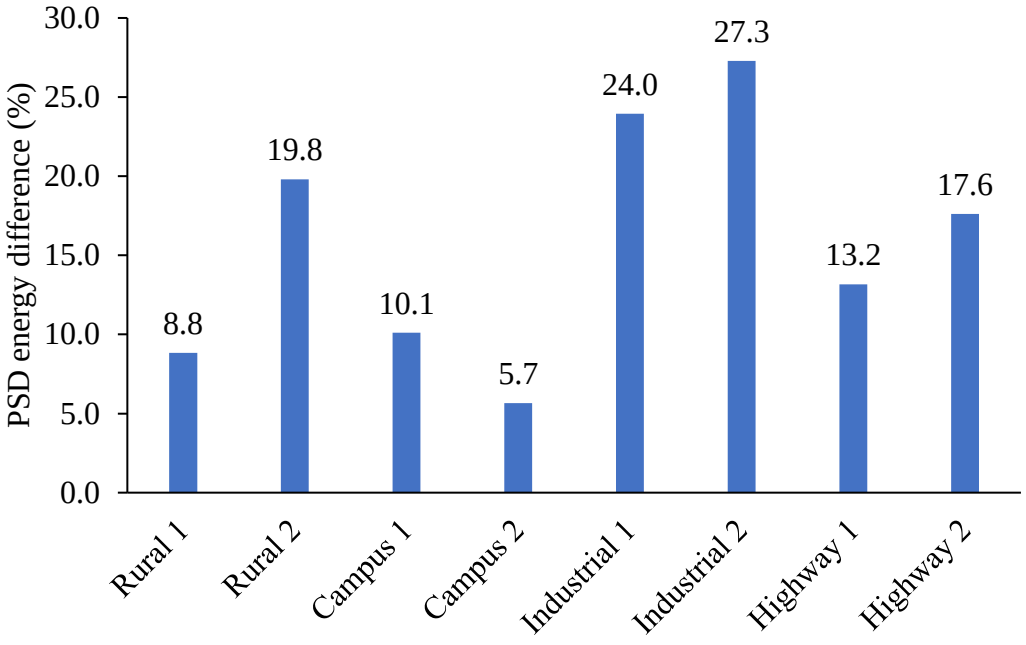

Figure 4.32 Difference in PSD energy of the simulated strain histories

In the fatigue life assessment, the rainflow algorithm was implemented to count the fatigue cycles in each strain signal and the respective fatigue damage was then computed using strain-life models. The rainflow histograms are important to evaluate the fatigue behaviours of strain signals as well as fatigue life calculation (Marsh et al. 2016). Figures 4.33–4.40 illustrate the rainflow and damage histograms of the experimental measured strain signals which provide the details of the fatigue cycles and fatigue damage counted at specific mean and amplitude range. To compare the fatigue properties between the simulated and experimental strain signals, the rainflow cycles and fatigue damage in the simulated signals were also determined. Figures 4.41–4.48 show the rainflow and damage histograms of the simulated strain signals converted from the vibration signals. Since there are four fatigue life models, which are Coffin-Manson, Morrow, SWT, and ESD used in the analysis, only the damage histograms computed using Morrow model are shown in Figures 4.33–4.48 for illustration purpose as the Coffin-Manson and SWT models gave similar trend (Putra, Husaini & Machmud 2020).

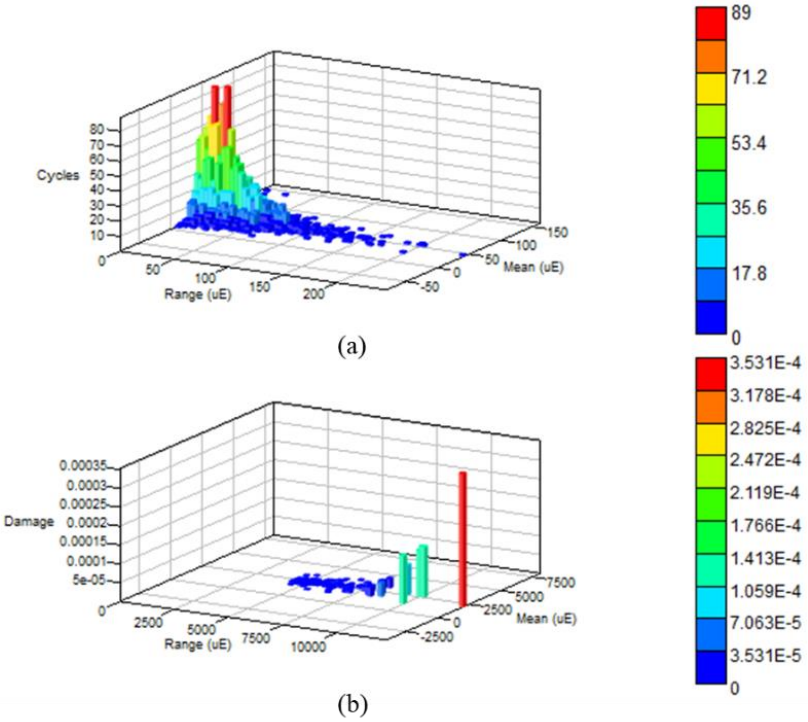

Figure 4.33 Histograms of experimental strain signal of Rural 1, indicating: (a) rainfall cycles, (b) fatigue damage

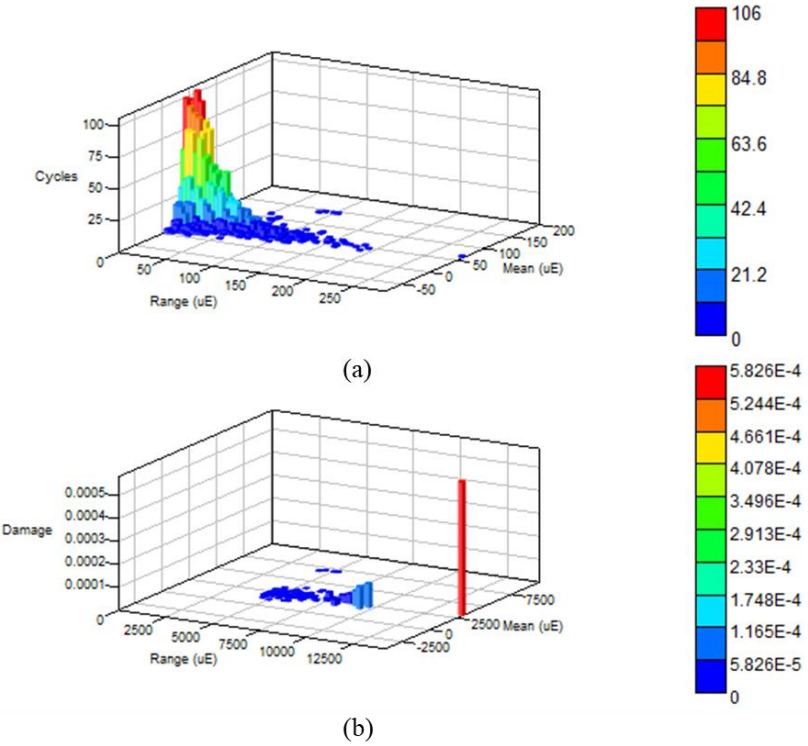

Figure 4.34 Histograms of experimental strain signal of Rural 2, indicating: (a) rainfall cycles, (b) fatigue damage

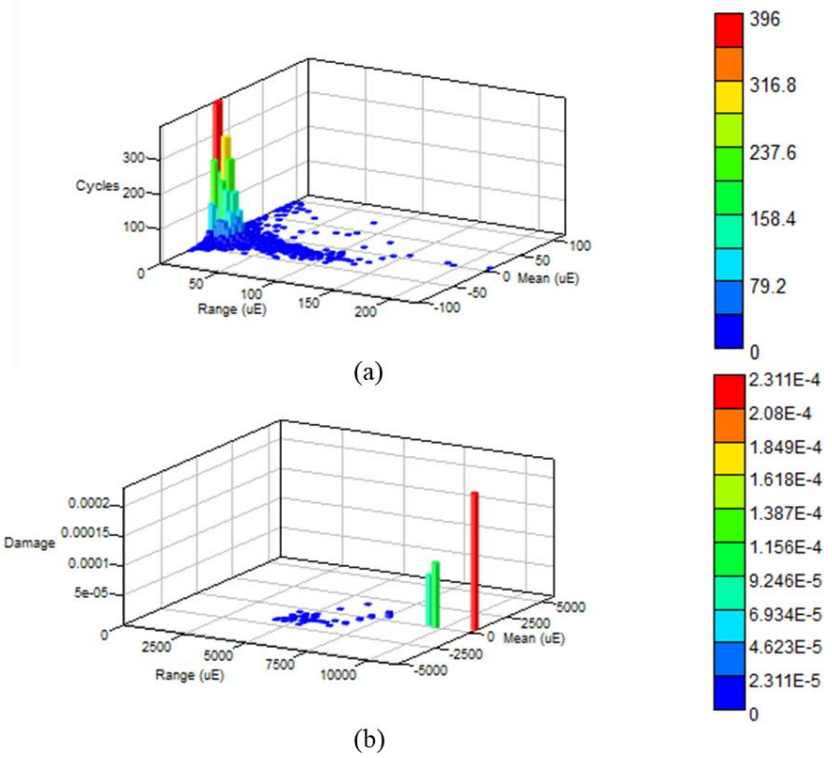

Figure 4.35 Histograms of experimental strain signal of Campus 1, indicating: (a) rainflow cycles, (b) fatigue damage

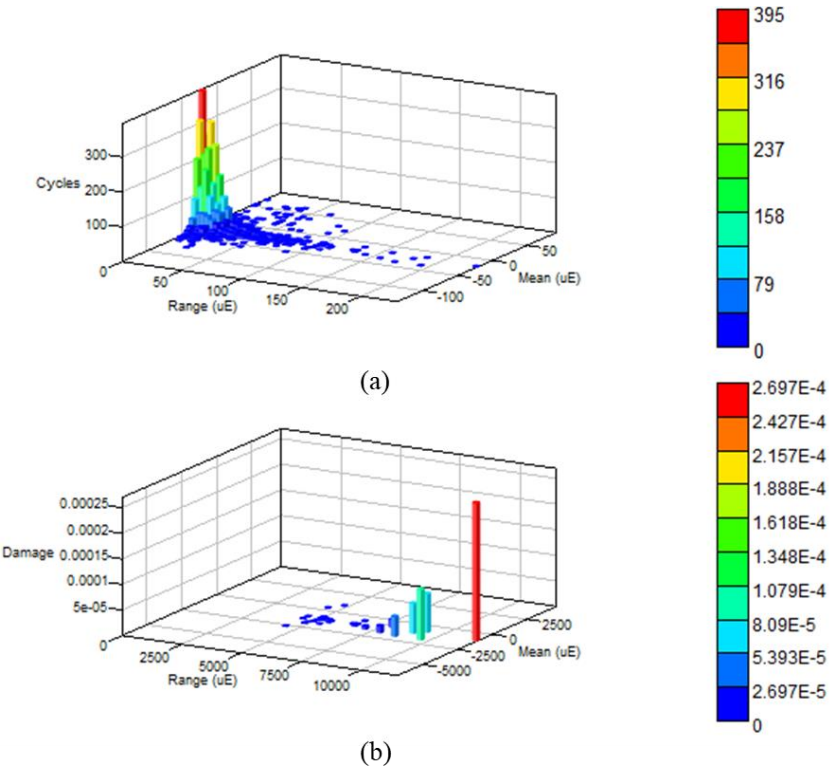

Figure 4.36 Histograms of experimental strain signal of Campus 2, indicating: (a) rainflow cycles, (b) fatigue damage

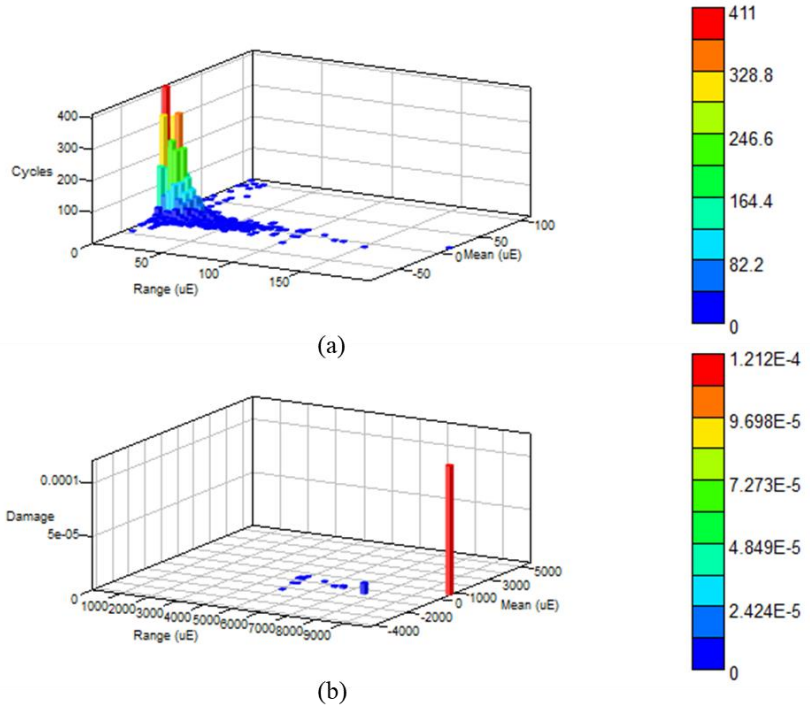

Figure 4.37 Histograms of experimental strain signal of Industrial 1, indicating: (a) rainflow cycles, (b) fatigue damage

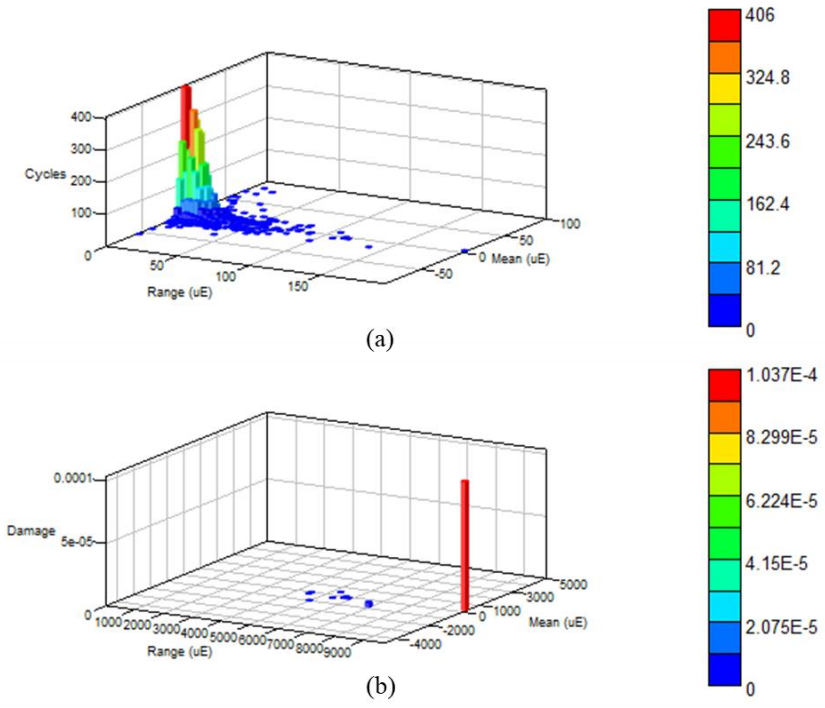

Figure 4.38 Histograms of experimental strain signal of Industrial 2, indicating: (a) rainflow cycles, (b) fatigue damage

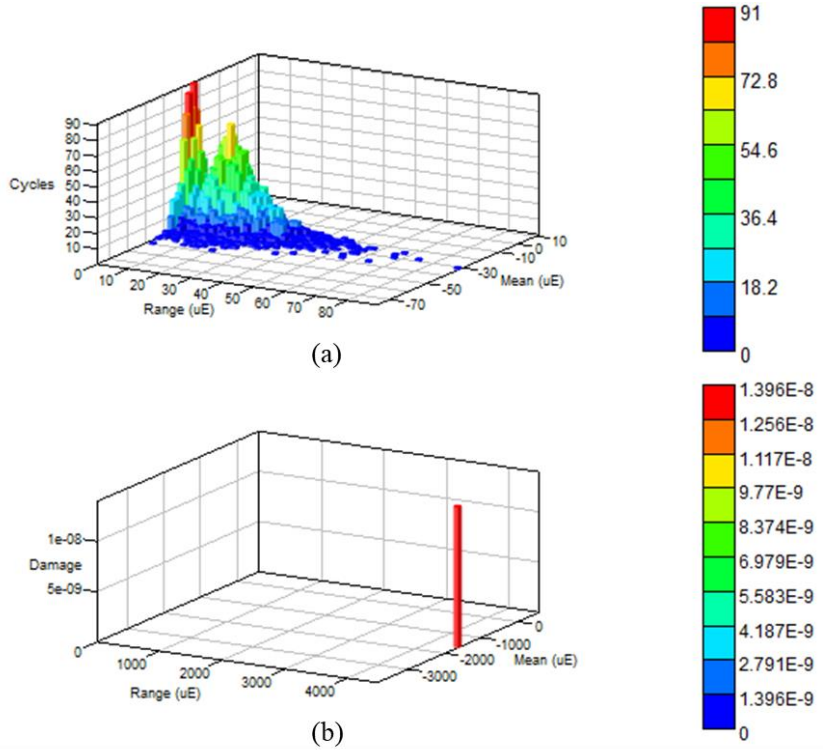

Figure 4.39 Histograms of experimental strain signal of Highway 1, indicating: (a) rainflow cycles, (b) fatigue damage

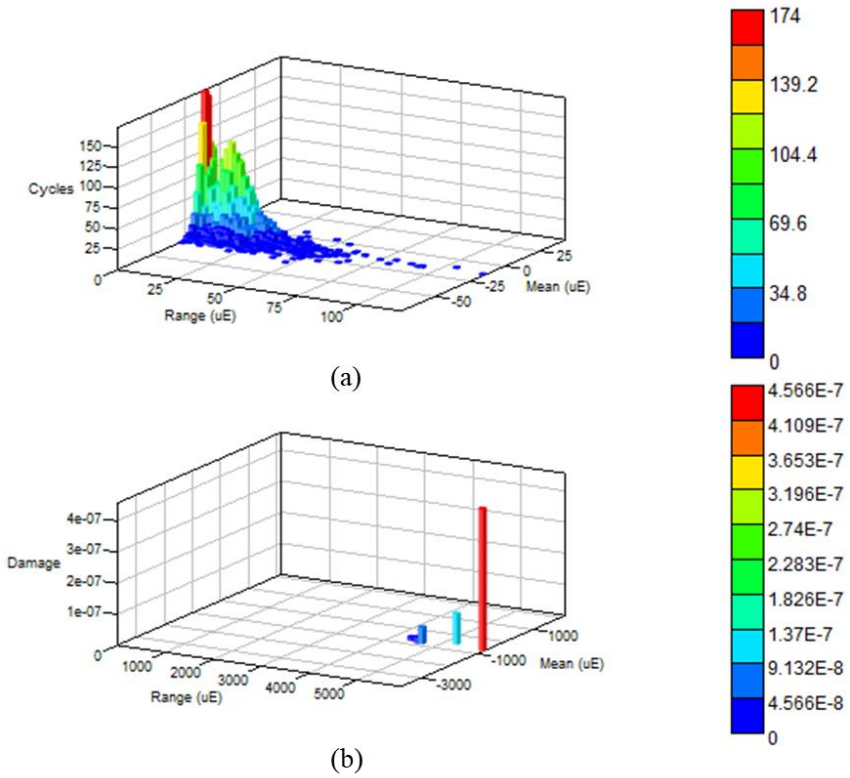

Figure 4.40 Histograms of experimental strain signal of Highway 2, indicating: (a) rainflow cycles, (b) fatigue damage

From the rainflow histograms, the rural signals were found to contain a large number of high amplitude cycles with amplitude range above 200 με. The corresponding damage histograms also confirmed that the high amplitude cycles in the signals had resulted in high fatigue damage. The highest fatigue damage of 5.862×10^{-4} was recorded in Rural 2. With reference to the previous studies by Pratumnopharat, Leung & Court (2013, 2014) and Putra et al. (2017b), it had been proven that the high amplitude cycles in loading histories had contributed more than 90% of fatigue damage. In contrast, most fatigue cycles in highway signals were low amplitude cycles with amplitude range of less than 100 με due to the smooth road surface profile. The cycles with the maximum strain amplitude range in Highway 1 only contributed to a fatigue damage of 1.396×10^{-8}. Therefore, the highway signals resulted in the longest fatigue lives among loading signals.

From Figures 4.41–4.49, the simulated strain signals exhibited less fatigue cycles compared to the corresponding experimental data. Most missing cycles were found to be low amplitude cycles with very minimal contribution to fatigue damage (Duraffourg et al. 2015). Therefore, the missing fatigue cycles, regardless of their large quantities, would have no significant impact on the fatigue life assessment. These low amplitude cycles were not simulated by the MBD simulation due to the light effects of the cycles on the spring responses. Hence, the damage histograms showed similar fatigue damage in the simulated strain signals compared to the experimental strain signals. The missing low amplitude cycles had very limited contribution to fatigue damage because of the low amplitude ranges and thus these cycles were negligible in durability analysis. In addition, the simulated strain signals also showed increased amplitude range compared to the experimental strain signals. For example, high amplitude cycles with the range of 300 με were found in the simulated strain signal of Rural 1 while the highest amplitude range in the experimental strain signal was around 250 με, as shown in Figures 4.33a and 4.41a. This was due to the signal drifting effects resulting from the MBD simulation, as previously discussed. The findings confirmed that the application of the CASAS model associated to the MBD simulation was effective to simulate strain signals that matched the experimental results.

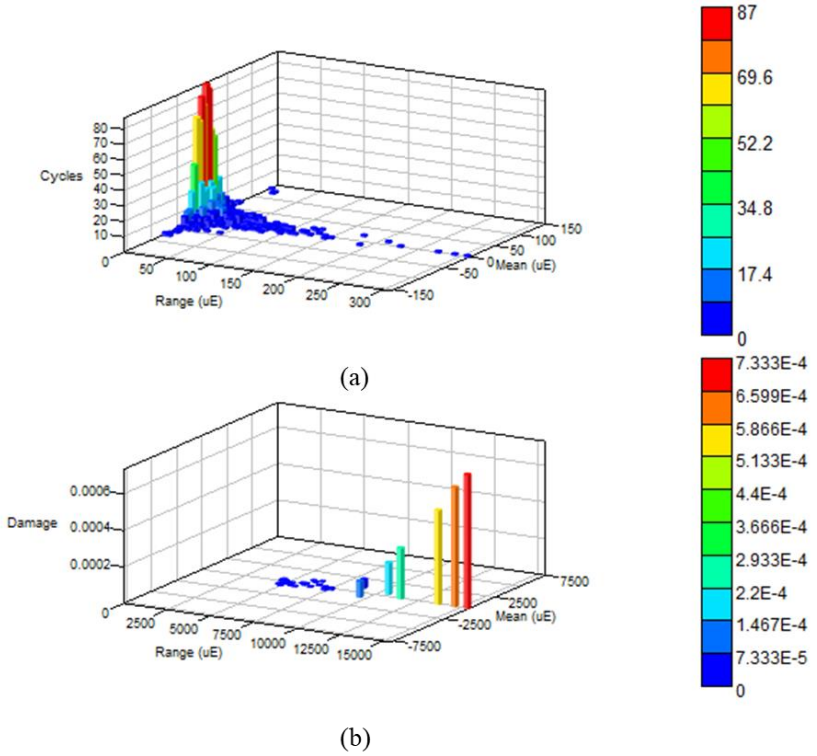

Figure 4.41 Histograms of simulated strain signal of Rural 1, indicating: (a) rainflow cycles, (b) fatigue damage

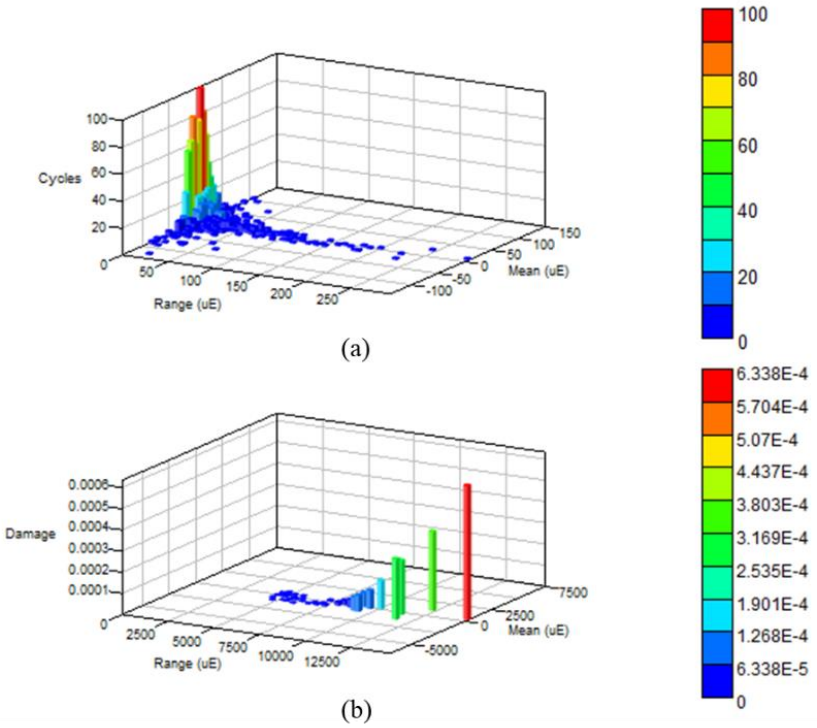

Figure 4.42 Histograms of simulated strain signal of Rural 2, indicating: (a) rainflow cycles, (b) fatigue damage

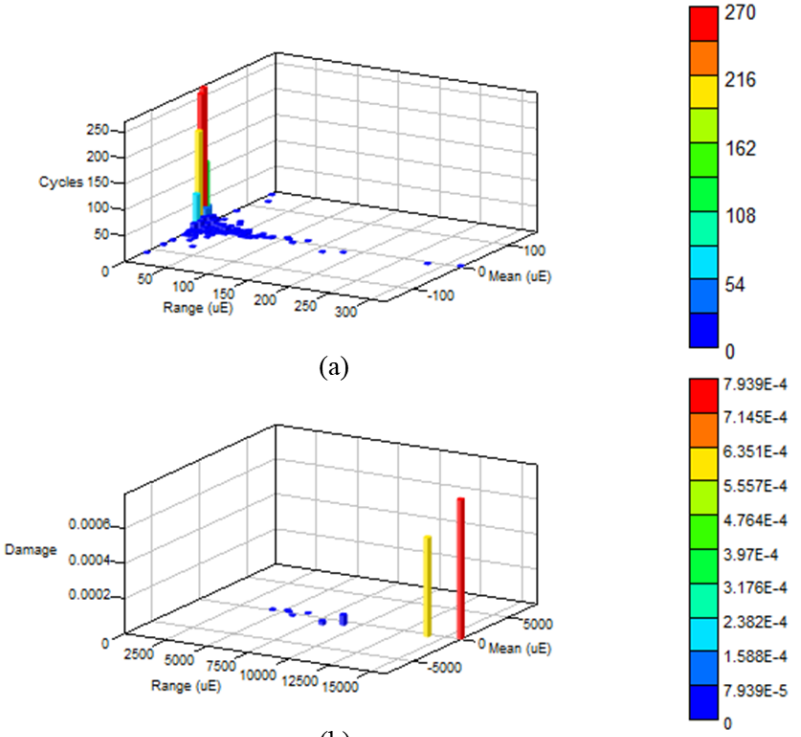

Figure 4.43 Histograms of simulated strain signal of Campus 1, indicating: (a) rainflow cycles, (b) fatigue damage

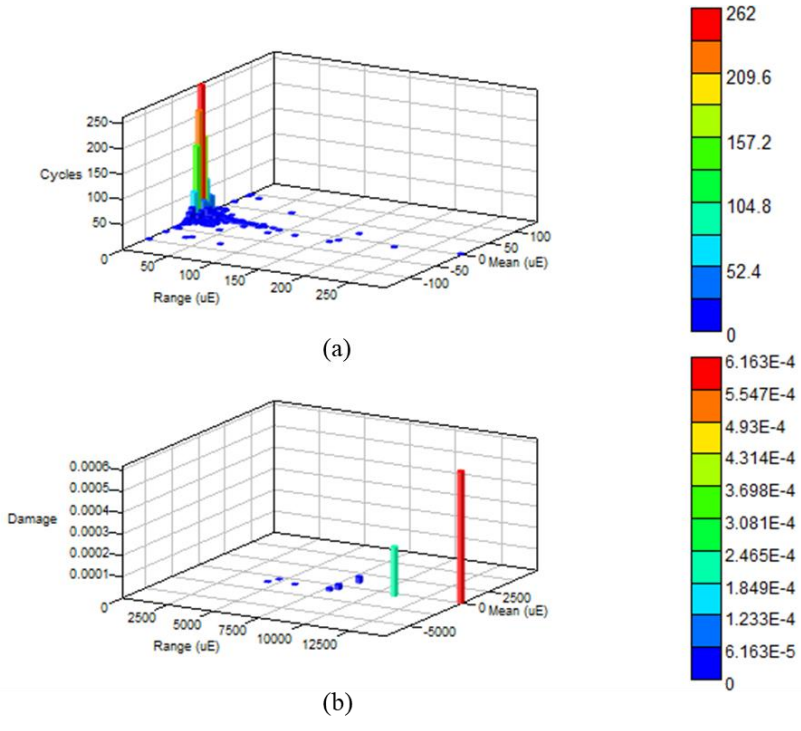

Figure 4.44 Histograms of simulated strain signal of Campus 2, indicating: (a) rainflow cycles, (b) fatigue damage

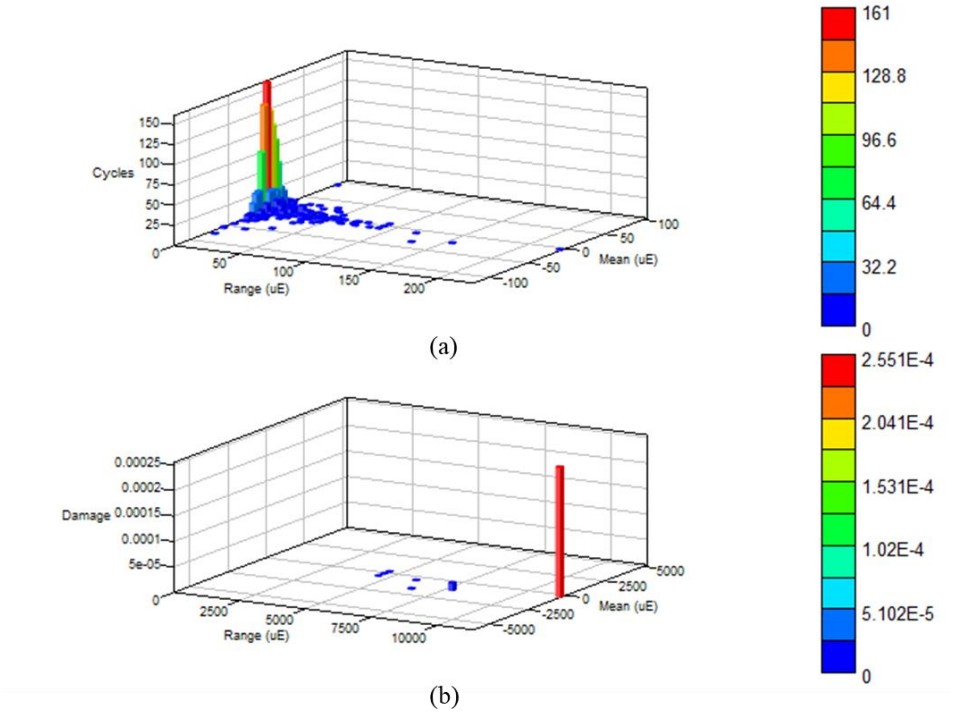

Figure 4.45 Histograms of simulated strain signal of Industrial 1, indicating: (a) rainflow cycles, (b) fatigue damage

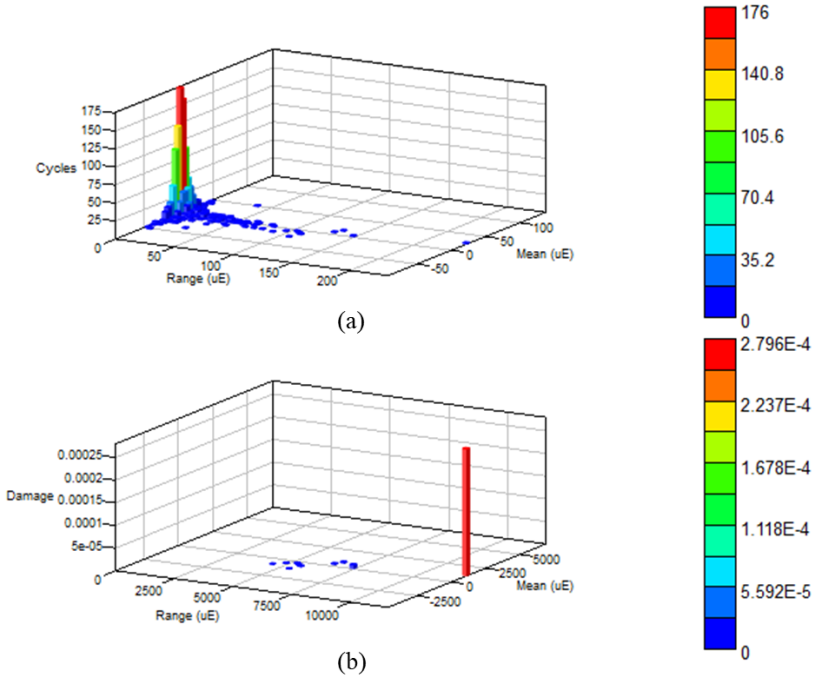

Figure 4.46 Histograms of simulated strain signal of Industrial 2, indicating: (a) rainflow cycles, (b) fatigue damage

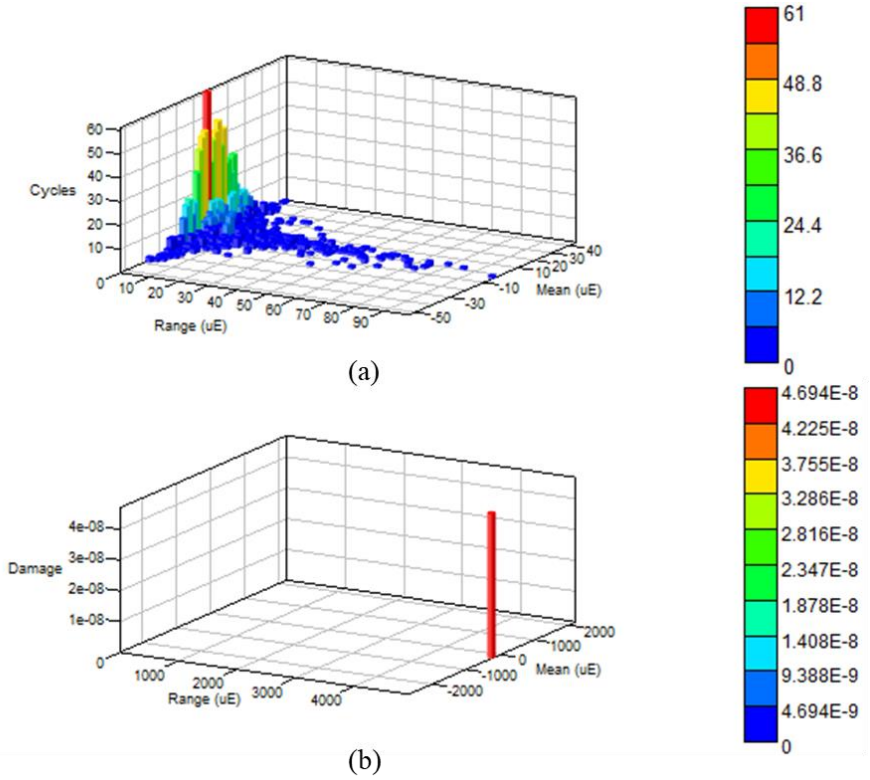

Figure 4.47 Histograms of simulated strain signal of Highway 1, indicating: (a) rainflow cycles, (b) fatigue damage

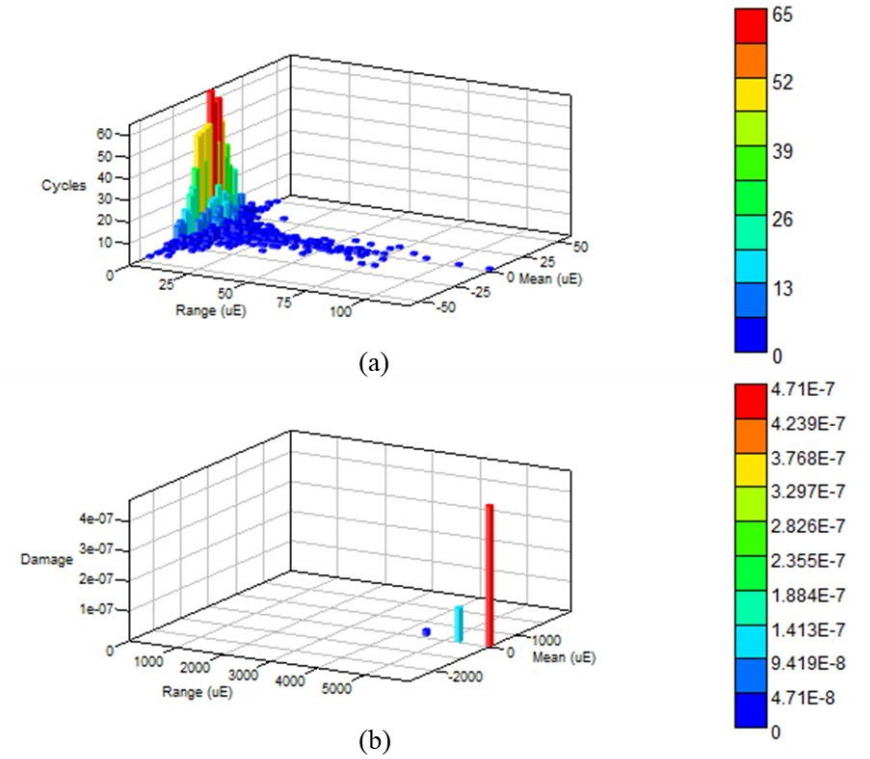

Figure 4.48 Histograms of simulated strain signal of Highway 2, indicating: (a) rainflow cycles, (b) fatigue damage

In order to validate the CASAS model, the Kong-Abdullah model proposed by Kong et al. (2019a) had been compared because it was also derived from the torsional shear stress, which is the dominant shear stress in a coil spring. However, Kong-Abdullah model did not consider the MBD interactions between the suspension components, which are very important to accurately predict the spring responses under vibration loading. This model assumed the relative displacement between the sprung and unsprung masses as the total spring displacement and it could lead to erroneous prediction as the real orientation of the coil spring in suspension system was not taken into account. Using the Kong-Abdullah model, strain signals were simulated from the vibration signals and compared to the corresponding experimental strain signals, as shown in Figures 4.49–4.52. Compared to the simulated strain signals using CASAS model, there are also many large amplitude fluctuations found in the strain signals simulated by Kong-Abdullah model. These were also due to the signal drifting during the MBD simulation. This can hence cause serious error in the predicted fatigue life, especially with the consideration of load sequence effect, since the large amplitude fluctuations seriously disrupted the cycle sequences in the strain loading histories.

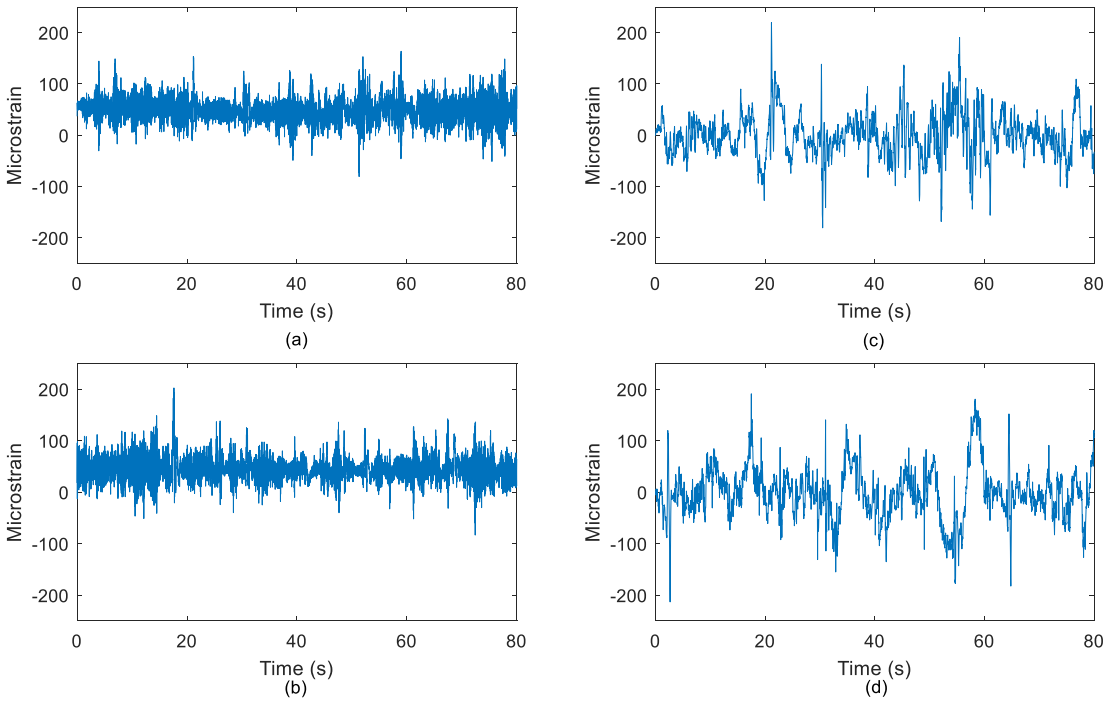

Figure 4.49 Comparison between simulated strain loading histories using Kong-Abdullah model with experimental strain signals under rural road condition: (a) Rural 1 experimental, (b) Rural 2 experimental, (c) Rural 1 simulated, (d) Rural 2 simulated

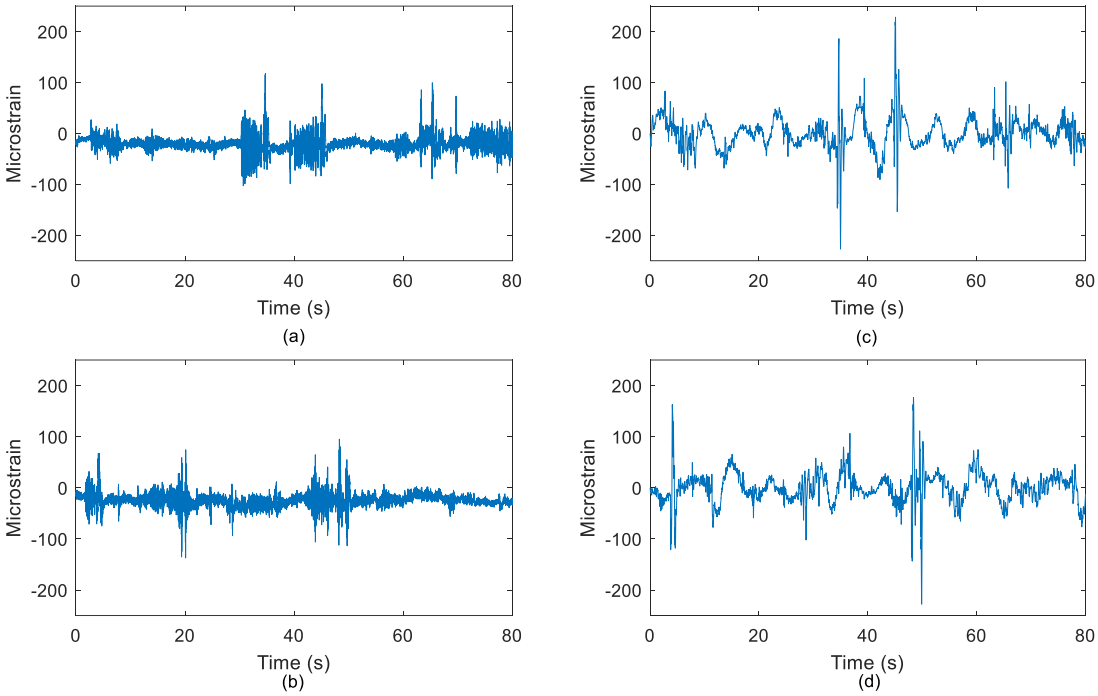

Figure 4.50 Comparison between simulated strain loading histories using Kong-Abdullah model with experimental strain signals under university campus road condition: (a) Campus 1 experimental, (b) Campus 2 experimental, (c) Campus 1 simulated, (d) Campus 2 simulated

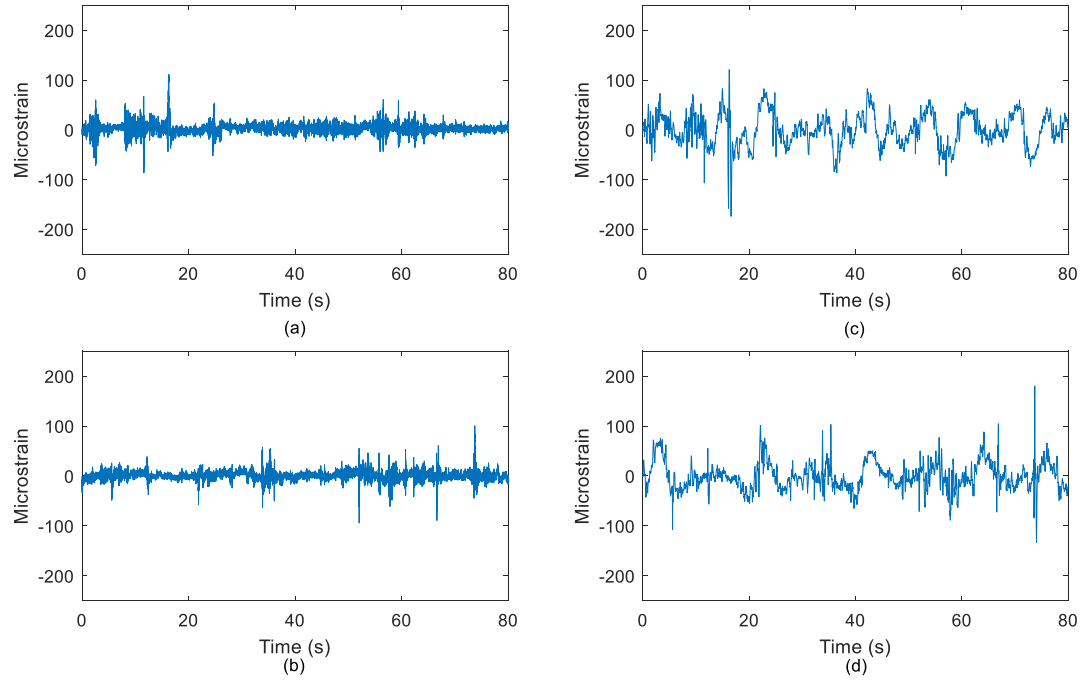

Figure 4.51 Comparison between simulated strain loading histories using Kong-Abdullah model with experimental strain signals under industrial road condition: (a) Industrial 1 experimental, (b) Industrial 2 experimental, (c) Industrial 1 simulated, (d) Industrial 2 simulated

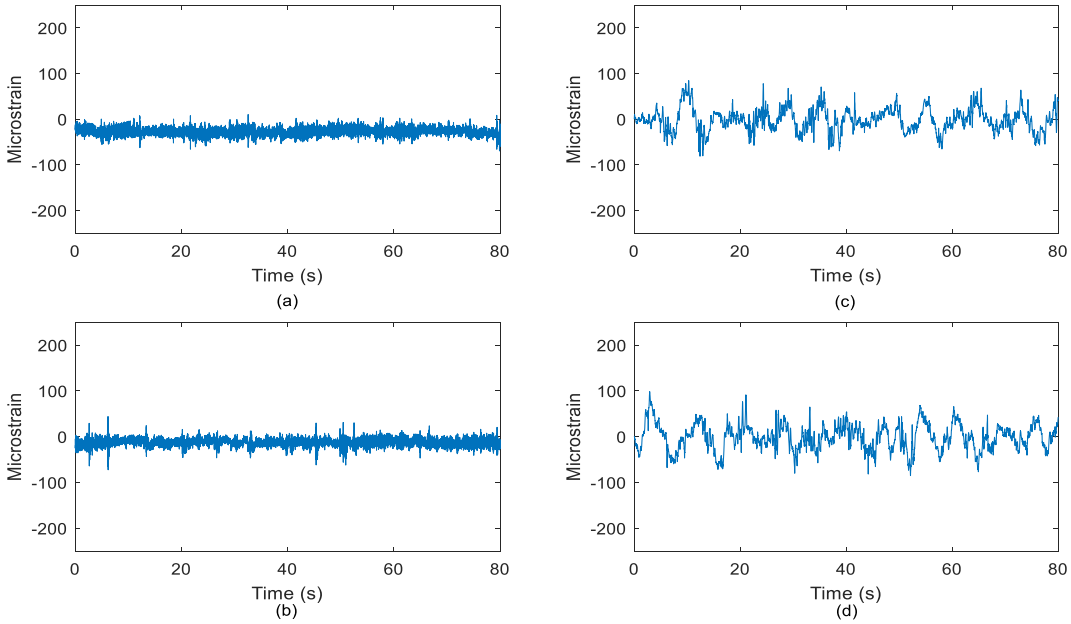

Figure 4.52 Comparison between simulated strain loading histories using Kong-Abdullah model with experimental strain signals under highway road condition: (a) Highway 1 experimental, (b) Highway 2 experimental, (c) Highway 1 simulated, (d) Highway 2 simulated

Fatigue lives of the simulated and experimental strain signals were predicted using four fatigue models including Coffin-Manson, Morrow, SWT, and ESD models. Tables 4.6-4.9 listed the predicted fatigue lives from the experimental and the corresponding simulated strain signals with Coffin-Manson, Morrow, SWT, and ESD models, respectively. The experimental strain signals acquired in rural area had the shortest fatigue lives between 10^3 and 10^4 blocks to failure. Meanwhile, the highway signals had the longest fatigue lives between 10^7 to 10^9 blocks to failure. The strain signals obtained from university campus and industrial area had intermediate fatigue lives in the range of 10^4–10^5 blocks to failure. It can be related to the occurrences of high amplitude events in the loading signals (Altamura & Straub 2014). Rural 1 and Rural 2 had the highest occurrences of high amplitude events as revealed by the rainflow cycle counting due to high surface roughness of the road. Hence, the fatigue lives of rural signals were the shortest among all the signals. In contrast, most of the fatigue cycles in Highway 1 and Highway 2 were low amplitude cycles which had very limited contribution to fatigue damage and thus resulted in the longest fatigue lives. The simulated strain signals had exhibited similar trend as the experimental strain signals, in which the shortest fatigue life was found in rural signal and the longest in highway signal. This indicated that the proposed model for acceleration-strain conversion could

generate realistic strain signals with similar fatigue behaviours as the experimental strain signals.

Table 4.6 Fatigue lives predicted from experimental and simulated strain using Coffin-Manson strain-life model

Road condition	Fatigue life (Blocks to failure)				
	Experimental strain	Simulated strain	Difference in log scale (%)	Strain obtained from Kong-Abdullah model	Difference in log scale (%)
Rural 1	3.10×10^4	3.75×10^4	1.8	1.10×10^4	10.0
Rural 2	6.07×10^3	3.40×10^4	19.8	1.05×10^4	6.3
Campus 1	1.11×10^5	3.47×10^4	10.0	1.12×10^4	19.7
Campus 2	8.57×10^4	5.49×10^4	3.9	1.89×10^4	13.3
Industrial 1	3.69×10^5	1.84×10^5	5.4	4.33×10^4	16.7
Industrial 2	4.59×10^5	1.72×10^5	7.5	4.65×10^4	17.6
Highway 1	3.58×10^9	1.07×10^9	5.5	1.30×10^6	36.0
Highway 2	7.83×10^7	8.29×10^7	0.3	4.60×10^5	28.3

Table 4.7 Fatigue lives predicted from experimental and simulated strain using Morrow strain-life model

Road condition	Fatigue life (Blocks to failure)				
	Experimental strain	Simulated strain	Difference in log scale (%)	Strain obtained from Kong-Abdullah model	Difference in log scale (%)
Rural 1	2.49×10^4	3.73×10^4	4.0	1.08×10^4	8.3
Rural 2	5.35×10^3	3.33×10^4	21.3	1.01×10^4	7.4
Campus 1	1.07×10^5	3.47×10^4	9.7	1.11×10^4	19.6
Campus 2	1.15×10^5	5.51×10^4	6.3	1.89×10^4	15.5
Industrial 1	3.22×10^5	2.00×10^5	3.8	4.49×10^4	15.5
Industrial 2	4.38×10^5	1.50×10^5	8.2	4.34×10^4	17.8
Highway 1	2.29×10^9	1.41×10^9	2.3	1.17×10^6	35.2
Highway 2	1.79×10^8	7.64×10^7	4.5	4.05×10^5	32.1

The fatigue life conservative analysis was also performed to determine the conservative of the predicted fatigue life from the simulated strain signals. Figure 4.53 shows the conservative between the predicted fatigue life from simulated and experimental strain signals. All the simulated strain signals were found to have good fatigue life correlation with the experimental strain signals within 1:2 and 2:1 correlation boundary. This confirmed that the simulated strain signals through the proposed model had similar fatigue properties with the experimental strain signals. Compared to the proposed model, the fatigue lives predicted from simulated strain signals using Kong-Abdullah model showed large differences for Highway 1 and

Highway 2. It was found that the Kong-Abdullah model provided non-conservative fatigue life predictions beyond 2:1 correlation boundary for Highway 1 and Highway 2. This was due to the large fluctuations in the simulated strain signals due to signal drifting, as shown in Figure 4.52. The large fluctuation in the signals contributed to load sequence effect that significantly changed the fatigue properties of the signals.

Table 4.8 Fatigue lives predicted from experimental and simulated strain using Smith-Watson-Topper strain-life model

Road condition	Fatigue life (Blocks to failure)				
	Experimental strain	Simulated strain	Difference in log scale (%)	Strain obtained from Kong-Abdullah model	Difference in log scale (%)
Rural 1	2.20×10^4	3.70×10^4	5.2	1.07×10^4	7.2
Rural 2	4.96×10^3	3.26×10^4	22.1	9.92×10^3	8.1
Campus 1	1.05×10^5	3.48×10^4	9.6	1.11×10^4	19.4
Campus 2	1.37×10^5	5.52×10^4	7.7	1.89×10^4	16.7
Industrial 1	3.00×10^5	2.11×10^5	2.8	4.67×10^4	14.7
Industrial 2	4.27×10^5	1.38×10^5	8.7	4.13×10^4	18.0
Highway 1	4.47×10^9	1.95×10^9	3.7	1.10×10^6	37.4
Highway 2	4.42×10^8	6.99×10^7	9.3	3.80×10^5	35.5

Table 4.9 Fatigue lives predicted from experimental and simulated strain using Effective-strain-damage model

Road condition	Fatigue life (Blocks to failure)				
	Experimental strain	Simulated strain	Difference in log scale (%)	Strain obtained from Kong-Abdullah model	Difference in log scale (%)
Rural 1	3.46×10^3	2.76×10^4	25.5	1.34×10^4	16.6
Rural 2	2.91×10^3	2.21×10^4	25.4	5.07×10^3	7.0
Campus 1	2.13×10^4	2.98×10^4	3.4	6.25×10^3	12.3
Campus 2	4.02×10^4	4.89×10^4	1.8	1.38×10^4	10.1
Industrial 1	5.78×10^4	1.61×10^5	9.3	2.73×10^4	6.8
Industrial 2	1.30×10^5	8.81×10^4	3.3	2.09×10^4	15.5
Highway 1	1.08×10^8	5.10×10^7	4.1	4.85×10^4	41.7
Highway 2	1.37×10^6	6.39×10^5	5.4	3.49×10^4	26.0

Figure 4.54 shows the differences of fatigue lives in logarithm scale of base 10 between the experimental and simulated data. It was found that the Kong-Abdullah model had comparable performance with the CASAS model in low and moderate fatigue cycle regimes between 10^3 and 10^6 blocks. In Rural 2 condition, the Kong-Abdullah model was found outperformed the CASAS model with lower fatigue life differences from the experimental results. This can be due to the high-pass filtering

process in CASAS model that inevitably reduced some amplitude of the simulated strain signals and thus caused a large reduction in the fatigue damage, especially in rural signals which contained many high amplitude cycles. However, in high fatigue cycle regime above 10^6 cycles, especially the Highway 1 signal simulated using the Kong-Abdullah model, a large difference of fatigue life between the simulated and experimental data as high as 41.7% was recorded. These findings were in agreement with previous study (Kong et al. 2019a) which remarked that the Kong-Abdullah model had limitations in simulating the strain signals in high fatigue cycle regime. It was noted that high-pass filtering was not applied in the simulated strain signals using the Kong-Abdullah model to remove the ultra-low frequencies. The effects of these amplitude fluctuations became more pronounced in high fatigue cycle signal above 10^6 cycles and thus resulted in a large deviation with experimental results.

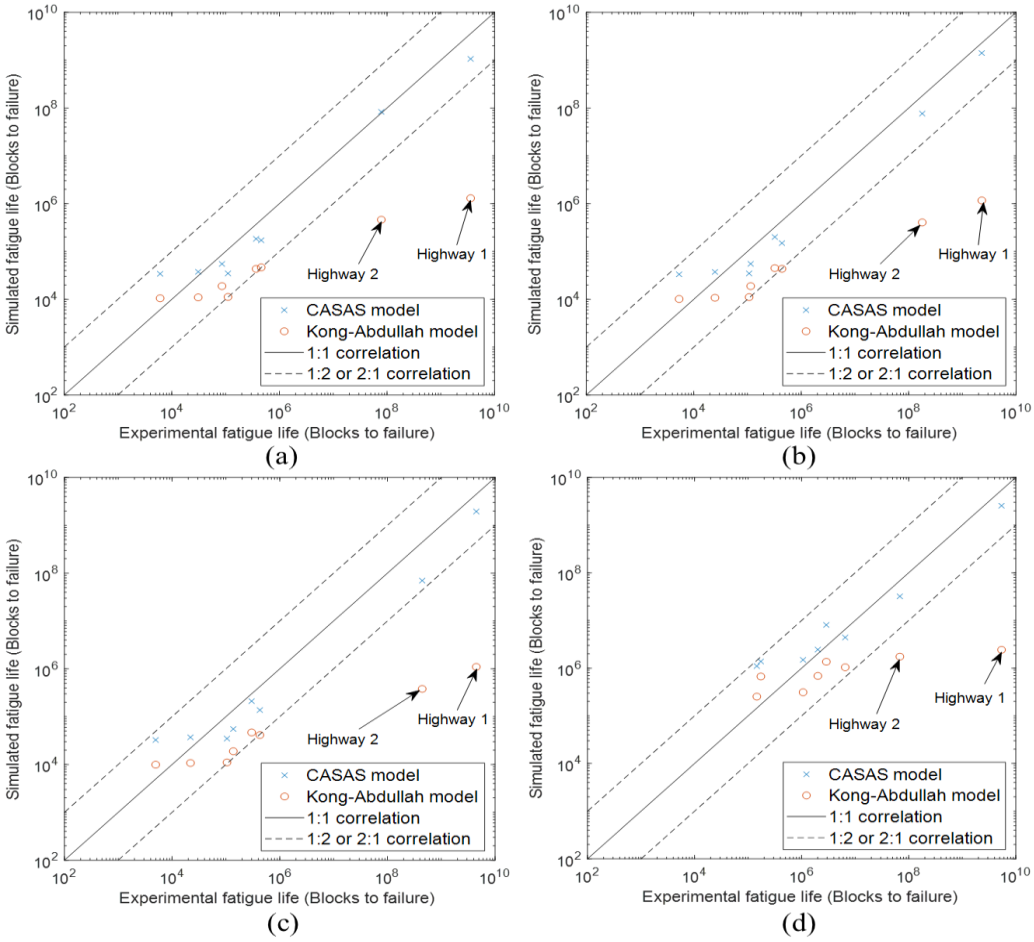

Figure 4.53 Fatigue life conservative analysis between simulated and experimental fatigue lives predicted with different fatigue models:
(a) Coffin-Manson, (b) Morrow, (c) SWT, (d) ESD models

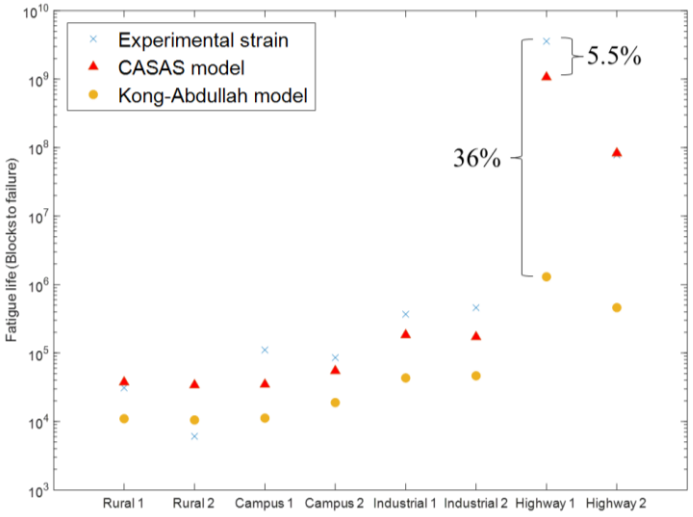

(a)

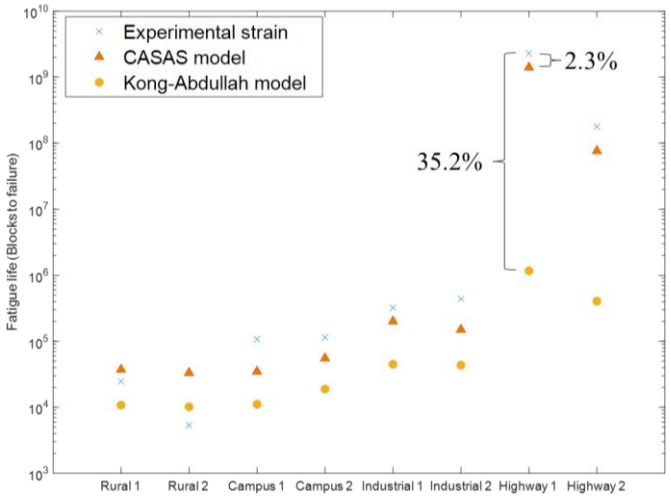

(b)

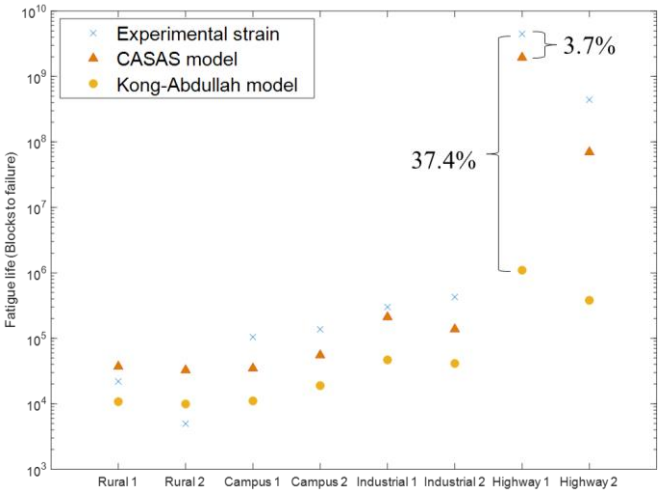

(c)

Continue…

…continued

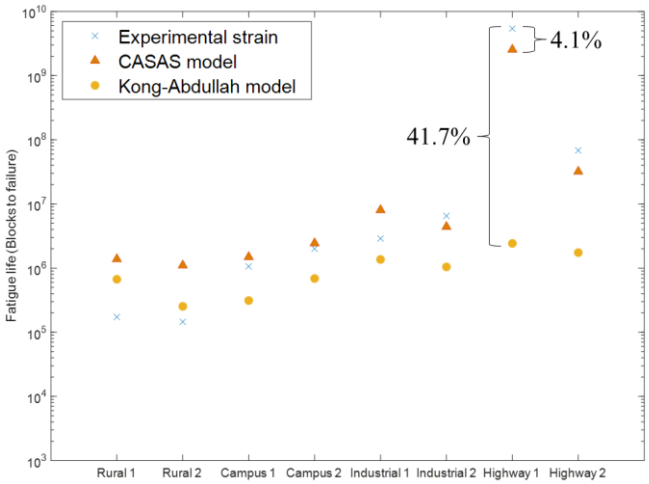

(d)

Figure 4.54 Differences between predicted fatigue lives from strain data simulated by CASAS and Kong-Abdullah models with different fatigue models: (a) Coffin-Manson, (b) Morrow, (c) SWT, (d) ESD models

Table 4.10 shows the root-mean-square-errors (RMSE) of the simulated fatigue data in logarithm scale predicted by the CASAS model and Kong-Abdullah model. For all fatigue life data based on different fatigue models, the CASAS model was found to have lower RMSE (0.42–0.52) compared to Kong-Abdullah model (1.39–1.80). These findings suggested that the CASAS model in this study provided better accuracy than Kong-Abdullah model in simulating strain data in a wide range of fatigue cycle regime. Therefore, the CASAS model was validated with accuracy in simulating strain data for suspension coil spring from various types of vibration data.

Table 4.10 Comparison of root-mean-square-errors of fatigue life data between the CASAS and Kong-Abdullah models

Fatigue model	**Root-mean-square-error (RMSE)**	
	CASAS Model	**Kong-Abdullah Model**
Coffin-Manson	0.42	1.60
Morrow	0.43	1.63
Smith-Watson-Topper	0.52	1.80
Effective-strain-damage	0.51	1.39

4.3 MACHINE LEARNING MODELLING FOR DURABILITY PREDICTION

In vibration fatigue analysis, the relevant signals had been treated as the loading histories of components to assess the structural integrity. These signals were not only

used in time-domain-based analyses, such as transient or impact analysis, but the frequency spectrums of vibration signals can also represent the loading conditions in vibration fatigue analysis. Various frequency-domain-based durability prediction models, such as Dirlik, Lalanne, Narrowband, and others, were introduced for fatigue life assessment based on vibration loading (Benasciutti & Tovo 2018; Mršnik, Slavič & Boltežar 2018). These models predict the fatigue life of components based on some statistical features determined from the loading spectrums, and it is necessary to determine the fatigue-related characteristics of the vibration signals.

4.3.1 Hölder Singularities for Low-Frequency Signal Energy

To characterise the local irregularity of the vibration signals, Hölder continuity condition was applied to determine the locations where the signals became discontinued or indifferentiable at higher order. The discontinued points in the signals, determined based on Hölder continuity, are known as Hölder singularities. In this study, the Hölder singularities with their corresponding local Hölder exponents (HEs) were identified using the WTMM method. The signals were first filtered using CWT and the WTMM in the time-scale domain was determined. The time position where the WTMMs converged at fine scale indicated the existence of singularities. In singularity analysis, the chosen wavelet function with suitable vanishing moment was very important to obtain the desired results. This study utilised the derivative of Gaussian (DOG) wavelet for singularity analysis given its well-defined vanishing moments corresponding to its order of derivative (Venkatakrishnan et al. 2014). Higher order of DOG wavelet had high vanishing moment number which can detect singularities with higher differentiation order and HEs.

To select the most appropriate wavelet function for singularity analysis, 2^{nd}, 4^{th}, and 6^{th} order DOG wavelet were used. This was because studies (Zhang et al. 2016; Zhou et al. 2020) recommended a wavelet function with the lowest possible vanishing moment to avoid redundant singularities that could not represent low frequency components. Figures 4.55–4.57 show the comparison of the reconstructed vibration signals from Hölder singularities obtained using the 2^{nd}, 4^{th}, and 6^{th} order DOG wavelet functions, respectively, with the original signal. It was found that the vibration signal

reconstructed using the 2nd order DOG wavelet had the highest similarity with the original signal. It had retained high amplitude events or cycles in the original signal, as shown in Figure 4.55. The preservation of high amplitude events is very important in durability analysis because these cycles contribute to a major portion of the fatigue damage. In Figures 4.56 and 4.57, some high amplitude cycles were found missing in the reconstructed signals. This indicated that the 4th and 6th order DOG wavelets were unable to capture singularities in high amplitude cycles. This was because the high amplitude cycles in vibration signals happened at low frequency range of 1–12 Hz, as confirmed through the CWT analysis. Hence, the 4th and 6th order DOG wavelets with high vanishing moment were not favourable to detect low frequency singularities (Zhou et al. 2020).

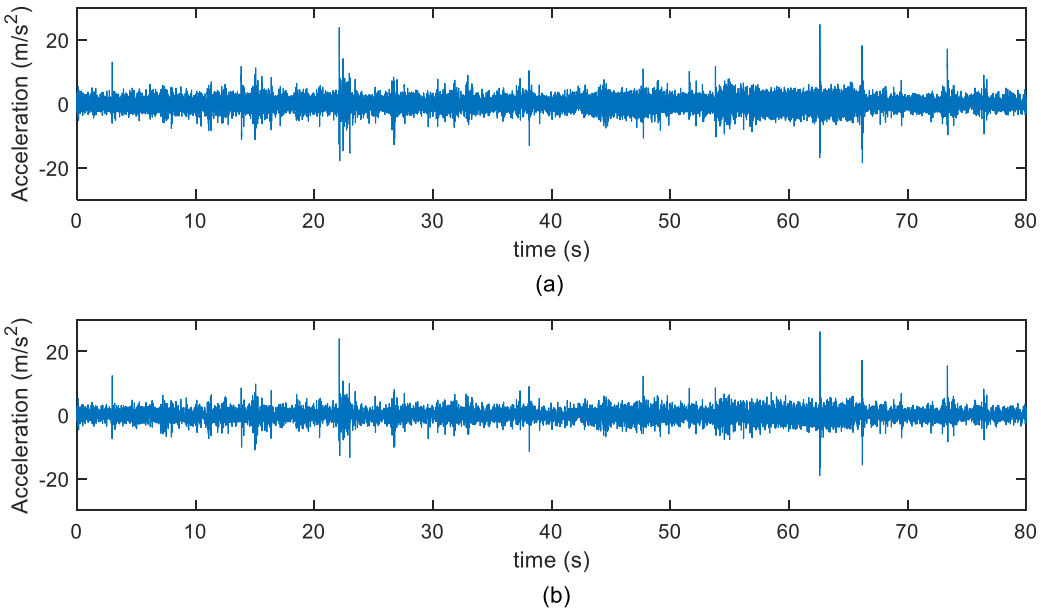

Figure 4.55 Reconstructed signals from the Hölder singularities obtained by 2nd order DOG wavelet: (a) original vibration signal, (b) reconstructed signal from the Hölder singularities

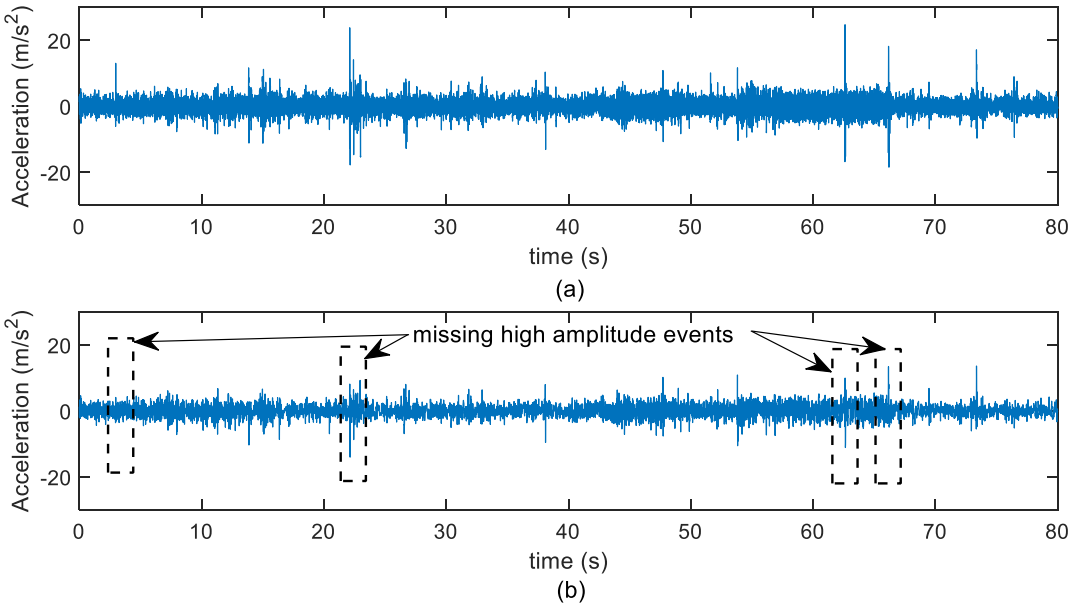

Figure 4.56 Reconstructed signals from the Hölder singularities obtained by 4th order DOG wavelet: (a) original vibration signal, (b) reconstructed signal from the Hölder singularities

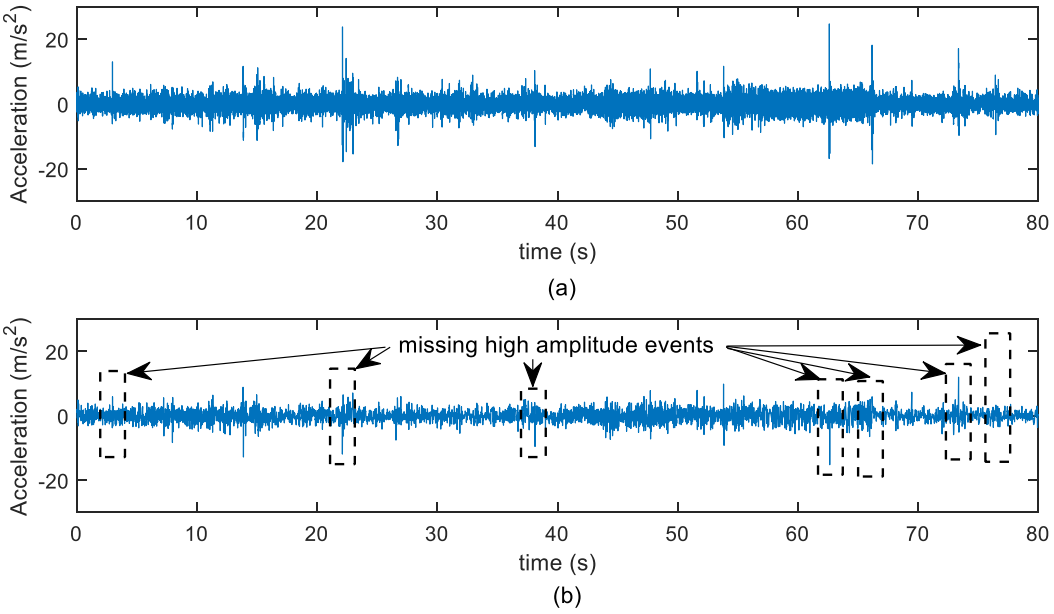

Figure 4.57 Reconstructed signals from the Hölder singularities obtained by 6th order DOG wavelet: (a) original vibration signal, (b) reconstructed signal from the Hölder singularities

The statistical parameters, including RMS and kurtosis, were computed to determine the preservation of the original signal behaviour in each reconstructed signal, as shown in Table 4.11. Figure 4.58 shows the percentage of difference in RMS and

kurtosis values between the reconstructed and original vibration signals. Low deviations of statistical properties (2.1–8.7%) in reconstructed signal using 2nd order DOG wavelet compared to other higher order DOG wavelets were found. This proved that the statistical behaviours of the original signal had been well preserved in the reconstructed signal using 2nd order DOG wavelet. Large differences in statistical behaviours of reconstructed vibration signals using 4th and 6th order DOG wavelets were mainly because of the missing high amplitude events due to the higher vanishing moments of wavelet functions.

Table 4.11 Differences in RMS and kurtosis of the reconstructed signals using 2nd, 4th and 6th order DOG wavelets

Statistical parameter	Original signal	2nd order	Difference (%)	4th order	Difference (%)	6th order	Difference (%)
RMS (με)	2.04	1.99	2.1	1.78	12.8	1.71	16.2
Kurtosis	9.67	10.50	8.7	5.79	40.1	5.83	39.7

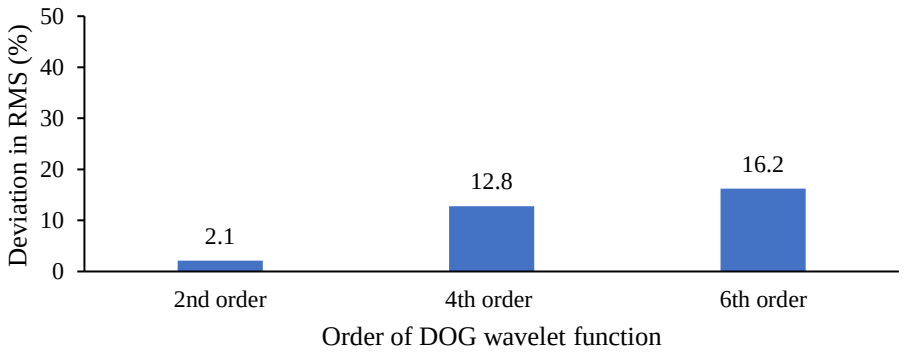

(a)

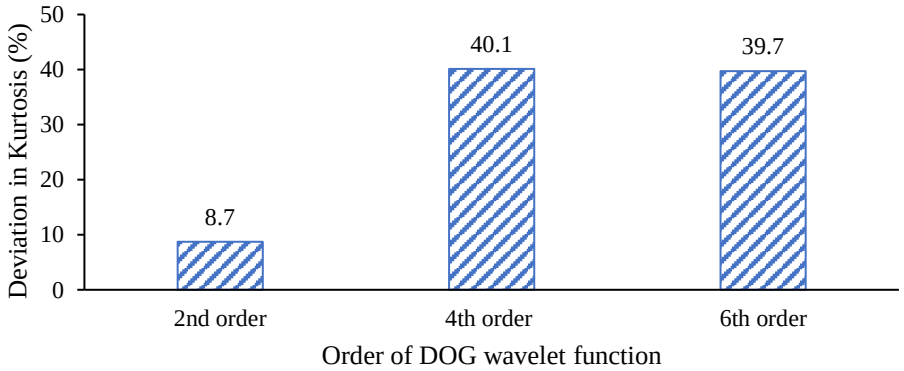

(b)

Figure 4.58 Deviations of (a) RMS and (b) kurtosis of reconstructed signal using different order of DOG wavelet functions

Figures 4.59–4.66 show the Hölder singularities with their corresponding local HEs computed from the vibration signals obtained under various road conditions. Through singularity analysis using the 2nd order DOG wavelet function, singularities in the vibration signals with HEs below two had been identified. The number of vanishing moment of the used wavelet function determined the upper bound of the HE value being identified (Régis, Doncescu & Desachy 2008). Using the 2nd order DOG wavelet with two vanishing moments, all the singularities in the vibration signals with HEs below two could be determined. The use of a wavelet function with higher vanishing moment cannot provide significant information required but can cause additional number of maxima lines and problems to the numerical estimation of the HEs (Zhang et al. 2016). It aligned with the significant deviations in statistical behaviours of the reconstructed signals using 4th and 6th order DOG wavelets, as presented in Table 4.11.

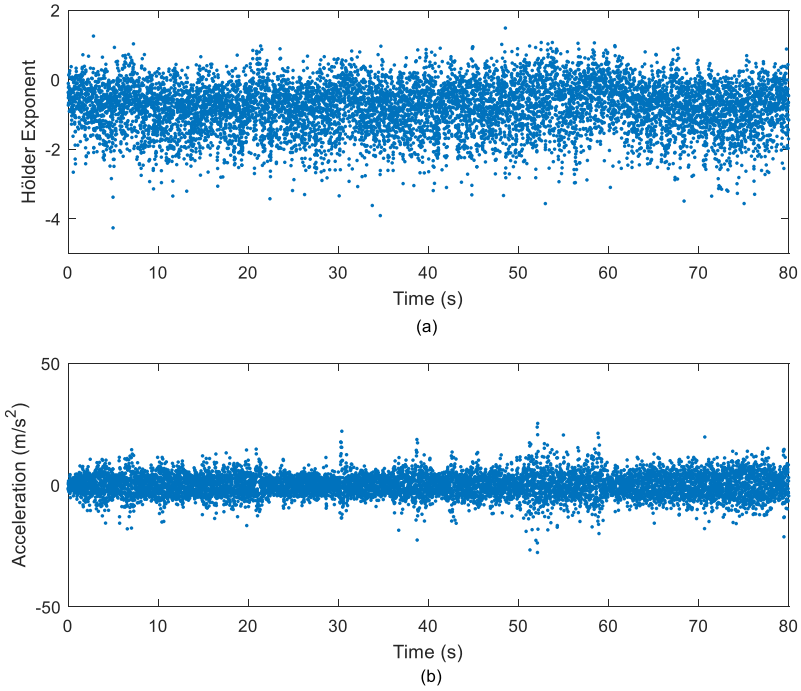

Figure 4.59 Singularity analysis using Hölder continuity condition on Rural 1: (a) Hölder exponents, (b) location of Hölder singularities

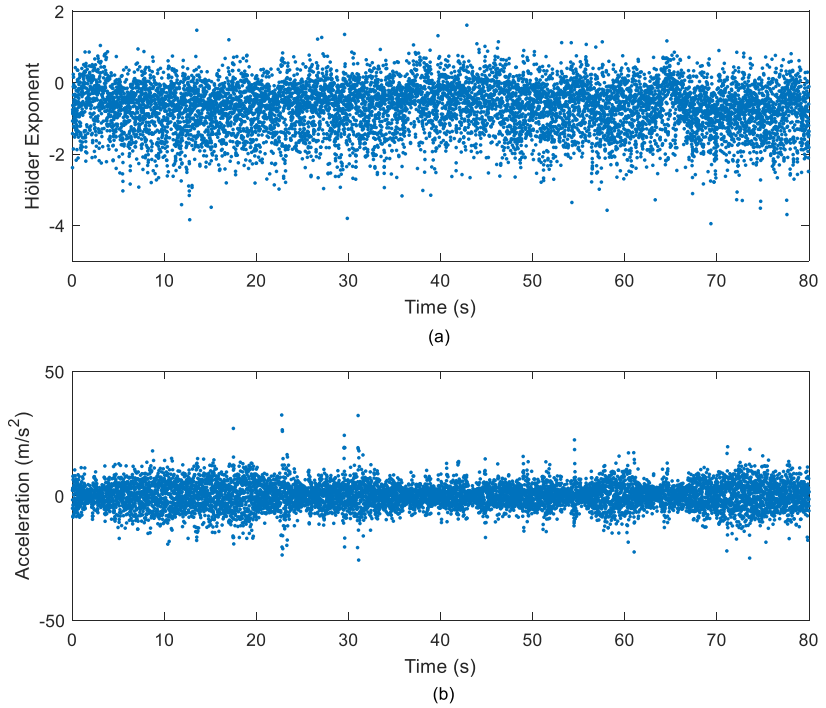

Figure 4.60 Singularity analysis using Hölder continuity condition on Rural 2: (a) Hölder exponents, (b) location of Hölder singularities

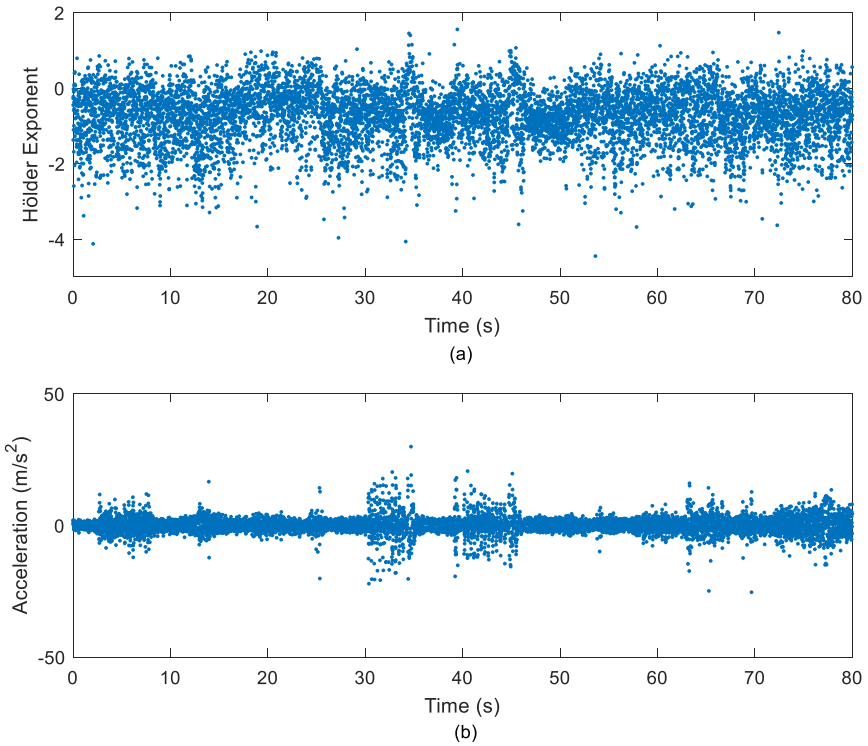

Figure 4.61 Singularity analysis using Hölder continuity condition on Campus 1: (a) Hölder exponents, (b) location of Hölder singularities

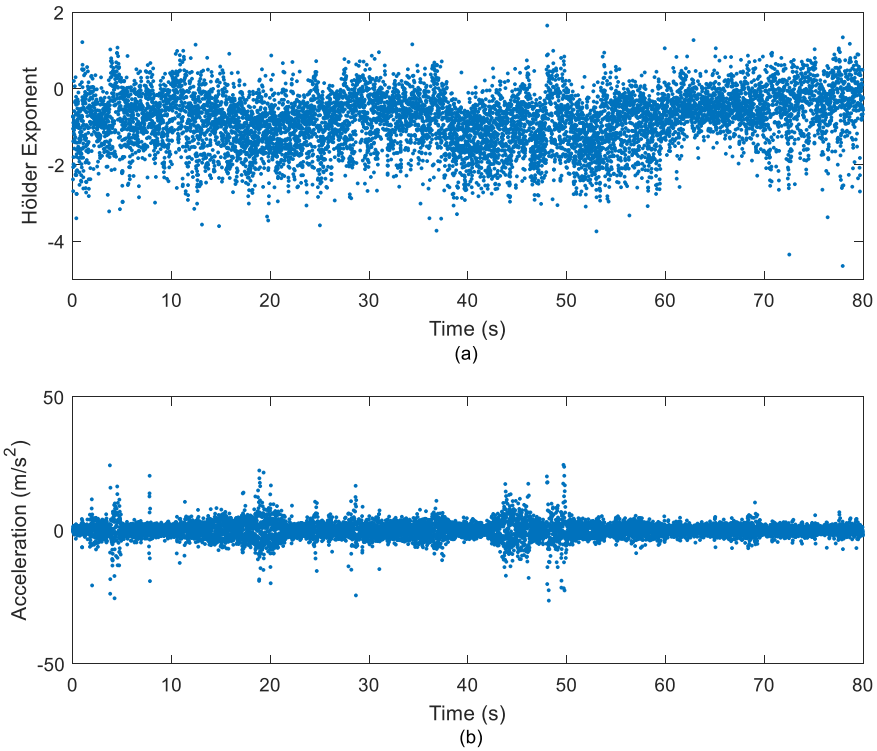

Figure 4.62 Singularity analysis using Hölder continuity condition on Campus 2: (a) Hölder exponents, (b) location of Hölder singularities

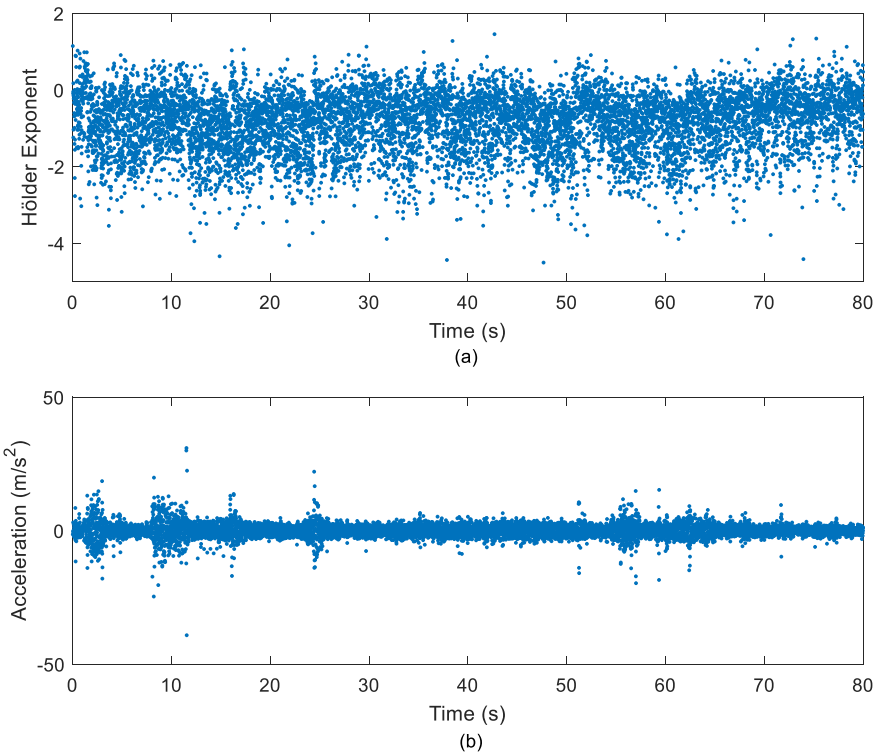

Figure 4.63 Singularity analysis using Hölder continuity condition on Industrial 1: (a) Hölder exponents, (b) location of Hölder singularities

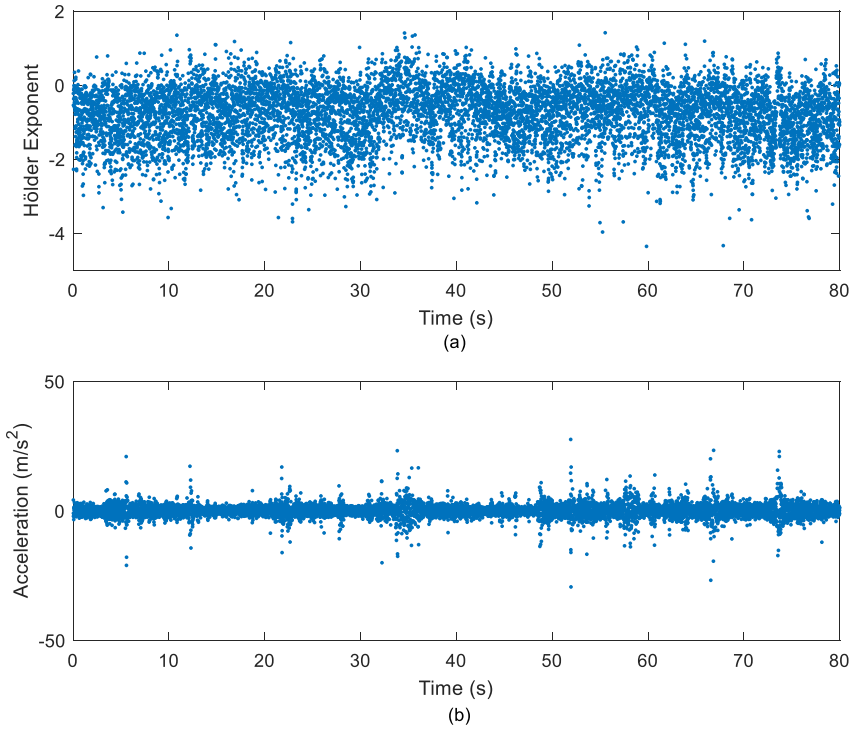

Figure 4.64 Singularity analysis using Hölder continuity condition on Industrial 2: (a) Hölder exponents, (b) location of Hölder singularities

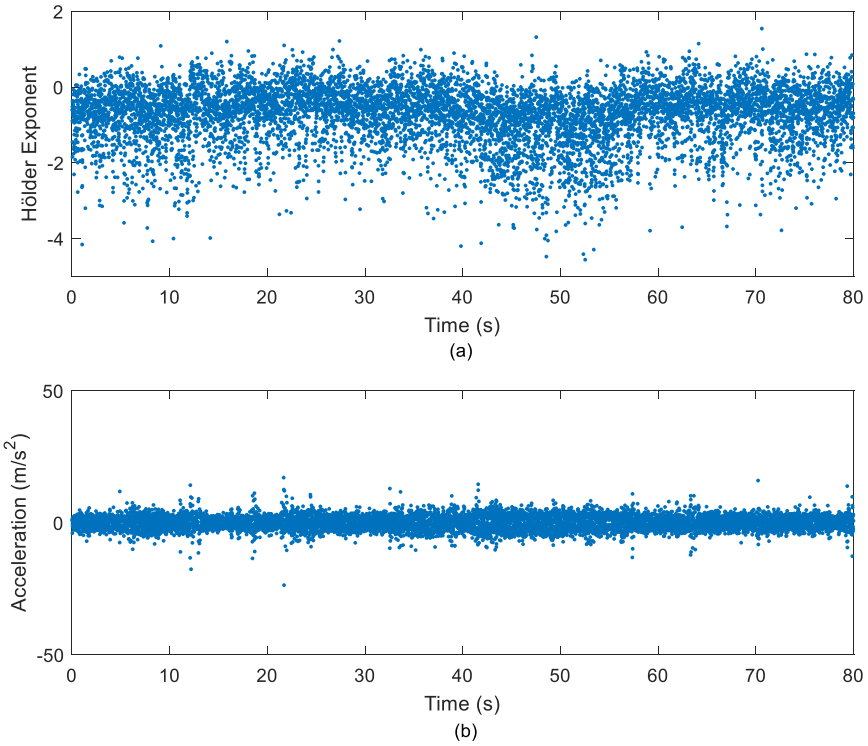

Figure 4.65 Singularity analysis using Hölder continuity condition on Highway 1: (a) Hölder exponents, (b) location of Hölder singularities

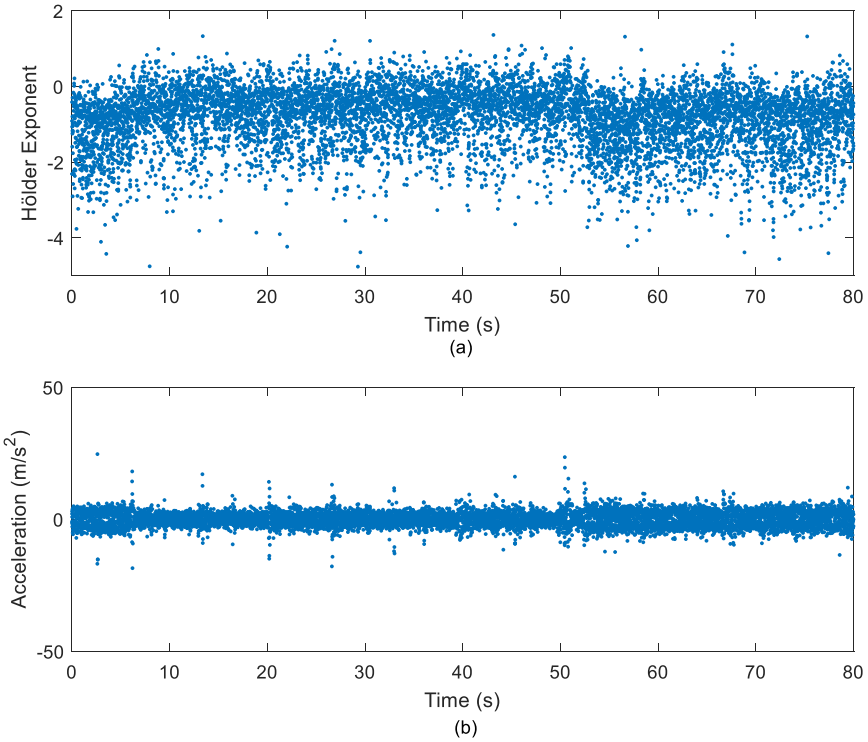

Figure 4.66 Singularity analysis using Hölder continuity condition on Highway 2: (a) Hölder exponents, (b) location of Hölder singularities

The local HE describes the pointwise regularity of signal as well as to denote the differentiability of a signal. Larger HE values indicate that the signal is differentiable to a higher order. A signal is indifferentiable at a certain point with HE being less than one, while HE below zero shows that there is a discontinuity in the function at the point. Otherwise, points with HE values larger than one will then be regarded as differentiable points. The HE is closely related to the local smoothness or ruggedness of a signal, where high HE values are found in smooth profile of time signal (Bianchi & Pianese 2018). Zhou et al. (2020) remarked that singularities with high HEs often appeared as high frequency components in vibration signals and HEs below two were appropriate to identify the low frequency feature in a vibration signal. Since high amplitude cycles in road excitations usually occur at low frequency range below 50 Hz (Kong et al. 2017), the singularities with HEs below two could represent the high amplitude events in the vibration signals that brought high fatigue damage to the component.

Figures 4.67–4.70 illustrate the reconstructed vibration signals with zero-mean properties based on the Hölder singularities using linear interpolation method. It was found that the reconstructed signals highly matched the original signals, as shown in Figures 4.7–4.10. Important features, such as high amplitude cycles in the original signals, were well preserved. This was particularly important in durability analysis because the fatigue properties of the loading signals were closely related to these high amplitude cycles (Marsh et al. 2016; Mršnik, Slavič & Boltežar 2018). Furthermore, the statistical properties of the reconstructed signals were determined and compared to the original signals, as listed in Table 4.12. Figures 4.71–4.73 show the percentage of difference in RMS, skewness, and kurtosis between the reconstructed and original vibration signals obtained under various road conditions, respectively.

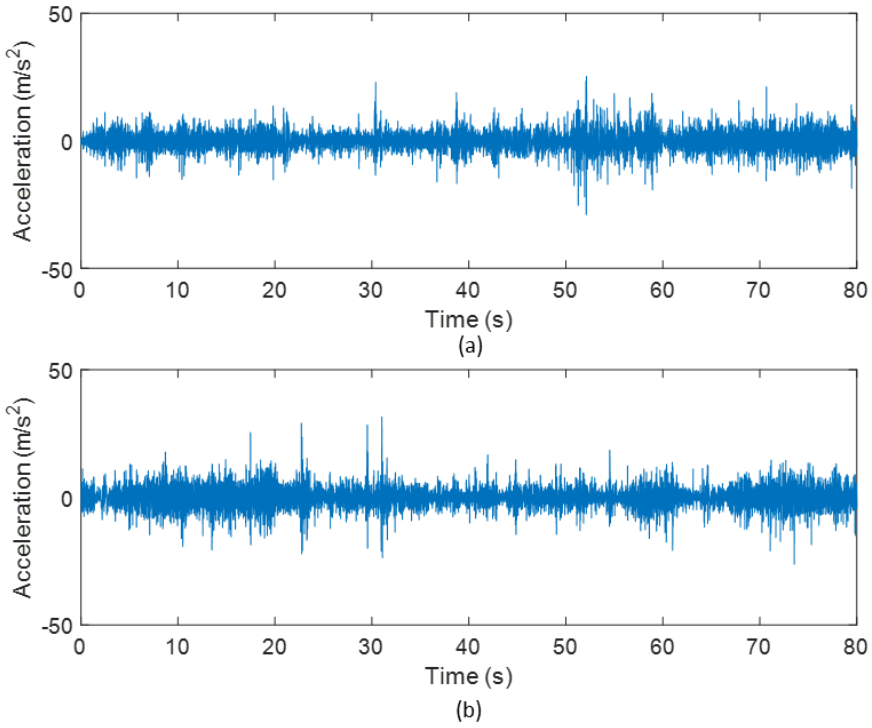

Figure 4.67 Reconstructed signals based on Hölder singularities: (a) Rural 1, (b) Rural 2

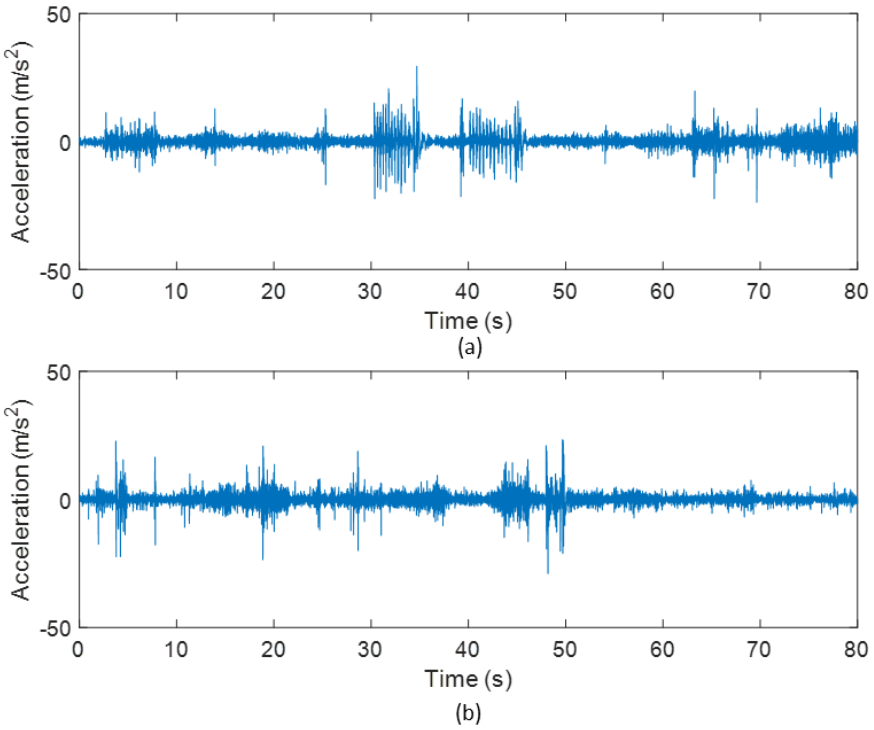

Figure 4.68 Reconstructed signals based on Hölder singularities: (a) Campus 1, (b) Campus 2

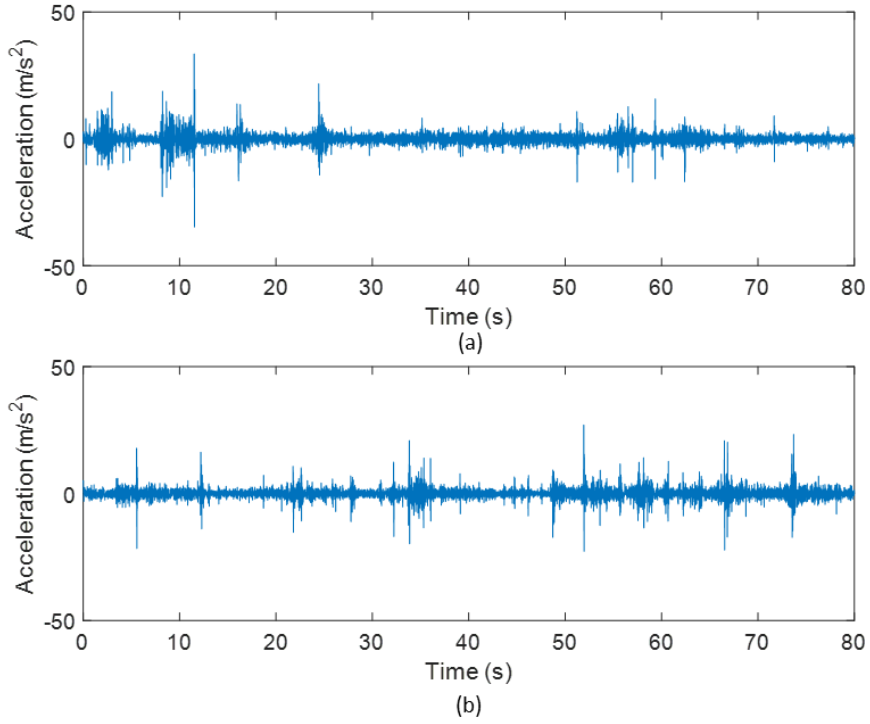

Figure 4.69 Reconstructed signals based on Hölder singularities: (a) Industrial 1, (b) Industrial 2

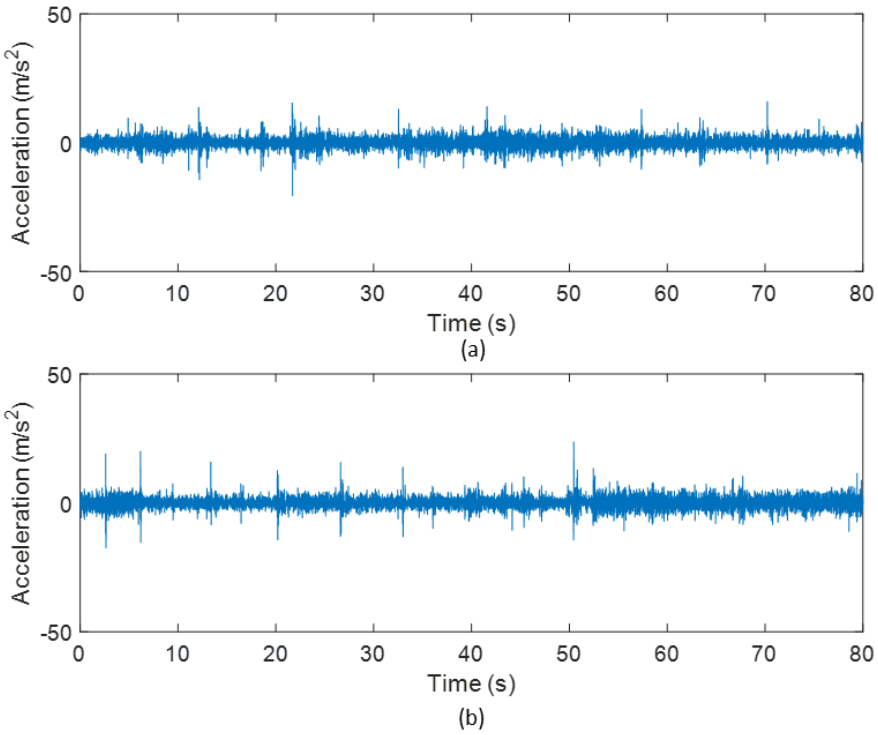

Figure 4.70 Reconstructed signals based on Hölder singularities: (a) Highway 1, (b) Highway 2

Table 4.12 Differences in statistical parameters of the reconstructed signals based on Hölder singularities

Road condition	RMS (με)		Skewness		Kurtosis	
	Value	Difference (%)	Value	Difference (%)	Value	Difference (%)
Rural 1	3.64	3.4	-0.02	5.0	5.80	0.7
Rural 2	4.00	3.0	-0.01	0.0	5.45	2.5
Campus 1	2.60	3.8	-0.07	2.7	14.01	0.9
Campus 2	2.50	4.5	-0.20	17.6	19.14	4.4
Industrial 1	2.19	2.4	-0.36	15.4	29.00	5.9
Industrial 2	2.22	2.5	0.05	1.4	20.87	2.1
Highway 1	2.13	1.0	-0.22	10.2	8.01	1.0
Highway 2	2.24	0.9	0.12	11.4	7.96	7.8

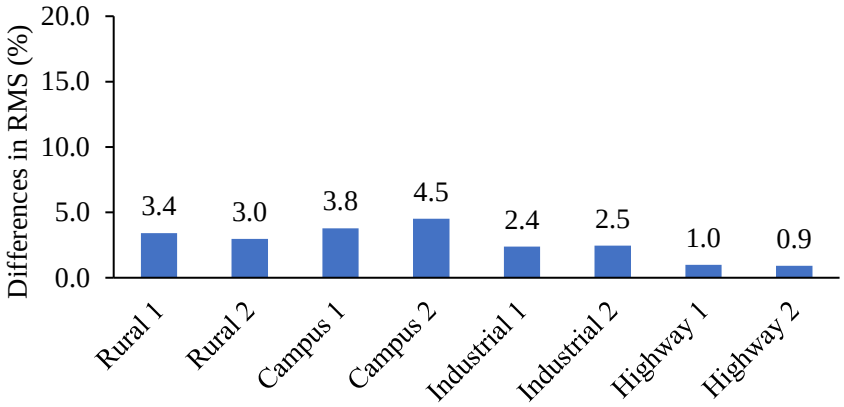

Figure 4.71 Differences in RMS of reconstructed signals under various road conditions

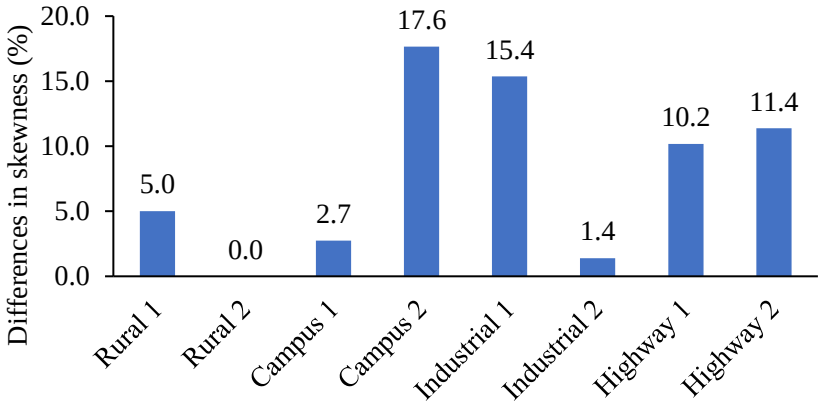

Figure 4.72 Differences in skewness of reconstructed signals under various road conditions

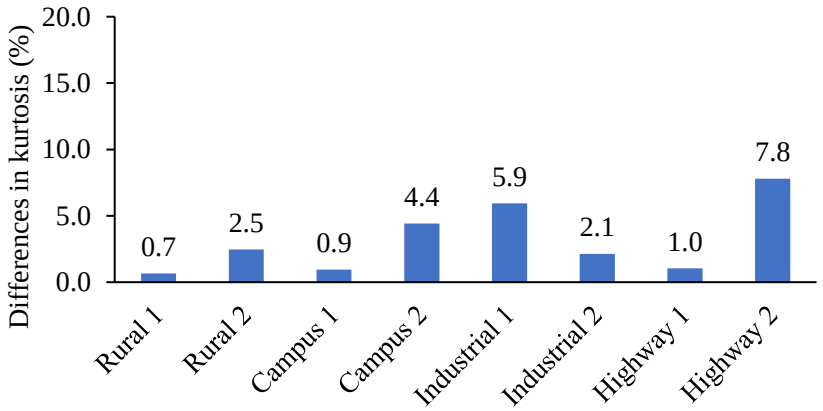

Figure 4.73 Differences in kurtosis of reconstructed signals under various road conditions

Figure 4.71 shows that the reconstructed signals had the largest deviation in RMS of 4.5% in Campus 2 signal while the lowest RMS difference of 0.9% was recorded in Highway 2. The low deviations in RMS strongly suggested that high amplitude cycles had been preserved in the reconstructed signals since the RMS was an amplitude-related statistical parameter (Gu et al. 2012). For skewness properties, the highest difference was 17.6%, also found in Campus 2. This can be due to the elimination of many non-singular data points that eventually disturbed the symmetry of the data distribution. Nonetheless, the difference in the skewness property was acceptable as it was below 20%. The differences in kurtosis values of the reconstructed signals were found below 10% and the highest difference of 7.8% was recorded in Highway 2 signal. This was due to the elimination of non-singular points in the signals that had resulted in the increase of peak sharpness of the data distribution. Given the low deviations of the statistical parameters, it can be confirmed that the reconstructed signals had similar properties with the original vibration signals. The singularity analysis can effectively identify high amplitude features in the vibration signals without compromising the loss of information in the original signals.

The main purpose of determining the Hölder singularities of the vibration signals is to eliminate the high frequency noises that do not contribute to fatigue damage. This is essential to ensure the accurate results of signal energy characterisation because the high frequency noises could contribute to high energy amount, regardless of their minimal fatigue damage contribution (Putra et al. 2017b). Figures 4.74 to 4.77 depict the comparison of the PSDs between the reconstructed and original vibration signals obtained under different road conditions. The signal energy was characterised from the PSDs, as listed in Table 4.13. The loading signals obtained from rural area road were found to have the highest PSD amplitude and the highest signal energy of 13.36–16.95 $\mu\varepsilon^2$. This was mainly attributed to the large amplitude range of rural signals due to the rough road surface profile. Meanwhile, the lowest signal energy of 4.42–5.00 $\mu\varepsilon^2$ was recorded in highway signals since the highway road had smooth surface.

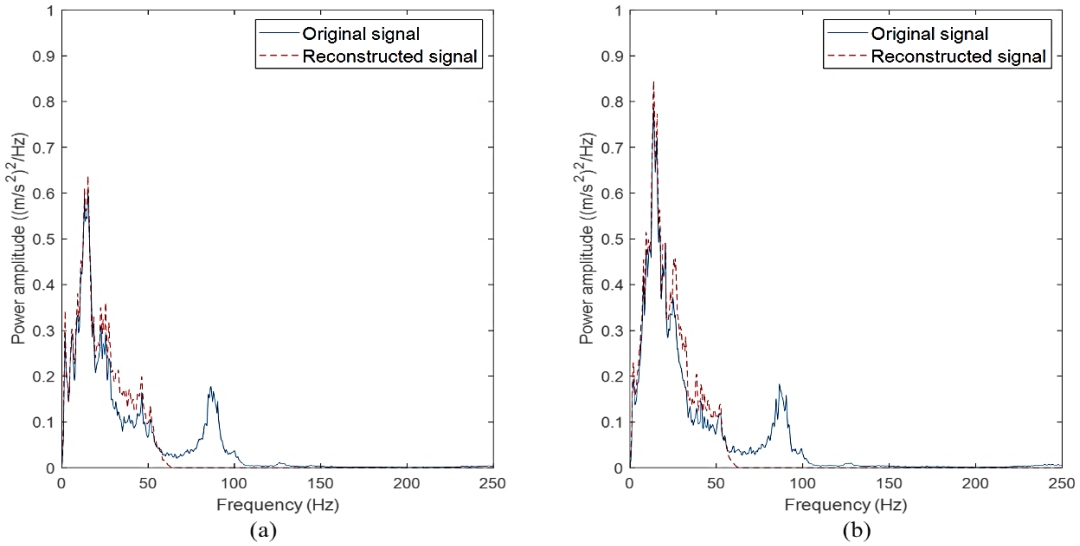

Figure 4.74 PSD of the original and reconstructed signals from road conditions: (a) Rural 1, (b) Rural 2

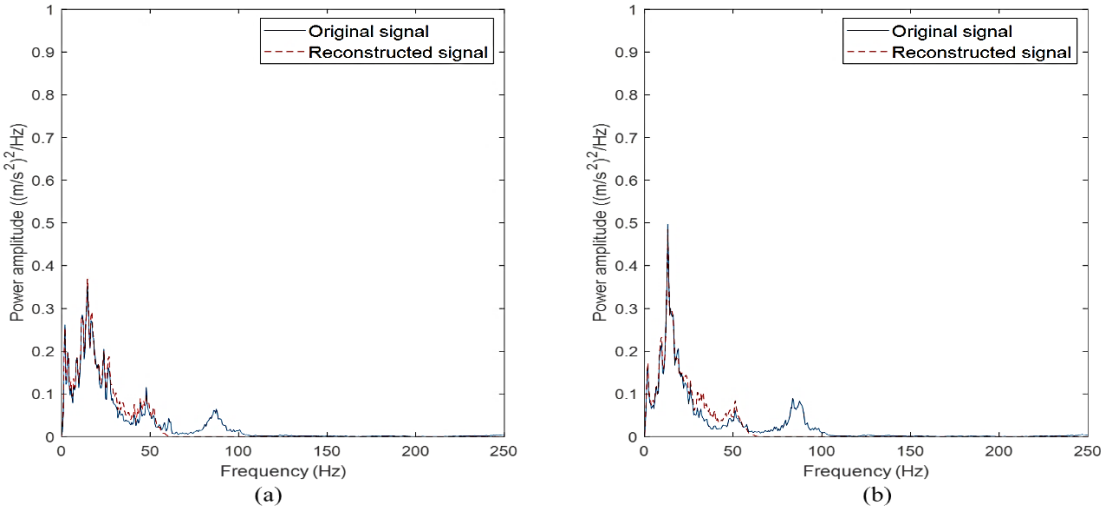

Figure 4.75 PSD of the original and reconstructed signals from road conditions: (a) Campus 1, (b) Campus 2

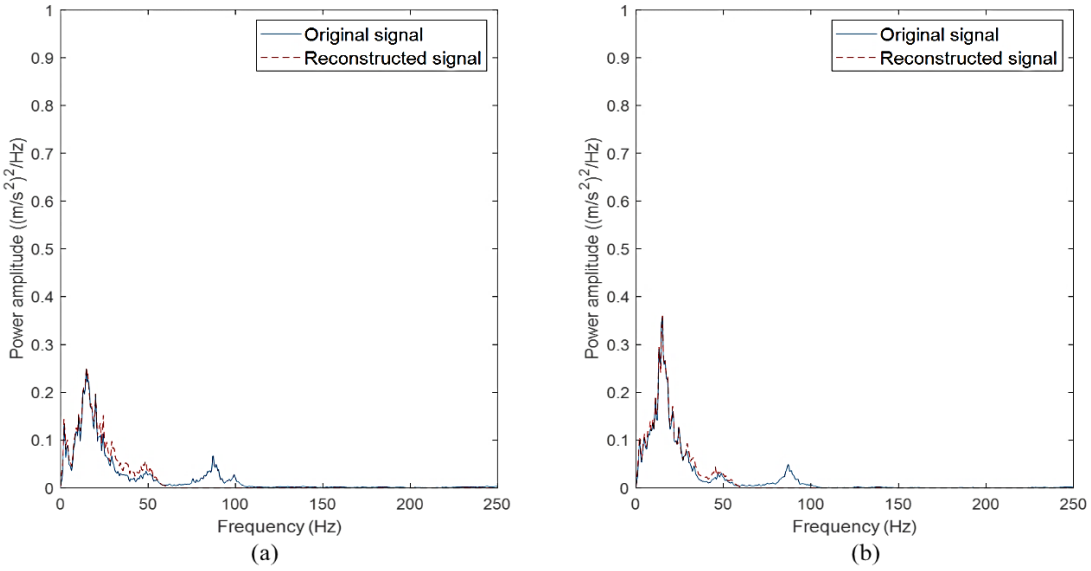

Figure 4.76 PSD of the original and reconstructed signals from road conditions: (a) Industrial 1, (b) Industrial 2

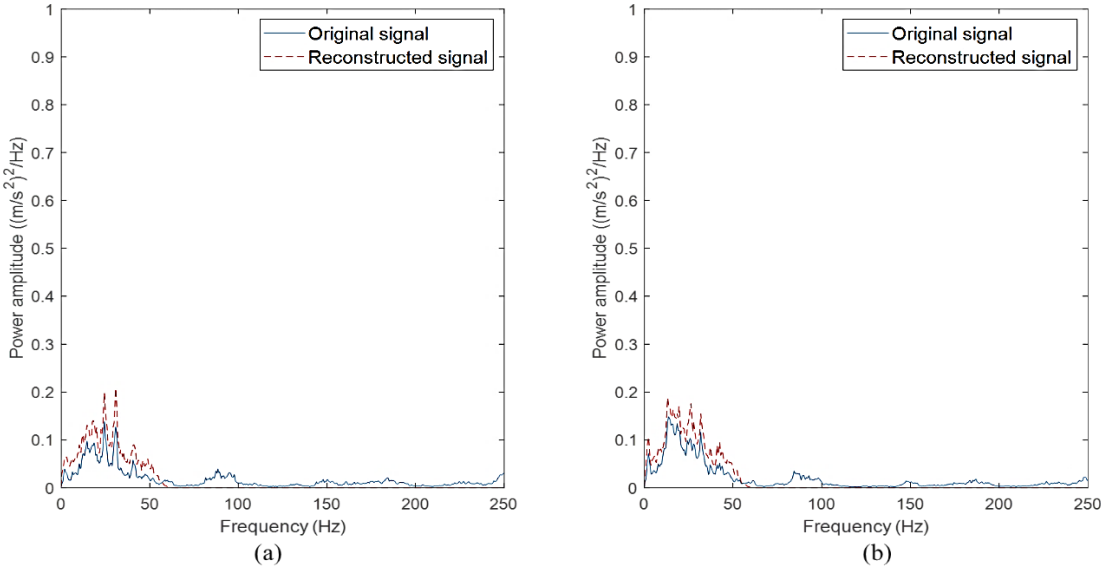

Figure 4.77 PSD of the original and reconstructed signals from road conditions: (a) Highway 1, (b) Highway 2

Table 4.13 Differences in PSD energy of the reconstructed signals based on Hölder singularities

Road condition	PSD energy $(m/s^2)^2$		Percentage of differences (%)
	Original signal	Reconstructed signal	
Rural 1	14.36	13.36	7.0
Rural 2	16.95	16.00	5.6
Campus 1	7.35	6.79	7.7
Campus 2	6.95	6.31	9.2
Industrial 1	5.02	4.78	4.7
Industrial 2	5.25	4.98	5.3
Highway 1	4.42	4.47	0.9
Highway 2	4.95	5.00	1.1

From the PSDs, the original vibration signals showed high peaks at frequency between 10 and 20 Hz. This finding agrees with Kong et al. (2018a) which had reported high peaks at frequency between 0 and 20 Hz in the PSDs of loading signals obtained from vehicle suspension system. This was due to the road excitations categorised as low frequency loading that occurred between 0.5 and 12 Hz (Minaker & Yao 2017). Furthermore, the signals also had other peaks at high frequency between 70 and 90 Hz. The highway signals also exhibited more high frequencies above 100 Hz, albeit with low amplitudes. These are high frequency noises resulting from the low amplitude cycles that contributed to very limited fatigue damage. The engine vibrations or instrument noises can be the main reasons for the occurrence of high frequencies and hence noise reduction was necessary to ensure accuracy in the energy analysis (Bi, Ma & Wang 2019). By extracting Hölder singularities with HE values below two, it was found that the high frequency noises above 50 Hz had been effectively removed. The PSDs of the reconstructed signals only exhibited the frequency peaks between 0 and 50 Hz of the original signals. This proved that the Hölder singularities with HEs below two could represent the low-frequency features of the vibration signals that had contributed to significant fatigue damage. Since the singularity method effectively reduced the high frequency noises in vibration loading signals, it was necessary to be applied before the signal energy characterisation from PSDs to ensure the accuracy of results.

Figure 4.78 shows the difference in PSD energy between the reconstructed and original signals. The reconstructed signals had differences in PSD energy of below 10%. The highest PSD energy difference of 9.2% was found in Campus 2 signal. The 9.2%

energy difference was due to the elimination of high frequency energy. The findings confirmed that majority of the signal energy in the vibration signals came from the low-frequency cycles with frequency range below 50 Hz. Previous studies (Kong et al. 2017; Kowalski et al. 2001) also agreed that loadings due to road excitations happened at low frequency range between 0 and 50 Hz. Therefore, it can be suggested that the reconstructed signal using Hölder singularities had retained the low-frequency energy in the vibration signals and were appropriate to be used for durability predictions.

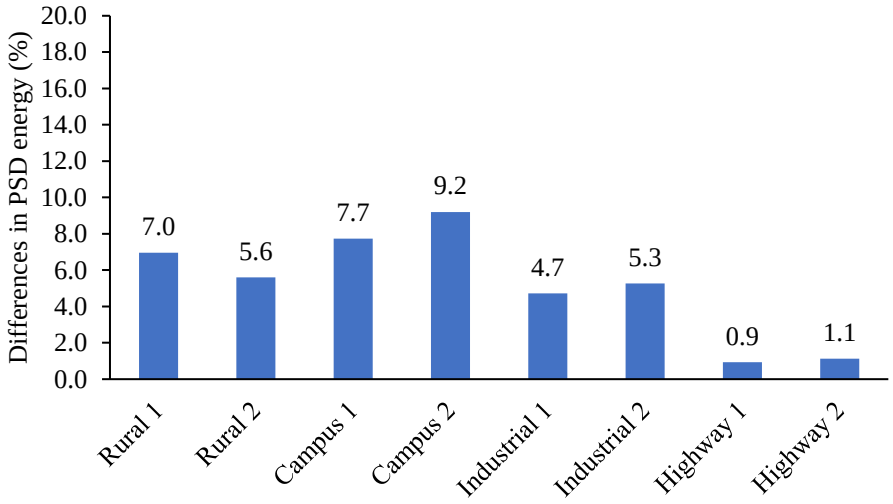

Figure 4.78 Differences in PSD energy of reconstructed signals under various road conditions

4.3.2 Multifractal Characterisation of Vibration Signals

Multifractal analysis was performed to investigate the multifractal properties of the vibration signals due to road excitations. Multiple numerical methods are available for multifractal analysis, including WTMM, MFDFA, and wavelet leaders (WL). In this study, the WL method was applied given its less computational cost and suitability for non-stationary signals (Du et al. 2014; Pnevmatikos et al. 2020). The WL method is a Discrete Wavelet Transform (DWT)-based method in which DWT was performed to obtain the wavelet coefficients. Compared to CWT which provided detailed information in a continuous manner, DWT had scales in the factor of two and thus provided only important information which took less computational effort. Figures 4.79–4.82 show the time-scale wavelet coefficient mapping of vibration signals under different road conditions obtained through DWT. The Daubechies 2 (*db2*) wavelet with two vanishing

moments was applied as this wavelet function was appropriate to be used for multifractal analysis of non-stationary time series (Du et al. 2014; Zhou et al. 2020). From the results, DWT had revealed high magnitude sections of the vibration signals at high scale (low frequency). This confirmed that the DWT was effective in determining the scaling properties of the vibration signals.

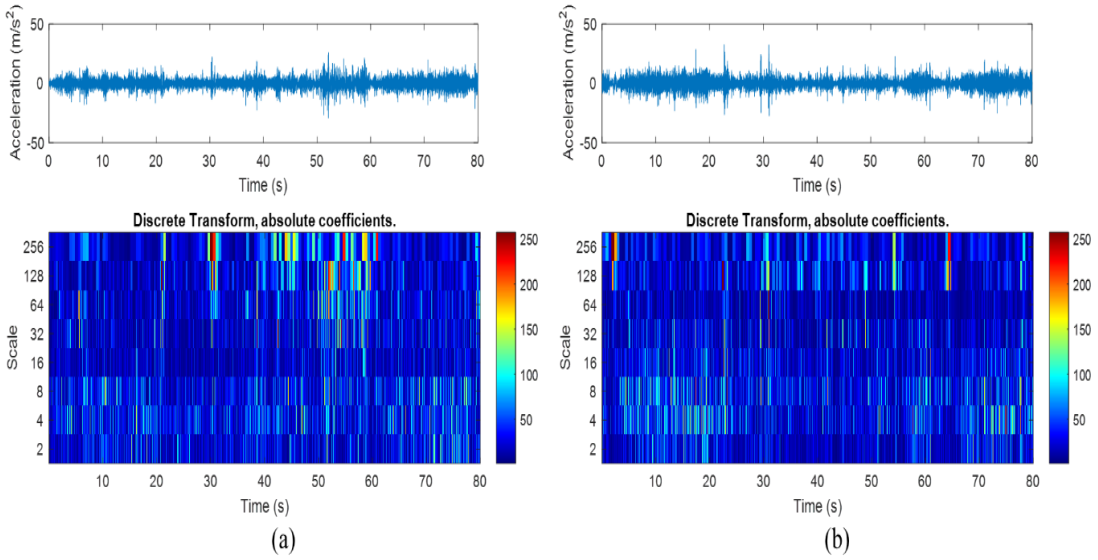

Figure 4.79 DWT analysis of vibration signals obtained from rural road conditions: (a) Rural 1, (b) Rural 2

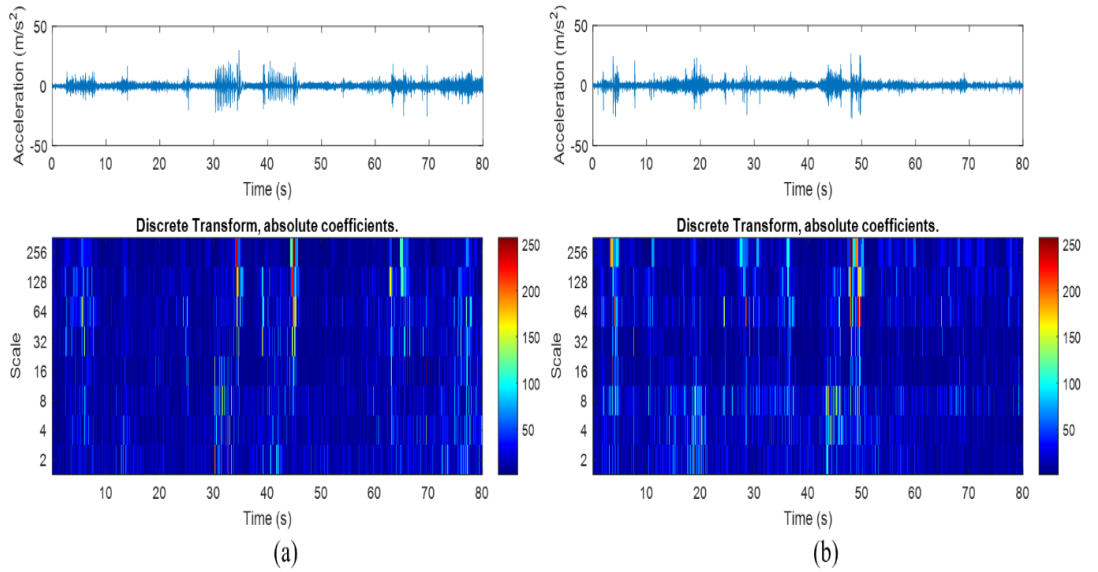

Figure 4.82 DWT analysis of vibration signals obtained from university campus road conditions: (a) Campus 1, (b) Campus 2

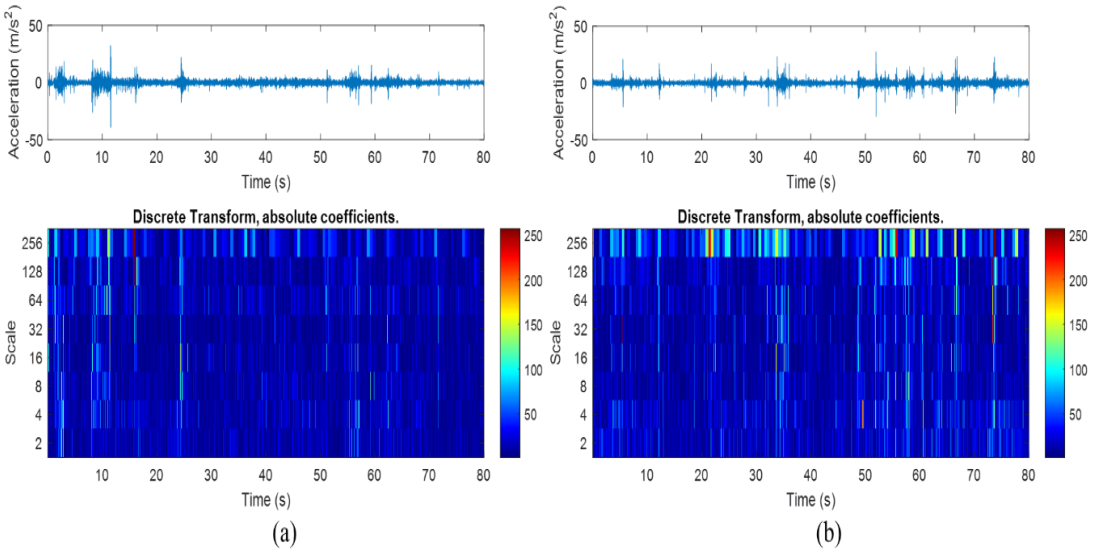

Figure 4.81 DWT analysis of vibration signals obtained from industrial road conditions: (a) Industrial 1, (b) Industrial 2

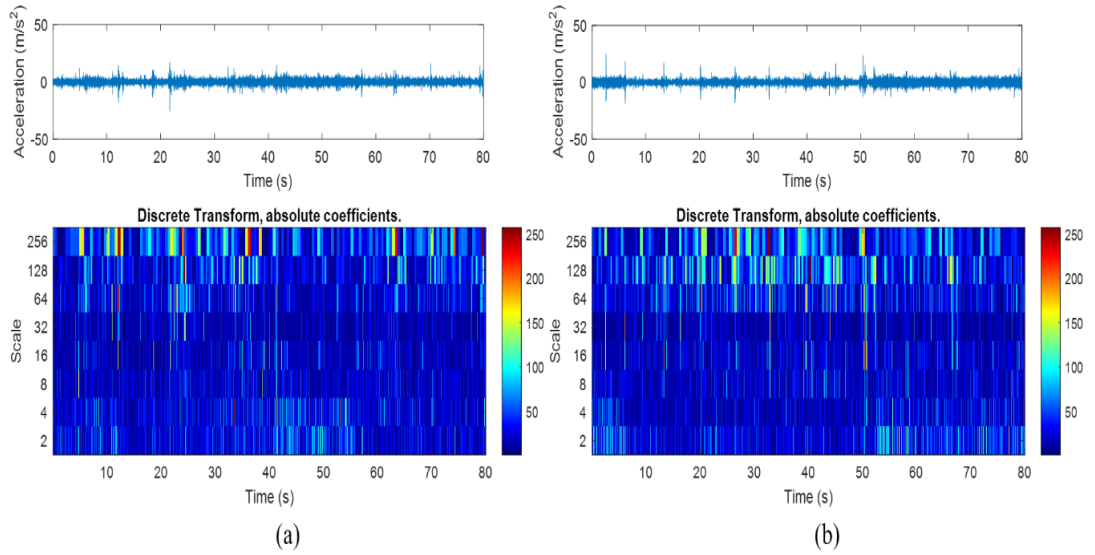

Figure 4.82 DWT analysis of vibration signals obtained from highway road conditions: (a) Highway 1, (b) Highway 2

Multifractal spectrums were computed from the wavelet leaders in time-scale domain of the vibration signals. Figures 4.83–4.86 illustrate the multifractal spectrums of the vibration signals under different road conditions. From the spectrums, all vibration signals exhibited multifractal properties due to their wide spectrum width above 0.05 (Makowiec & Fulinski 2010). Thus, these vibration signals due to road excitations were categorised as multifractal signals and this finding is in agreement with

Quan et al. (2013) which had determined the multifractal properties of pavement surface roughness.

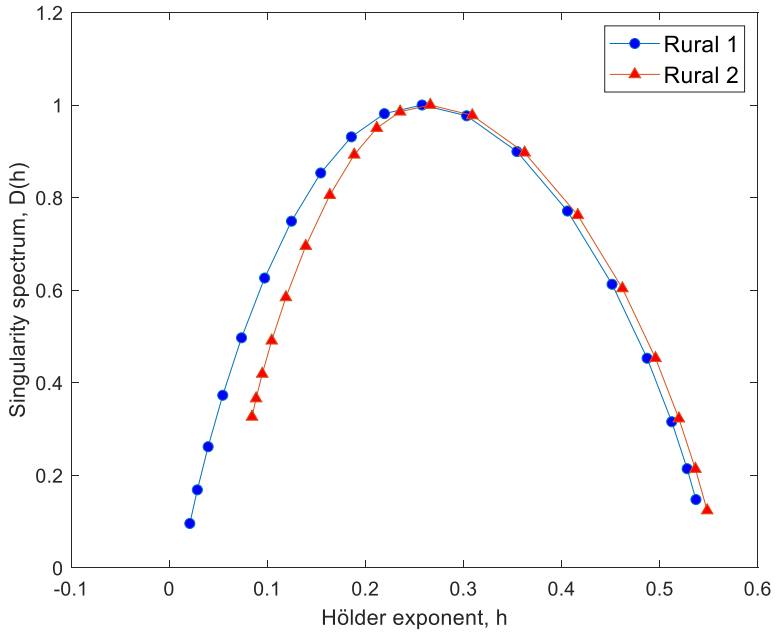

Figure 4.83 Multifractal spectrums of vibration signals obtained from rural road condition

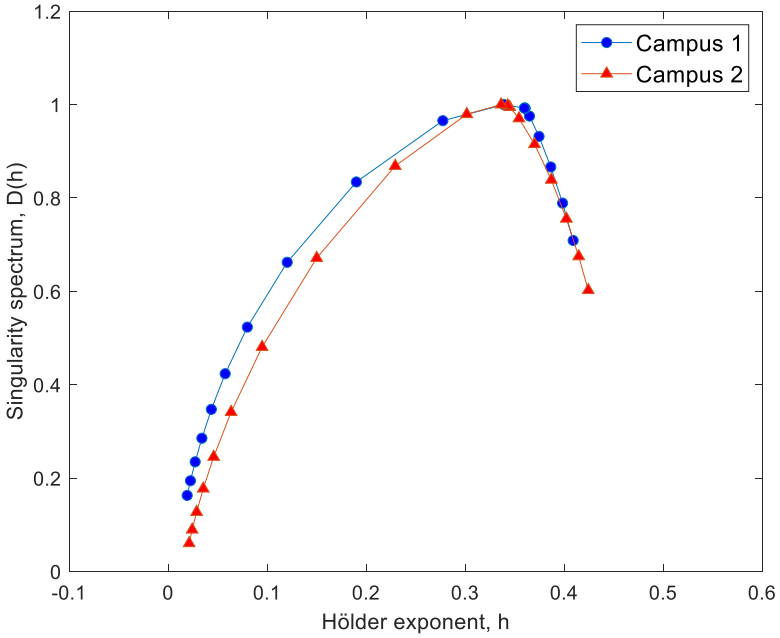

Figure 4.84 Multifractal spectrums of vibration signals obtained from university campus road condition

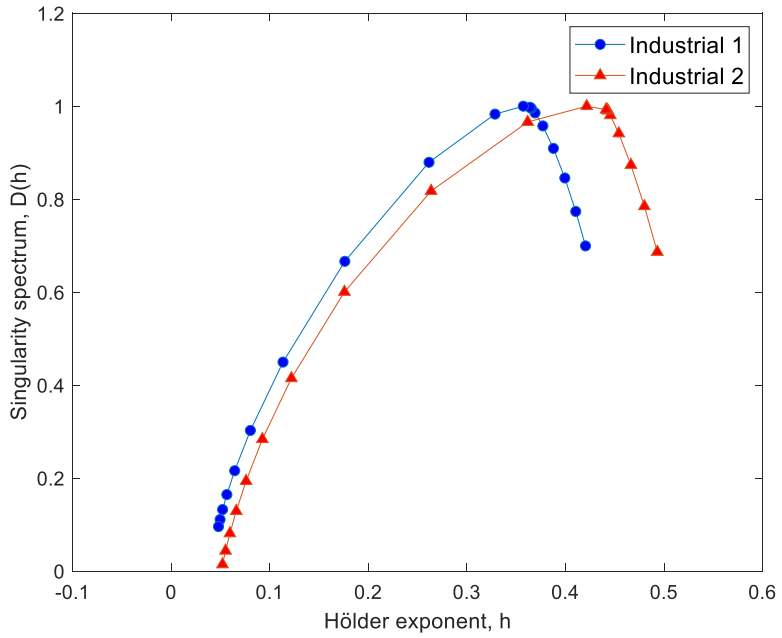

Figure 4.85 Multifractal spectrums of vibration signals obtained from industrial road condition

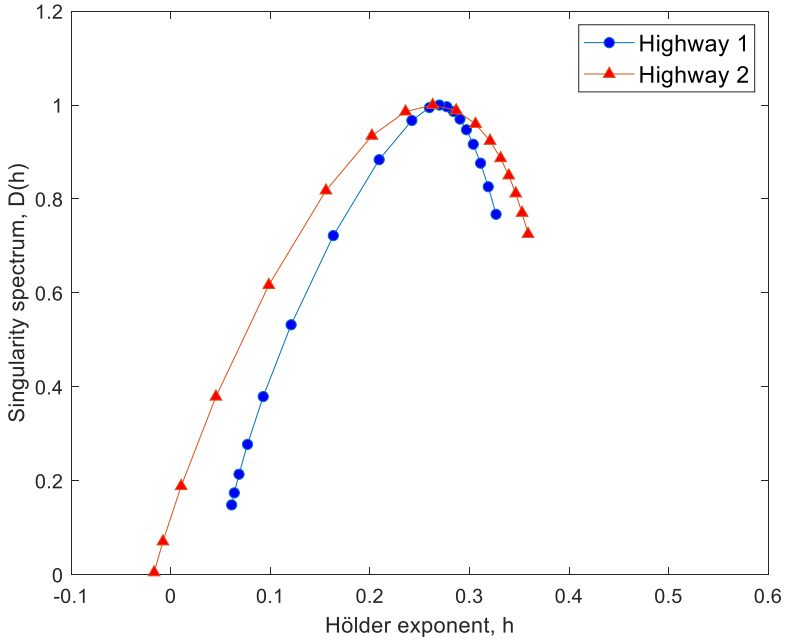

Figure 4.86 Multifractal spectrums of vibration signals obtained from highway road condition

The degree of multifractality of the signals were evaluated from the spectrum width, as shown in Table 4.14. It was observed that signals obtained from the same road conditions exhibited similar pattern of multifractal spectrums and resulted in close

spectrum parameters (h_{min}, h_{max} and h_0). Multifractal analysis was ideal for classification of vibration signals under different road conditions. The central HE (h_0) of the multifractal spectrum described the structure of the signal, whether the signal was correlated (Krzyszczak et al. 2019). A correlated signal showed higher h_0 value compared to a less correlated signal. The signal correlation was related to the consistency of transient or irregular events, such as bumps and potholes on the road surfaces. The rural and highway signals had lower h_0 values compared to campus and industrial signals, as both signals consistently contained high and low amplitude cycles, respectively. In campus and industrial signals, high amplitude events occurred occasionally and thus rendered the signals to become more correlated, as shown by the higher h_0 values. The trend of h_0 values in the loading signals was found to be identical with their kurtosis values, as shown in Table 4.2. This indicates that the h_0 values of vibration signals were related to the extreme value in the data.

Table 4.14 Multifractality of vibration signals determined from the spectrum width of multifractal spectrums

Road condition	h_{min}	h_{max}	**Central Hölder exponent, h_0**	**Multifractality (Δh)**
Rural 1	0.021	0.537	0.258	0.516
Rural 2	0.084	0.548	0.266	0.464
Campus 1	0.019	0.409	0.339	0.390
Campus 2	0.021	0.424	0.336	0.403
Industrial 1	0.048	0.420	0.357	0.372
Industrial 2	0.052	0.493	0.422	0.441
Highway 1	0.061	0.327	0.270	0.266
Highway 2	-0.023	0.359	0.263	0.382

Figure 4.87 shows the comparison the multifractality of various vibration signals collected from different road conditions. It was found that the signals with the highest multifractality is Rural 1, which had a multifractality of 0.516. At the same time, Highway 1 appeared to be the signal with the least multifractality of 0.266. The big gap of multifractality between highway and rural signals was because of the difference in high amplitude event between two roads. In this case, the multifractal properties of the loading signals were closely related to the roughness or irregularities of the road surfaces (Quan et al. 2013). The rural road surface was unpaved and highly irregular and thus this gave more complex excitations to the suspension system and eventually resulted in highly multifractal loading signals. In contrast, the highway road had a

smooth surface profile with very limited irregular events such as bumps and potholes. This is the main reason of low multifractality in highway loading signals. It is commonly known that high amplitude excitations from road surface are directly related to the durability of suspension coil spring. Since the multifractality of loading signals are related to their road surface roughness, the multifractality can thus become a fatigue related parameter for durability prediction of coil spring.

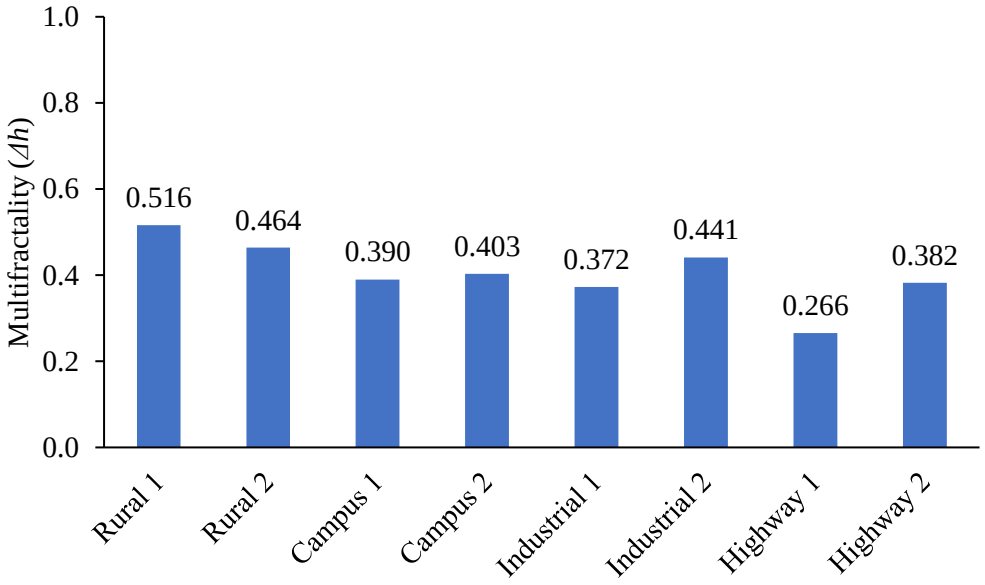

Figure 4.87 Multifractality of vibration signals obtained from different road conditions

4.3.3 Establishment of Durability Prediction Models with Machine Learning Modelling

A three-inputs one-output ANFIS model for durability predictions has been developed. The low-frequency energy and the multifractality determined from the vibration signals as well as the spring constant had been used as the input or predictors of the ANFIS modelling. Since the purpose of the ANFIS modelling was to predict durability of coil spring, the output of the model was the fatigue life of coil spring. Subtractive clustering method (SCM) was used to group the training data into several clusters, with each cluster associated with a fuzzy rule and membership function (MF). The clustering methods were employed to determine the MFs by partitioning the data samples into different clusters in which the data in a cluster shared similar behaviours (Keshavarzi et al. 2017). When the training data were divided into smaller clusters, the

ANFIS model was more fitted to the training dataset and produced accurate outcome (Zhang et al. 2019a). However, overfitting might happen once the model becomes too influenced by the pattern of the training dataset and could result in high errors when fresh data are fitted into the model (de Campos Souza 2020). An increased number of MF indicates a more complex ANFIS structure, and this increases the computational load of the modelling (Zhang et al. 2019a). Therefore, it is necessary to optimise the number of MFs or fuzzy rules in the ANFIS model to obtain the most optimum structure for fatigue life prediction.

The optimisation of the fuzzy rule number was performed by adjusting the predefined radius of influence (ROI) during SCM to obtain different fuzzy rule number between 2 and 7. The training process or learning process was repeated with various fuzzy rule numbers. The test data, which was not involved in the training process, was prepared by taking 10% of the data from the original dataset. The rest of the data was then used as the training data. Test data was necessary to validate the general use of the ANFIS model and to monitor if overfitting happened (Zhang et al. 2019a).

To evaluate the accuracy of the trained ANFIS models, mean-square-errors (MSEs) were computed based on the training and testing dataset. The testing dataset was randomly selected from 10% of the total data (Vassilopoulos & Bedi 2008; Zhang et al. 2019a). MSEs based on the training data was known as the training error while MSEs of test data was known as the testing error. Tables 4.15 to 4.18 list the training and testing errors obtained from the trained ANFIS models with different number of fuzzy rules. The MSEs were important indicator to measure the accuracy of the trained model in fatigue life prediction in which lower MSE represented higher accuracy. Figures 4.88–4.91 show the trends of the training and testing errors of ANFIS models. It was found that the training errors of all ANFIS models shared similar decreasing trend when the number of fuzzy rules increased. This was an indication that the ANFIS models had become more fitted to the training dataset with a greater number of fuzzy rules. When more MFs were involved, the non-linear relationships between the input variables and the output variable can be predicted more accurately (Zuo et al. 2014). Nonetheless, it was also necessary to observe if overfitting occurred while gaining more accurate predictions by increasing fuzzy rules. It can be done by observing the trends

of testing errors. Increase in testing errors was an important indication in which the models started to become overfitted to the training dataset and thus resulted in large error when fresh data was fitted.

Table 4.15 Training and testing errors of Coffin-Manson-based fatigue life predictions with ANFIS model at different number of fuzzy rules

Number of fuzzy rules	Training error	Testing error
2	0.552	0.504
3	0.523	0.449
4	0.520	0.511
6	0.419	0.630
7	0.402	0.776

Table 4.16 Training and testing errors of Morrow-based fatigue life predictions with ANFIS model at different number of fuzzy rules

Number of fuzzy rules	Training error	Testing error
2	0.555	0.510
3	0.523	0.435
4	0.514	0.512
5	0.475	0.568
6	0.423	0.660
7	0.401	0.773

Table 4.17 Training and testing errors of SWT-based fatigue life predictions with ANFIS model at different number of fuzzy rules

Number of fuzzy rules	Training error	Testing error
2	0.555	0.501
3	0.529	0.453
4	0.528	0.445
5	0.472	0.582
6	0.450	0.915
7	0.436	1.699

Table 4.18 Training and testing errors of ESD-based fatigue life predictions with ANFIS model at different number of fuzzy rules

Number of fuzzy rules	Training error	Testing error
2	0.226	0.232
3	0.221	0.222
4	0.206	0.194
5	0.208	0.197
6	0.195	0.231
7	0.188	0.253

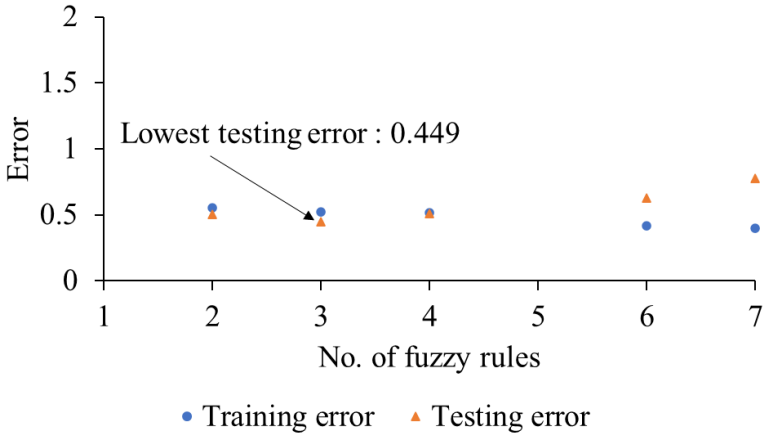

Figure 4.88 Optimisation of fuzzy rule number of ANFIS models based on training and testing errors for fatigue data predicted by Coffin-Manson model

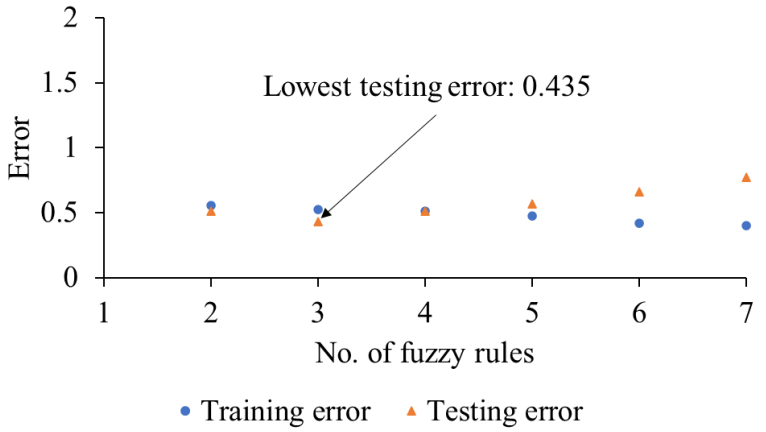

Figure 4.89 Optimisation of fuzzy rule number of ANFIS models based on training and testing errors for fatigue data predicted by Morrow model

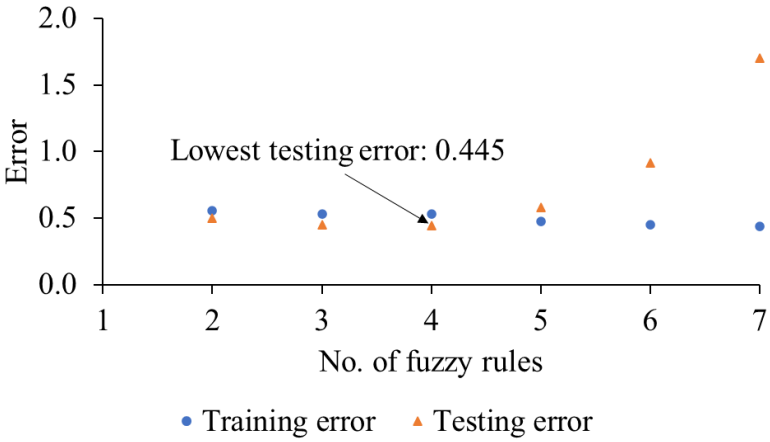

Figure 4.90 Optimisation of fuzzy rule number of ANFIS models based on training and testing errors for fatigue data predicted by SWT model

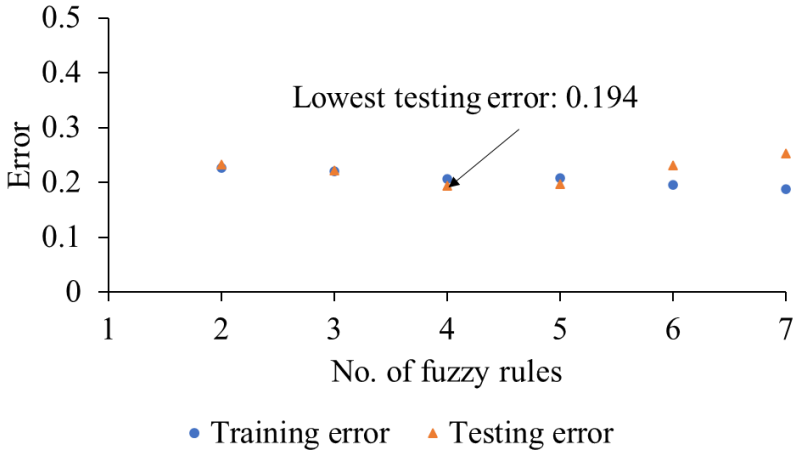

Figure 4.91 Optimisation of fuzzy rule number of ANFIS models based on training and testing errors for fatigue data predicted by ESD model

From Figures 4.89–4.89, the testing errors increased after three fuzzy rules for the Coffin-Manson- and Morrow-based ANFIS models. Meanwhile, testing errors showed increased trend after four fuzzy rules for SWT- and ESD-based models, as illustrated in Figures 4.90 and 4.91. These findings indicated that further increase of fuzzy rules resulted in overfitting of the models (Zhang et al. 2019a). Therefore, the appropriate number of fuzzy rules for Coffin-Manson- and Morrow-based models were three fuzzy rules while for SWT- and ESD-based models were four fuzzy rules.

4.3.4 Machine Learning Models for Fatigue Life Prediction

During the learning process in ANFIS modelling, the MFs of each input variable were adjusted in each Epoch of training to obtain the most accurate output with the least error. Figure 4.92 shows the optimised MFs of the input variables in Coffin-Manson-based ANFIS model after the learning process is completed. The MFs of the input variables employed in this study were Gaussian type MF, which was represented by mean (μ) and standard deviation (σ) parameters. Table 4.19 lists the optimised parameters of the input variables' MFs. For the MFs of output variable, the MFs appeared in the form of linear function as expressed by Equation 3.18. The three coefficients o, p, and q were corresponding to the signal energy, multifractality, and spring constant, respectively. Table 4.20 shows the optimised parameter values of the output linear MFs. From Figure 4.92, for Coffin-Manson-based ANFIS model, the signal energy and multifractality are characterised by three MFs while the spring constant is represented

by two MFs. The MF clusters were named after the ascending order of their mean values. MFs are unique notations in a fuzzy set theory to convert a crisp value of a parameter into fuzzy values that represent the uncertainty or vagueness of the parameter. Each MF describes a parameter with the degree of membership between 0 and 1, that indicates how true a parameter belongs to the group represented by the MF. The degree of membership value of 1 indicating the parameter is 100% belonging to the group while 0 indicates that the parameter does not belong to the group. The Coffin-Manson-based ANFIS model was found to be appropriate to be governed by three fuzzy if-then rules, such that:

Rule 1: If *E* is *E_cluster 1* and *Δh* is *Δh_cluster 1* and *k is k_cluster 1*, then N_f is N_f*_cluster 1*
Rule 2: If *E* is *E_cluster 2* and *Δh* is *Δh_cluster 2* and *k is k_cluster 2*, then N_f is N_f*_cluster 2*
Rule 3: If *E* is *E_cluster 3* and *Δh* is *Δh_cluster 3* and *k is k_cluster 2*, then N_f is N_f*_cluster 3*

The fuzzy rules were important in ANFIS modelling that related the inputs' MFs with the output's MFs to predict the output values.

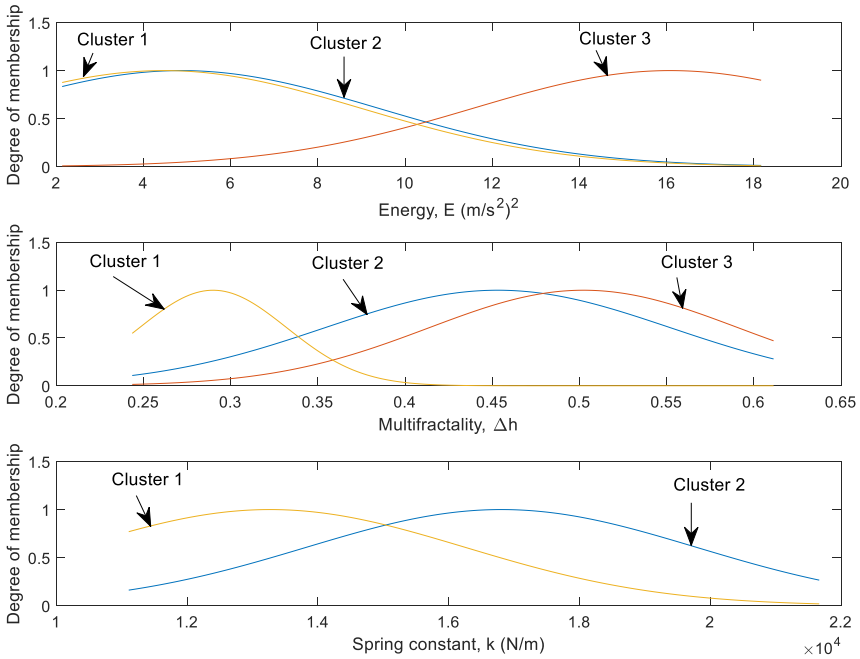

Figure 4.92 Optimised membership functions of predictive parameters in ANFIS models to predict Coffin-Manson-based fatigue life

Table 4.19 Gaussian membership function parameters of input variables of Coffin-Manson-based ANFIS model after training process

Input variable	Cluster Number	Gaussian membership function parameter	
		Mean (μ)	Standard deviation (σ)
Signal Energy, E	Cluster 1	4.465	4.535
	Cluster 2	4.866	4.535
	Cluster 3	16.08	4.534
Multifractality, Δh	Cluster 1	0.290	0.042
	Cluster 2	0.453	0.099
	Cluster 3	0.502	0.089
Spring constant, k	Cluster 1	1.327×10^4	2987
	Cluster 2	1.681×10^4	2987

Table 4.20 Linear membership function parameters of output variable of Coffin-Manson-based ANFIS model after training process

Output variable	Cluster Number	Linear membership function parameter			
		o	p	q	r
Fatigue life, N_f (logarithm scale)	Cluster 1	-0.428	-7.456	-1.019×10^{-4}	12.71
	Cluster 2	-0.220	-3.374	-8.660×10^{-5}	9.007
	Cluster 3	-0.113	-0.638	-8.252×10^{-5}	7.989

The Morrow-based model also had similar cluster number of the input variables as the Coffin-Manson-based model, as shown in Figure 4.93. The vibration features had similar behaviours towards fatigue properties of coil spring determined from the Coffin-Manson and Morrow models. Tables 4.21 and 4.22 list the optimised MF parameters of the input and output variables, respectively. Similar to the Coffin-Manson-based model, there were also three fuzzy rules that governed the Morrow-based ANFIS model, such that:

Rule 1: If E is *E_cluster 1* and Δh is *Δh_cluster 1* and *k is k_cluster 1*, then N_f is *N_f_cluster 1*

Rule 2: If E is *E_cluster 2* and Δh is *Δh_cluster 2* and *k is k_cluster 2*, then N_f is *N_f_cluster 2*

Rule 3: If E is *E_cluster 3* and Δh is *Δh_cluster 3* and *k is k_cluster 2*, then N_f is *N_f_cluster 3*

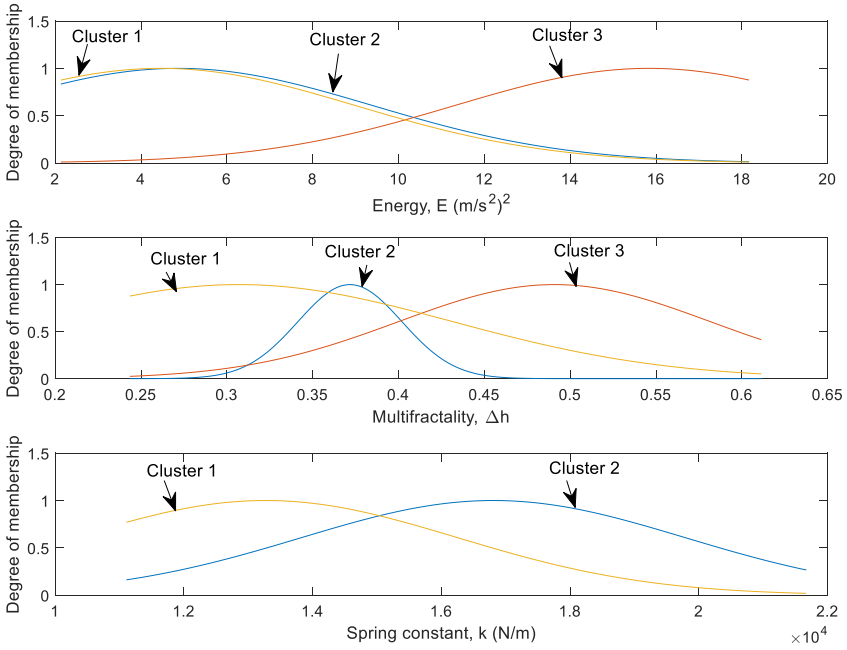

Figure 4.93 Optimised membership functions of predictive parameters in ANFIS models to predict Morrow-based fatigue life

Table 4.21 Gaussian membership function parameters of Morrow-based ANFIS model after training process

Input variable	Cluster Number	Gaussian membership function parameter	
		Mean (μ)	Standard deviation (σ)
Signal Energy, E	Cluster 1	4.465	4.533
	Cluster 2	4.865	4.536
	Cluster 3	15.84	4.535
Multifractality, Δh	Cluster 1	0.307	0.125
	Cluster 2	0.372	0.030
	Cluster 3	0.491	0.091
Spring constant, k	Cluster 1	1.327×10^4	2987
	Cluster 2	1.681×10^4	2987

Table 4.22 Linear membership function parameters of output variable of Morrow-based ANFIS model after training process

Output variable	Cluster Number	Linear membership function parameter			
		o	p	q	r
Fatigue life, N_f (logarithm scale)	Cluster 1	-0.421	-7.04	-1.568×10^{-4}	12.88
	Cluster 2	-0.031	-16.61	-2.829×10^{-5}	11.96
	Cluster 3	-0.079	-1.547	-1.077×10^{-4}	8.254

From Figures 4.92 and 4.93, the MF clusters 1 and 2 of low-frequency signal energy are very close to each other, with a slight gap between the means. This is because much input data had been distributed within the range from 2 to 10 $(m/s^2)^2$, hence, the SCM determined two cluster centres with the range. Clusters 1 and 2 had covered the

low and medium ranges of signal energy while cluster 3 represented high energy level. For multifractality, the MFs were evenly scattered within the entire data range. Clusters 1, 2, and 3 represented low, medium, and high ranges of multifractality, respectively. The spring constant was supposed to have three MFs since there were three fuzzy rules for the models. However, the spring constant was a controlled variable in this study and hence MFs could overlap and combine to become one. This agrees with findings from Zhang et al. (2019a) in which some controlled input parameter had less MF number than the fuzzy rule number. Therefore, two MFs could effectively represent the spring constant variable in the ANFIS models.

From the optimisation of the fuzzy rule numbers for SWT-based ANFIS model, four fuzzy rules were found appropriate to obtain the most accurate prediction of fatigue life. The SWT-based fatigue lives had more complex relationship with the input variables and thus more fuzzy rules were needed to represent the SWT-based ANFIS model. Figure 4.94 shows the optimised MFs of the input variables including the low-frequency signal energy, multifractality, and spring constant. Tables 4.23 and 4.24 list the optimised MF parameters of the input and output variables of SWT-based ANFIS model, respectively. It can be observed that both low-frequency energy and multifractality had four MFs. The first three clusters of low-frequency energy were close with each other while the fourth cluster was found in the range of high energy. For multifractality, four MF clusters represented multifractality of the loading signal at different levels. It should be noted that the spring constant parameter had only one cluster, indicating that data distribution of the spring constant had no significant effect on the SWT-based fatigue lives. The MFs of input variables and output variables' MFs of the SWT-based ANFIS model were related through the following fuzzy rules:

Rule 1: If E is *E_cluster 1* and Δh is *Δh_cluster 1* and *k is k_cluster 1,* then N_f is N_f*_cluster 1*
Rule 2: If E is *E_cluster 2* and Δh is *Δh_cluster 2* and *k is k_cluster 1,* then N_f is N_f*_cluster 2*
Rule 3: If E is *E_cluster 3* and Δh is *Δh_cluster 3* and *k is k_cluster 1,* then N_f is N_f*_cluster 3*
Rule 4: If E is *E_cluster 4* and Δh is *Δh_cluster 4* and *k is k_cluster 1,* then N_f is N_f*_cluster 4*

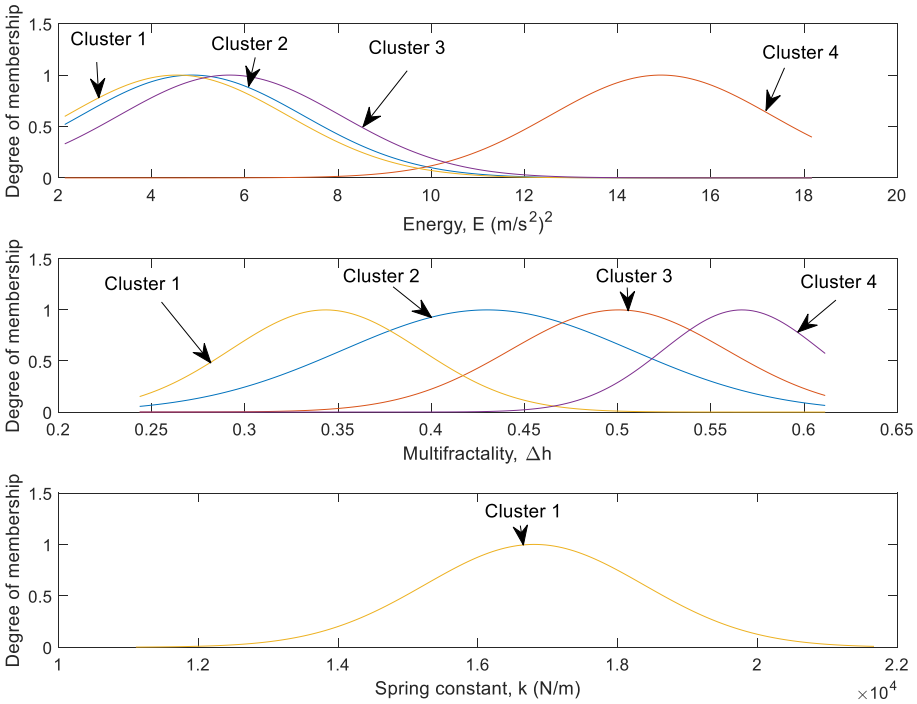

Figure 4.94 Optimised membership functions of predictive parameters in ANFIS models to predict SWT-based fatigue life

Table 4.23 Gaussian membership function parameters of SWT-based ANFIS model after training process

Input variable	**Cluster Number**	**Gaussian membership function parameter**	
		Mean (μ)	**Standard deviation (σ)**
Signal Energy, E	Cluster 1	4.542	2.376
	Cluster 2	4.865	2.387
	Cluster 3	5.675	2.381
	Cluster 4	14.93	2.381
Multifractality, Δh	Cluster 1	0.343	0.051
	Cluster 2	0.430	0.078
	Cluster 3	0.500	0.058
	Cluster 4	0.567	0.042
Spring constant, k	Cluster 1	1.681×10^4	1568

Table 4.24 Linear membership function parameters of output variable of SWT-based ANFIS model after training process

Output variable	**Cluster Number**	**Linear membership function parameter**			
		o	***p***	***q***	***r***
Fatigue life, N_f (logarithm scale)	Cluster 1	-0.166	-14.63	-1.689×10^{-4}	15.22
	Cluster 2	-0.209	8.964	-9.197×10^{-5}	3.565
	Cluster 3	-0.273	5.389	-9.783×10^{-5}	4.248
	Cluster 4	-0.085	-0.599	-8.583×10^{-5}	7.468

The ESD-based ANFIS model had a similar number of fuzzy rules with the SWT-based model that produced the most accurate results. Hence, there were four MFs for each input variable as shown in Figure 4.95. Tables 4.25 and 4.26 show the optimised MF parameters of the input and output variables of ESD-based ANFIS model, respectively. However, the spring constant had only two MFs with the same reason as the Coffin-Manson- and Morrow-based ANFIS models. It shows that the fatigue life of coil spring was not as sensitive to the changes in spring constant as the loading features. Therefore, less MFs were needed to relate the spring constant with fatigue life of coil spring. The fuzzy rules that governed the ESD-based ANFIS model are shown as follows:

Rule 1: If E is *E_cluster 1* and Δh is *Δh_cluster 1* and k *is k_cluster 1*, then N_f is N_f*_cluster 1*
Rule 2: If E is *E_cluster 2* and Δh is *Δh_cluster 2* and k *is k_cluster 2*, then N_f is N_f*_cluster 2*
Rule 3: If E is *E_cluster 3* and Δh is *Δh_cluster 3* and k *is k_cluster 2*, then N_f is N_f*_cluster 3*
Rule 4: If E is *E_cluster 4* and Δh is *Δh_cluster 4* and k *is k_cluster 2*, then N_f is N_f*_cluster 4*

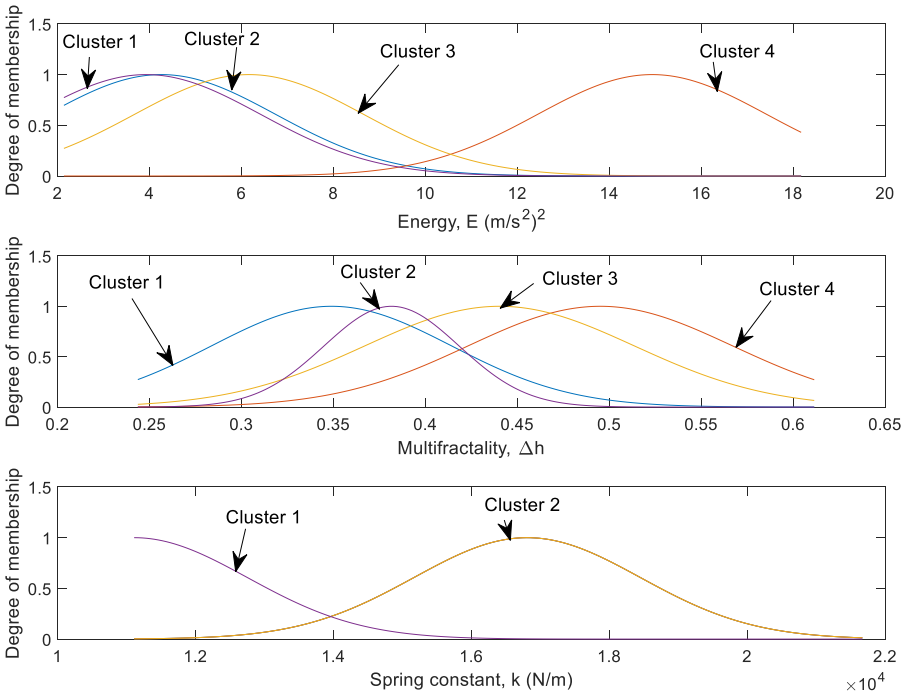

Figure 4.95 Optimised membership functions of predictive parameters in ANFIS models to predict ESD-based fatigue life

Table 4.25 Gaussian membership function parameters of ESD-based ANFIS model after training process

Input variable	Cluster Number	Gaussian membership function parameter	
		Mean (μ)	Standard deviation (σ)
Signal Energy, E	Cluster 1	3.922	2.494
	Cluster 2	4.252	2.491
	Cluster 3	6.160	2.497
	Cluster 4	14.93	2.496
Multifractality, Δh	Cluster 1	0.349	0.065
	Cluster 2	0.382	0.037
	Cluster 3	0.440	0.073
	Cluster 4	0.495	0.072
Spring constant, k	Cluster 1	1.111e4	1643
	Cluster 2	1.681e4	1643

Table 4.26 Linear membership function parameters of output variable of ESD-based ANFIS model after training process

Output variable	Cluster Number	Linear membership function parameter			
		o	p	q	r
Fatigue life, N_f (logarithm scale)	Cluster 1	-0.148	0.032	-1.454×10^{-4}	7.568
	Cluster 2	-0.236	-8.152	-6.004×10^{-5}	9.339
	Cluster 3	-0.237	-5.118	-5.620×10^{-5}	9.627
	Cluster 4	-0.075	-0.159	-5.871×10^{-5}	6.523

After the optimisation of the input and output MFs through the learning process, the fatigue life of coil spring can be predicted using the trained models. Figure 4.96 shows the response surface plots predicted by the ANFIS models based on the multifractality and low-frequency energy of the vibration signals. The spring constant was not included in the surface plots since this study emphasised the relationship between features of vibration loading signal and the durability performance of coil spring. From the response surface plots, it can be observed that the relationships between fatigue life of coil spring and the vibrational features were highly nonlinear. All the ANFIS models predicted the longest fatigue life of the coil spring at a low energy and multifractality. A typical example of this type of signal was the highway signal which had a smooth surface profile with the least irregularities. The low-frequency energy and multifractal properties of the loading signals were closely related to the road surface conditions. Farrahi, Ahmadi & Reza Kasyzadeh (2020) agreed that the road surface roughness was the main factor responsible for fatigue failures of automotive components. Bumpy roads with rough surface profile, such as the rural and industrial area roads, were most likely to result in loading signals with high multifractality (Quan et al. 2013). On the other hand, high amplitude events, such as bumps, potholes, and

rough surface profile, also contributed to high energy in frequency range below 50 Hz (Kong et al. 2017). Therefore, both low-frequency energy and multifractality of the vibration signals were found to have significant impacts on the durability performance of the coil springs and these features were suitable to predict the fatigue life.

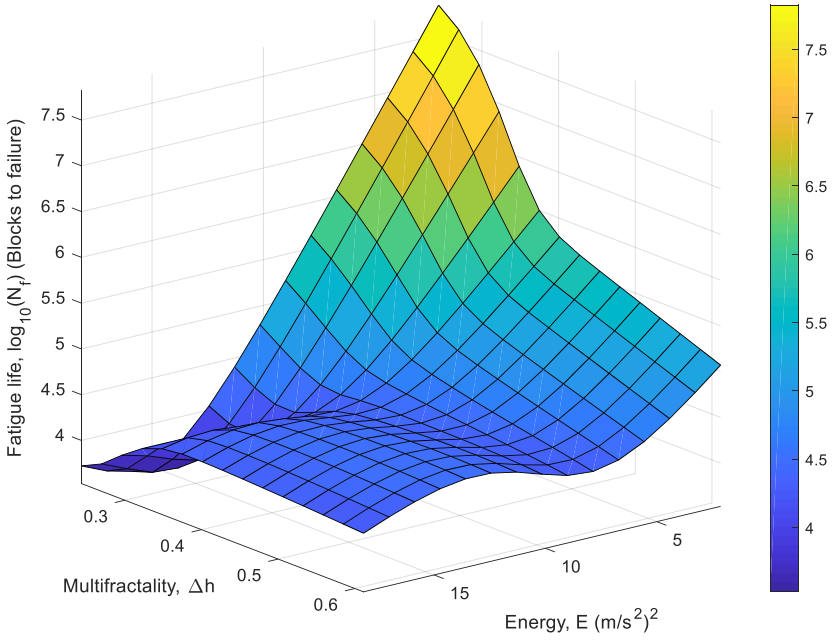

(a)

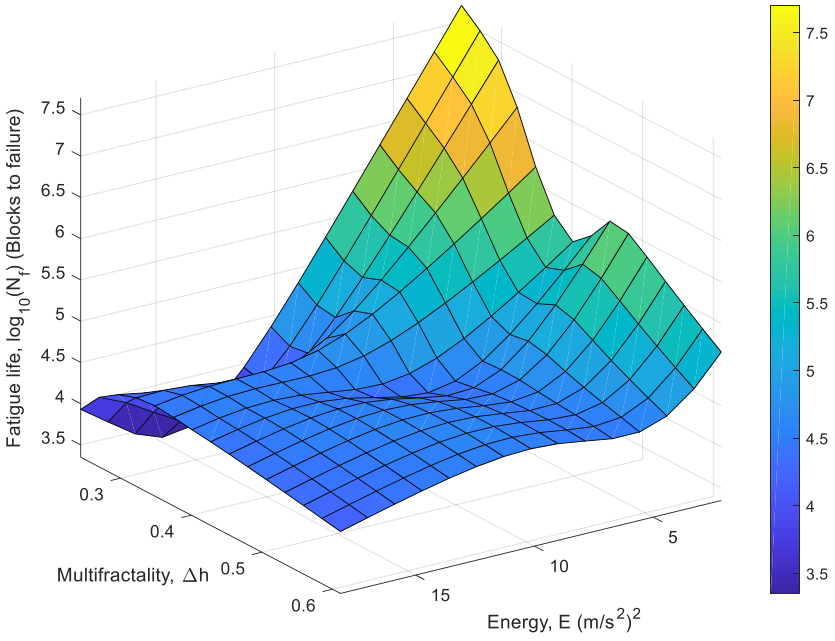

(b)

continue…

…continued

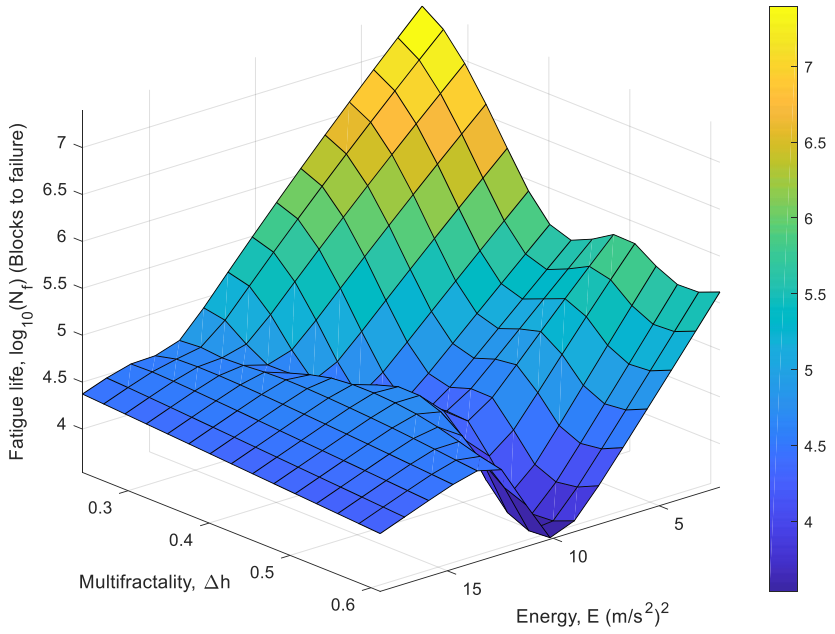

(c)

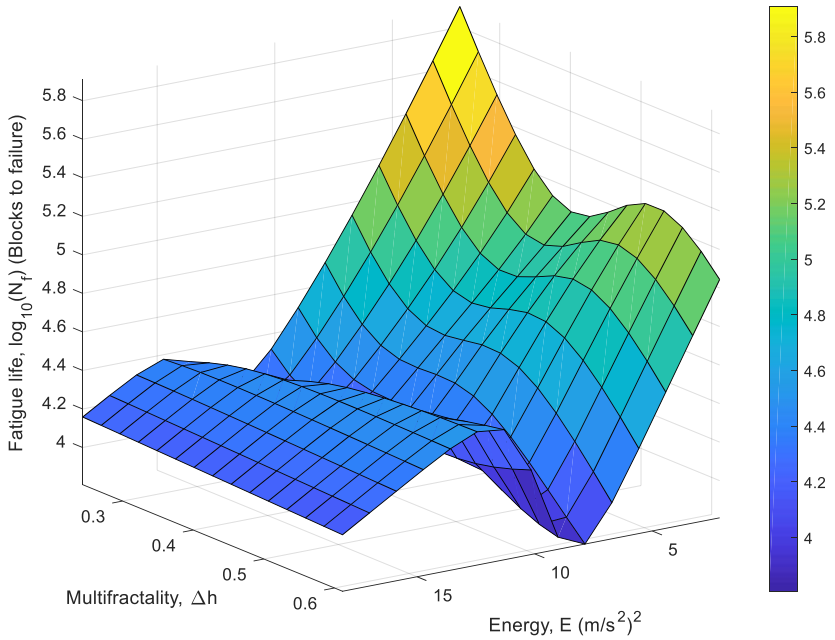

(d)

Figure 4.96 Responses surfaces between signal energy, multifractality and fatigue life predicted by ANFIS-based model associated to: (a) Coffin-Manson, (b) Morrow, (c) SWT, (d) ESD models

Compared to other ANFIS models, the ESD-based model predicted lower fatigue lives. This is primality because the ESD model gave more conservative

prediction compared to the strain-life models. The ESD model took the load sequence effect of the loading signals into account which was not considered in conventional strain-life model (Kadhim, Abdullah & Ariffin 2012). The overloads in the vibration signals resulted in high amplitude events caused by high crack-opening stress at the crack tip and encouraged the crack propagation (El-Zeghayar, Topper & Bonnen 2013). Hence, the predicted fatigue lives were lower with the consideration of load sequence effect between overloads in the loading signals. It was shown that the load sequence effect of the loading signals resulted in lower fatigue life, especially in the highway loading signals. Thus, consideration of load sequence effect during fatigue life estimation was important to prevent over-optimistic predictions. Kadhim, Abdullah & Ariffin (2012) reported high accuracy of ESD model in predicting fatigue life of VAL signals with only 12% of difference between the predicted fatigue lives with experimental results. Furthermore, large differences (55%–79%) in predicted fatigue lives with the experimental resulted using strain-life approaches were also reported.

Fatigue life conservative analysis was performed to evaluate the conservative of the predicted fatigue life by the ANFIS models. The predicted fatigue lives using the trained ANFIS models were compared to the fatigue lives obtained through strain-life models as shown in Figure 4.97. Two separate datasets including the training data and testing data were involved in the fatigue life conservative analysis. Results showed that all the trained ANFIS models provided good conservative of fatigue life predictions since there were more than 90% of the predicted fatigue lives that had survived within the 1:2 and 2:1 correlation boundary. Furthermore, the trained models had more than 95% of data survivability within acceptable boundary using the testing data. This strongly indicates that the trained ANFIS models were suitable for general use as these models were adapted to fresh datasets. The trained Coffin-Manson-, Morrow-, and SWT-based models were found to be provided with over-conservative fatigue life prediction in high fatigue cycle regime above 10^6 blocks to failure since many fatigue life correlation data in that region had scattered below the 1:2 correlation boundary (Manouchehrynia, Abdullah & Singh 2020), as shown in Figure 4.97. This can be due to the highly nonlinear fatigue behaviours that were more pronounced at high fatigue cycle regime and thus affected the fatigue life prediction in the region. It was noteworthy that the ESD-based ANFIS model had the most satisfactory outcome in the

fatigue life conservative analysis as the model had 100% of data survivability using both training and testing datasets.

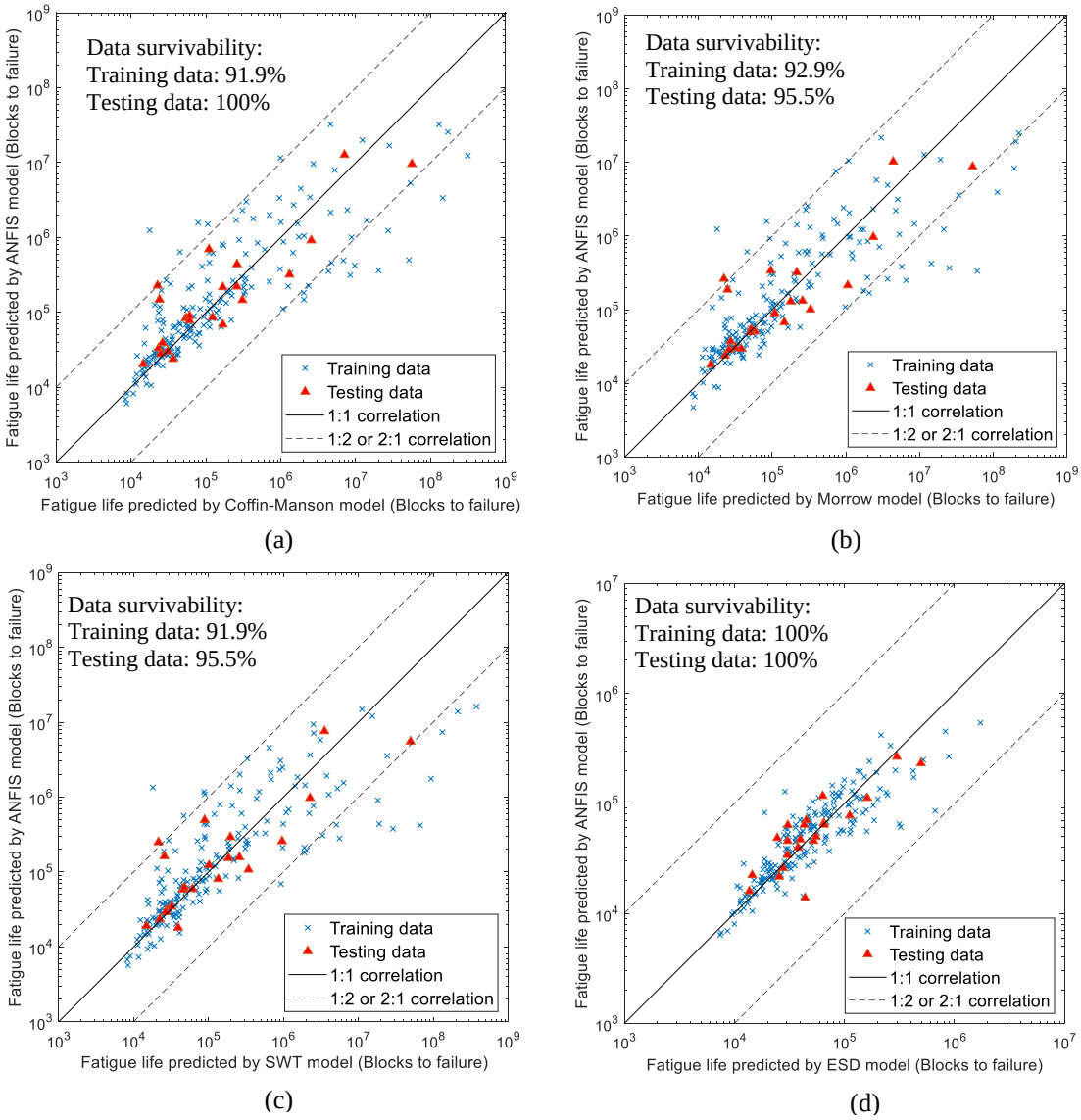

Figure 4.97 Fatigue life conservative analysis between fatigue lives predicted by ANFIS models and different fatigue models: (a) Coffin-Manson, (b) Morrow, (c) SWT, (d) ESD models

Other than the fatigue life conservative analysis, the data survivability of the predicted fatigue life within 95% confidence interval was also tested. Figure 4.98 shows the fatigue life correlation between fatigue lives predicted using ANFIS models and strain-life models. The fatigue lives in this analysis were obtained from the testing dataset because the testing dataset gave more meaningful representation for general use of the models (Kong et al. 2019d). Moreover, the correlation between the predicted

fatigue lives using ANFIS models and strain-life models were also assessed by determining the Pearson coefficients (*r*). Figure 4.99 depicts the linear correlation between fatigue life data and *r* values of each ANFIS model.

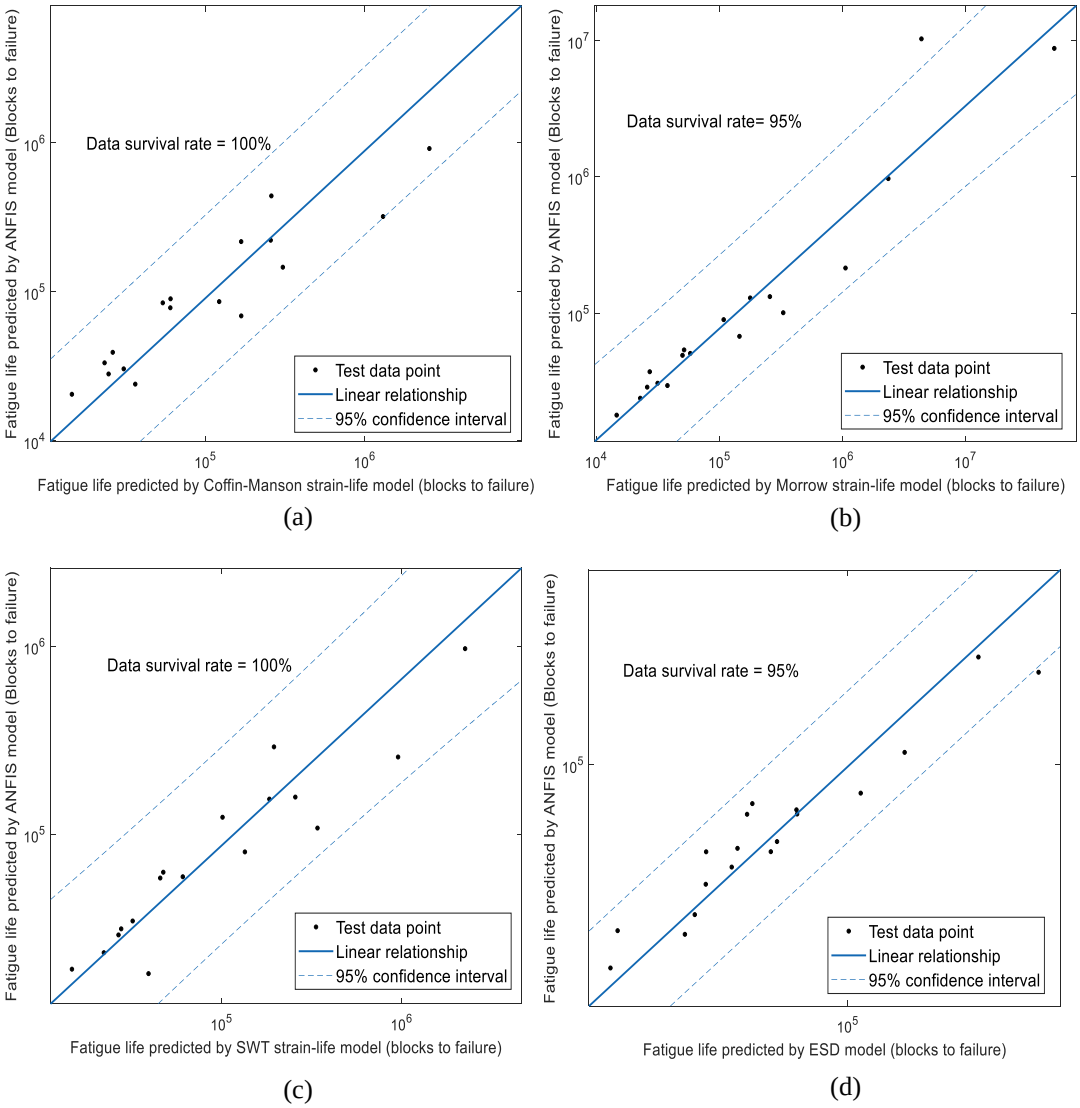

Figure 4.98 Fatigue life data survival analysis within 95% confidence interval based on fatigue life correlation predicted by different fatigue models: (a) Coffin-Manson, (b) Morrow, (c) SWT, (d) ESD models

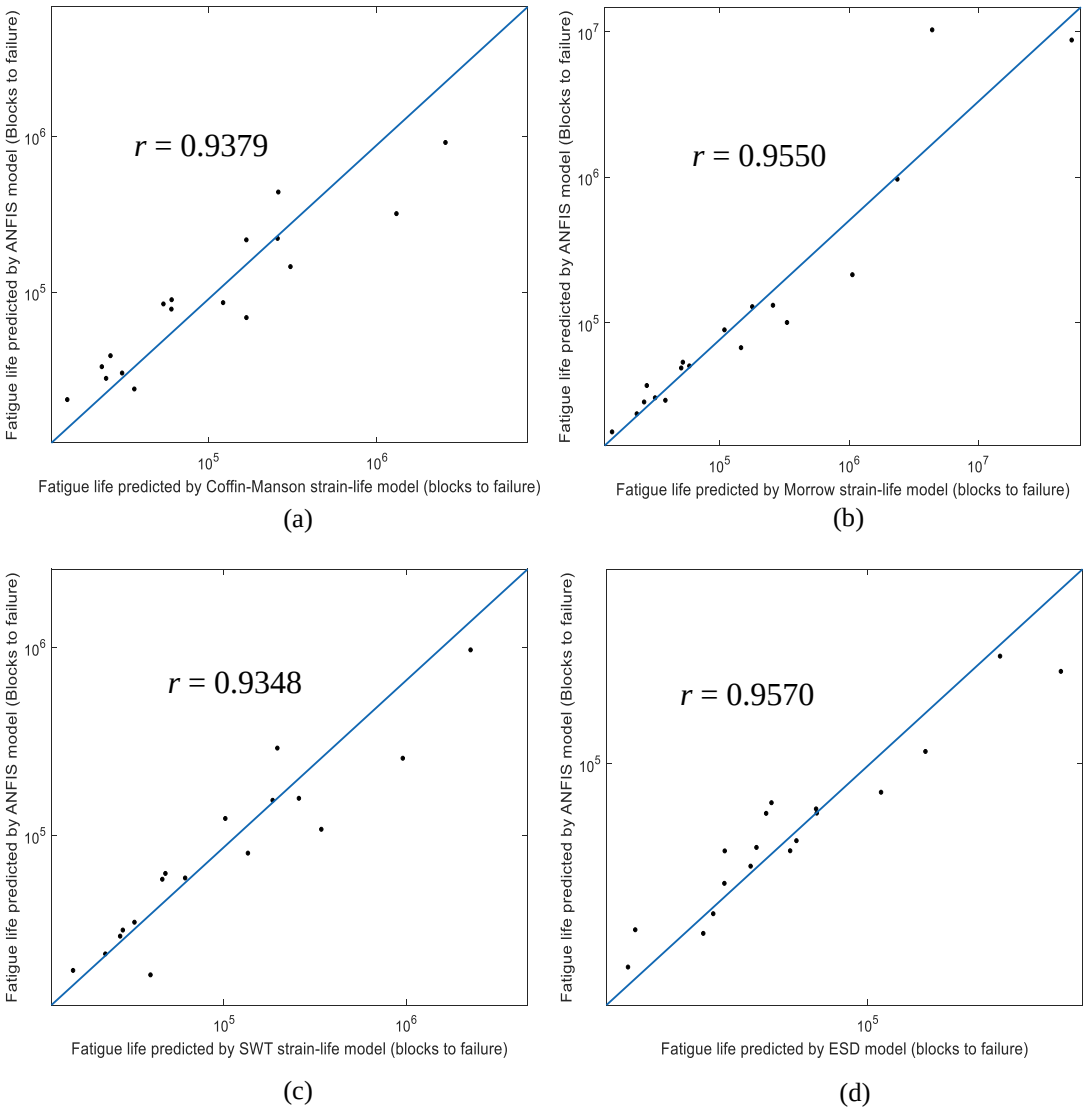

Figure 4.99 Fatigue life linear correlation and Pearson coefficient (r) based on fatigue life data predicted by ANFIS models and different fatigue models: (a) Coffin-Manson, (b) Morrow, (c) SWT, (d) ESD models

In terms of data survivability within the 95% confidence interval, the ANFIS models exhibited excellent survivability above 95%. These findings had provided probabilistic validation to the acceptability of fatigue life predictions using the trained ANFIS models. From Figure 4.99, the ANFIS models had r values higher than 0.9, indicating a very close correlation between the predicted fatigue lives by the ANFIS models and strain-life models. The ESD-based model showed the highest r value of 0.957, showing that this model had the closest match with strain-life model in fatigue life prediction.

To evaluate the accuracy of the trained ANFIS models in predicting the durability of coil spring, root-mean-square-errors (RMSE) of the predicted fatigue lives by the models were calculated and shown in Table 4.27. Figure 4.100 compares the RMSE between different ANFIS models using training and testing data. It was shown that the Coffin-Manson-, Morrow-, and SWT-based ANFIS models had similar accuracy as there were only slight differences between their RMSEs. The ESD-based ANFIS model had the lowest training and testing RMSEs of 0.454 and 0.441, respectively. This strongly suggested that the ESD-based ANFIS model had the highest accuracy of fatigue life prediction compared to other three models. This was due to the consideration of the load sequence effects in fatigue life assessment using ESD model that had given more accurate results (El-Zeghayar, Topper & Bonnen 2013). Therefore, it can be confirmed that ESD-based ANFIS model had provided the most accurate fatigue life prediction with excellent fatigue life conservative and fatigue life correlation with the strain-life model.

Table 4.27 Root-mean-square-errors of predicted fatigue lives using trained ANFIS models based on the training and testing fatigue datasets

ANFIS-based durability model	**Root-mean-square-error (RMSE)**		
	Training data	**Testing data**	**Differences (%)**
Coffin-Manson	0.723	0.670	7.3
Morrow	0.723	0.660	8.7
SWT	0.726	0.667	8.1
ESD	0.454	0.441	2.9

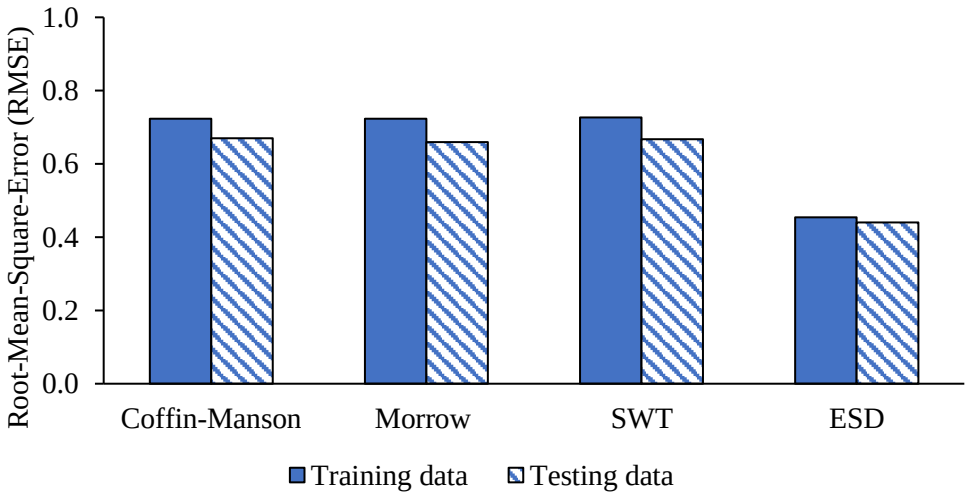

Figure 4.100 Root-mean-square-errors of predicted fatigue lives using trained ANFIS models based on the training and testing fatigue datasets

4.4 VALIDATION OF MACHINE LEARNING MODELS

This section focuses on the validation of the trained ANFIS models using fatigue reliability approaches. Fatigue failure is a random process due to many uncertainties in the loading and assumptions made in durability analysis. Therefore, it is essential to ensure that the trained models have similar probabilistic properties with the experimental results. Fatigue reliability approaches consider the uncertainties of the significant data by evaluating the probabilistic function of the data towards the fatigue life assessment. This section discusses the determination of appropriate probability distribution for the fatigue life data based on AIC criterion, computation of probability density functions (PDF), cumulative density functions (CDF), reliability functions, and hazard rate functions of the simulated and experimental results. Finally, a new approach for replacing MTTF has been introduced in this work, mentioning the mean-cycle-to-failure (McTF), for simulated and experimental results data. They were then determined and compared to validate the ANFIS models.

4.4.1 Determination of Acceptable Probability Distribution

To select the most appropriate probability distribution for reliability analysis, simulated and experimental fatigue life data were fitted to different probability distributions including the Normal, Weibull, and Lognormal distributions. Subsequently, the log-likelihood of the distributions were obtained using the MLE method. The Akaike's Information Criterion (AIC) index was then computed from the log-likelihood to determine the most suitable probability distribution. The AIC index was chosen to select the appropriate distribution because AIC index provides straight forward quantification on the data fitness to a specific distribution. This allows direct comparison between different probability distribution and hence AIC index had been widely applied (Abdullah et al. 2021; Cai et al. 2018). Table 4.28 shows the log-likelihood and AIC indices of the fatigue life data that was fitted to different probability distributions. Figure 4.101 compares the AIC indices of various models for the selection of suitable probability distribution. A low value index indicates a better fitness of the data to a distribution (Cavanaugh & Neath 2019; Manouchehrynia, Abdullah & Singh 2020).

Table 4.28 Log-likelihood and AIC indices of fatigue life data predicted from strain measurements and ANFIS modelling to determine appropriate probability distribution

Fatigue Model	Distribution	Log-Likelihood		AIC index	
		Strain data predicted fatigue life	ANFIS predicted fatigue life	Strain data predicted fatigue life	ANFIS predicted fatigue life
Coffin-Manson	Normal	-367.94	-299.11	739.88	602.21
	Weibull	-397.70	-330.80	799.40	665.60
	Lognormal	-336.01	-280.66	676.01	565.32
Morrow	Normal	-367.50	-285.79	738.99	575.58
	Weibull	-399.08	-320.92	802.16	645.84
	Lognormal	-333.62	-265.97	671.24	535.93
SWT	Normal	-368.63	-290.49	741.26	584.98
	Weibull	-401.31	-319.79	806.62	643.58
	Lognormal	-333.26	-273.85	670.52	551.70
ESD	Normal	-140.63	-77.06	285.25	158.11
	Weibull	-188.46	-109.82	380.91	223.63
	Lognormal	-127.96	-73.09	259.91	150.18

From Figure 4.101, the Lognormal distribution fitted the best with the simulated and experimental fatigue life data obtained through different durability models from the lowest AIC values among the three probability distributions. The lowest AIC index value of 150.18 was recorded in the Lognormal distribution fitted by fatigue life data obtained using ESD-based ANFIS model. This indicates that the ANFIS model predicted fatigue lives that were best represented by Lognormal distribution. It is important to select the most appropriate distribution that best represents the fatigue life data behaviours to obtain accurate results in reliability analysis. According to the findings, the Lognormal distribution was chosen as the most appropriate probability distribution for further reliability analysis. This finding was found in agreement with previous studies (Altamura & Straub 2014; Chen et al. 2021) that had proposed Lognormal distribution as a suitable distribution to fit fatigue data under variable amplitude loading.

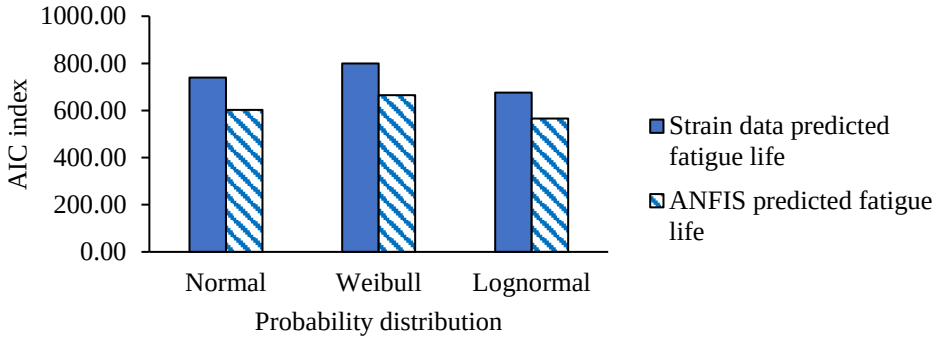

(a)

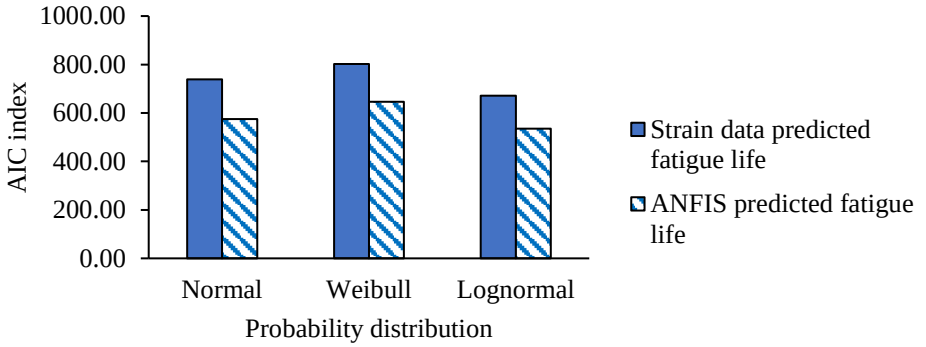

(b)

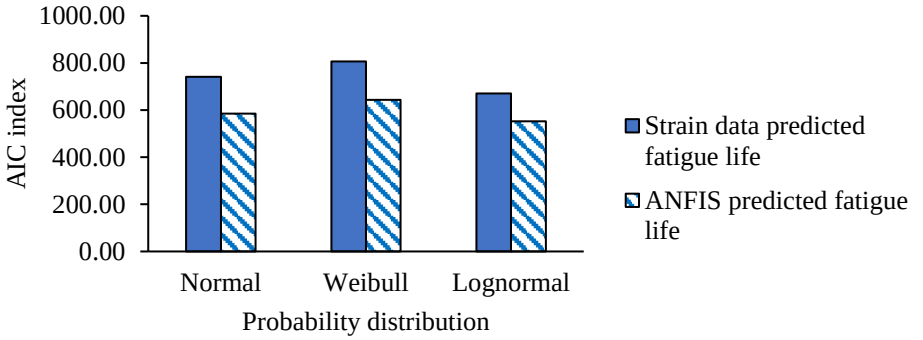

(c)

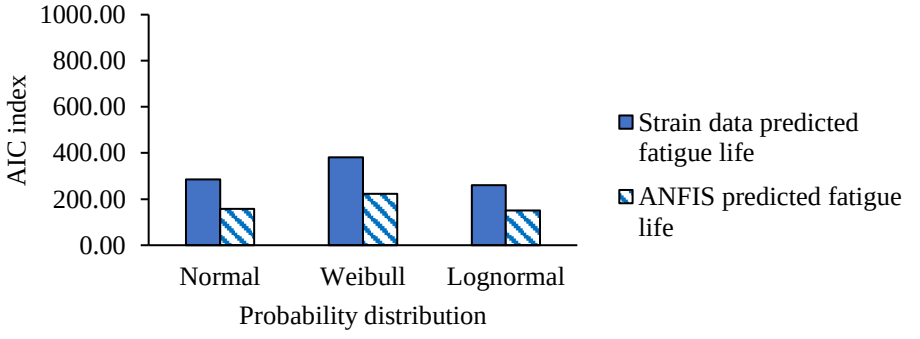

(d)

Figure 4.101 AIC index of probability functions fitted with fatigue data predicted using ANFIS models and strain measurements based on different fatigue models: (a) Coffin-Manson, (b) Morrow, (c) SWT, (d) ESD models

4.4.2 Fatigue Reliability Characteristics of Fatigue Data

The fatigue life data obtained through experimental strain measurement and ANFIS modelling were fitted into Lognormal distribution to obtain the PDFs. Subsequently, CDFs, reliability curves, and hazard curves were computed from the PDFs. Figures 4.102–4.109 illustrate the PDFs, CDFs, reliability curves, and hazard curves from experimental and simulated fatigue life data. In fatigue reliability analysis, the predicted fatigue lives were assumed to be the failure data of coil spring due to fatigue failure. Fatigue reliability analysis is associated with the computation of failure probability of components after a period of service life cycles (Masoudi Nejad et al. 2021). The PDF shows the failure probability of coil spring under random road excitations at specific service life cycles. The CDF is the cumulative failure probability of the coil spring, and the component will definitely experience fatigue failure when the CDF reaches one. Reliability curve is the inverse of CDFs that shows the deterioration of component with increasing service life cycles (Gao & Liu 2021). The reliability curve plays an important role in fatigue reliability analysis to evaluate the rate of deterioration and the hazard level of the component at a specific service life cycle. Lower reliability level of the component indicates a higher probability of fatigue failure. Lastly, the hazard curves provide instantaneous hazard rate of the component at specific service life cycle.

Figure 4.110 compares the PDFs of the experimental and simulated fatigue life data. The PDFs of the Coffin-Manson, Morrow, and SWT strain-life models were very similar. That can be attributed to the zero-mean property of the experimental and simulated strain histories. The removal of mean values of strain histories was necessary for a fair comparison between the experimental and simulated strain histories as the simulated strain histories inherited zero-mean property of vibration signals from the acceleration-strain conversion process (Putra et al. 2015, 2017a). This had, therefore, minimised the mean stress effect in the strain histories and thus the Morrow and SWT strain-life models predicted similar fatigue life with the Coffin-Manson model from the same strain signal, even though under consideration of mean stress effect. Compared to the strain-life models, fatigue life data predicted by ESD model showed sharper peaks with lower mean value. This is because the ESD model predicted lower fatigue lives

compared to other durability models with the consideration of load sequence effect, especially for the highway signals (Kadhim, Abdullah & Ariffin 2012).

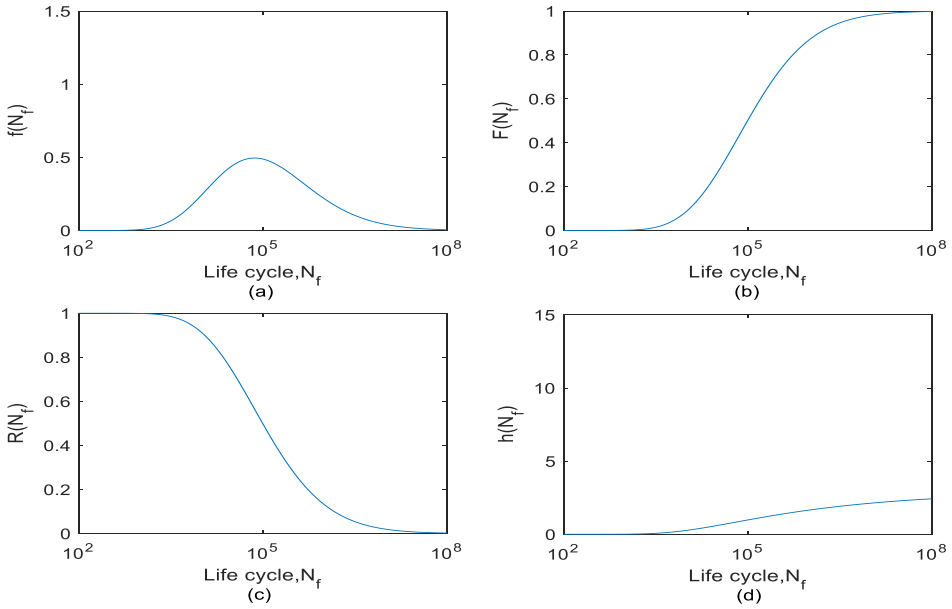

Figure 4.102 Probabilistic-reliability properties of Coffin-Manson-based fatigue life data predicted by strain data measurement: (a) Lognormal probability density function, (b) cumulative density function, (c) reliability curve, (d) hazard curve

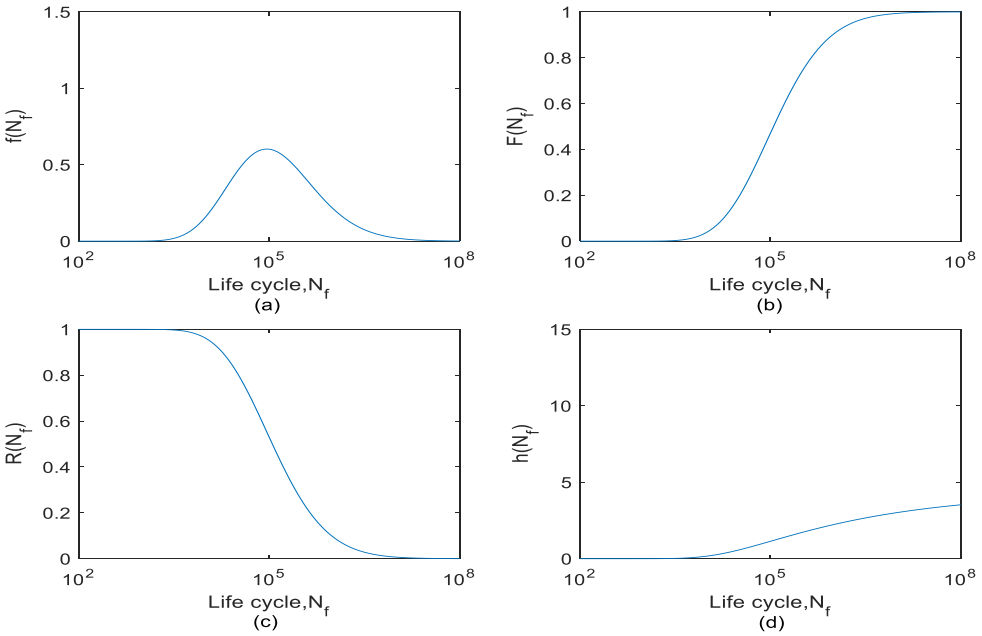

Figure 4.103 Probabilistic-reliability properties of Coffin-Manson-based fatigue life data predicted by ANFIS modelling: (a) Lognormal probability density function, (b) cumulative density function, (c) reliability curve, (d) hazard curve

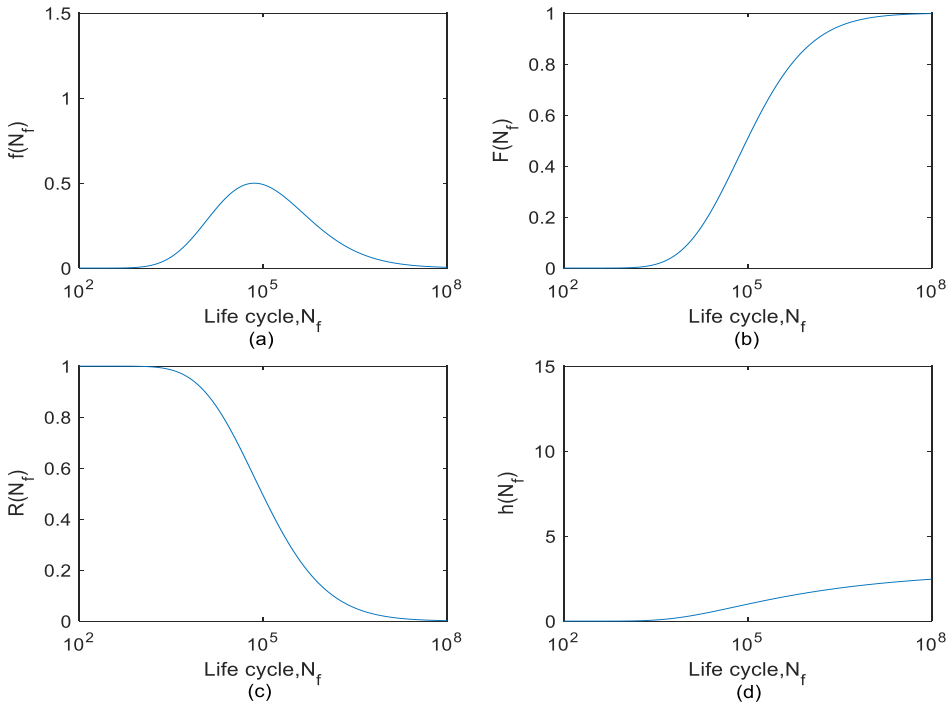

Figure 4.104 Probabilistic-reliability properties of Morrow-based fatigue life data predicted by strain data measurement: (a) Lognormal probability density function, (b) cumulative density function, (c) reliability curve, (d) hazard curve

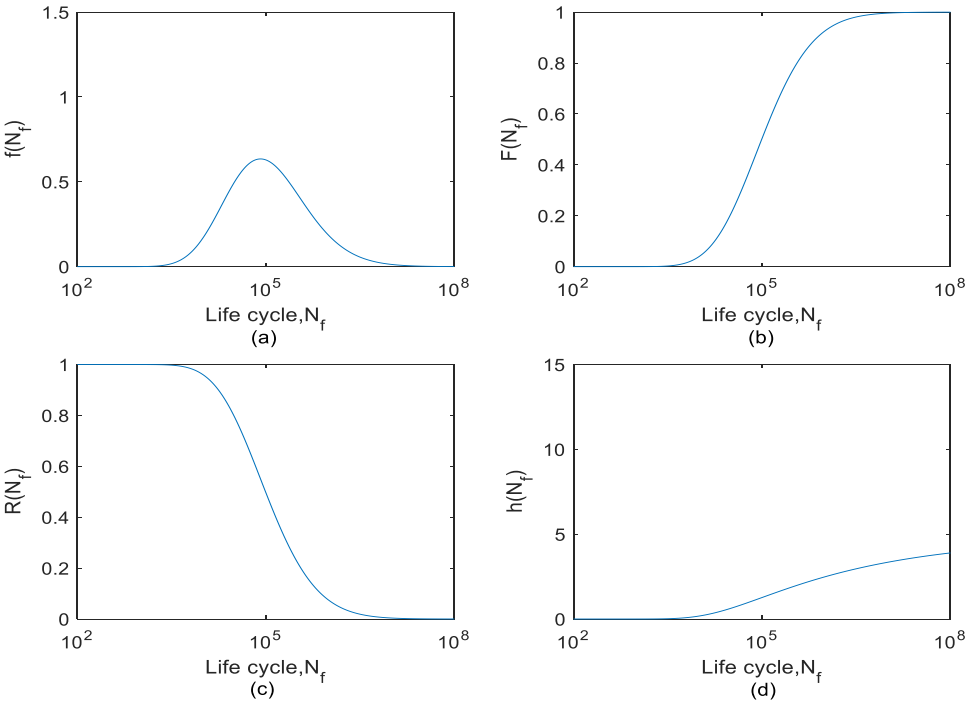

Figure 4.105 Probabilistic-reliability properties of Morrow-based fatigue life data predicted by ANFIS modelling: (a) Lognormal probability density function, (b) cumulative density function, (c) reliability curve, (d) hazard curve

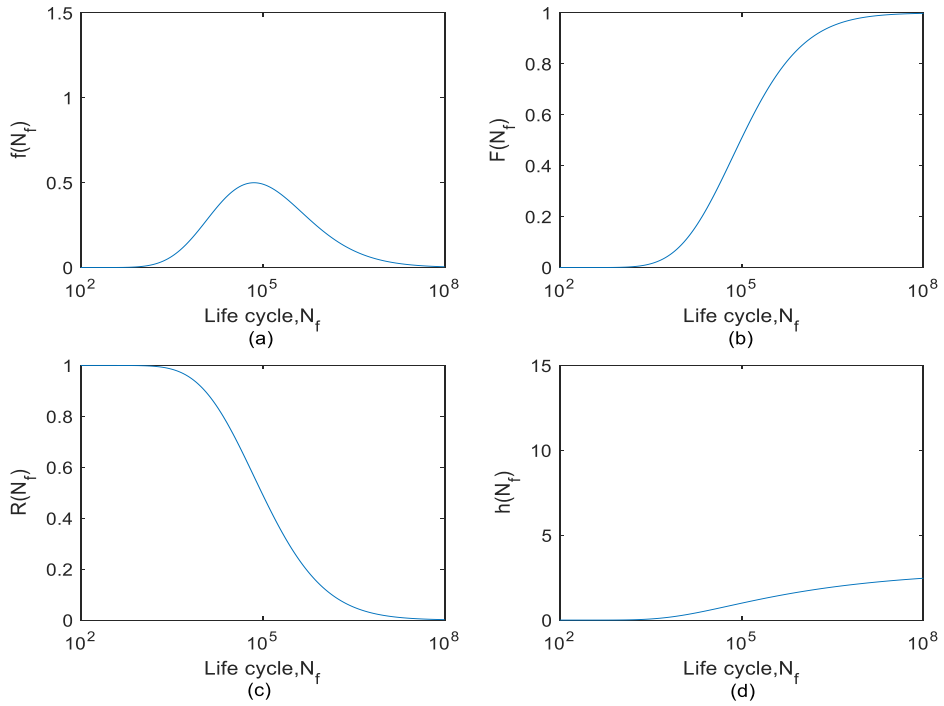

Figure 4.106 Probabilistic-reliability properties of SWT-based fatigue life data predicted by strain data measurement: (a) Lognormal probability density function, (b) cumulative density function, (c) reliability curve, (d) hazard curve

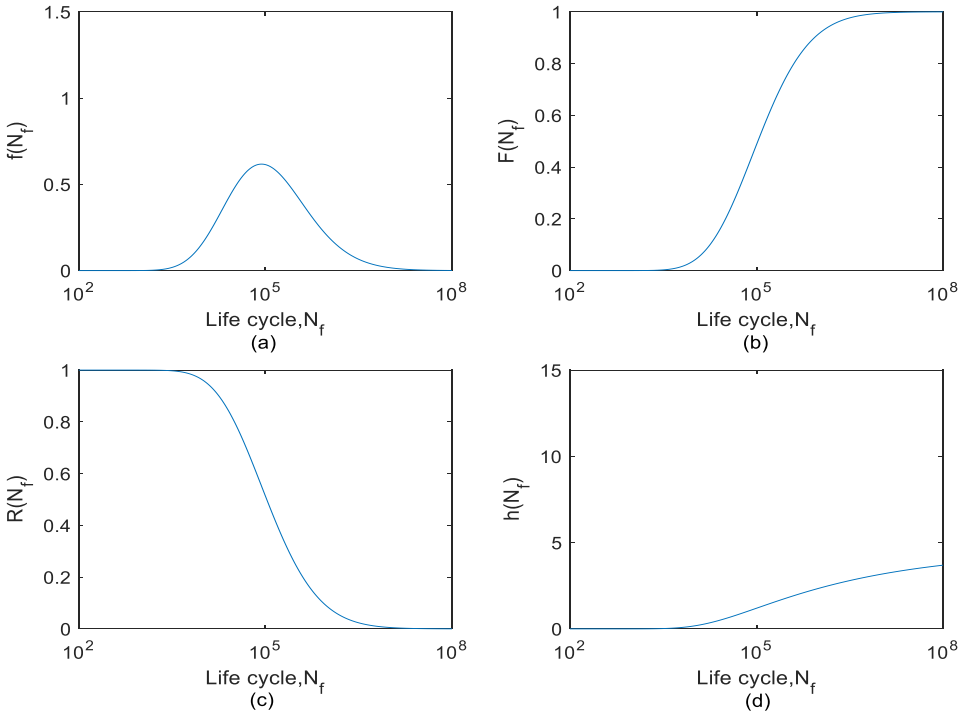

Figure 4.107 Probabilistic-reliability properties of SWT-based fatigue life data predicted by ANFIS modelling: (a) Lognormal probability density function, (b) cumulative density function, (c) reliability curve, (d) hazard curve

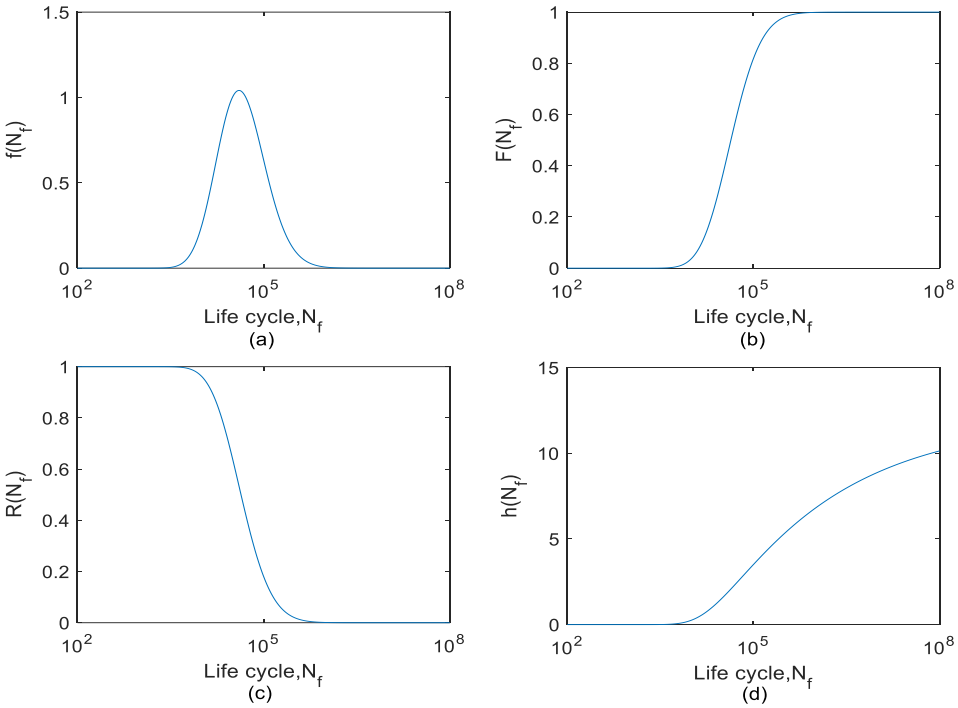

Figure 4.108 Probabilistic-reliability properties of ESD-based fatigue life data predicted by strain data measurement: (a) Lognormal probability density function, (b) cumulative density function, (c) reliability curve, (d) hazard curve

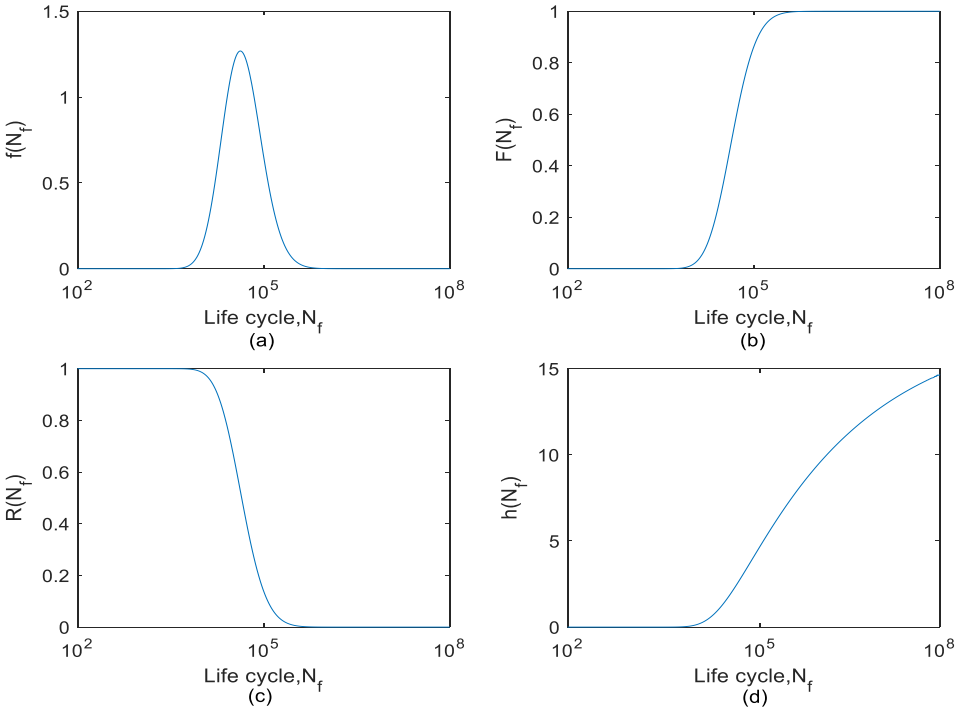

Figure 4.109 Probabilistic-reliability properties of ESD-based fatigue life data predicted by ANFIS modelling: (a) Lognormal probability density function, (b) cumulative density function, (c) reliability curve, (d) hazard curve

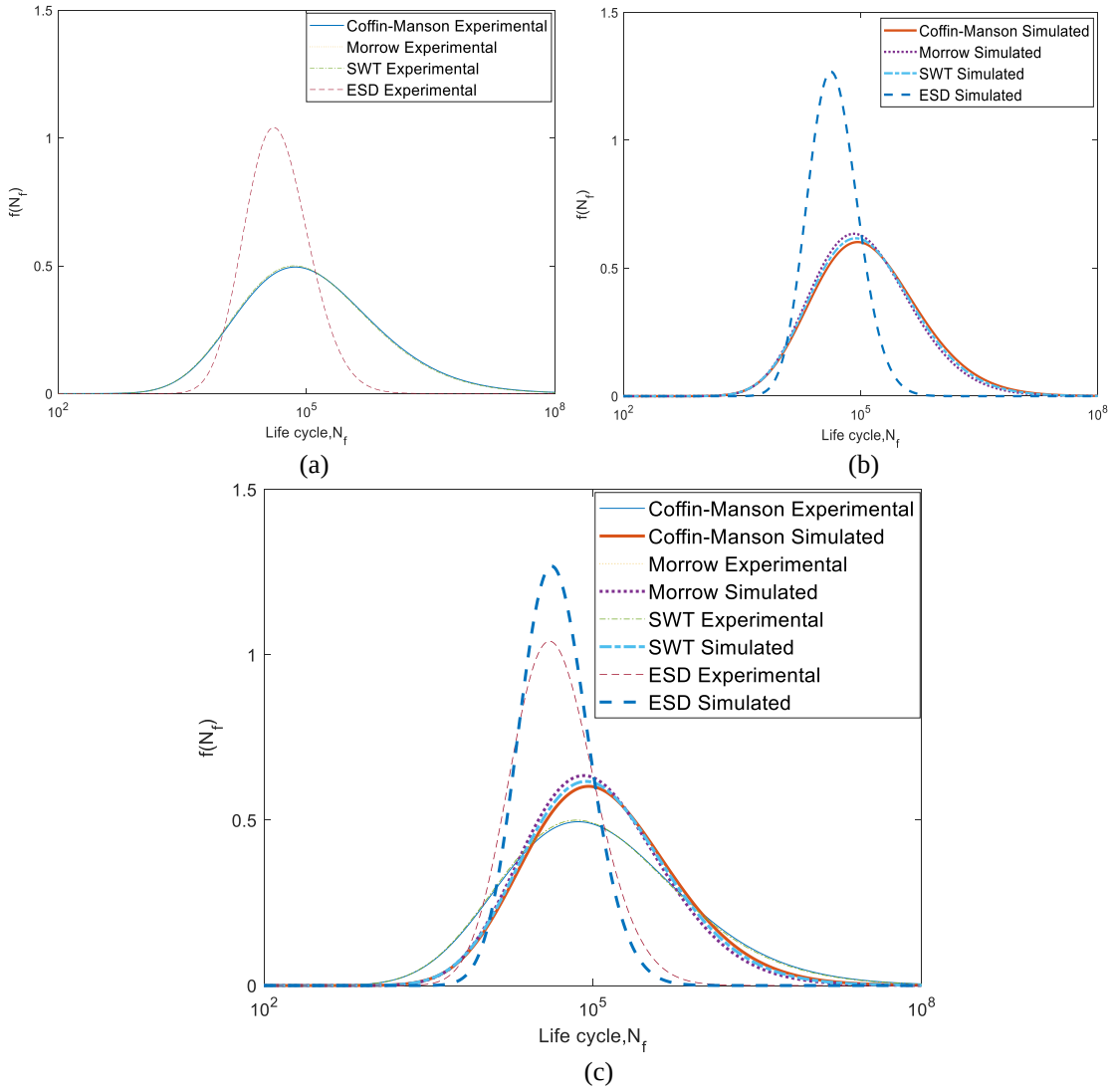

Figure 4.110 Comparison of probability density functions between (a) experimental fatigue life data, (b) simulated fatigue life data and (c) experimental and simulated fatigue life data

Due to the similarity between the PDFs estimated from Coffin-Manson-, Morrow-, and SWT-based fatigue life data, their corresponding CDFs also exhibited similar trends, as shown in Figure 4.111. Similar situation was also found in the reliability and hazard curves as shown in Figures 4.112 and 4.113, respectively. The CDFs represented the cumulative failure probability of the coil spring at given service life cycles (Nasir et al. 2020). Given the sharp PDFs of ESD-based fatigue life data, the CDFs had shown rapid increasing of failure probability associated with fast deterioration of reliability curves after service life of 10^4 blocks of loading. The reliability curves were important to represent the reliability level of the component with

respect to the service life period. Based on the ESD fatigue life data, the reliability level of the component had plunged below 0.2 after 10^5 cycles. Compared to the ESD-based fatigue life data, reliability curves of fatigue life data predicted using strain-life models exhibited slower deterioration after 10^5 cycles of service period. This indicates that load sequence had a significant impact on the fatigue life assessment of variable amplitude loading (Fiedler & Vormwald 2016). The conventional strain-life models tend to provide over-optimistic results and could potentially pose big problems in estimating the reasonable service life of the components.

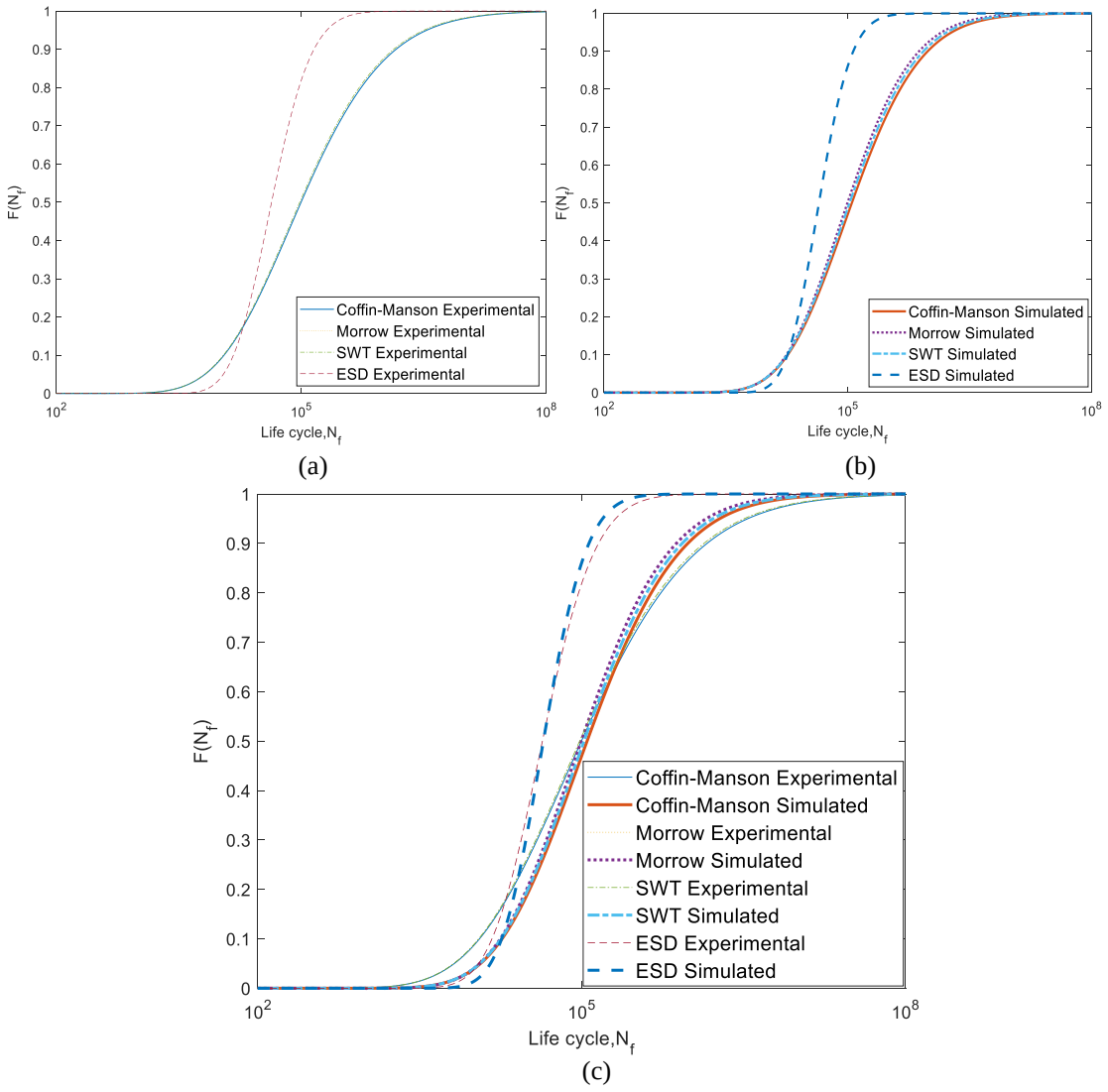

Figure 4.111 Comparison of cumulative density functions between (a) experimental fatigue life data, (b) simulated fatigue life data and (c) experimental and simulated fatigue life data

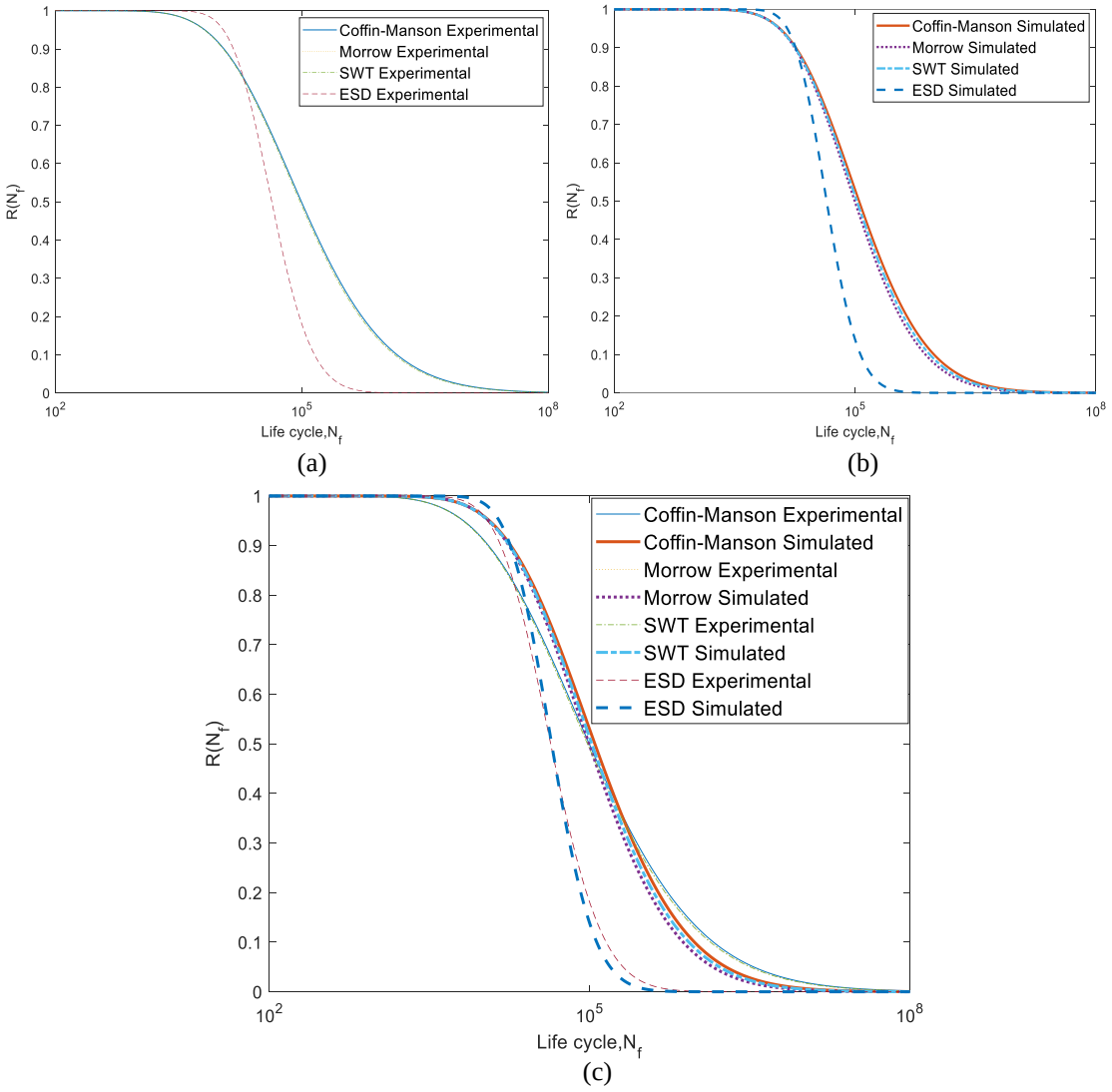

Figure 4.112 Comparison of reliability curves between (a) experimental fatigue life data, (b) simulated fatigue life data and (c) experimental and simulated fatigue life data

The rapid deterioration in ESD-based reliability curves had also greatly boosted the hazard level of coil spring after 10^4 blocks of loading of service period, as shown in Figure 4.113. The hazard levels of the coil spring started to increase rapidly after 10^3 cycles of service period. Compared to the experimental data, the simulated ESD-based fatigue life data estimated a higher rate of increment in hazard level. This is because of the ESD-based ANFIS model which predicted most fatigue lives within the range of 10^4 and 10^5 blocks of loading, as shown in Figure 4.110b. This indicates that the coil spring had a very high chance of fatigue failure after 10^4 blocks of loading. Unlike the ESD-based fatigue life data, the data predicted by strain-life models showed a low

increment rate of hazard level. The hazard levels were kept below 4 after 10^8 cycles of service period, indicating a long service life of coil spring without fatigue failure. This is mainly because the ESD model predicted lower fatigue lives compared to strain-life models after the consideration of load sequence effect.

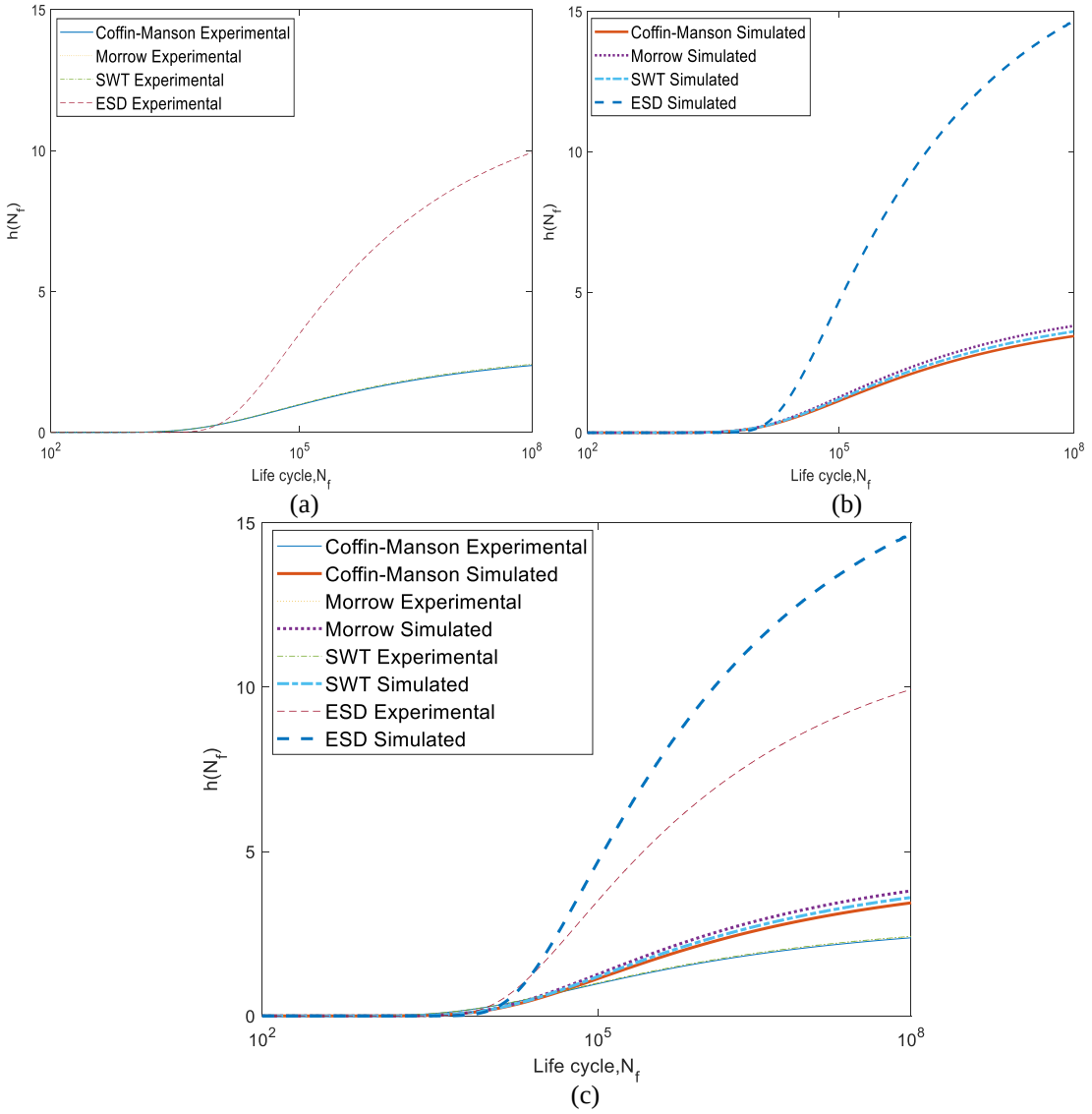

Figure 4.113 Comparison of hazard curves between (a) experimental fatigue life data, (b) simulated fatigue life data and (c) experimental and simulated fatigue life data

4.4.3 Comparison of Mean-Cycle-To-Failure between Simulated and Experimental Data

Mean-cycle-to-failure (McTF) is an important indication of the fatigue reliability properties of coil spring. In fatigue reliability analysis, the McTF represents the expected service period of the components until the first fatigue failure occurs (Nasir et al. 2020). Hence, McTF can also be a good indicator to estimate the reasonable service life of coil springs subjected to random road excitations. The McTFs were computed from the fatigue life datasets predicted by strain measurements and ANFIS models. Table 4.29 shows the estimated McTFs from different fatigue life datasets and the differences between the experimental and simulated McTFs. It was found that the McTF values predicted from ESD-based fatigue life data (4.490-4.529 × 10^4 blocks to failure) were lower than the McTFs prediction from strain-life models (1.086-1.243 × 10^5 blocks to failure), indicating that the load sequence effect in the loading signals significantly decreased the reliability value of coil spring.

Table 4.29 McTF of fatigue life data predicted by strain measurements and ANFIS modelling

Fatigue Life Model	McTF (blocks to failure)		Percentage of difference (%)
	Strain measurement	ANFIS modelling	
Coffin-Manson	1.160×10^5	1.243×10^5	7.1
Morrow	1.127×10^5	1.086×10^5	3.7
Smith-Watson-Topper	1.113×10^5	1.159×10^5	4.1
Effective-Strain-Damage	4.490×10^4	4.529×10^4	0.9

Figures 4.114 and 4.115 show the reliability level of the coil spring at the McTFs obtained from experimental and simulated fatigue life data, respectively. It was found that the coil spring had reliability of around 0.5 at the service life approaching the McTFs. This shows that the McTFs were appropriate to represent reasonable estimation of service life of the coil spring subjected to random road excitations. This estimation is essential to determine the service period duration in which an inspection is needed to be performed on the coil spring. Therefore, it can be suggested that the probabilistic-reliability method could give an acceptable prediction on the service life of the coil spring subjected to random vibrational loading.

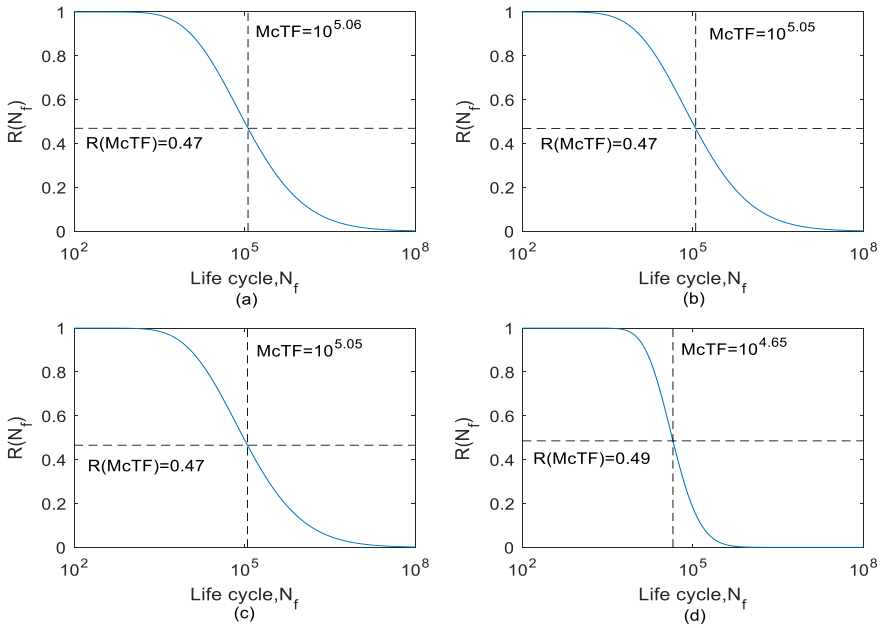

Figure 4.114 Reliability of coil spring at McTF based on experimental fatigue life data obtained from various fatigue models: (a) Coffin-Manson, (b) Morrow, (c) SWT, (d) ESD

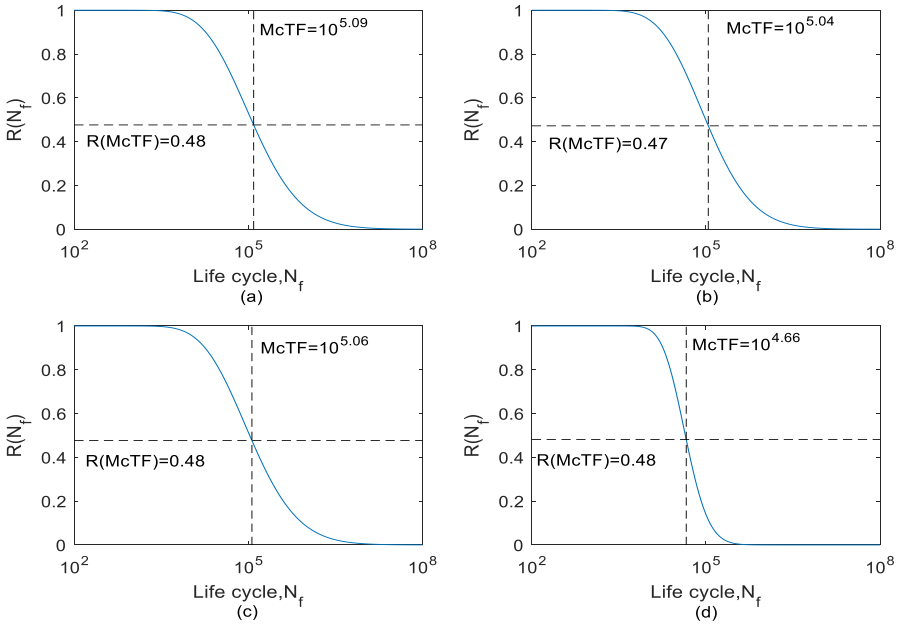

Figure 4.115 Reliability of coil spring at McTF based on simulated fatigue life data obtained from various fatigue models: (a) Coffin-Manson, (b) Morrow, (c) SWT, (d) ESD

To validate the accuracy of trained ANFIS model, the McTFs estimated using fatigue life data predicted by ANFIS modelling were compared with the experimental

fatigue life data. A conservative analysis was performed between the experimental and simulated McTF as shown in Figure 4.116. The results showed a good conservative between the McTFs obtained by experimental and simulation approaches since 100% of McTF data scattered within the 1:2 and 2:1 boundary. This further confirmed the accuracy of predicted fatigue life data using the ANFIS models.

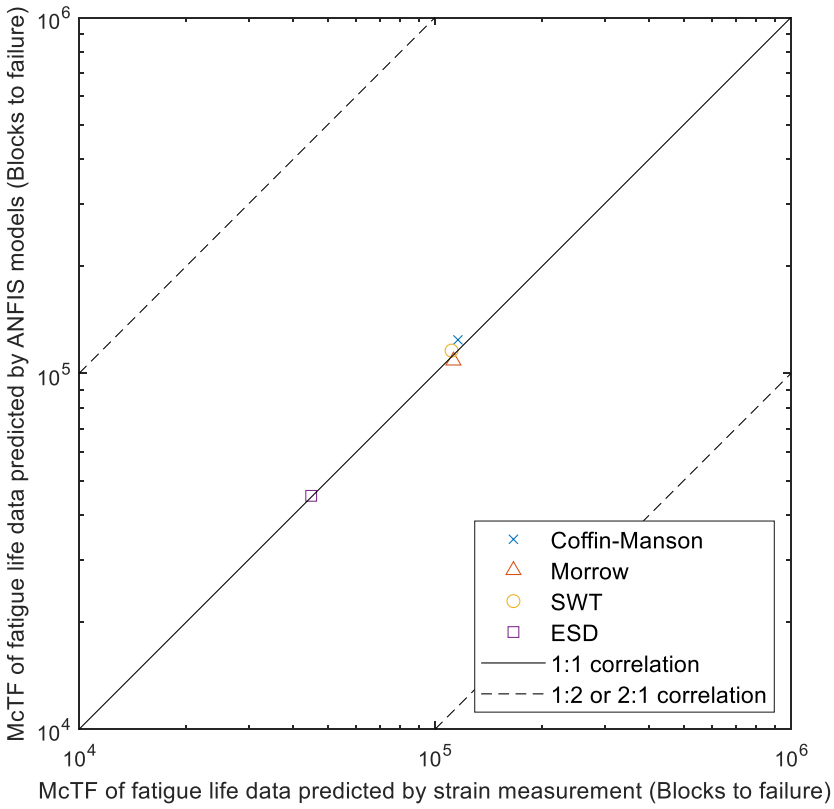

Figure 4.116 Conservative analysis of McTF

On the other hand, the linear relationship between the experimental and simulated McTFs was also determined and the Pearson coefficient (r) of the correlation was calculated. It is used to justify if the simulated McTFs were comparable to the experimental results. Figure 4.117 depicts the linear correlation between McTFs obtained from the simulated and experimental fatigue life data. A good linear correlation between the experimental and simulated McTFs can be observed when an r value above 0.99 was recorded. Data survivability analyses of the McTFs within 90% and 95% confidence intervals were also conducted. Figures 4.118 and 4.119 show the data survivability of the McTF data within 90% and 95% confidence intervals,

respectively. Data survivability of 100% had been recorded within 90% and 95% confidence intervals. The findings were strong evidence to suggest that the trained ANFIS models predicted fatigue lives that matched the experimental results. Therefore, the accuracy of the trained ANFIS models in durability prediction can be validated.

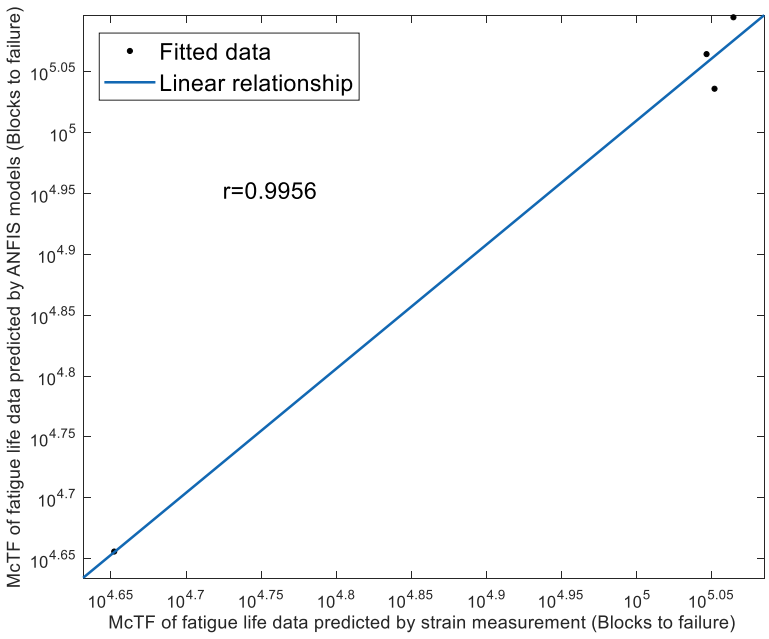

Figure 4.117 Linear correlation and Pearson coefficient (r) value between McTFs obtained from experimental and simulation fatigue data

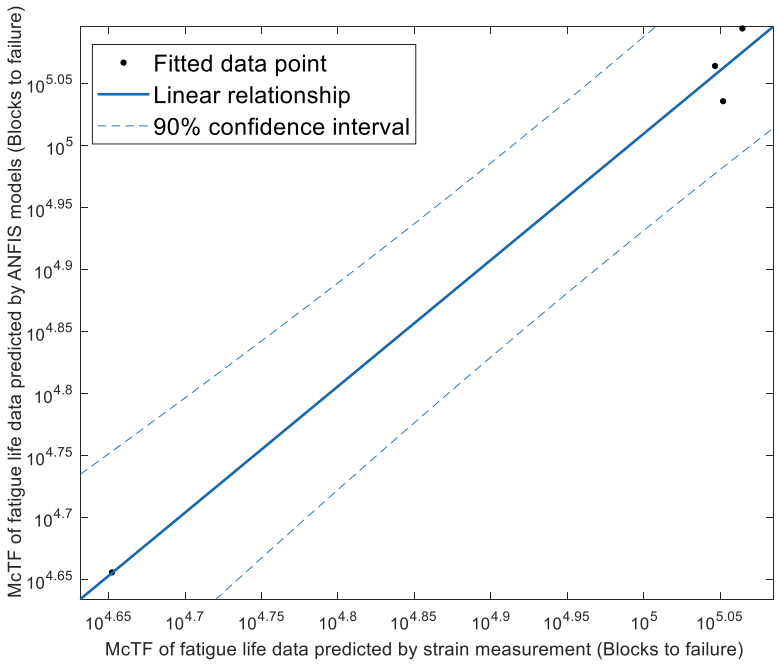

Figure 4.118 McTF data survival analysis with 90% confidence intervals

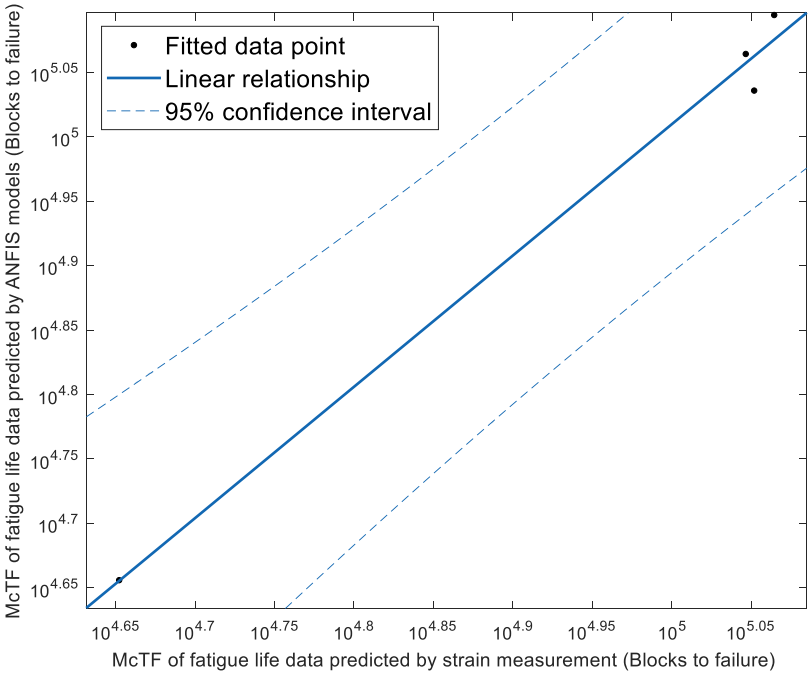

Figure 4.119 McTF data survival analysis with 95% confidence intervals

Figure 4.120 compares the percentage of differences between the experimental and simulated McTFs. Overall, there is a slight difference between the experimental and simulated McTFs with the highest difference of 7.1% recorded in Coffin-Manson-based ANFIS model. Meanwhile, the lowest difference of only 0.9% was found in ESD-based ANFIS model, indicating that the ESD-based ANFIS model predicted fatigue lives that matched the best with the experimental results. This finding agreed with the lowest RMSE of the ESD-based ANFIS model. Hence, it can be concluded that the ESD-based ANFIS model had provided the most accurate durability predictions among the trained ANFIS models. Since the differences in McTF of the models did not exceed 10%, the accuracy of all trained ANFIS models could be validated. In summary, this study has successfully established durability prediction models that provided acceptable fatigue life predictions for suspension coil spring of different designs based on the multifractality and low-frequency energy of vibrational loading signals.

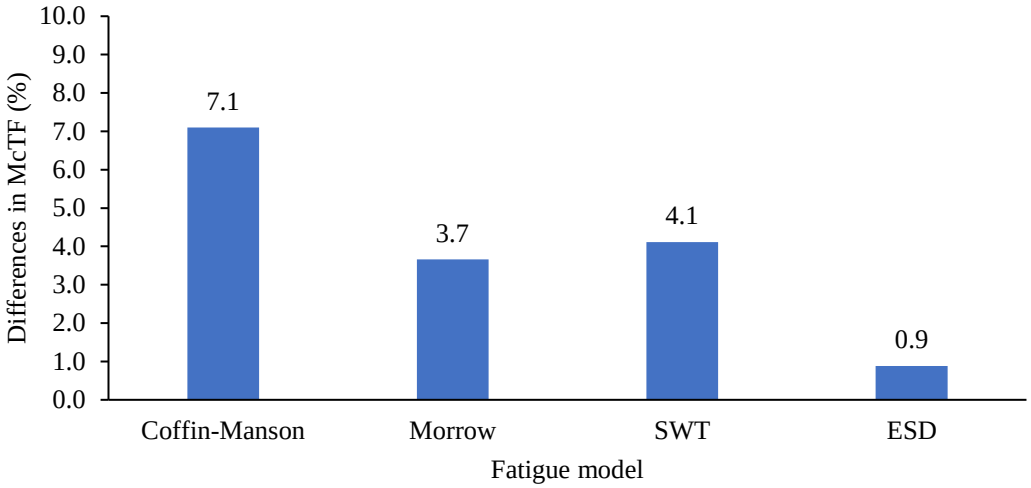

Figure 4.120 Difference in Mean-Cycle-to-Failure (McTF) between fatigue data obtain by ANFIS modelling and strain measurement

4.5 SUMMARY

This chapter has presented the results of the analyses and discussions in the sequence of the three research objectives to achieve the contribution of the work. The two main contributions to knowledge are achieved through this research. The first contribution is the modification of the acceleration-strain conversion model by considering the torsional stress in coil spring, spring curvature effects, and MBD effects between suspension components. The enhanced acceleration-strain conversion model enables a more realistic strain signal generation that matches the experimental results. The second contribution of this research is the establishment of vibration-based fatigue life prediction models for coil spring with different spring designs. Fatigue-related features, including the low-frequency energy and multifractality, are determined from the vibration loading signals of car suspension. ANFIS modelling technique is employed to establish the nonlinear relationship between the input variables and fatigue life of coil spring. Results of the fatigue life conservativity analysis, statistical analysis, and Pearson coefficient determination confirm the accuracy of the established ANFIS models in prediction of the coil springs fatigue life. Finally, the established durability prediction models are further validated using probabilistic-reliability approaches and the results have been convincing.

The established durability prediction models could provide acceptable fatigue life predictions of the coil spring of different designs based on the low-frequency energy and multifractality of vibration signals. This could significantly reduce the need of strain measurement for durability prediction of coil springs which had inconsistence results. Besides that, the established models could also avoid the time consuming MBD simulation to predict the spring responses under vibration loading. Therefore, the durability prediction process of coil spring can be greatly expedited using the proposed models in this thesis.

CHAPTER V

CONCLUSION AND RECOMMENDATIONS

5.1 CONCLUSION

This thesis aims to establish vibration fatigue prediction models for a suspension coil spring with different spring constants using the low-frequency energy and multifractality of the vibration loading signals as the inputs. The main contribution of knowledge is the establishment of a vibration fatigue prediction model using an adaptive neuro-fuzzy inference system (ANFIS) modelling approach, which is achieved with the implementation of these steps:

1. Determine the acceleration-strain conversion model for suspension coil spring from previous models by considering torsional stress, spring curvature effects, and multibody dynamics (MBD) interaction between suspension components.

2. Formulate vibration-based durability prediction models and optimise the models to obtain the most accurate prediction.

3. Validate the established models using probabilistic-reliability approaches and compare the simulation results with experimental results.

The execution of methodology based on the three objectives produced vibration fatigue prediction models that provided acceptable fatigue life prediction for coil springs of different designs from vibration loading signals.

5.1.1 Determine Acceleration-Strain Conversion Model for Strain Generation

The first objective of this thesis focused on the establishment of the acceleration-strain conversion model to generate strain signals for the durability prediction of coil springs through the modification of previous models. The modified acceleration-strain conversion model considered the torsional stress in coil springs and spring curvature effects. A quarter-car MBD model of the suspension system was developed to simulate the spring responses of coil spring under random loading. The generated strain signals using the modified model demonstrated high compatibility with the strain signals collected experimentally. The fatigue-related properties, especially the high amplitude cycles were found to be well preserved in the simulated strain signals. The proposed model was found to have a lower root-mean-square error (RMSE) of 0.42–0.52 compared to the Kong-Abdullah model (1.39–1.80), suggesting that the modifications enhanced the accuracy in predicting the fatigue life of coil springs. Furthermore, it was also found that the simulated strain signals using the proposed model also preserved the load sequence effect as the fatigue lives predicted from the simulated strain signals highly matched the experimental results, with 100% of data survivability within the acceptable boundary. The determination of the acceleration-strain conversion model with significantly improved performance is the first contribution of this research.

5.1.2 Formulation of Vibration-Based Durability Prediction Models

The second objective of this thesis involves the establishment of vibration-based durability prediction models using machine learning modelling method. Using wavelet-based techniques (i.e., Hölder singularity analysis and wavelet leader multifractal analysis), the low-frequency energy and multifractality were characterised from the vibration loading signals, respectively. Both vibration-based parameters, together with the spring constant representing different spring designs, were used as the inputs for ANFIS modelling to establish the relationship of the inputs with the fatigue life of the coil spring. The trained ANFIS models using the fatigue life data predicted by different durability models showed good conservative of fatigue life predictions and were highly correlated with the experimental results as the predicted fatigue lives by the trained ANFIS models recorded the r values above 0.9. Among the ANFIS models, the

effective-strain-damage (ESD)-based ANFIS model achieved 100% of data survivability in the fatigue life conservative analysis, with the highest *r* value of 0.9570 and the lowest RMSE of 0.441. Therefore, it can be confirmed that the ESD-based ANFIS model provides the most accurate fatigue life prediction. The ANFIS-based model presents an alternative for fatigue life assessment of a coil spring without the need for strain measurement.

5.1.3 Validation of Trained ANFIS Model using Probabilistic-Reliability Method

In order to validate the trained ANFIS models, the fatigue reliability properties of the fatigue life data predicted by the models were compared with the experimental fatigue life data obtained through strain measurements. Through the computation of Akaike's information criterion (AIC) indices, the Lognormal distribution was confirmed to be the most appropriate probability distribution that fitted the fatigue life data. Fatigue reliability properties of the fatigue life data, including the cumulative density functions, reliability curves, and hazard curves were computed from the probability density functions of the data. The results showed a good correlation between the simulated and experimental fatigue life data, with an *r* value of 0.9956. The differences of McTFs between the simulated and experimental data below 10% were recorded. This indicated that the trained ANFIS models provided fatigue life predictions that highly matched the experimental results. The least McTF difference of 0.9% was found in the ESD-based ANFIS model, confirming that the model was the most accurate model. These findings contributed to statistical validations of the established vibration fatigue prediction models and determined the most accurate model for durability prediction of the coil springs.

5.2 RESEARCH CONTRIBUTIONS

Fatigue life assessment for suspension coil springs with conventional time-domain approaches, such as strain-life methods, often requires high experimental costs and long computational time. Furthermore, the acquisition of accurate strain data from the suspension coil spring with a very limited workspace and complex geometry is a difficult task. Therefore, this study proposed vibration fatigue prediction models with

low-frequency energy, multifractality of vibration loading, and spring constant as the inputs. The established models reduced the dependence on the strain data measurement for durability analysis while providing accurate fatigue life prediction. With the established prediction models, the durability analysis of coil springs can be greatly accelerated as the complex process of durability analysis can be skipped. The research outcomes offer an alternative to the automotive industry in solving issues related to prototyping costs and time. This will have significant impacts on the automotive industry by accelerating the development process of the suspension system of vehicles at lower cost. In addition, the study also provides a better understanding of the durability of the vehicle vibration characteristics towards automobile design by means of the fatigue life of a suspension system.

5.3 RECOMMENDATIONS

There are several recommendations for future works to improve current research, which are:

1. The consideration of multiaxial loading in the durability assessment of coil springs is suggested. This is because the springs are subjected to multiaxial loading under realistic circumstances given their helical geometry, which results in complex stress states. Therefore, it is recommended to collect multiaxial strain signals using rosettes and consider the effect of multiaxial loading during durability analysis.

2. The modelling of fatigue life data for accurate durability prediction using machine learning approaches often requires a large amount of data. Therefore, data optimisation is needed to prepare input data of good quality for the modelling process. It is suggested in future work to characterise the fatigue life data based on different vibration statistical behaviours to select the desired dataset.

3. The durability prediction models proposed in this study were developed using the vibration features, including the low-frequency energy and multifractality of

vibration loading signals. This can be further expanded by including additional parameters that are related to the fatigue life of coil springs, such as material properties, damping of suspension, tyre stiffness, and others in order to achieve a more feasible suspension design. Apart from that, feature classification is also needed to differentiate different features for a more detailed understanding of the influence of vibration loading towards the durability of coil springs.

4. Other machine learning modelling techniques (e.g., artificial neural network) can be used to establish the relationship between the loading characteristics and the fatigue life of coil springs. The focus will be emphasised on the pattern recognition of fatigue life data in a large sample size to understand the non-linear behaviours between loading parameters and durability properties using different modelling techniques.

5. The established vibration fatigue prediction model can be applied in the design of highly durable coil springs. This is essential to evaluate the effectiveness of the model in facilitating the development process of coil springs. Conventional time-domain approaches can be used as the reference technique to assess the effectiveness of the new technique.

6. This study primarily focused on the application of phenomenological models for fatigue life prediction of coil spring. A physically-based constitutive fatigue life prediction model that can consider the plasticity for fatigue life prediction is suggested for future work.

REFERENCES

Abdelkareem, M.A.A., Xu, L., Ali, M.K.A., Elagouz, A., Mi, J., Guo, S., Liu, Y. & Zuo, L. 2018. Vibration energy harvesting in automotive suspension system: A detailed review. *Applied Energy* 229: 672–699.

Abdullah, L., Singh, S.S.K., Abdullah, S., Azman, A.H. & Ariffin, A.K. 2021. Fatigue reliability and hazard assessment of road load strain data for determining the fatigue life characteristics. *Engineering Failure Analysis* 123: 105314.

Abdullah, S., Choi, J.C., Giacomin, J.A. & Yates, J.R. 2006. Bump extraction algorithm for variable amplitude fatigue loading. *International Journal of Fatigue* 28(7): 675–691.

Abdullah, S., Nizwan, C.K.E. & Nuawi, M.Z. 2009. A study of fatigue data editing using the Short-Time Fourier Transform (STFT). *American Journal of Applied Sciences* 6(4): 565–575.

Abidin, M.I.Z., Mahmud, J., Latif, M.J.A. & Jumahat, A. 2013. Experimental and Numerical Investigation of SUP12 Steel Coil Spring. *Procedia Engineering* 68: 251–257.

Akiniwa, Y., Stanzl-Tschegg, S., Mayer, H., Wakita, M. & Tanaka, K. 2008. Fatigue strength of spring steel under axial and torsional loading in the very high cycle regime. *International Journal of Fatigue* 30(12): 2057–2063.

Alhasan, A., White, D.J. & De Brabanterb, K. 2016. Continuous wavelet analysis of pavement profiles. *Automation in Construction* 63: 134–143.

Aljarah, I., Faris, H. & Mirjalili, S. 2018. Optimizing connection weights in neural networks using the whale optimization algorithm. *Soft Computing* 22(1): 1–15.

Almalki, S.J. & Nadarajah, S. 2014. Modifications of the Weibull distribution: A review. *Reliability Engineering & System Safety* 124: 32–55.

Altamura, A. & Straub, D. 2014. Reliability assessment of high cycle fatigue under variable amplitude loading: Review and solutions. *Engineering Fracture Mechanics* 121–122: 40–66.

ALTobi, M.A.S., Bevan, G., Wallace, P., Harrison, D. & Ramachandran, K.P. 2019. Fault diagnosis of a centrifugal pump using MLP-GABP and SVM with CWT. *Engineering Science and Technology, an International Journal* 22(3): 854–861.

Amin, W., Davis, M.R., Thomas, G.A. & Holloway, D.S. 2013. Analysis of wave slam induced hull vibrations using continuous wavelet transforms. *Ocean Engineering* 58: 154–166.

Arshad, A. Bin, Nazir, A. & Jeng, J.-Y. 2022. Design and performance evaluation of multi-helical springs fabricated by Multi Jet Fusion additive manufacturing technology. *The International Journal of Advanced Manufacturing Technology* 118(1): 195–206.

Bajric, R., Zuber, N., Skrimpas, G.A. & Mijatovic, N. 2016. Feature extraction using discrete wavelet transform for gear fault diagnosis of wind turbine gearbox. *Shock and Vibration* 2016: 1–10.

Balkwill, J. 2018. Chapter 7 - Suspension Kinematics. Dlm. Balkwill, J. B. T.-P. V. D. (pnyt.). hlm. 197–239. Butterworth-Heinemann.:

Banerjee, S., Balamurugan, V. & Krishnakumar, R. 2016. Ride Comfort Analysis of Math Ride Dynamics Model of Full Tracked Vehicle with Trailing Arm Suspension. *Procedia Engineering* 144: 1110–1118.

Barbieri, N., de Sant'Anna Vitor Barbieri, G., Martins, B.M., de Sant'Anna Vitor Barbieri, L. & de Lima, K.F. 2019. Analysis of automotive gearbox faults using vibration signal. *Mechanical Systems and Signal Processing* 129: 148–163.

Barelli, L., Barluzzi, E., Bidini, G. & Bonucci, F. 2012. Cylinders diagnosis system of a 1MW internal combustion engine through vibrational signal processing using DWT technique. *Applied Energy* 92: 44–50.

Benabou, L., Nguyen-Van, T.A., Tao, Q.B., Le, V.N., Ould Ouali, M. & Nguyen-Xuan, H. 2020. Methodology for DIC-based evaluation of the fracture behaviour of solder materials under monotonic and creep loadings. *Engineering Fracture Mechanics* 239: 107285.

Benasciutti, D. & Tovo, R. 2018. Frequency-based analysis of random fatigue loads: Models, hypotheses, reality. *Materialwissenschaft und Werkstofftechnik* 49(3): 345–367.

Bergh, F., Silva, G.C., Silva, C. & Paiva, P. 2021. Analysis of an automotive coil spring fracture. *Engineering Failure Analysis* 129: 105679.

Bi, F., Ma, T. & Wang, X. 2019. Development of a novel knock characteristic detection method for gasoline engines based on wavelet-denoising and EMD decomposition. *Mechanical Systems and Signal Processing* 117: 517–536.

Bianchi, S. & Pianese, A. 2018. Time-varying Hurst–Hölder exponents and the dynamics of (in)efficiency in stock markets. *Chaos, Solitons & Fractals* 109: 64–75.

Bianco, R. 2019. Enhanced Coil Spring Modeling in Passenger Car Suspension for Improved Target Setting Process. *SAE International Journal of Passenger Cars - Mechanical Systems* 12(1): 51–62.

Brancati, R., Rocca, E. & Savino, S. 2015. A gear rattle metric based on the wavelet multi-resolution analysis: Experimental investigation. *Mechanical Systems and Signal Processing* 50–51: 161–173.

Branco, R., Prates, P.A., Costa, J.D., Borrego, L.P., Berto, F., Kotousov, A. & Antunes, F. V. 2019. Rapid assessment of multiaxial fatigue lifetime in notched components using an averaged strain energy density approach. *International Journal of Fatigue* 124: 89–98.

Burdzik, R. 2017. Novel method for research on exposure to nonlinear vibration transferred by suspension of vehicle. *International Journal of Non-Linear Mechanics* 91: 170–180.

Burger, M., Dreßler, K. & Speckert, M. 2021. Load assumption process for durability design using new data sources and data analytics. *International Journal of Fatigue* 145: 106116.

Cai, Y., Zhao, Y., Ma, X., Yang, Z. & Ding, Y. 2018. An Extended Model for Fatigue Life Prediction and Acceleration Considering Load Frequency Effect. *IEEE Access* 6: 21064–21074.

Cain, M.K., Zhang, Z. & Yuan, K.-H. 2017. Univariate and multivariate skewness and kurtosis for measuring nonnormality: Prevalence, influence and estimation. *Behavior Research Methods* 49(5): 1716–1735.

Čakmak, D., Tomičević, Z., Wolf, H., Božić, Ž., Semenski, D. & Trapić, I. 2019. Vibration fatigue study of the helical spring in the base-excited inerter-based isolation system. *Engineering Failure Analysis* 103: 44–56.

Calderon-Uriszar-Aldaca, I. & Biezma, M. V. 2017. A plain linear rule for fatigue analysis under natural loading considering the sequence effect. *International Journal of Fatigue* 103: 386–394.

de Campos Souza, P.V. 2020. Fuzzy neural networks and neuro-fuzzy networks: A review the main techniques and applications used in the literature. *Applied Soft Computing* 92: 106275.

Canuto, C., Tabacco, A. & Urban, K. 1999. The Wavelet Element Method: Part I. Construction and Analysis. *Applied and Computational Harmonic Analysis* 6(1): 1–52.

Canuto, C., Tabacco, A. & Urban, K. 2000. The Wavelet Element Method Part II. Realization and Additional Features in 2D and 3D. *Applied and Computational Harmonic Analysis* 8(2): 123–165.

Cao, M., Radzieński, M., Xu, W. & Ostachowicz, W. 2014. Identification of multiple damage in beams based on robust curvature mode shapes. *Mechanical Systems and Signal Processing* 46(2): 468–480.

Capponi, L., Česnik, M., Slavič, J., Cianetti, F. & Boltežar, M. 2017. Non-stationarity index in vibration fatigue: Theoretical and experimental research. *International Journal of Fatigue* 104: 221–230.

Cavanaugh, J.E. & Neath, A.A. 2019. The Akaike information criterion: Background, derivation, properties, application, interpretation, and refinements. *WIREs Computational Statistics* 11(3): e1460.

Champion, R. & Champion, W.L. 2011. Departure from linear mechanical behaviour of a helical spring. *Mathematical and Computer Modelling* 53(5): 915–926.

Chauhan, P., Sah, K. & Kaushal, R. 2021. Design, modeling and simulation of suspension geometry for formula student vehicles. *Materials Today: Proceedings* 43: 17–27.

Chen, D., Fan, J. & Zhang, F. 2013. Extraction the unbalance features of spindle system using wavelet transform and power spectral density. *Measurement* 46(3): 1279–1290.

Chen, J., Li, Z., Pan, J., Chen, G., Zi, Y., Yuan, J., Chen, B. & He, Z. 2016. Wavelet transform based on inner product in fault diagnosis of rotating machinery: A review. *Mechanical Systems and Signal Processing* 70–71: 1–35.

Chen, W.-H. & Wu, C.-W. 1995. A spline wavelets element method for frame structures vibration. *Computational Mechanics* 16(1): 11–21.

Chen, X. 2014. Analysis of crosswind fatigue of wind-excited structures with nonlinear aerodynamic damping. *Engineering Structures* 74: 145–156.

Chen, Z., Li, T., Xue, X., Zhou, Y. & Jing, S. 2021. Fatigue Reliability Analysis and Optimization of Vibrator Baseplate Based on Fuzzy Comprehensive Evaluation Method. *Engineering Failure Analysis*: 105357.

Chetan, J., Khushbu, P. & Nauman, M. 2012. The fatigue analysis of a vehicle suspension system – a review article. *International Journal of Advanced Computer Research* 2(6): 386 – 390.

Cianetti, F., Palmieri, M., Braccesi, C. & Morettini, G. 2018. Correction formula approach to evaluate fatigue damage induced by non-Gaussian stress state. *Procedia Structural Integrity* 8: 390–398.

Cianetti, F., Palmieri, M., Slavič, J., Braccesi, C. & Morettini, G. 2017. The effort of the dynamic simulation on the fatigue damage evaluation of flexible mechanical systems loaded by non-Gaussian and non stationary loads. *International Journal of Fatigue* 103: 60–72.

Cruz, P., Mendes, A. & Magalhães, F.D. 2001. Using wavelets for solving PDEs: an adaptive collocation method. *Chemical Engineering Science* 56(10): 3305–3309.

Dai, Y., Zhang, H., Mao, X. & Shang, P. 2018. Complexity–entropy causality plane based on power spectral entropy for complex time series. *Physica A: Statistical Mechanics and its Applications* 509: 501–514.

Das, S., Nayak, B., Sarangi, S.K. & Biswal, D.K. 2016. Condition Monitoring of Robust Damage of Cantilever Shaft Using Experimental and Adaptive Neuro-fuzzy Inference System (ANFIS). *Procedia Engineering* 144: 328–335.

Deshmukh, A.R., Venkatachalam, G. & Saraf, M.R. 2019. Fatigue life prediction of joggle weld joint using virtual strain gauge and its validation through experiments. *MECHANICS & INDUSTRY* 19(6).

Dong, Y. & Dave, V. 2020. Experimentation for Design Improvements for Coil Spring in the Independent Suspension. *SAE Technical Paper 2020-01-0503*: 9.

Dong, Y., Garbatov, Y. & Guedes Soares, C. 2021. Strain-based fatigue reliability assessment of welded joints in ship structures. *Marine Structures* 75: 102878.

Dowling, N.E. 2004. Mean Stress Effects in Stress-Life and Strain-Life Fatigue. *SAE Technical Paper 2004-01-2227*: 13.

Dragoni, E. & Bagaria, W.J. 2011. Mechanical design of bimaterial helical springs with circular cross-section. *Journal of Strain Analysis for Engineering Design* 46(4): 304–314.

Du, W., Tao, J., Li, Y. & Liu, C. 2014. Wavelet leaders multifractal features based fault diagnosis of rotating mechanism. *Mechanical Systems and Signal Processing* 43(1): 57–75.

Du, Y., Wei, J., Yuan, J., Lai, Y. & Sun, D. 2020. Experimental research on fatigue behavior of prestressed concrete beams under constant-amplitude and variable-amplitude fatigue loading. *Construction and Building Materials* 259: 119852.

DuQuesnay, D.L., Pompetzki, M.A. & Topper, T.H. 1993. Fatigue Life Prediction for Variable Amplitude Strain Histories. *SAE Technical Paper 930400*: 13.

DuQuesnay, D.L., Topper, T.H., Yu, M.T. & Pompetzki, M.A. 1992. The effective stress range as a mean stress parameter. *International Journal of Fatigue* 14(1): 45–50.

Duraffourg, S., Argoul, P., Vasseur, E. & Cumunel, G. 2015. New Spot Weld Fatigue Criteria and Fatigue Data Editing Technique. *Procedia Engineering* 133: 433–453.

El-Zeghayar, M., Topper, T. & Bonnen, J.J. 2013. Derivation of Effective Strain-Life Data, Crack Closure Parameters and Effective Crack Growth Data from Smooth Specimen Fatigue Tests. *SAE Int. J. Mater. Manf.* 6(3): 576–588.

El-Zeghayar, M., Topper, T.H. & Soudki, K.A. 2011. A model of crack opening stresses in variable amplitude loading using smooth specimen fatigue test data for three steels. *International Journal of Fatigue* 33(10): 1337–1350.

Farrahi, G.H., Ahmadi, A. & Reza Kasyzadeh, K. 2020. Simulation of vehicle body spot weld failures due to fatigue by considering road roughness and vehicle velocity. *Simulation Modelling Practice and Theory* 105: 102168.

Fattahi, H., Shojaee, S., Farsangi, M.A.E. & Mansouri, H. 2013. Hybrid Monte Carlo simulation and ANFIS-subtractive clustering method for reliability analysis of the excavation damaged zone in underground spaces. *Computers and Geotechnics* 54: 210–221.

Feng, Y., Gao, C., He, Y., An, T., Fan, C. & Zhang, H. 2016. Investigation on tension–tension fatigue performances and reliability fatigue life of T700/MTM46 composite laminates. *Composite Structures* 136: 64–74.

Fernández-Martínez, M. & Sánchez-Granero, M.A. 2015. How to calculate the Hausdorff dimension using fractal structures. *Applied Mathematics and Computation* 264: 116–131.

Fiedler, M. & Vormwald, M. 2016. Considering fatigue load sequence effects by applying the Local Strain Approach and a fracture mechanics based damage parameter. *Theoretical and Applied Fracture Mechanics* 83: 31–41.

Fu, B., Zhao, J., Li, B., Yao, J., Mouafo Teifouet, A.R., Sun, L. & Wang, Z. 2020. Fatigue reliability analysis of wind turbine tower under random wind load. *Structural Safety* 87: 101982.

Gan, L., Wu, H. & Zhong, Z. 2021. Multiaxial fatigue life prediction based on a simplified energy-based model. *International Journal of Fatigue* 144: 106036.

Gandhi, P., Adarsh, S. & Ramachandran, K.I. 2017. Performance Analysis of Half Car Suspension Model with 4 DOF using PID, LQR, FUZZY and ANFIS Controllers. *Procedia Computer Science* 115: 2–13.

Gao, K. & Liu, G. 2021. Novel nonlinear time-varying fatigue reliability analysis based on the probability density evolution method. *International Journal of Fatigue* 149: 106257.

Gates, N.R. & Fatemi, A. 2018. Multiaxial variable amplitude fatigue life analysis using the critical plane approach, Part II: Notched specimen experiments and life estimations. *International Journal of Fatigue* 106: 56–69.

Gonçalves, V.R.M., Canale, L.C.F., Leskovšek, V. & Podgornik, B. 2016. Influence of Cryogenic Treatment on the Fracture Toughness of Conventional and Super Clean Spring Steels. *SAE Technical Paper 2016-36-0064*: 5.

Gu, D., Kim, J., Kelimu, T., Huh, S.-C. & Choi, B.-K. 2012. Evaluation of the use of envelope analysis and DWT on AE signals generated from degrading shafts. *Materials Science and Engineering: B* 177(19): 1683–1690.

Hariharan, G. & Kannan, K. 2014. Review of wavelet methods for the solution of reaction–diffusion problems in science and engineering. *Applied Mathematical Modelling* 38(3): 799–813.

He, B., Wang, S. & Gao, F. 2010. Failure analysis of an automobile damper spring tower. *Engineering Failure Analysis* 17(2): 498–505.

Henkel, M., Weijtjens, W. & Devriendt, C. 2019. Validation of Virtual Sensing on Subsoil Strain Data of An Offshore Wind Turbine. *8TH IOMAC INTERNATIONAL OPERATIONAL MODAL ANALYSIS CONFERENCE*: 765–774.

Heyes, A.M. 1998. Automotive component failures. *Engineering Failure Analysis* 5(2): 129–141.

Hoeltgebaum, T., Luft, R., Elisii, J. & Vieira, R. 2012. A Design Comparison between Coil Springs and Torsion Bars. *SAE Technical Paper 2012-36-0172*: 9.

Horn, J.-T., Krokstad, J.R. & Leira, B.J. 2019. Impact of model uncertainties on the fatigue reliability of offshore wind turbines. *Marine Structures* 64: 174–185.

Huang, Y.-S., Huang, C.-D. & Ho, J.-W. 2017. A customized two-dimensional extended warranty with preventive maintenance. *European Journal of Operational Research* 257(3): 971–978.

Idris, R., Abdullah, S., Thamburaja, P. & Omar, M.Z. 2018. The need to generate entropy characteristics for fatigue life prediction in low-carbon steel. *Journal of the Brazilian Society of Mechanical Sciences and Engineering* 40(9): 409.

Ince, A. & Glinka, G. 2011. A modification of Morrow and Smith–Watson–Topper mean stress correction models. *Fatigue & Fracture of Engineering Materials & Structures* 34(11): 854–867.

Iriarte, X., Aginaga, J., Gainza, G., Ros, J. & Bacaicoa, J. 2021. Optimal strain-gauge placement for mechanical load estimation in circular cross-section shafts. *Measurement* 174: 108938.

Jadhav, P., Rajguru, G., Datta, D. & Mukhopadhyay, S. 2020. Automatic sleep stage classification using time–frequency images of CWT and transfer learning using convolution neural network. *Biocybernetics and Biomedical Engineering* 40(1): 494–504.

Janssens, K.G.F. 2020. Universal cycle counting for non-proportional and random fatigue loading. *International Journal of Fatigue* 133: 105409.

Jin, C., Ran, Y., Wang, Z., Huang, G., Xiao, L. & Zhang, G. 2020. Reliability analysis of gear rotation meta-action unit based on Weibull and inverse Gaussian competing failure process. *Engineering Failure Analysis* 117: 104953.

Julius S. Bendat & Piersol, A.G. 2010. Random Data: Analysis and Measurement Procedures. Edisi ke-4. John Wiley & Son: New York, US.

Juvinall, R.C. & Marshek, K.M. 2017. Fundamentals of Machine Component Design. Edisi ke-6th. John Wiley & Sons, Ltd: New York, US.

Kadhim, N.A., Abdullah, S. & Ariffin, A.K. 2012. Effective strain damage model associated with finite element modelling and experimental validation. *International Journal of Fatigue* 36(1): 194–205.

Kahoul, H., Belhour, S., Bellaouar, A. & Dron, J.P. 2019. Fatigue life prediction of upper arm suspension using strain life approach. *Journal of Engineering, Design and Technology* 17(1): 25–40.

Kaiser, B., Pyttel, B. & Berger, C. 2011. VHCF-behavior of helical compression springs made of different materials. *International Journal of Fatigue* 33(1): 23–32.

Kallel, F., Ghorbel, M., Frikha, M., Berger-Vachon, C. & Ben Hamida, A. 2012. A noise cross PSD estimator based on improved minimum statistics method for two-microphone speech enhancement dedicated to a bilateral cochlear implant. *Applied Acoustics* 73(3): 256–264.

Kaluza, A., Kleemann, S., Fröhlich, T., Herrmann, C. & Vietor, T. 2017. Concurrent Design & Life Cycle Engineering in Automotive Lightweight Component Development. *Procedia CIRP* 66: 16–21.

Kantelhardt, J.W., Zschiegner, S.A., Koscielny-Bunde, E., Havlin, S., Bunde, A. & Stanley, H.E. 2002. Multifractal detrended fluctuation analysis of nonstationary time series. *Physica A: Statistical Mechanics and its Applications* 316(1): 87–114.

Kaoua, S.A., Taibi, K., Benghanem, N., Azouaoui, K. & Azzaz, M. 2011. Numerical modelling of twin helical spring under tensile loading. *Applied Mathematical Modelling* 35(3): 1378–1387.

Karthik, J., Chaitanya, K. & Sasanka, T. 2012. Fatigue life prediction of a parabolic spring under non-constant amplitude proportional loading using finite element method. *International Journal of Advanced Science and Technology* 46: 143–156.

Kashyzadeh, R.K., Ghorabi, M.J.O.A. & Arghavan, A. 2014. Investigating the effect of road roughness on automotive component. *Engineering Failure Analysis* 41: 96–107.

Kato, H. & Suzuki, H. 2021. Nonlinear deflection analysis of helical spring in elastic–perfect plastic material: Application to the plastic extension of piano wire spring. *Mechanics of Materials* 160: 103971.

Keshavarzi, A., Sarmadian, F., Shiri, J., Iqbal, M., Tirado-Corbalá, R. & Omran, E.-S.E. 2017. Application of ANFIS-based subtractive clustering algorithm in soil Cation Exchange Capacity estimation using soil and remotely sensed data. *Measurement* 95: 173–180.

Khalil, M. & Topper, T.H. 2003. Prediction of crack-opening stress levels for 1045 as-received steel under service loading spectra. *International Journal of Fatigue* 25(2): 149–157.

Khatir, S., Boutchicha, D., Le Thanh, C., Tran-Ngoc, H., Nguyen, T.N. & Abdel-Wahab, M. 2020. Improved ANN technique combined with Jaya algorithm for crack identification in plates using XIGA and experimental analysis. *Theoretical and Applied Fracture Mechanics* 107: 102554.

Kihm, F., Ferguson, N.S. & Antoni, J. 2015. Fatigue Life from Kurtosis Controlled Excitations. *Procedia Engineering* 133: 698–713.

Kirkby, J.L., Nguyen, D.H., Nguyen, D. & Nguyen, N.N. 2022. Maximum likelihood estimation of diffusions by continuous time Markov chain. *Computational Statistics & Data Analysis* 168: 107408.

Komorska, I. & Puchalski, A. 2021. Rotating Machinery Diagnosing in Non-Stationary Conditions with Empirical Mode Decomposition-Based Wavelet Leaders Multifractal Spectra. *SENSORS* 21(22).

Kong, Y., Abdullah, S., Schramm, D., Omar, M. & Haris, S. 2018a. Vibration Fatigue Analysis of Carbon Steel Coil Spring under Various Road Excitations. *Metals* 8(8): 617.

Kong, Y., Abdullah, S., Schramm, D., Omar, M. & Mohamed Haris, S. 2019a. Evaluation of Energy-Based Model Generated Strain Signals for Carbon Steel Spring Fatigue Life Assessment. *Metals* 9(2): 213.

Kong, Y.S., Abdullah, S., Omar, M.Z., Haris, S.M. & Schramm, D. 2018b. Generation of Artificial Road Profile for Automobile Spring Durability Analysis. *Jurnal Kejuruteraan* 30(2): 123–128.

Kong, Y.S., Abdullah, S., Schramm, D., Omar, M.Z. & Haris, S.M. 2019b. Design of artificial neural network using particle swarm optimisation for automotive spring durability. *Journal of Mechanical Science and Technology* 33(11): 5137–5145.

Kong, Y.S., Abdullah, S., Schramm, D., Omar, M.Z. & Haris, S.M. 2019c. Development of multiple linear regression-based models for fatigue life evaluation of automotive coil springs. *Mechanical Systems and Signal Processing* 118: 675–695.

Kong, Y.S., Abdullah, S., Schramm, D., Omar, M.Z. & Haris, S.M. 2019d. Optimization of spring fatigue life prediction model for vehicle ride using hybrid multi-layer perceptron artificial neural networks. *Mechanical Systems and Signal Processing* 122: 597–621.

Kong, Y.S., Abdullah, S., Schramm, D., Omar, M.Z., Haris, S.M. & Bruckmann, T. 2017. Mission profiling of road data measurement for coil spring fatigue life. *Measurement* 107: 99–110.

Kopel, R., Sladky, R., Laub, P., Koush, Y., Robineau, F., Hutton, C., Weiskopf, N., Vuilleumier, P., Van De Ville, D. & Scharnowski, F. 2019. No time for drifting: Comparing performance and applicability of signal detrending algorithms for real-time fMRI. *NeuroImage* 191: 421–429.

Kowalski, D., Rao, M., Blough, J. & Gruenberg, S. 2001. The Effects of Different Input Excitation on the Dynamic Characterization of an Automotive Shock Absorber. *SAE Technical Paper 2001-01-1442*: 14.

Krzyszczak, J., Baranowski, P., Zubik, M., Kazandjiev, V., Georgieva, V., Sławiński, C., Siwek, K., Kozyra, J. & Nieróbca, A. 2019. Multifractal characterization and comparison of meteorological time series from two climatic zones. *Theoretical and Applied Climatology* 137(3): 1811–1824.

Kushwah, S., Parekh, S. & Mangrola, M. 2020. Optimization of coil spring by finite element analysis method of automobile suspension system using different materials. *Materials Today: Proceedings* 42: 827–831.

Lafarge, B., Cagin, S., Curea, O. & Perret, A.H. 2016. From functional analysis to energy harvesting system design: application to car suspension. *International Journal on Interactive Design and Manufacturing (IJIDeM)* 10(1): 37–50.

Langat, P.K., Kumar, L. & Koech, R. 2019. Identification of the Most Suitable Probability Distribution Models for Maximum, Minimum, and Mean Streamflow.

Lashermes, B., Jaffard, S. & Abry, P. 2005. Wavelet leader based multifractal analysis. *Acoust. Speech Signal Process.* 4: 161–164.

Lee, Y.-L. & Tjhung, T. 2012. Chapter 3 - Rainflow Cycle Counting Techniques. Dlm. Lee, Y.-L., Barkey, M. E., & Kang, H.-T. B. T.-M. F. A. H. (pnyt.). *Metal Fatigue Analysis Handbook*, hlm. 89–114. Butterworth-Heinemann: Boston.

Li, B. & Chen, X. 2014. Wavelet-based numerical analysis: A review and classification. *Finite Elements in Analysis and Design* 81: 14–31.

Li, X.-Q., Bai, G.-C., Song, L.-K. & Wen, J. 2021. Fatigue reliability estimation framework for turbine rotor using multi-agent collaborative modeling. *Structures* 29: 1967–1978.

Li, Y. & Wang, L. 2019. A novel noise reduction technique for underwater acoustic signals based on complete ensemble empirical mode decomposition with adaptive noise, minimum mean square variance criterion and least mean square adaptive filter. *Defence Technology* 16(3): 543–554.

Liao, D. & Zhu, S.-P. 2019. Energy field intensity approach for notch fatigue analysis. *International Journal of Fatigue* 127: 190–202.

Liao, X., Wang, Y., Wang, Z., Feng, L. & Shi, Y. 2019. Effect of low temperatures on constant amplitude fatigue properties of Q345qD steel butt-welded joints. *Engineering Failure Analysis* 105: 597–609.

Liu, F., Zhou, S., Xia, C., Zeng, D. & Shi, T. 2016. Optimization of fatigue life distribution model and establishment of probabilistic S–N curves for a 165ksi grade super high strength drill pipe steel. *Journal of Petroleum Science and Engineering* 145(C): 527–532.

Liu, H., Huang, W., Wang, S. & Zhu, Z. 2014. Adaptive spectral kurtosis filtering based on Morlet wavelet and its application for signal transients detection. *Signal Processing* 96: 118–124.

Liu, N., Cui, X., Xiao, J., Lua, J. & Phan, N. 2020. A simplified continuum damage mechanics based modeling strategy for cumulative fatigue damage assessment of metallic bolted joints. *International Journal of Fatigue* 131: 105302.

Loganathan, T.G., Vinoth Kumar, K. & Madhu, S. 2020. Flexural and fatigue of a composite leaf spring using finite element analysis. *Materials Today: Proceedings* 22: 1014–1019.

Luo, H., Huang, M. & Zhou, Z. 2018. Integration of Multi-Gaussian fitting and LSTM neural networks for health monitoring of an automotive suspension component. *Journal of Sound and Vibration* 428: 87–103.

Luo, Y. & Huang, Y. 2018. A new combined approach on Hurst exponent estimate and its applications in realized volatility. *Physica A: Statistical Mechanics and its Applications* 492: 1364–1372.

Mahmud, M., Abdullah, S., Ariffin, A.K. & Nopiah, Z.M. 2018. On the need to adopt strain-based probabilistic approach in predicting fatigue life. *Journal of the Brazilian Society of Mechanical Sciences and Engineering* 40(2): 82.

Makowiec, D. & Fulinski, A. 2010. Multifractal detrended fluctuation analysis as the estimator of Long-range dependence. *Acta Physica Polonica B* 41: 1025–1050.

Manhertz, G. & Bereczky, A. 2021. STFT spectrogram based hybrid evaluation method for rotating machine transient vibration analysis. *Mechanical Systems and Signal Processing* 154: 107583.

Manouchehrynia, R., Abdullah, S. & Singh, S.S.K. 2020. Fatigue Reliability Assessment of an Automobile Coil Spring under Random Strain Loads Using Probabilistic Technique. *Metals* 10(1): 12.

Mansor, N.I.I., Abdullah, S. & Ariffin, A.K. 2019. Effect of loading sequences on fatigue crack growth and crack closure in API X65 steel. *Marine Structures* 65: 181–196.

Mansor, N.I.I., Abdullah, S., Ariffin, A.K. & Syarif, J. 2014. A review of the fatigue failure mechanism of metallic materials under a corroded environment. *Engineering Failure Analysis* 42: 353–365.

Mao, C., Jiang, Y., Wang, D., Chen, X. & Tao, J. 2015. Modeling and simulation of non-stationary vehicle vibration signals based on Hilbert spectrum. *Mechanical Systems and Signal Processing* 50–51: 56–69.

Marciniak, Z., Rozumek, D., Brighenti, R., Lesiuk, G. & Correia, J.A.F.O. 2019. Fatigue tests of materials with the controlled energy parameter amplitude. *Procedia Structural Integrity* 17: 503–508.

Marsh, G., Wignall, C., Thies, P.R., Barltrop, N., Incecik, A., Venugopal, V. & Johanning, L. 2016. Review and application of Rainflow residue processing techniques for accurate fatigue damage estimation. *International Journal of Fatigue* 82: 757–765.

Márton, L.F., Brassai, S.T., Bakó, L. & Losonczi, L. 2014. Detrended Fluctuation Analysis of EEG Signals. *Procedia Technology* 12: 125–132.

Masoudi Nejad, R., Liu, Z., Ma, W. & Berto, F. 2021. Reliability analysis of fatigue crack growth for rail steel under variable amplitude service loading conditions and wear. *International Journal of Fatigue* 152: 106450.

Mayer, H., Schuller, R., Karr, U., Fitzka, M., Irrasch, D., Hahn, M. & Bacher-Höchst, M. 2016. Mean stress sensitivity and crack initiation mechanisms of spring steel for torsional and axial VHCF loading. *International Journal of Fatigue* 93: 309–317.

McAlorum, J., Rubert, T., Fusiek, G., Niewczas, P. & Zorzi, G. 2018. Design and Demonstration of a Low-Cost Small-Scale Fatigue Testing Machine for Multi-Purpose Testing of Materials, Sensors and Structures. *Machines* 6(3): 30.

McCulloch, W.S. & Pitts, W. 1943. A logical calculus of the ideas immanent in nervous activity. *The bulletin of mathematical biophysics* 5(4): 115–133.

Mehdizadeh, M., Haghshenas, A. & Khonsari, M.M. 2021. In-situ Technique for Fatigue Life Prediction of Metals Based on Temperature Evolution. *International Journal of Mechanical Sciences* 192: 106113.

Mekonnen, Y., Aburbu, H. & Sarwat, A. 2018. Life cycle prediction of Sealed Lead Acid batteries based on a Weibull model. *Journal of Energy Storage* 18: 467–475.

Minaker, B.P. & Yao, Z. 2017. Design and Analysis of an Interconnected Suspension for A Small Off-Road Vehicle. *ARCHIVE OF MECHANICAL ENGINEERING* 64(1): 5–21.

Mintzelas, A., Sarlis, N. V & Christopoulos, S.-R.G. 2018. Estimation of multifractality based on natural time analysis. *Physica A: Statistical Mechanics and its Applications* 512: 153–164.

Mises, R. V. 1913. Mechanik der festen Körper im plastisch-deformablen Zustand. [Mechanics of Solid Bodies in Plastic Deformation State.]. *Nachrichten von der Gesellschaft der Wissenschaften zu Gottingen (Mathematisch-physikalische Klasse)* 1: 582–592.

Mitra, A.C., Desai, G.J., Patwardhan, S.R., Shirke, P.H., Kurne, W.M.H. & Banerjee, N. 2016. Optimization of Passive Vehicle Suspension System by Genetic Algorithm. *Procedia Engineering* 144: 1158–1166.

Mohanraj, T., Yerchuru, J., Krishnan, H., Nithin Aravind, R.S. & Yameni, R. 2020. Development of tool condition monitoring system in end milling process using wavelet features and Hoelder's exponent with machine learning algorithms. *Measurement*: 108671.

Mohanty, J. 2016. Fatigue Crack Growth Life Prediction of 6061 Al-Alloy under Load Ratio Effect by Using ANFIS. *International Journal of Advanced Engineering Research and Science* 3: 199–204.

Mohanty, J.R., Verma, B.B., Ray, P.K. & Parhi, D.R.K. 2010. Prediction of mode-I overload-induced fatigue crack growth rates using neuro-fuzzy approach. *Expert Systems with Applications* 37(4): 3075–3087.

Mohanty, J.R., Verma, B.B., Ray, P.K. & Parhi, D.R.K. 2011. Application of adaptive neuro-fuzzy inference system in modeling fatigue life under interspersed mixed-mode (I and II) spike overload. *Expert Systems with Applications* 38(10): 12302–12311.

Mršnik, M., Slavič, J. & Boltežar, M. 2013. Frequency-domain methods for a vibration-fatigue-life estimation – Application to real data. *International Journal of Fatigue* 47: 8–17.

Mršnik, M., Slavič, J. & Boltežar, M. 2018. Vibration fatigue using modal decomposition. *Mechanical Systems and Signal Processing* 98: 548–556.

Muc, A. 2020. Fuzzy approach in modeling static and fatigue strength of composite materials and structures. *Neurocomputing* 393: 156–164.

Murakami, Y., Kanezaki, T. & Sofronis, P. 2013. Hydrogen embrittlement of high strength steels: Determination of the threshold stress intensity for small cracks nucleating at nonmetallic inclusions. *Engineering Fracture Mechanics* 97: 227–243.

Nabagło, T., Jurkiewicz, A. & Kowal, J. 2021. Modeling verification of an advanced torsional spring for tracked vehicle suspension in 2S1 vehicle model. *Engineering Structures* 229: 111623.

Nagarkar, M.P., Vikhe Patil, G.J. & Zaware Patil, R.N. 2016. Optimization of nonlinear quarter car suspension–seat–driver model. *Journal of Advanced Research* 7(6): 991–1007.

Nakano, T., Sakakibara, T., Wakita, M. & Sugimoto, A. 2001. Effect of alloying elements and surface treatment on corrosion fatigue strength of high-strength suspension coil springs. *JSAE Review* 22(3): 337–342.

Nasir, N.N.M., Abdullah, S., Singh, S.S.K. & Haris, S.M. 2020. Risk-based life assessment of prediction models on suspension system for various road profiles. *Engineering Failure Analysis* 114: 104573.

Nguyen, C.T., Oterkus, S. & Oterkus, E. 2021. An energy-based peridynamic model for fatigue cracking. *Engineering Fracture Mechanics* 241: 107373.

Niederwanger, A., Ladinek, M., Lang, R., Timmers, R. & Lener, G. 2019. On the stability and sensitivity of the strain-life approach using the example of mild steel. *JOURNAL OF CONSTRUCTIONAL STEEL RESEARCH* 153: 483–494.

Niesłony, A. & Böhm, M. 2013. Mean stress effect correction using constant stress ratio S–N curves. *International Journal of Fatigue* 52: 49–56.

Nishawala, V. V & Ostoja-Starzewski, M. 2017. Acceleration waves on random fields with fractal and Hurst effects. *Wave Motion* 74: 134–150.

Nwobi-Okoye, C.C., Ochieze, B.Q. & Okiy, S. 2019. Multi-objective optimization and modeling of age hardening process using ANN, ANFIS and genetic algorithm: Results from aluminum alloy A356/cow horn particulate composite. *Journal of Materials Research and Technology* 8(3): 3054–3075.

Oh, C.-S. 2001. Application of wavelet transform in fatigue history editing. *International Journal of Fatigue* 23(3): 241–250.

Palmieri, M., Česnik, M., Slavič, J., Cianetti, F. & Boltežar, M. 2017. Non-Gaussianity and non-stationarity in vibration fatigue. *International Journal of Fatigue* 97: 9–19.

Panda, K.C. 2016. Dealing with Noise and Vibration in Automotive Industry. *Procedia Engineering* 144: 1167–1174.

Paraforos, D.S., Griepentrog, H.W. & Vougioukas, S.G. 2016. Country road and field surface profiles acquisition, modelling and synthetic realisation for evaluating fatigue life of agricultural machinery. *Journal of Terramechanics* 63: 1–12.

Pastorcic, D., Vukelic, G. & Bozic, Z. 2019. Coil spring failure and fatigue analysis. *Engineering Failure Analysis* 99: 310–318.

Pattar, S., Sanjay, S.J. & Math, V.B. 2014. Static analysis of helical compression spring. *Int J Res Eng Technol* 3: 835–838.

Pavlov, A.N. & Anishchenko, V.S. 2007. Multifractal analysis of complex signals. *Physics-Uspekhi* 50(8): 819.

Pawar, H.B. & Desale, D.D. 2018. Optimization of Three Wheeler Front Suspension Coil Spring. *Procedia Manufacturing* 20: 428–433.

Pejkowski, Ł. & Skibicki, D. 2019. Stress-strain response and fatigue life of four metallic materials under asynchronous loadings: Experimental observations. *International Journal of Fatigue* 128: 105202.

Pnevmatikos, N., Konstandakopoulou, F., Blachowski, B., Papavasileiou, G. & Broukos, P. 2020. Multifractal analysis and wavelet leaders for structural damage detection of structures subjected to earthquake excitation. *Soil Dynamics and Earthquake Engineering* 139: 106328.

Pöllänen, I. & Martikka, H. 2010. Optimal re-design of helical springs using fuzzy design and FEM. *Advances in Engineering Software* 41(3): 410–414.

Portet, S. 2020. A primer on model selection using the Akaike Information Criterion. *Infectious Disease Modelling* 5: 111–128.

Pramod, C.P. & Pillai, G.N. 2021. K-Means clustering based Extreme Learning ANFIS with improved interpretability for regression problems. *Knowledge-Based Systems* 215: 106750.

Prastiyo, W. & Fiebig, W. 2021. Multibody simulation and statistical comparison of the linear and progressive rate double wishbone suspension dynamical behavior. *Simulation Modelling Practice and Theory* 108: 102273.

Pratumnopharat, P., Leung, P.S. & Court, R.S. 2013. Extracting fatigue damage parts from the stress–time history of horizontal axis wind turbine blades. *Renewable Energy* 58: 115–126.

Pratumnopharat, P., Leung, P.S. & Court, R.S. 2014. Wavelet transform-based stress-time history editing of horizontal axis wind turbine blades. *Renewable Energy* 63: 558–575.

Prawoto, Y., Ikeda, M., Manville, S.K. & Nishikawa, A. 2008. Design and failure modes of automotive suspension springs. *Engineering Failure Analysis* 15(8): 1155–1174.

Puchalski, A. & Komorska, I. 2017. Multifractal nature of diesel engine rattle noise in vehicle. *Archives of Acoustics* 42(3): 469–474.

Puchalski, A., Slezak, M., Komorska, I. & Wiśniowski, P. 2018. Multifractal analysis vehicle's in-use speed profile for application in driving cycles. *Eksploatacja i Niezawodnosc - Maintenance and Reliability* 20(2): 177–181.

Putra, T.E., Abdullah, S. & Schramm, D. 2020. Effect of cycle amplitude removal of fatigue strain loadings associated to signal energy characteristics. *Engineering Failure Analysis* 116: 104723.

Putra, T.E., Abdullah, S., Schramm, D., Nuawi, M.Z. & Bruckmann, T. 2015. Generating strain signals under consideration of road surface profiles. *Mechanical Systems and Signal Processing* 60–61: 485–497.

Putra, T.E., Abdullah, S., Schramm, D., Nuawi, M.Z. & Bruckmann, T. 2017a. The need to generate realistic strain signals at an automotive coil spring for durability simulation leading to fatigue life assessment. *Mechanical Systems and Signal Processing* 94: 432–447.

Putra, T.E., Abdullah, S., Schramm, D., Nuawi, M.Z. & Bruckmann, T. 2017b. Reducing cyclic testing time for components of automotive suspension system utilising the wavelet transform and the Fuzzy C-Means. *Mechanical Systems and Signal Processing* 90: 1–14.

Putra, T.E., Husaini & Machmud, M.N. 2020. Predicting the fatigue life of an automotive coil spring considering road surface roughness. *Engineering Failure Analysis* 116: 104722.

Pyttel, B., Brunnera, I., Kaisera, B., Bergera, C. & Mani, M. 2014. Fatigue behaviour of helical compression springs at a very high number of cycles – Investigation of various influences. *International Journal of Fatigue* 60: 101–109.

Qian, J. & Fatemi, A. 1995. Cyclic deformation and fatigue behaviour of ion-nitrided steel. *International Journal of Fatigue* 17(1): 15–24.

Qiu, Y., Shen, W., Yan, R., Xu, L. & Liu, E. 2021. Fatigue reliability evaluation of thin plate welded joints considering initial welding deformation. *Ocean Engineering* 236: 109440.

Quan, W., Wang, H., Liu, X. & Zhang, S. 2013. Multi-fractal Analysis for Pavement Roughness Evaluation. *Procedia - Social and Behavioral Sciences* 96: 2684–2691.

Rabi, J., Balusamy, T. & Raj Jawahar, R. 2019. Analysis of vibration signal responses on pre induced tunnel defects in friction stir welding using wavelet transform and empirical mode decomposition. *Defence Technology* 15(6): 885–896.

Rahim, A.A.A., Abdullah, S., Singh, S.S.K. & Nuawi, M.Z. 2020. Selection of the optimum decomposition level using the discrete wavelet transform for automobile suspension system. *Journal of Mechanical Science and Technology* 34(1): 137–142.

Rahim, A.A.A., Abdullah, S., Singh, S.S.K. & Nuawi, M.Z. 2021. Fatigue strain signal reconstruction technique based on selected wavelet decomposition levels of an automobile coil spring. *Engineering Failure Analysis*: 105434.

Rahul, M.S. & Rameshkumar, K. 2020. Multi-objective optimization and numerical modelling of helical coil spring for automotive application. *Materials Today: Proceedings*.

Reddy, K.V., Kodati, M., Chatra, K. & Bandyopadhyay, S. 2016. A comprehensive kinematic analysis of the double wishbone and MacPherson strut suspension systems. *Mechanism and Machine Theory* 105: 441–470.

Régis, S., Doncescu, A. & Desachy, J. 2008. Detection and characterization of physiological states in bioprocesses based on Hölder exponent. *Knowledge-Based Systems* 21(1): 70–79.

Repetto, M.P. & Torrielli, A. 2017. Long term simulation of wind-induced fatigue loadings. *Engineering Structures* 132: 551–561.

Reu, P. 2015. Virtual Strain Gage Size Study. *Experimental Techniques* 39: 1–3.

Risaliti, E., Tamarozzi, T., Vermaut, M., Cornelis, B. & Desmet, W. 2019. Multibody model based estimation of multiple loads and strain field on a vehicle suspension system. *Mechanical Systems and Signal Processing* 123: 1–25.

Rizvi, S.M.H., Abid, M., Khan, A.Q., Satti, S.G. & Latif, J. 2018. H∞ control of 8 degrees of freedom vehicle active suspension system. *Journal of King Saud University - Engineering Sciences* 30(2): 161–169.

Roostaei, A.A., Pahlevanpour, A., Behravesh, S.B. & Jahed, H. 2019. On the definition of elastic strain energy density in fatigue modelling. *International Journal of Fatigue* 121: 237–242.

Sadd, M.H. 2019. Chapter 4 - Force and Stress. Dlm. Sadd, M. H. B. T.-C. M. M. of M. B. (pnyt.). *Continuum Mechanics Modeling of Material Behavior*, hlm. 111–138. Academic Press.:

Saikia, T. & Sarma, K. 2015. Multilevel-DWT-Based Image Denoising Using Adaptive Neuro-Fuzzy Inference System. Dlm. Bora, P., Prasanna, S., Sarma, K., Saikia, N. (pnyt.). *Advances in Communication and Computing*, hlm. 93–102.

Salat, H., Murcio, R. & Arcaute, E. 2017. Multifractal methodology. *Physica A: Statistical Mechanics and its Applications* 473: 467–487.

Santecchia, E., Hamouda, A.M.S., Musharavati, F., Zalnezhad, E., Cabibbo, M., El Mehtedi, M. & Spigarelli, S. 2016. A Review on Fatigue Life Prediction Methods for Metals. *Advances in Materials Science and Engineering* 2016: 26.

Sarfaraz, R. 2015. 3 - Understanding fatigue loading conditions in adhesively-bonded composite joints. Dlm. Vassilopoulos, A. P. B. T.-F. and F. of A.-B. C. J. (pnyt.). *Fatigue and Fracture of Adhesively-Bonded Composite Joints*, hlm. 73–89. Woodhead Publishing.:

Schramm, D., Hiller, M. & Bardini, R. 2014. Vehicle Dynamics: Modeling and Simulation. Edisi ke-1. Springer-Verlag Berlin Heidelberg: Berlin Heidelberg.

Scuracchio, B.G., de Lima, N.B. & Schön, C.G. 2013. Role of residual stresses induced by double peening on fatigue durability of automotive leaf springs. *Materials & Design* 47: 672–676.

Serrano, E. & Figliola, A. 2009. Wavelet Leaders: A new method to estimate the multifractal singularity spectra. *Physica A: Statistical Mechanics and its Applications* 388(14): 2793–2805.

Shangguan, W. Bin, Zheng, G.F., Rakheja, S. & Yin, Z. 2020. A method for editing multi-axis load spectrums based on the wavelet transforms. *Measurement: Journal of the International Measurement Confederation* 162: 107903.

Sharma, S.K., Pare, V., Chouksey, M. & Rawal, B.R. 2016. Numerical Studies Using Full Car Model for Combined Primary and Cabin Suspension. *Procedia Technology* 23: 171–178.

Shihabudheen, K. V & Pillai, G.N. 2018. Recent advances in neuro-fuzzy system: A survey. *Knowledge-Based Systems* 152: 136–162.

Shinde, S.D., Maheshwari, S. & Kumar, S. 2018. Literature review on analysis of various Components of McPherson suspension. *Materials Today: Proceedings* 5(9, Part 3): 19102–19108.

Singh, D.K. 2021. Torsion of Circular Members. Dlm. Singh, D. K. (pnyt.). *Strength of Materials*, hlm. 319–364. Springer International Publishing: Cham.

Singh, S.S.K., Abdullah, S. & Ariffin, A.K. 2020. Fatigue reliability assessment in time domain using stochastic-induced random stress loads due to limited experimental data. *Engineering Failure Analysis* 117: 104794.

Sinha, N. & Das, A. 2020. Automatic diagnosis of cardiac arrhythmias based on three stage feature fusion and classification model using DWT. *Biomedical Signal Processing and Control* 62: 102066.

Sivák, P. & Ostertagová, E. 2012. Evaluation of Fatigue Tests by Means of Mathematical Statistics. *Procedia Engineering* 48: 636–642.

Škrjanc, I., Iglesias, J.A., Sanchis, A., Leite, D., Lughofer, E. & Gomide, F. 2019. Evolving fuzzy and neuro-fuzzy approaches in clustering, regression, identification, and classification: A Survey. *Information Sciences* 490: 344–368.

Smith, C., Hill, B., Wheatley, G., Masoudi Nejad, R. & Sina, N. 2022. Fatigue reliability assessment of the new design of rear suspension system of the JCU motorsport car. *Structures* 36: 473–481.

Steinwolf, A., Giacomin, J.A. & Staszewski, W.J. 2002. On the need for bump event correction in vibration test profiles representing road excitations in automobiles. *Proceedings of the Institution of Mechanical Engineers, Part D: Journal of Automobile Engineering* 216(4): 279–295.

Sun, W., Thompson, D. & Zhou, J. 2019. A mechanism for overcoming the effects of the internal resonances of coil springs on vibration transmissibility. *Journal of Sound and Vibration*: 115145.

Suzuki, T., Chauvicourt, F., Fujimoto, H. & IEEE. 2021. High-Bandwidth Suspension Resonance Analysis of In-Wheel Motor Vehicle Using Multibody Dynamics.

Szymański, G.M., Josko, M., Tomaszewski, F. & Filipiak, R. 2015. Application of time–frequency analysis to the evaluation of the condition of car suspension. *Mechanical Systems and Signal Processing* 58–59: 298–307.

Teixeira, G.M., Roberts, M. & Silva, J. 2019. Random vibration fatigue of welded structures - Applications in the automotive industry. *Procedia Structural Integrity* 19: 175–193.

Theunissen, J., Tota, A., Gruber, P., Dhaens, M. & Sorniotti, A. 2021. Preview-based techniques for vehicle suspension control: a state-of-the-art review. *Annual Reviews in Control* 51: 206–235.

Topper, T.H. & Lam, T.S. 1997. Effective strain–fatigue life data for variable amplitude fatigue. *International Journal of Fatigue* 19(93): 137–143.

Tran-Ngoc, H., Khatir, S., De Roeck, G., Bui-Tien, T. & Abdel Wahab, M. 2019. An efficient artificial neural network for damage detection in bridges and beam-like structures by improving training parameters using cuckoo search algorithm. *Engineering Structures* 199: 109637.

Twomey, J.M., Chen, D.Y., Osterman, M.D. & Pecht, M.G. 2020. Development of a cycle counting algorithm with temporal parameters. *Microelectronics Reliability* 109: 113652.

Ugras, R.C., Alkan, O.K., Orhan, S., Kutlu, M. & Mugan, A. 2019. Real time high cycle fatigue estimation algorithm and load history monitoring for vehicles by the use of frequency domain methods. *Mechanical Systems and Signal Processing* 118: 290–304.

Urda, P., Muñoz, S., Aceituno, J.F. & Escalona, J.L. 2020. Wheel-rail contact force measurement using strain gauges and distance lasers on a scaled railway vehicle. *Mechanical Systems and Signal Processing* 138: 106555.

Vassilopoulos, A.P. & Bedi, R. 2008. Adaptive neuro-fuzzy inference system in modelling fatigue life of multidirectional composite laminates. *Computational Materials Science* 43(4): 1086–1093.

Vdovin, D. & Chichekin, I. 2016. Loads and Stress Analysis Cycle Automation in the Automotive Suspension Development Process. *Procedia Engineering* 150: 1276–1279.

Venkatakrishnan, P., Sangeetha, S., Gnanasekaran, J.S., Vishnukumar, M.G. & Padmanaban, A.S. 2014. Analysis of Vibration in gearbox sensor data using Lipschitz Exponent (LE) function: A Wavelet approach. *IFAC Proceedings Volumes* 47(1): 1067–1071.

Wang, B.J., Li, Q., Ren, Z.S. & Sun, S.G. 2019. Improving the fatigue reliability of metro vehicle bogie frame based on load spectrum. *International Journal of Fatigue*: 105389.

Wang, H., Liu, J., Wen, G. & Xie, Y.M. 2020a. The robust fail-safe topological designs based on the von Mises stress. *Finite Elements in Analysis and Design* 171: 103376.

Wang, L., Burger, R. & Aloe, A. 2017. Considerations of Vibration Fatigue for Automotive Components. *SAE International Journal of Commercial Vehicles* 10(1).

Wang, Y., Pan, R., Yang, D., Tang, X. & Chen, Z. 2017. Remaining Useful Life Prediction of Lithium-ion Battery Based on Discrete Wavelet Transform. *Energy Procedia* 105: 2053–2058.

Wang, Y., Serra, R. & Argoul, et P. 2019. Based on the virtual experiment study of the impact of load sequence on the calculation process of random vibration fatigue damage. *Procedia Structural Integrity* 19: 682–687.

Wang, Y.S., Guo, H., Li, Y.R., Liu, N.N. & Yang, C. 2020b. Active control for vehicle interior noise based on DWT-FxLMS algorithm using a piezoelectric feedback system. *Applied Acoustics* 167: 107409.

Wolfsteiner, P. 2017. Fatigue assessment of non-stationary random vibrations by using decomposition in Gaussian portions. *International Journal of Mechanical Sciences* 127: 10–22.

Xia, F.-L., Zhu, S.-P., Liao, D., Dantas, R., Correia, J.A.F.O. & De Jesus, A.M.P. 2020. Isodamage curve-based fatigue damage accumulation model considering the exhaustion of static toughness. *Engineering Failure Analysis* 115: 104575.

Xia, Q. & Quail, F. 2016. Principles and validation of strain gauge shunt design for large dynamic strain measurement. *Sensors and Actuators A: Physical* 241: 124–134.

Xiong, G., Yu, W., Xia, W. & Zhang, S. 2016. Multifractal signal reconstruction based on singularity power spectrum. *Chaos, Solitons & Fractals* 91: 25–32.

Xiong, G., Yu, W. & Zhang, S. 2015. Singularity power spectrum distribution. *Physica A: Statistical Mechanics and its Applications* 431: 63–73.

Xiong, Q., Zhang, W., Xu, Y., Peng, Y. & Deng, P. 2018. Alpha-Stable Distribution and Multifractal Detrended Fluctuation Analysis-Based Fault Diagnosis Method Application for Axle Box Bearings. *Shock and Vibration* 2018: 12.

Xu, J. & Kong, F. 2019. Adaptive scaled unscented transformation for highly efficient structural reliability analysis by maximum entropy method. *Structural Safety* 76: 123–134.

Yaich, A. & El Hami, A. 2019. Multiaxial fatigue damage estimation of structures under random vibrations using Matsubara's criterion. *International Journal of Fatigue* 124: 253–264.

Yang, J., Ning, D., Sun, S.S., Zheng, J., Lu, H., Nakano, M., Zhang, S., Du, H. & Li, W.H. 2021. A semi-active suspension using a magnetorheological damper with nonlinear negative-stiffness component. *Mechanical Systems and Signal Processing* 147: 107071.

Yang, S., Yang, L. & Wang, Y.R. 2020. Determining the fatigue parameters in total strain life equation of a material based on monotonic tensile mechanical properties. *ENGINEERING FRACTURE MECHANICS* 226.

Yang, W.-X., Hull, J.B. & Seymour, M.D. 2006. Detecting the singularities in engineering signals. *Journal of Materials Processing Technology* 175(1): 439–445.

Ye, X.W., Su, Y.H. & Han, J.P. 2014. A State-of-the-Art Review on Fatigue Life Assessment of Steel Bridges. *Mathematical Problems in Engineering* 2014: 956473.

Yıldırım, H.C., Remes, H. & Nussbaumer, A. 2020. Fatigue properties of as-welded and post-weld-treated high-strength steel joints: The influence of constant and variable amplitude loads. *International Journal of Fatigue* 138: 105687.

Yuan-Chun, K. 2019. Fatigue Analysis of Suspension Control Arm Based on Road Spectrum. *IOP Conference Series: Materials Science and Engineering* 538(1).

Zadeh, L.A. 1965. Fuzzy sets. *Information and Control* 8(3): 338–353.

Zhan, Z. & Li, H. 2021. A novel approach based on the elastoplastic fatigue damage and machine learning models for life prediction of aerospace alloy parts fabricated by additive manufacturing. *International Journal of Fatigue* 145: 106089.

Zhang, H., Yu, X., Liu, B., Wu, Y. & Li, Y. 2016. Using wavelets to study spike-type compressor rotating stall inception. *Aerospace Science and Technology* 58: 467–479.

Zhang, M. & Jing, X. 2021. Switching logic-based saturated tracking control for active suspension systems based on disturbance observer and bioinspired X-dynamics. *Mechanical Systems and Signal Processing* 155: 107611.

Zhang, M., Sun, C.-N., Zhang, X., Goh, P.C., Wei, J., Hardacre, D. & Li, H. 2019a. High cycle fatigue life prediction of laser additive manufactured stainless steel: A machine learning approach. *International Journal of Fatigue* 128: 105194.

Zhang, R., Zhao, L., Qiu, X., Zhang, H. & Wang, X. 2020. A comprehensive comparison of the vehicle vibration energy harvesting abilities of the regenerative shock absorbers predicted by the quarter, half and full vehicle suspension system models. *Applied Energy* 272: 115180.

Zhang, W., Jiang, W., Li, H., Song, M., Yu, Y., Sun, G., Li, J. & Huang, Y. 2019b. Effect of tensile overload on fatigue crack behavior of 2205 duplex stainless steel: Experiment and finite element simulation. *International Journal of Fatigue* 128: 105199.

Zhou, C., Yang, B., Guo, K., Liu, J., Sun, J., Song, G., Zhu, S., Sun, C. & Jiang, Z. 2020. Vibration singularity analysis for milling tool condition monitoring. *International Journal of Mechanical Sciences* 166: 105254.

Zhou, Y. & Abdel Wahab, M. 2017. Damage detection using vibration data and dynamic transmissibility ensemble with auto-associative neural network. *Mechanics* 23.

Zhu, J.-H., Zhang, W.-H. & Xia, L. 2016. Topology Optimization in Aircraft and Aerospace Structures Design. *Archives of Computational Methods in Engineering* 23(4): 595–622.

Zhu, K., Wong, Y.S. & Hong, G.S. 2009. Wavelet analysis of sensor signals for tool condition monitoring: A review and some new results. *International Journal of Machine Tools and Manufacture* 49(7): 537–553.

Zhu, L.-F., Ke, L.-L., Zhu, X.-Q., Xiang, Y. & Wang, Y.-S. 2019a. Crack identification of functionally graded beams using continuous wavelet transform. *Composite Structures* 210: 473–485.

Zhu, S.-P., Lei, Q., Huang, H.-Z., Yang, Y.-J. & Peng, W. 2016. Mean stress effect correction in strain energy-based fatigue life prediction of metals. *International Journal of Damage Mechanics* 26(8): 1219–1241.

Zhu, S.-P., Liao, D., Liu, Q., Correia, J.A.F.O. & De Jesus, A.M.P. 2019b. Nonlinear fatigue damage accumulation: Isodamage curve-based model and life prediction aspects. *International Journal of Fatigue* 128: 105185.

Zhu, S.-P., Liu, Q. & Huang, H.-Z. 2017. Probabilistic Modeling of Damage Accumulation for Fatigue Reliability Analysis. *Procedia Structural Integrity* 4: 3–10.

Zhu, Y., Wang, Y. & Huang, Y. 2014. Failure analysis of a helical compression spring for a heavy vehicle's suspension system. *Case Studies in Engineering Failure Analysis* 2(2): 169–173.

Zuo, H., Luo, Z., Guan, J. & Wang, Y. 2014. Identification on rock and soil parameters for vibration drilling rock in metal mine based on fuzzy least square support vector machine. *Journal of Central South University* 21(3): 1085–1090.

APPENDIX A

PLASTICITY CHECK OF COIL SPRING UNDER EXTREME LOAD

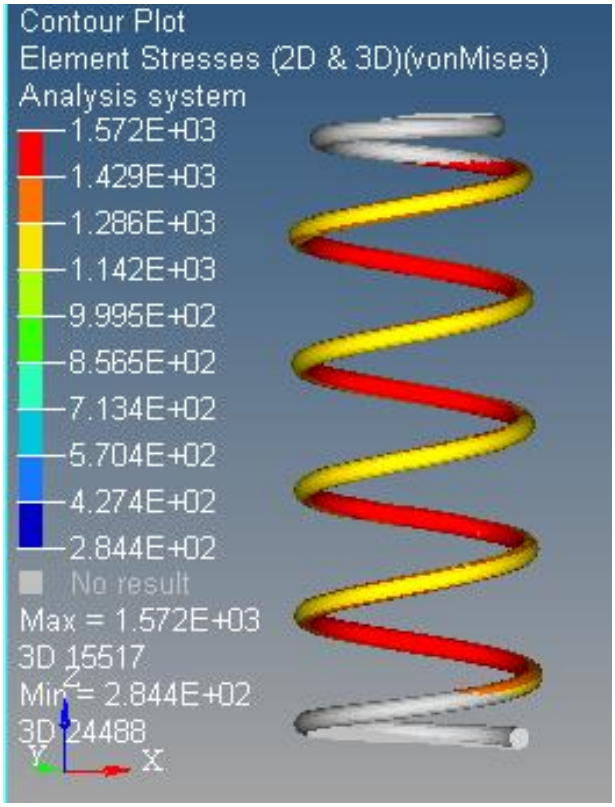

Stress distribution of coil spring under extreme load

Load applied = 4990 N (largest load level in the SAE load)

Maximum von-Mises stress = 1572 MPa

Yield strength of material = 1487 MPa

Conclusion:

The resulted von-Mises stress was higher than the yield strength of the material, indicating that the coil spring experienced plastic deformation under extreme loading condition.

APPENDIX B

VIBRATION SIGNALS ACQUIRED IN ROAD TESTS

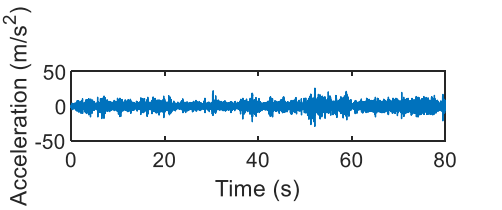

(1)

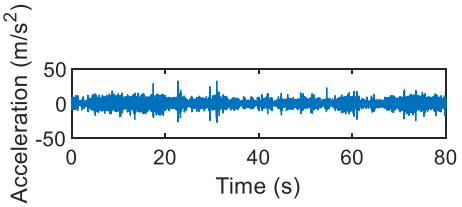

(2)

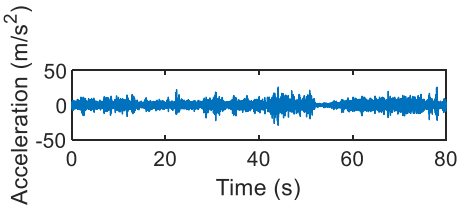

(3)

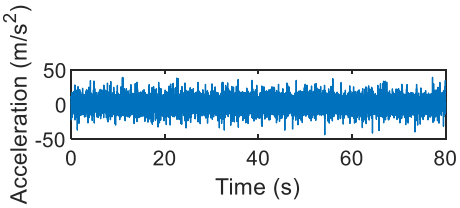

(4)

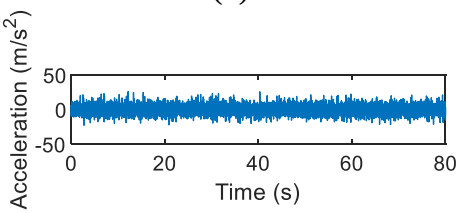

(5)

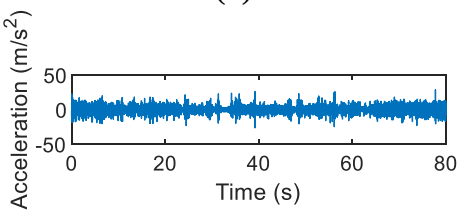

(6)

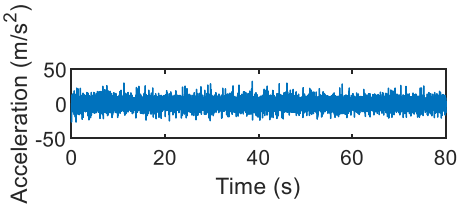

(7)

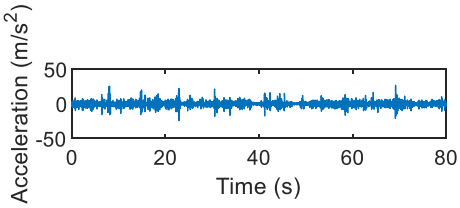

(8)

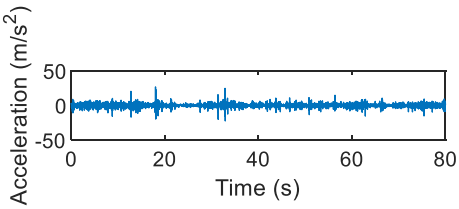

(9)

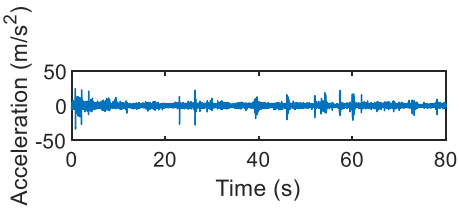

(10)

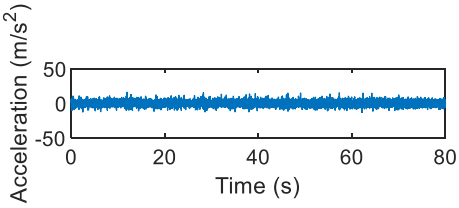

(11)

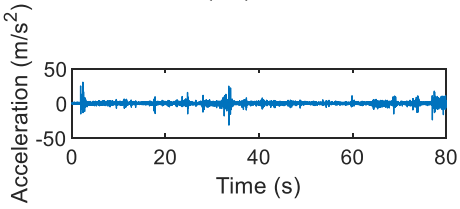

(12)

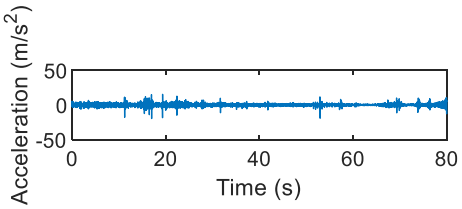

(13)

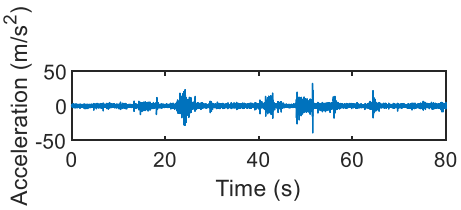

(14)

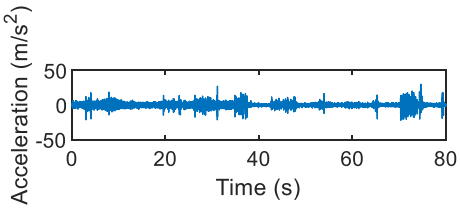

(15)

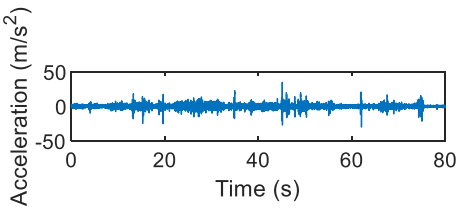

(16)

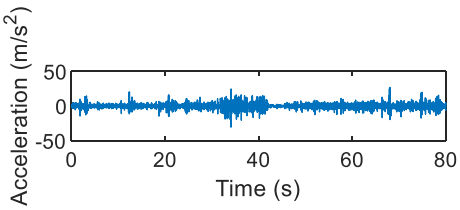

(17)

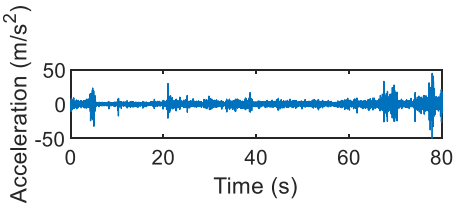

(18)

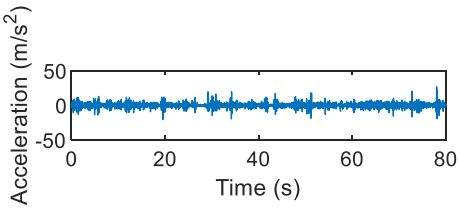

(19)

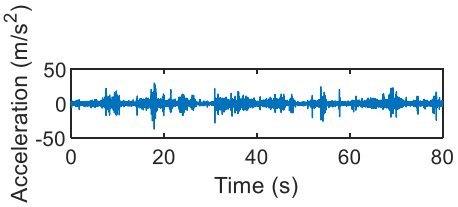

(20)

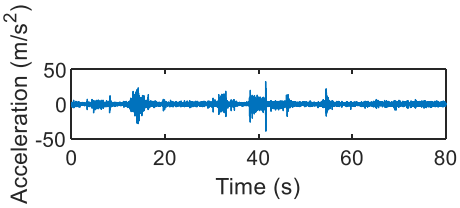

(21)

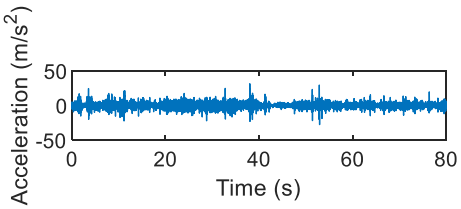

(22)

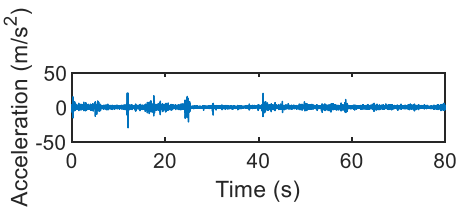

(23)

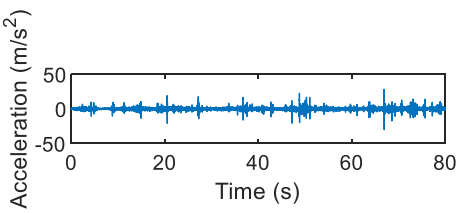

(24)

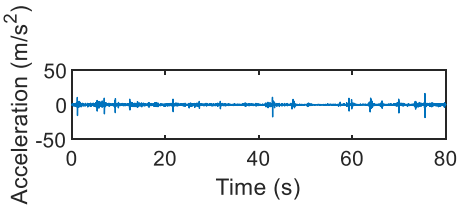

(25)

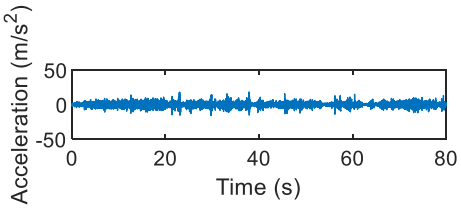

(26)

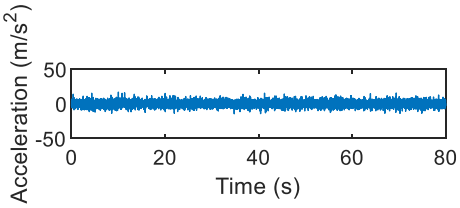

(27)

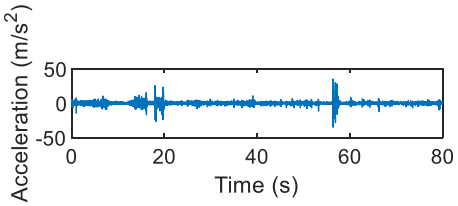

(28)

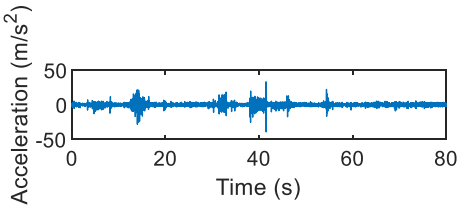

(29)

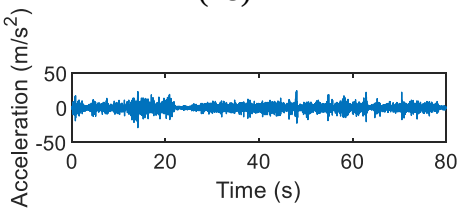

(30)

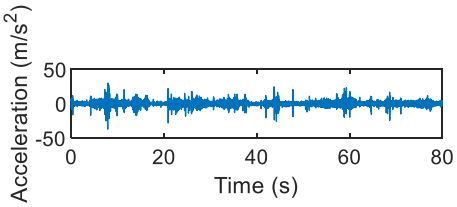

(31)

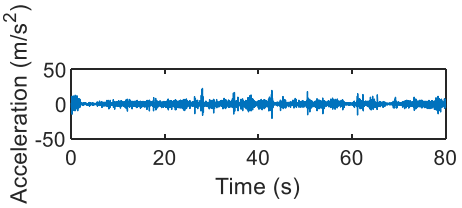

(32)

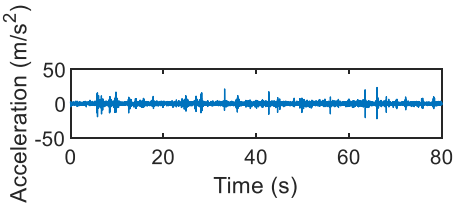

(33)

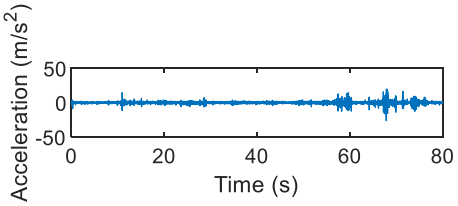

(34)

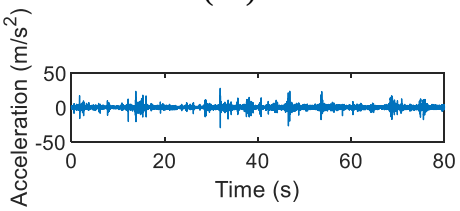

(35)

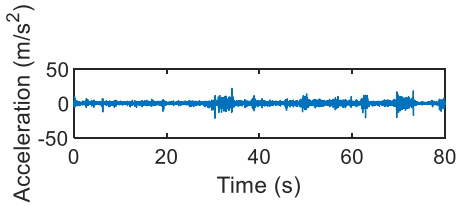

(36)

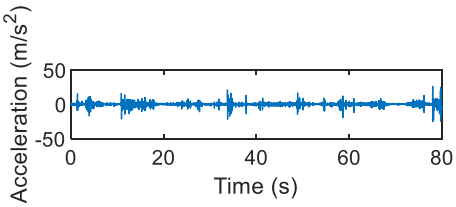

(37)

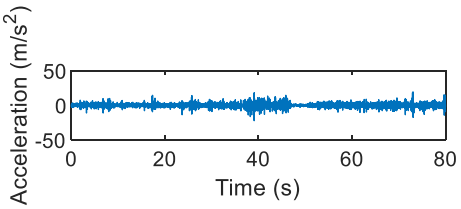

(38)

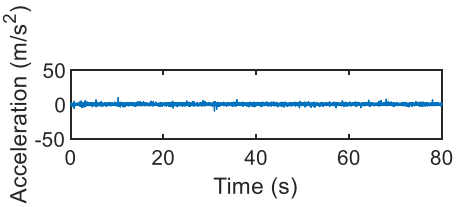

(39)

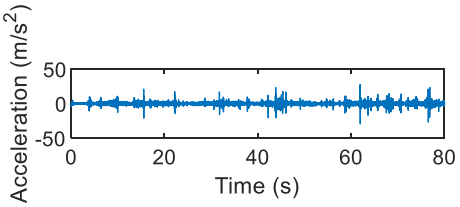

(40)

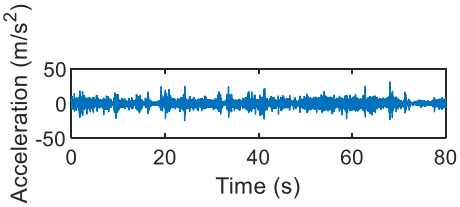

(41)

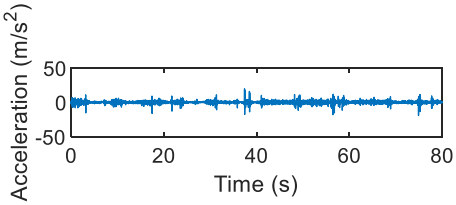

(42)

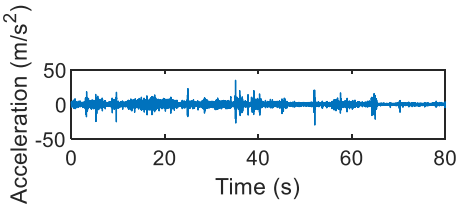

(43)

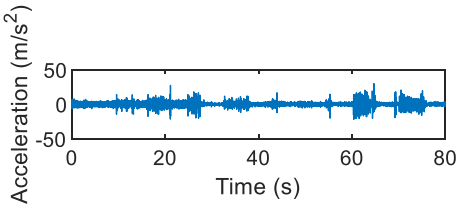

(44)

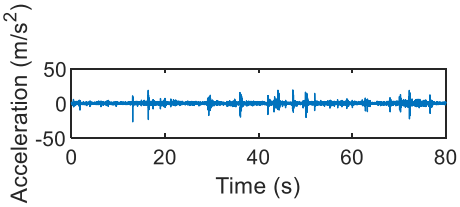

(45)

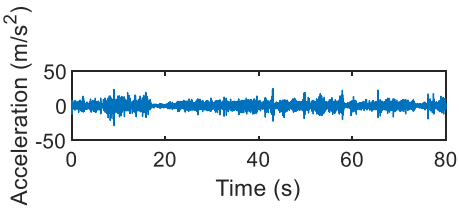

(46)

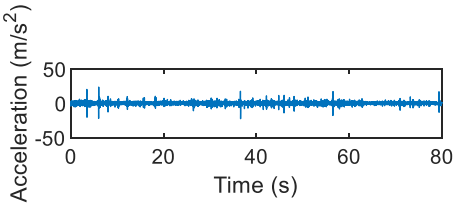

(47)

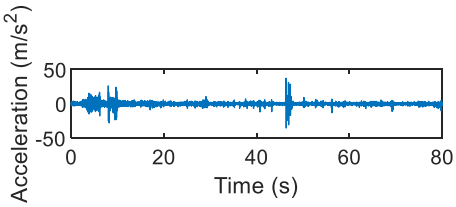

(48)

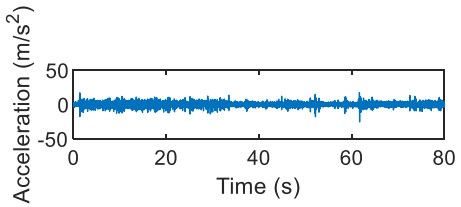

(49)

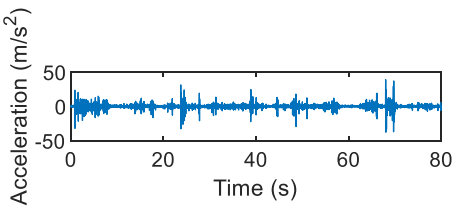

(50)

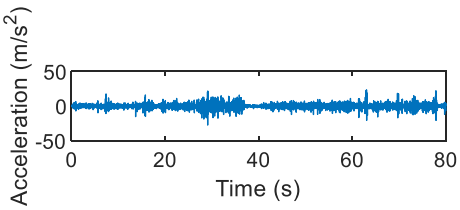

(51)

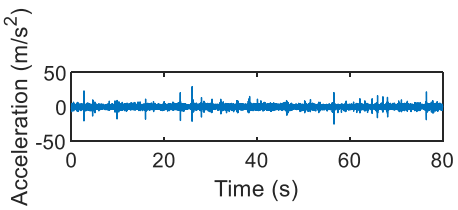

(52)

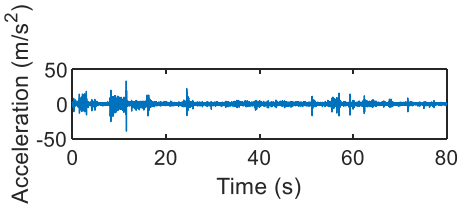

(53)

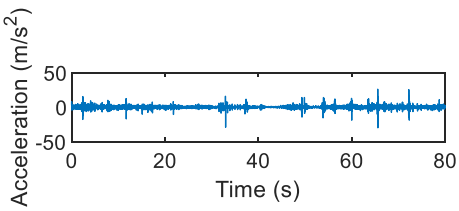

(54)

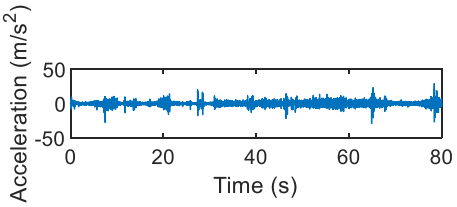

(55)

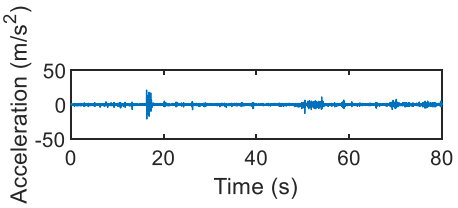

(56)

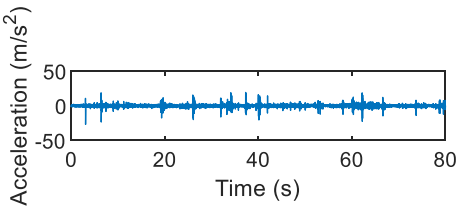

(57)

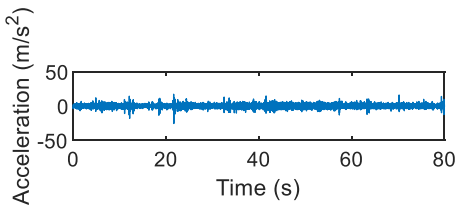

(58)

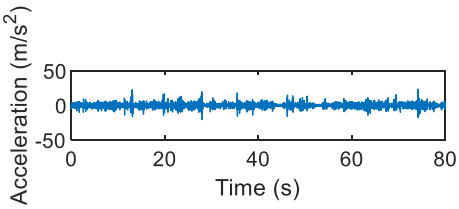

(59)

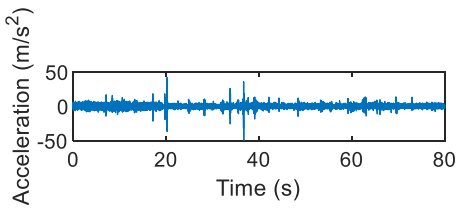

(60)

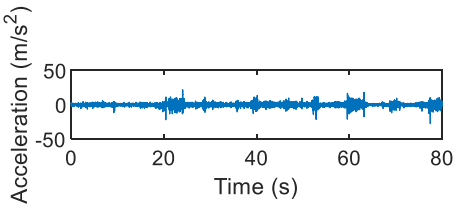

(61)

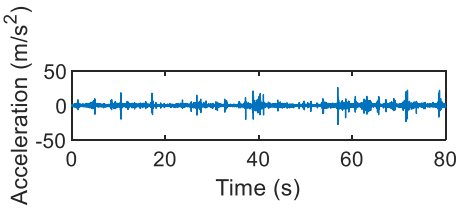

(62)

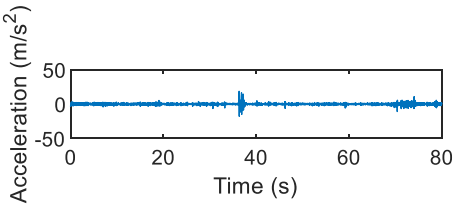

(63)

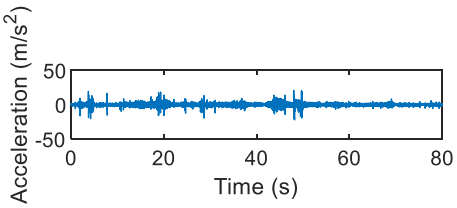

(64)

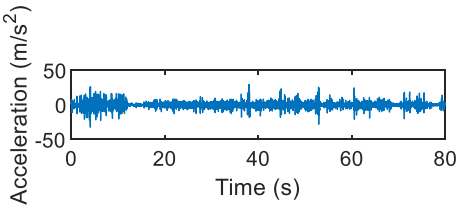

(65)

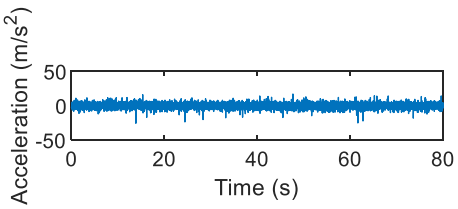

(66)

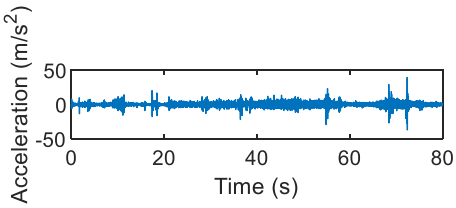

(67)

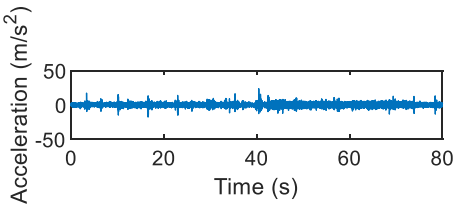

(68)

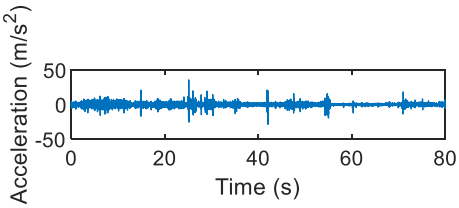

(69)

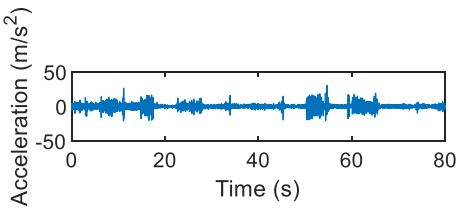

(70)

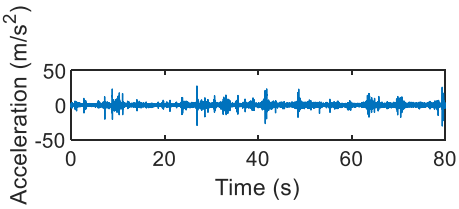

(71)

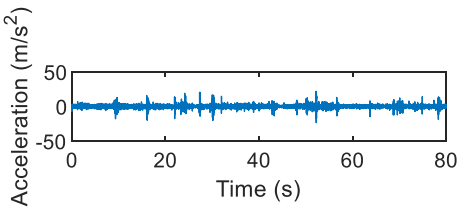

(72)

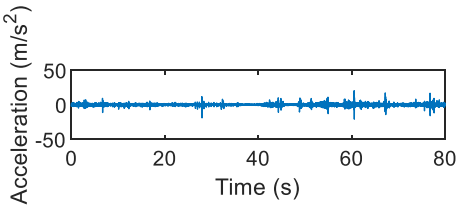

(73)

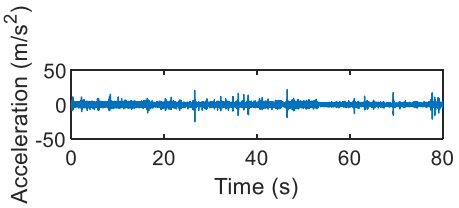

(74)

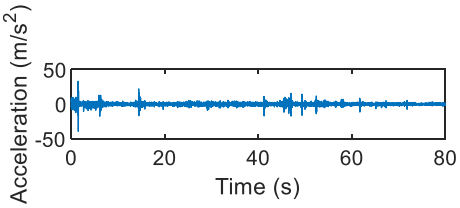

(75)

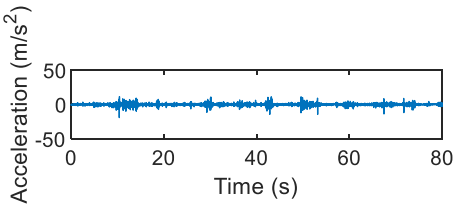

(76)

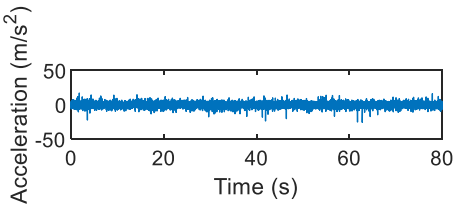

(77)

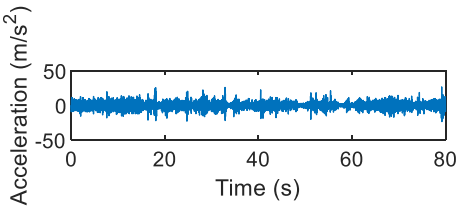

(78)

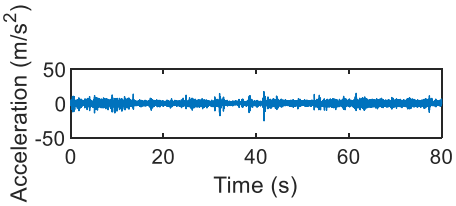

(79)

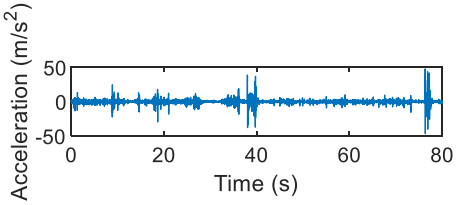

(80)

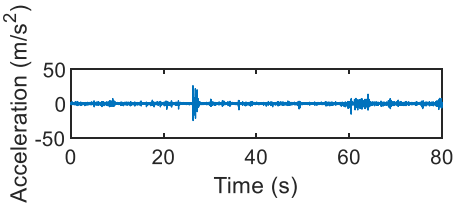

(81)

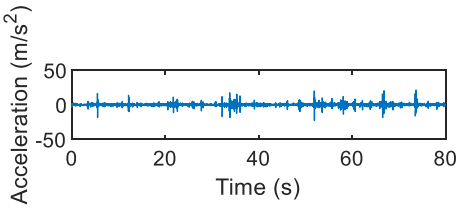

(82)

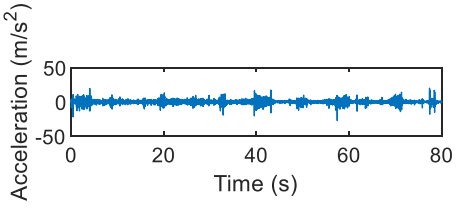

(83)

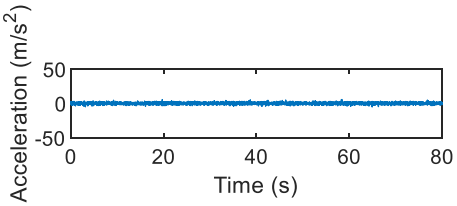

(84)

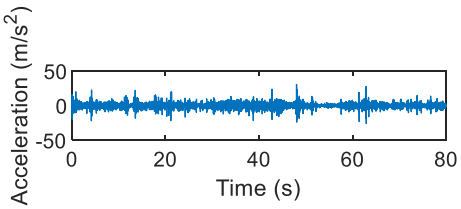

(85)

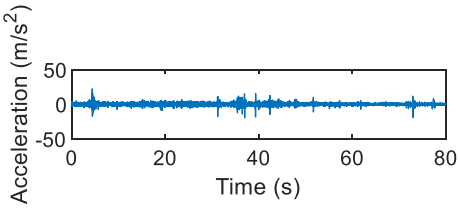

(86)

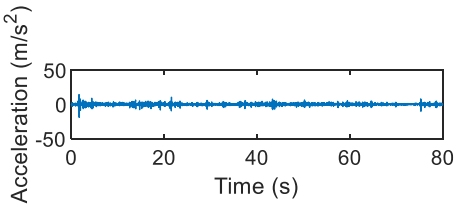

(87)

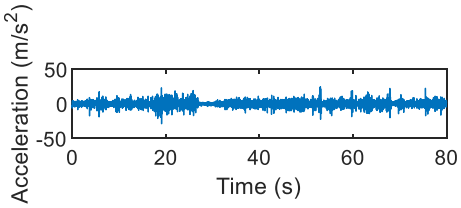

(88)

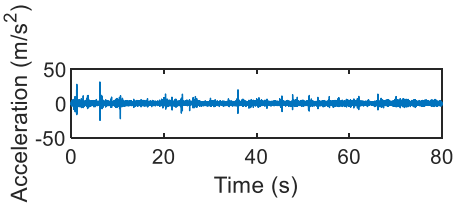

(89)

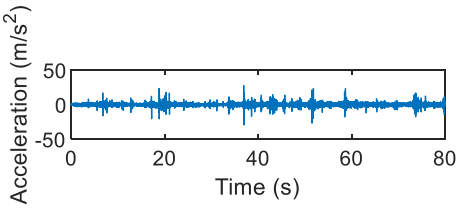

(90)

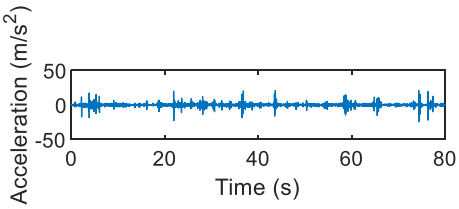

(91)

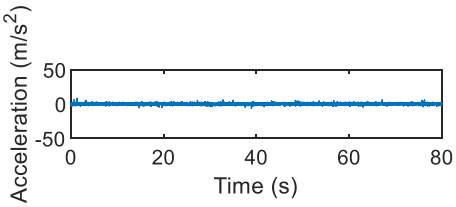

(92)

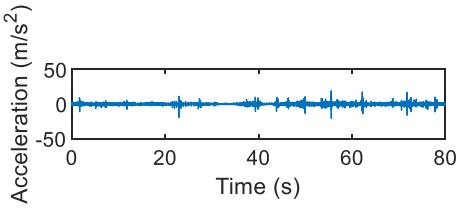

(93)

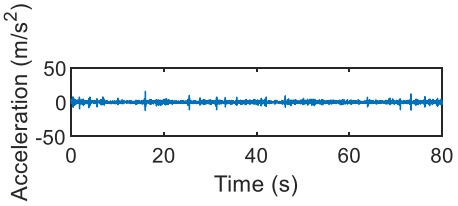

(94)

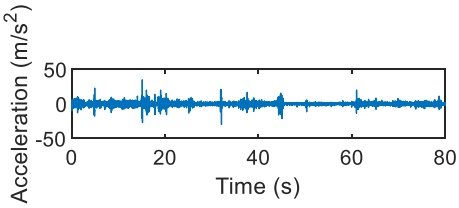

(95)

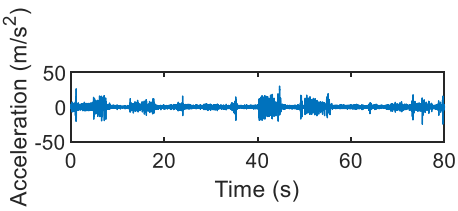

(96)

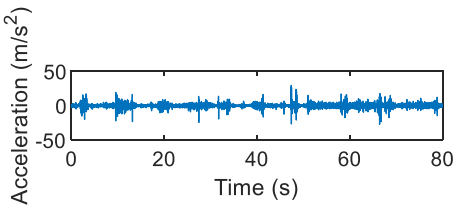

(97)

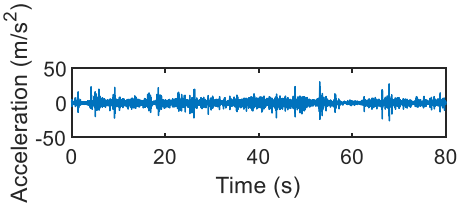

(98)

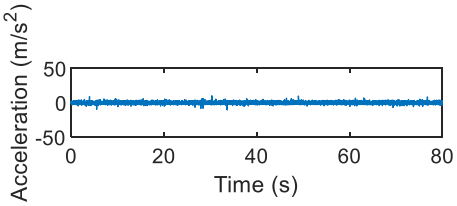

(99)

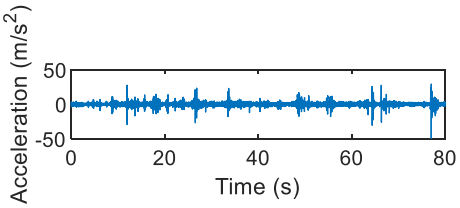

(100)

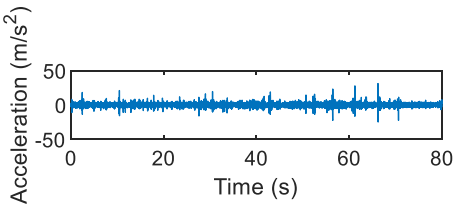

(101)

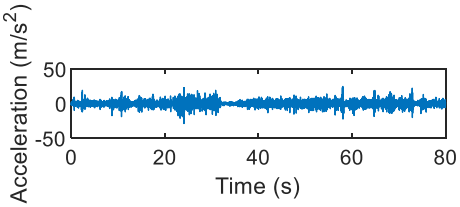

(102)

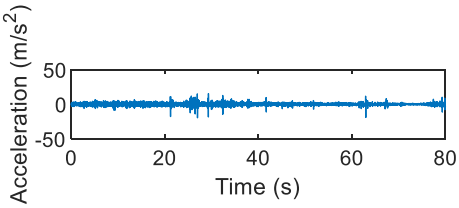

(103)

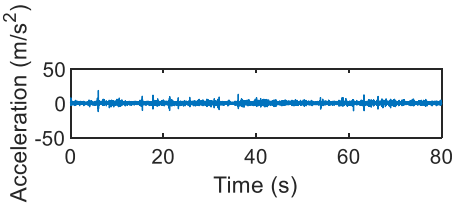

(104)

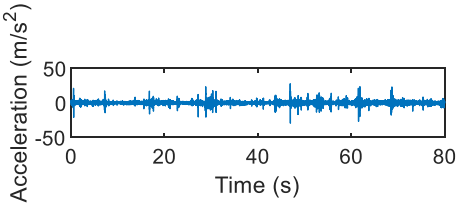

(105)

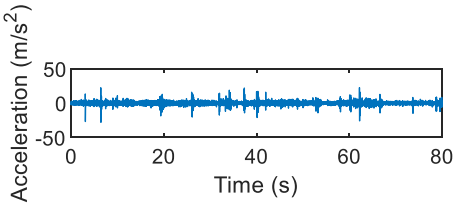

(106)

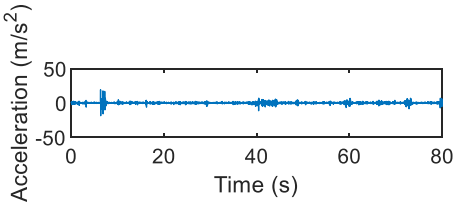

(107)

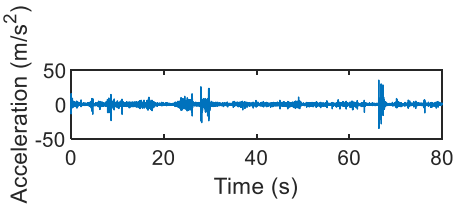

(108)

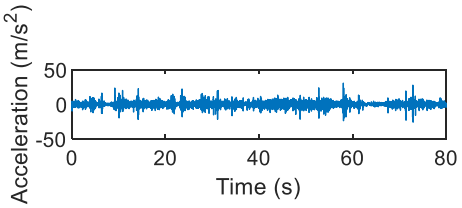

(109)

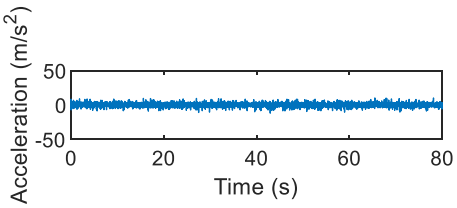

(110)

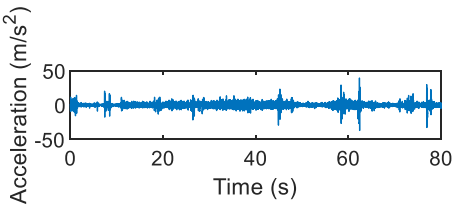

(111)

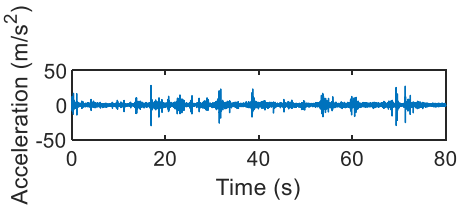

(112)

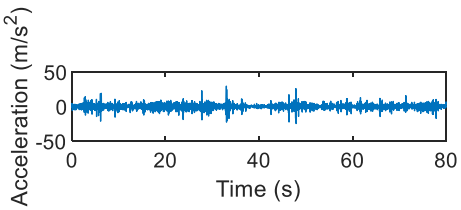

(113)

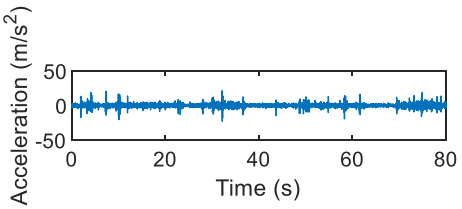

(114)

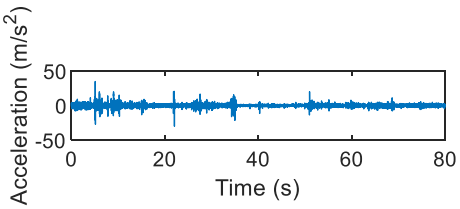

(115)

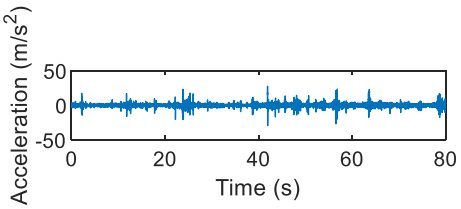

(116)

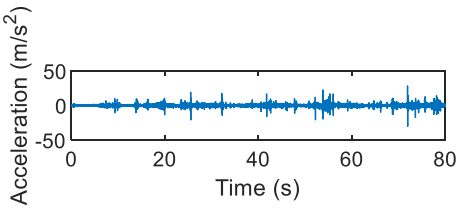

(117)

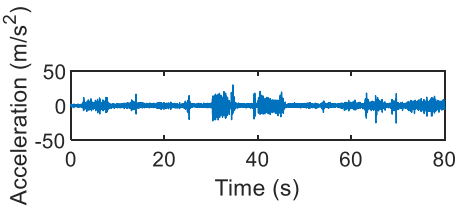

(118)

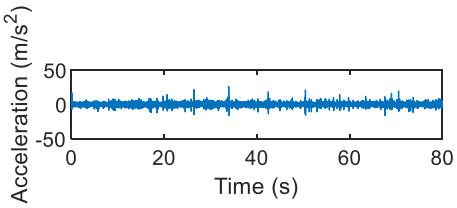

(119)

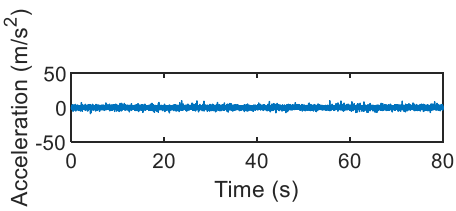

(120)

APPENDIX C

STRAIN LOADING HISTORIES ACQUIRED IN ROAD TESTS

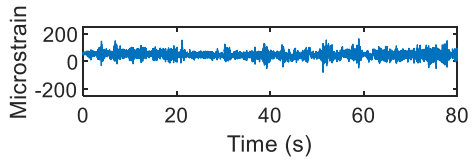

(1)

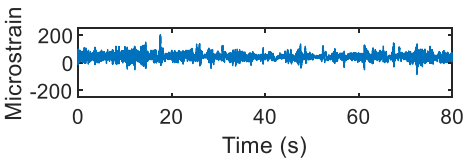

(2)

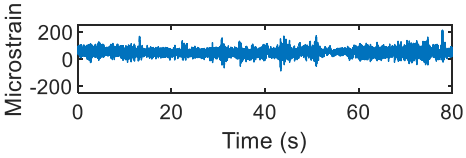

(3)

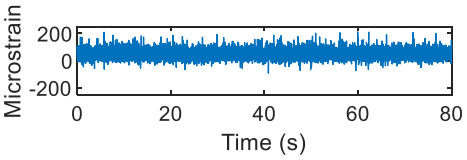

(4)

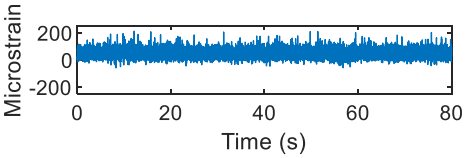

(5)

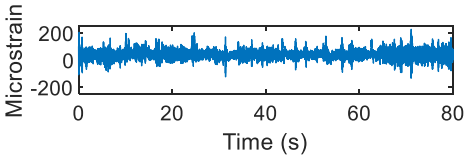

(6)

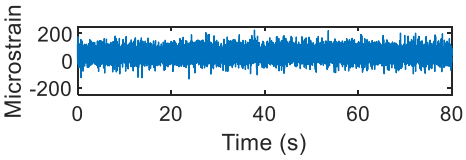

(7)

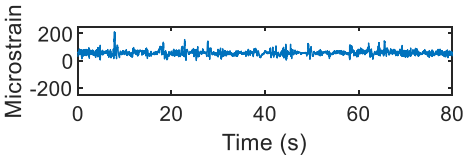

(8)

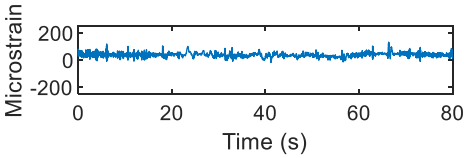

(9)

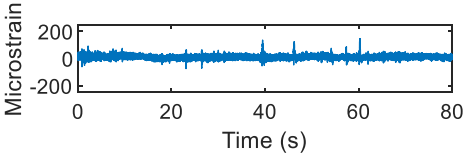

(10)

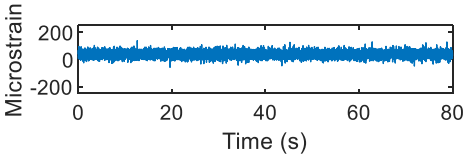

(11)

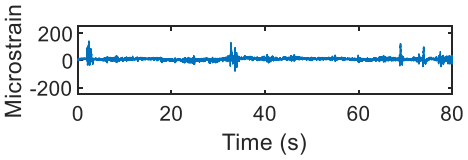

(12)

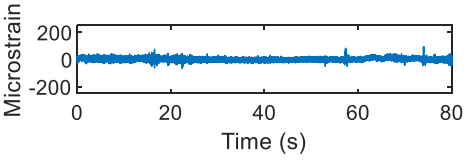

(13)

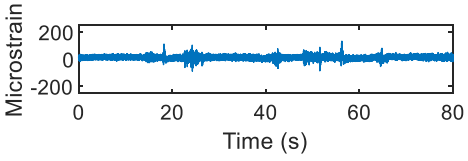

(14)

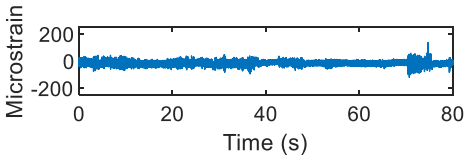

(15)

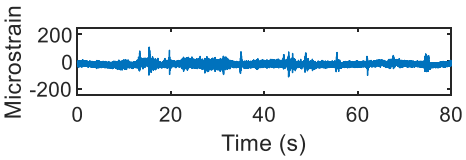

(16)

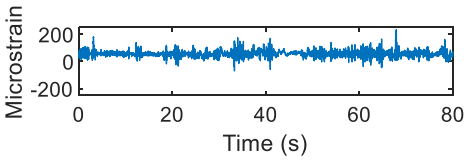

(17)

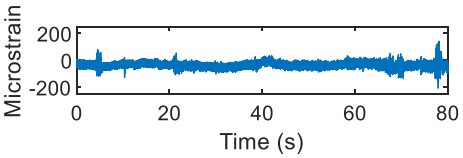

(18)

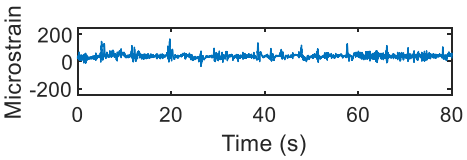

(19)

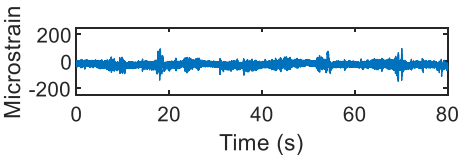

(20)

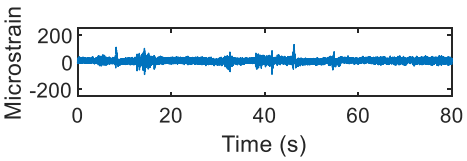

(21)

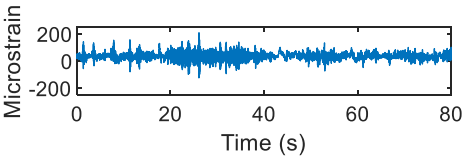

(22)

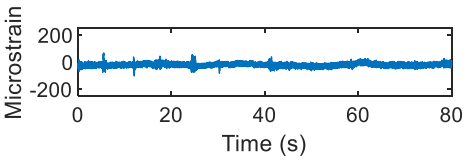

(23)

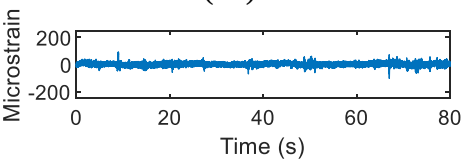

(24)

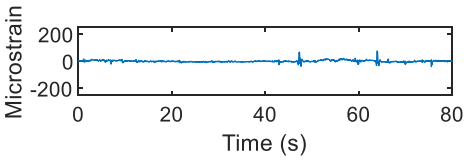

(25)

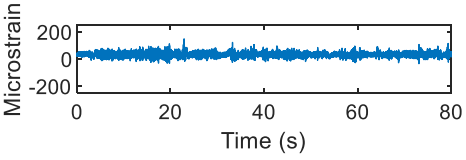

(26)

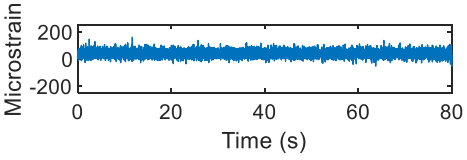

(27)

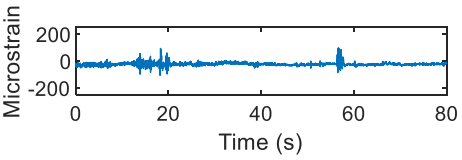

(28)

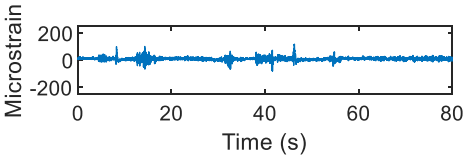

(29)

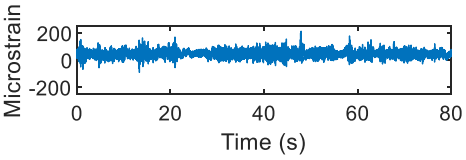

(30)

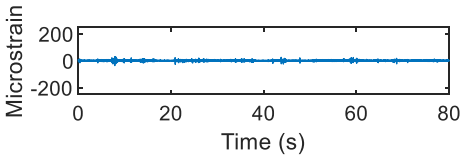

(31)

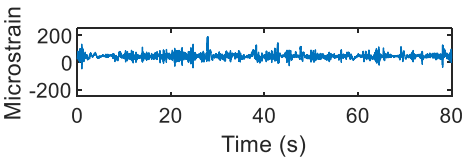

(32)

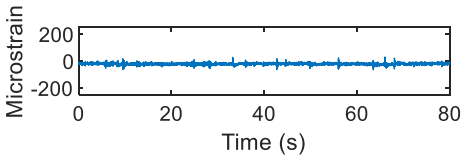

(33)

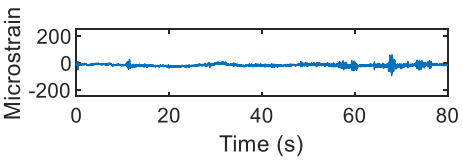

(34)

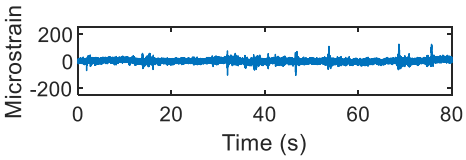

(35)

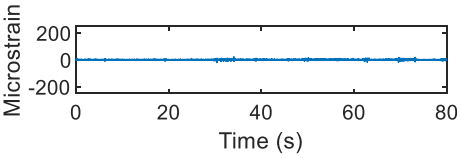

(36)

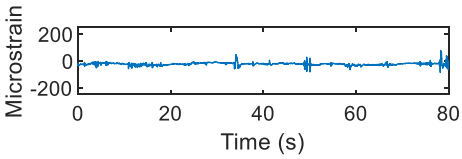

(37)

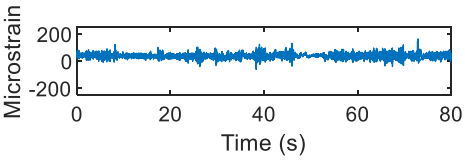

(38)

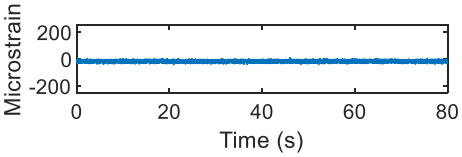

(39)

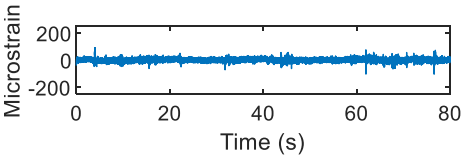

(40)

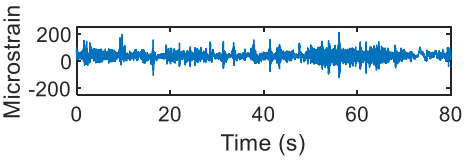

(41)

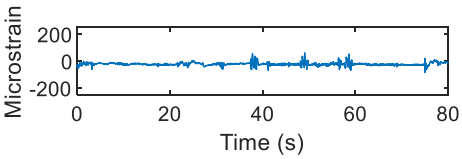

(42)

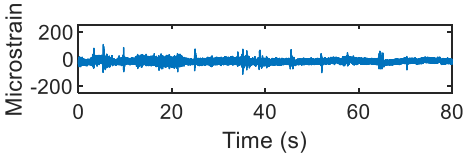

(43)

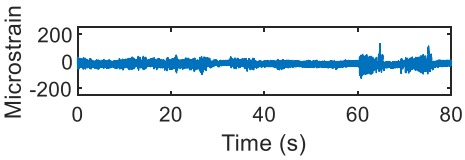

(44)

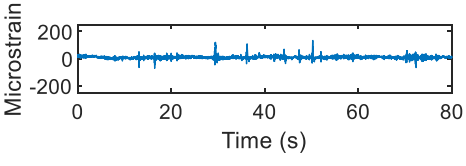

(45)

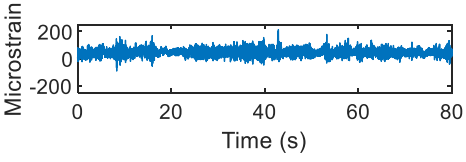

(46)

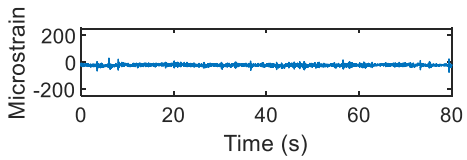

(47)

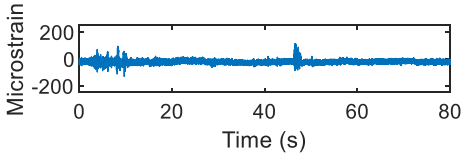

(48)

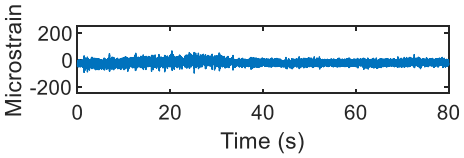

(49)

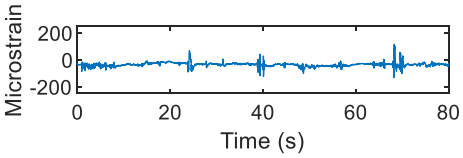

(50)

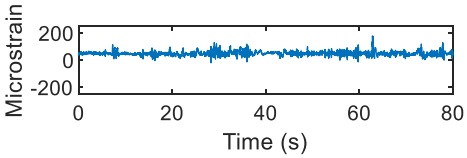

(51)

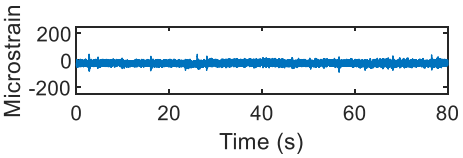

(52)

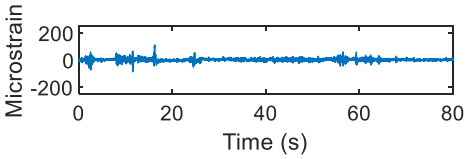

(53)

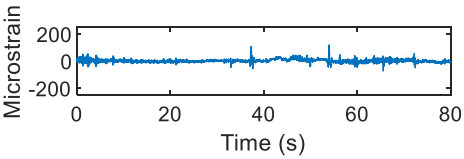

(54)

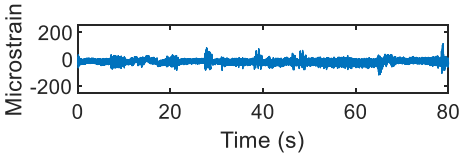

(55)

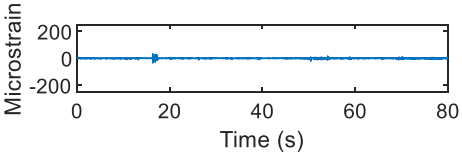

(56)

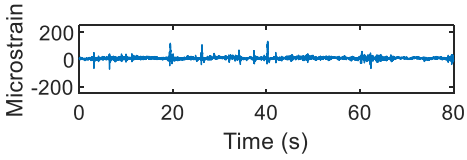

(57)

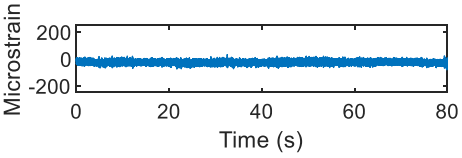

(58)

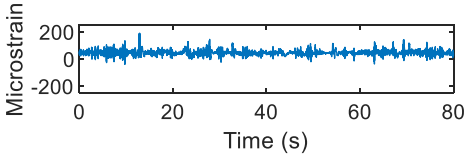

(59)

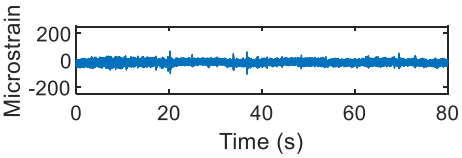

(60)

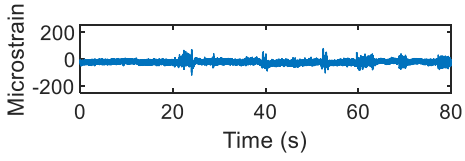

(61)

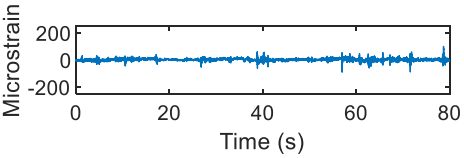

(62)

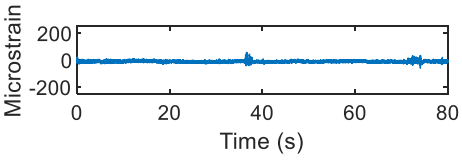

(63)

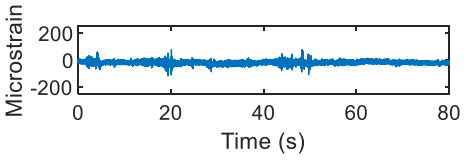

(64)

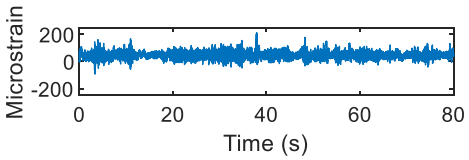

(65)

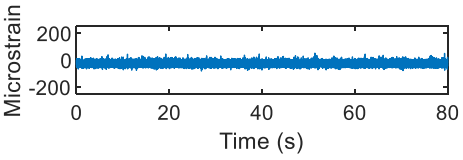

(66)

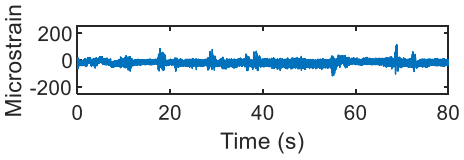

(67)

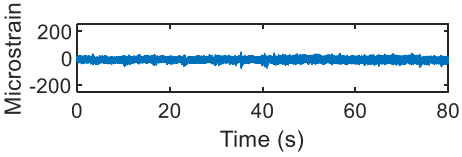

(68)

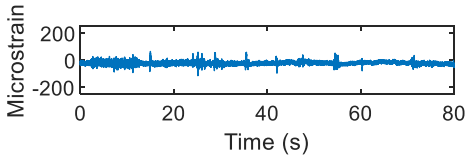

(69)

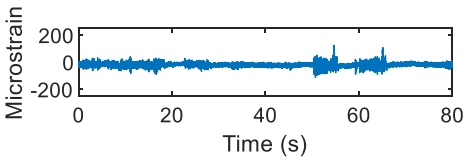

(70)

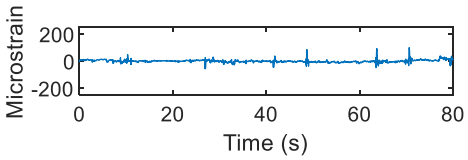

(71)

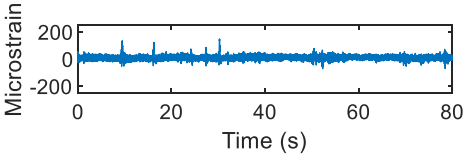

(72)

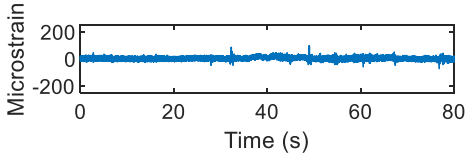

(73)

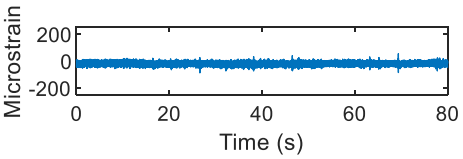

(74)

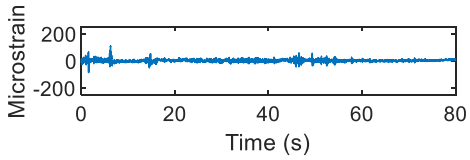

(75)

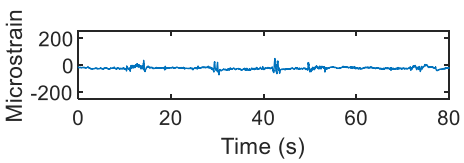

(76)

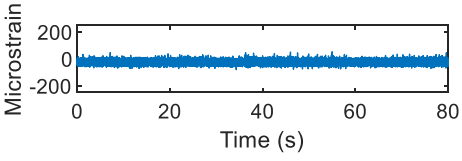

(77)

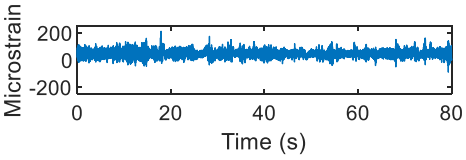

(78)

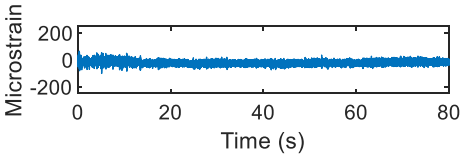

(79)

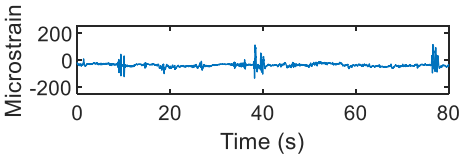

(80)

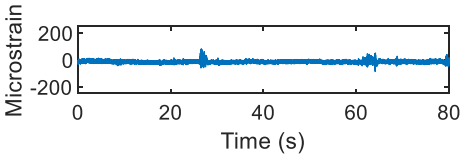

(81)

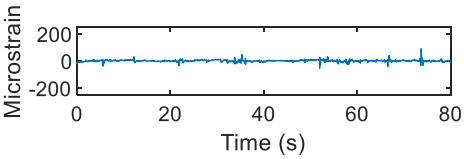

(82)

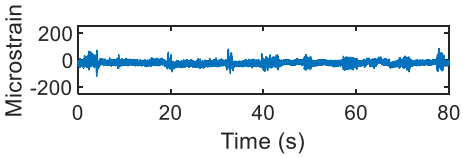

(83)

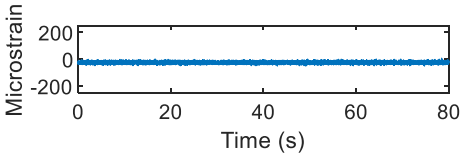

(84)

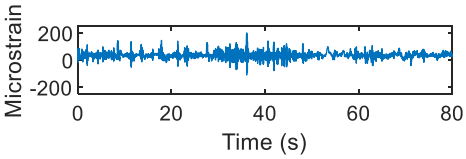

(85)

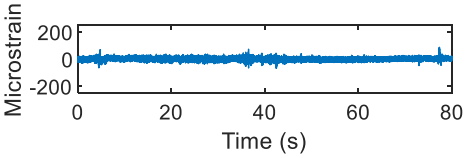

(86)

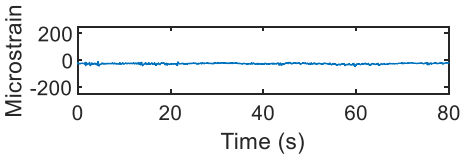

(87)

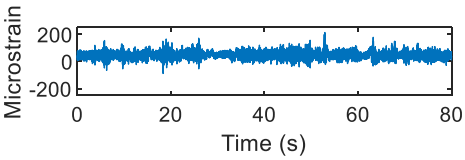

(88)

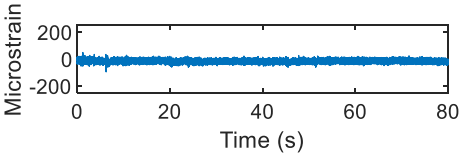

(89)

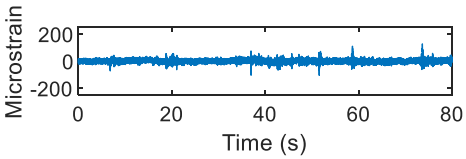

(90)

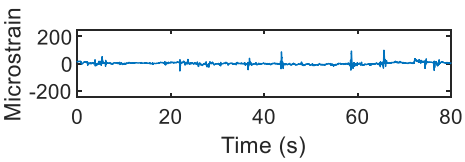

(91)

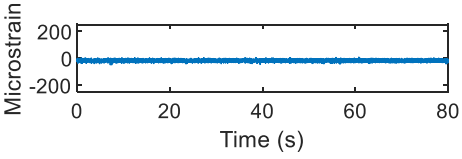

(92)

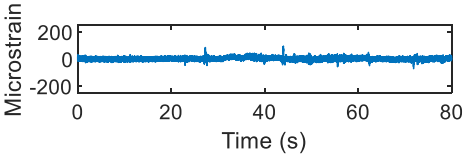

(93)

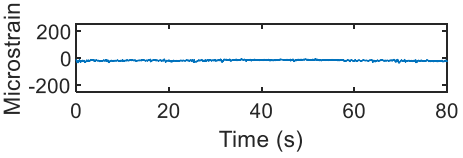

(94)

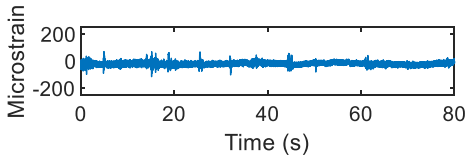

(95)

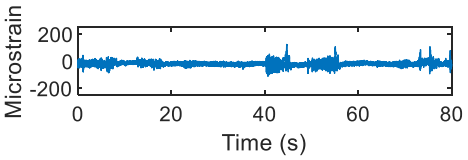

(96)

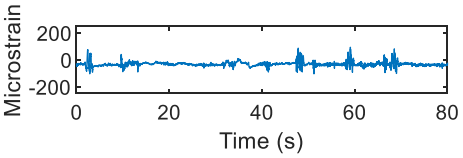

(97)

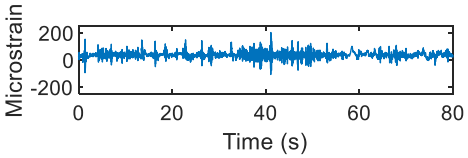

(98)

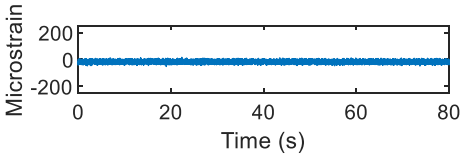

(99)

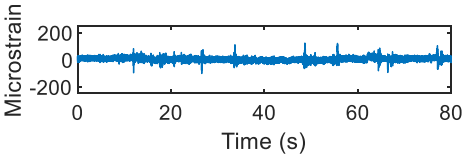

(100)

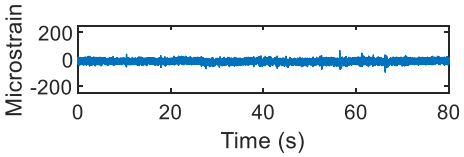

(101)

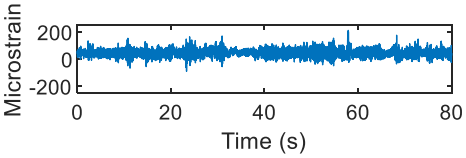

(102)

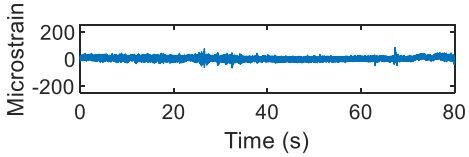

(103)

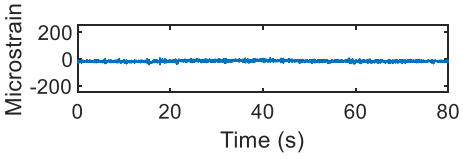

(104)

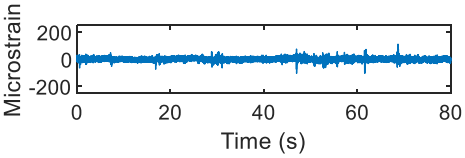

(105)

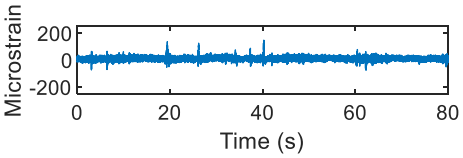

(106)

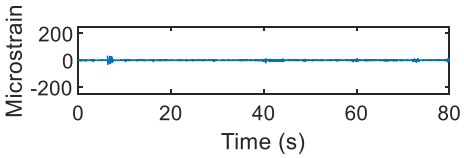

(107)

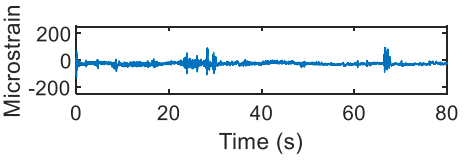

(108)

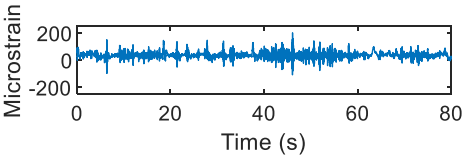

(109)

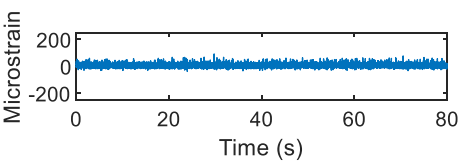

(110)

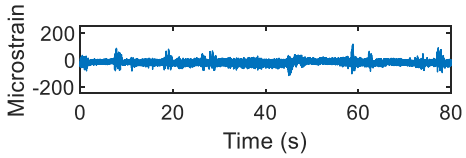

(111)

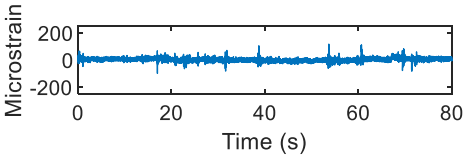

(112)

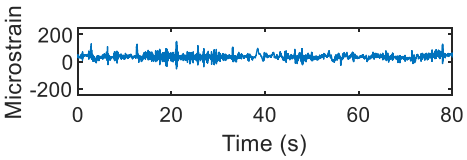

(113)

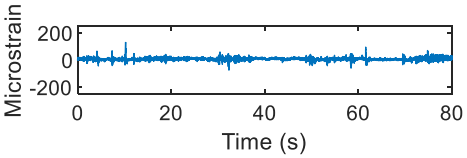

(114)

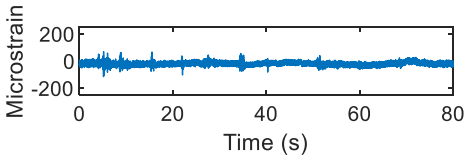

(115)

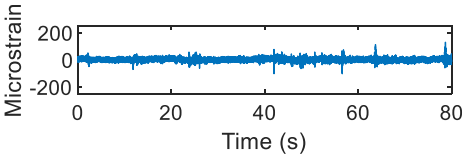

(116)

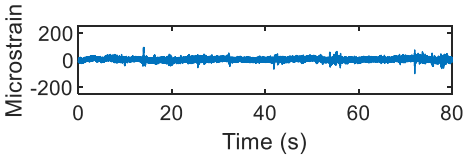

(117)

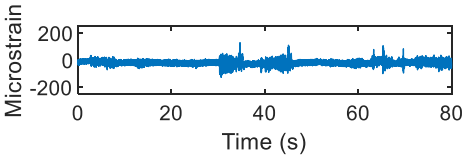

(118)

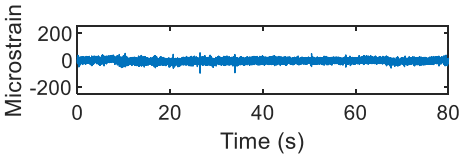

(119)

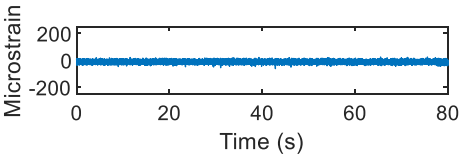

(120)

APPENDIX D

TRAINING AND TESTING DATASETS FOR ANFIS MODELLING

Training Dataset

No.	Energy	Multifractality	Spring stiffness	Fatigue life (Base 10 logarithm scale, Blocks to failure)			
				Coffin-Manson	Morrow	SWT	ESD
1	5.73	0.44	16806	4.43	4.42	4.41	4.41
2	5.22	0.43	16806	4.37	4.36	4.34	4.45
3	5.21	0.40	16806	4.39	4.38	4.37	4.47
4	5.19	0.41	16806	4.70	4.69	4.67	4.59
5	4.52	0.32	16806	4.25	4.25	4.26	4.27
6	5.65	0.39	16806	4.75	4.78	4.80	4.70
7	4.78	0.37	16806	4.81	4.87	4.91	4.94
8	3.44	0.51	16806	5.11	5.21	5.28	5.30
9	3.44	0.51	11107	5.99	6.24	6.40	5.95
10	3.44	0.51	13268	5.52	5.68	5.78	5.63
11	3.44	0.51	15731	5.21	5.32	5.39	5.38
12	3.44	0.51	18521	4.97	5.06	5.13	5.20
13	3.44	0.51	21667	4.79	4.87	4.92	5.05
14	2.60	0.36	16806	5.44	5.36	5.32	5.18
15	2.32	0.39	16806	5.10	5.02	4.98	4.90
16	2.32	0.39	11107	6.26	6.04	5.95	5.33
17	2.32	0.39	13268	5.63	5.48	5.42	5.13
18	2.32	0.39	15731	5.22	5.12	5.08	4.97
19	2.32	0.39	18521	4.95	4.89	4.85	4.82
20	2.32	0.39	21667	4.77	4.73	4.70	4.69
21	2.53	0.40	16806	5.05	4.98	4.95	4.90
22	2.13	0.36	16806	5.02	4.97	4.94	4.89
23	2.27	0.39	16806	5.04	4.98	4.94	4.76
24	4.02	0.46	16806	5.19	5.13	5.10	4.82
25	4.62	0.45	16806	5.17	5.12	5.09	4.84
26	4.62	0.45	11107	6.13	6.04	6.00	5.29
27	4.62	0.45	13268	5.61	5.54	5.51	5.06
28	4.62	0.45	15731	5.27	5.22	5.19	4.87
29	4.62	0.45	18521	5.04	4.99	4.96	4.75
30	4.62	0.45	21667	4.86	4.82	4.79	4.63
31	4.95	0.50	16806	4.97	4.91	4.87	4.69
32	4.98	0.46	16806	5.08	5.02	4.99	4.70
33	5.20	0.45	16806	5.09	5.04	5.01	4.62
34	5.20	0.45	11107	5.84	5.79	5.76	5.08
35	5.20	0.45	13268	5.35	5.30	5.28	4.86
36	5.20	0.45	15731	5.02	4.99	4.97	4.68
37	5.20	0.45	18521	4.80	4.77	4.75	4.55

Continue…

…continued

38	5.20	0.45	21667	4.63	4.61	4.59	4.45
39	5.33	0.51	16806	4.91	4.86	4.83	4.56
40	5.79	0.45	16806	4.77	4.69	4.65	4.56
41	6.16	0.47	16806	4.74	4.68	4.64	4.56
42	6.62	0.39	16806	4.66	4.61	4.58	4.59
43	6.62	0.39	11107	5.36	5.30	5.26	5.04
44	6.62	0.39	13268	4.99	4.93	4.90	4.83
45	6.62	0.39	15731	4.74	4.69	4.66	4.66
46	6.62	0.39	18521	4.55	4.51	4.49	4.51
47	6.62	0.39	21667	4.41	4.38	4.36	4.39
48	4.35	0.35	16806	6.99	7.16	7.28	5.50
49	4.49	0.36	16806	7.31	7.40	7.46	5.51
50	4.60	0.38	16806	6.10	6.24	6.31	5.20
51	3.28	0.37	16806	7.71	7.78	7.82	5.82
52	2.78	0.25	16806	8.23	8.31	8.33	5.92
53	2.59	0.25	16806	8.11	8.35	8.58	6.24
54	5.32	0.30	16806	6.31	6.30	6.29	5.27
55	5.36	0.30	16806	6.24	6.19	6.16	5.05
56	4.93	0.30	16806	6.23	6.20	6.19	5.09
57	4.51	0.30	16806	5.85	5.84	5.83	5.04
58	4.51	0.30	11107	7.09	7.06	7.05	5.62
59	4.51	0.30	13268	6.44	6.42	6.40	5.32
60	4.51	0.30	15731	5.98	5.97	5.96	5.11
61	4.51	0.30	18521	5.69	5.68	5.68	4.95
62	4.51	0.30	21667	5.50	5.49	5.49	4.83
63	4.54	0.28	16806	6.39	6.37	6.36	5.07
64	4.13	0.37	16806	6.93	6.82	6.75	5.08
65	3.84	0.37	16806	6.64	6.57	6.52	5.09
66	3.84	0.37	11107	8.16	8.06	7.97	5.72
67	3.84	0.37	13268	7.43	7.33	7.26	5.39
68	3.84	0.37	15731	6.84	6.76	6.71	5.17
69	3.84	0.37	18521	6.37	6.32	6.28	4.99
70	3.84	0.37	21667	6.03	5.99	5.97	4.86
71	3.46	0.32	16806	6.89	6.68	6.58	5.09
72	4.47	0.33	16806	6.94	6.73	6.61	4.83
73	4.47	0.33	11107	8.50	8.28	8.12	5.46
74	4.47	0.33	13268	7.73	7.53	7.39	5.14
75	4.47	0.33	15731	7.14	6.93	6.80	4.91
76	4.47	0.33	18521	6.68	6.46	6.34	4.73
77	4.47	0.33	21667	6.31	6.09	5.99	4.61
78	5.73	0.24	16806	5.49	5.51	5.52	4.46
79	7.58	0.36	16806	5.21	5.14	5.10	4.39
80	3.92	0.35	16806	6.16	6.08	6.04	4.67
81	4.13	0.38	16806	5.53	5.53	5.53	4.56
82	3.97	0.35	16806	5.53	5.47	5.44	4.53

Continue…

…continued

83	3.92	0.38	16806	5.48	5.49	5.50	4.68
84	3.92	0.38	11107	6.67	6.70	6.72	5.23
85	3.92	0.38	13268	6.03	6.06	6.07	4.95
86	3.92	0.38	15731	5.61	5.62	5.63	4.74
87	3.92	0.38	18521	5.33	5.34	5.34	4.60
88	3.92	0.38	21667	5.14	5.14	5.14	4.51
89	4.80	0.38	16806	5.29	5.32	5.34	4.60
90	4.54	0.31	16806	6.00	5.89	5.84	4.68
91	4.54	0.31	11107	7.45	7.28	7.19	5.14
92	4.54	0.31	13268	6.72	6.57	6.49	4.89
93	4.54	0.31	15731	6.17	6.05	5.99	4.71
94	4.54	0.31	18521	5.79	5.69	5.64	4.60
95	4.54	0.31	21667	5.52	5.44	5.40	4.49
96	7.73	0.49	16806	4.63	4.62	4.61	4.38
97	7.42	0.45	16806	4.40	4.39	4.38	4.26
98	7.42	0.45	11107	4.92	4.90	4.89	4.68
99	7.42	0.45	13268	4.65	4.64	4.63	4.49
100	7.42	0.45	15731	4.46	4.45	4.44	4.32
101	7.42	0.45	18521	4.31	4.31	4.30	4.18
102	7.42	0.45	21667	4.20	4.20	4.19	4.07
103	6.79	0.41	16806	4.40	4.39	4.39	4.27
104	6.57	0.50	16806	4.91	4.90	4.89	4.72
105	6.38	0.45	16806	4.87	4.87	4.87	4.73
106	2.96	0.34	16806	5.40	5.34	5.30	4.92
107	2.96	0.34	11107	6.66	6.48	6.40	5.42
108	2.96	0.34	13268	6.00	5.86	5.81	5.18
109	2.96	0.34	15731	5.54	5.46	5.42	4.99
110	2.96	0.34	18521	5.24	5.18	5.15	4.83
111	2.96	0.34	21667	5.02	4.98	4.96	4.72
112	3.48	0.46	16806	6.31	6.29	6.28	5.26
113	4.87	0.43	16806	4.82	4.85	4.88	4.97
114	5.26	0.44	16806	4.84	4.87	4.91	5.05
115	9.08	0.44	16806	4.59	4.60	4.61	4.62
116	8.54	0.47	16806	4.59	4.58	4.57	4.46
117	8.07	0.39	16806	4.52	4.53	4.54	4.52
118	6.31	0.42	16806	4.59	4.59	4.59	4.53
119	7.13	0.37	16806	5.05	5.00	4.97	4.67
120	6.18	0.40	16806	4.36	4.36	4.37	4.49
121	4.25	0.38	16806	4.53	4.54	4.56	4.72
122	5.08	0.37	16806	4.41	4.40	4.40	4.55
123	5.08	0.37	11107	4.90	4.93	4.95	5.00
124	5.08	0.37	13268	4.65	4.66	4.67	4.80
125	5.08	0.37	15731	4.47	4.47	4.47	4.62
126	5.08	0.37	18521	4.32	4.31	4.31	4.47
127	5.08	0.37	21667	4.20	4.19	4.19	4.34

Continue…

…continued

128	4.06	0.42	16806	5.05	5.00	4.98	4.62
129	4.25	0.44	16806	5.05	5.00	4.97	4.67
130	4.83	0.53	16806	4.63	4.63	4.62	4.49
131	4.83	0.53	11107	5.51	5.50	5.49	4.95
132	4.83	0.53	13268	5.05	5.05	5.04	4.73
133	4.83	0.53	15731	4.73	4.73	4.72	4.55
134	4.83	0.53	18521	4.51	4.50	4.50	4.40
135	4.83	0.53	21667	4.34	4.33	4.33	4.27
136	4.71	0.52	16806	4.56	4.57	4.57	4.46
137	5.12	0.46	16806	4.42	4.44	4.46	4.48
138	5.67	0.56	16806	4.51	4.53	4.54	4.47
139	6.24	0.60	16806	4.26	4.29	4.30	4.13
140	6.24	0.60	11107	4.83	4.84	4.84	4.55
141	6.24	0.60	13268	4.55	4.58	4.59	4.35
142	6.24	0.60	15731	4.33	4.36	4.38	4.19
143	6.24	0.60	18521	4.16	4.19	4.20	4.05
144	6.24	0.60	21667	4.03	4.05	4.07	3.94
145	7.05	0.46	16806	4.18	4.19	4.20	4.08
146	8.01	0.48	16806	4.08	4.09	4.09	4.05
147	13.08	0.51	16806	4.33	4.34	4.35	4.30
148	13.33	0.48	16806	4.40	4.41	4.42	4.34
149	14.13	0.58	16806	4.32	4.33	4.34	4.31
150	14.48	0.48	16806	4.46	4.46	4.46	4.40
151	14.71	0.52	16806	4.37	4.38	4.38	4.38
152	14.61	0.58	16806	4.36	4.36	4.37	4.41
153	14.71	0.49	16806	4.32	4.33	4.34	4.37
154	14.68	0.50	16806	4.40	4.40	4.40	4.42
155	13.34	0.49	16806	4.42	4.42	4.42	4.37
156	12.92	0.61	16806	4.47	4.46	4.47	4.53
157	13.17	0.47	16806	4.54	4.55	4.55	4.49
158	13.83	0.51	16806	4.49	4.49	4.49	4.42
159	14.09	0.53	16806	4.44	4.44	4.44	4.33
160	13.65	0.53	16806	4.46	4.45	4.45	4.43
161	18.15	0.40	16806	4.15	4.14	4.14	4.06
162	18.15	0.40	11107	4.70	4.70	4.70	4.49
163	18.15	0.40	13268	4.43	4.42	4.42	4.28
164	18.15	0.40	15731	4.22	4.21	4.21	4.11
165	18.15	0.40	18521	4.06	4.05	4.05	4.00
166	18.15	0.40	21667	3.93	3.92	3.92	3.88
167	18.17	0.52	16806	4.16	4.15	4.15	4.05
168	18.17	0.52	11107	4.71	4.70	4.70	4.47
169	18.17	0.52	13268	4.44	4.43	4.42	4.26
170	18.17	0.52	15731	4.23	4.22	4.22	4.10
171	18.17	0.52	18521	4.07	4.06	4.06	3.98
172	18.17	0.52	21667	3.94	3.93	3.93	3.87

Continue…

…continued

173	17.12	0.56	16806	4.19	4.19	4.19	4.13
174	16.91	0.49	16806	4.17	4.18	4.18	4.19
175	16.91	0.49	11107	4.75	4.76	4.77	4.64
176	16.91	0.49	13268	4.46	4.47	4.47	4.42
177	16.91	0.49	15731	4.24	4.25	4.26	4.25
178	16.91	0.49	18521	4.08	4.08	4.09	4.12
179	16.91	0.49	21667	3.95	3.95	3.95	4.00
180	16.08	0.50	16806	4.20	4.19	4.18	4.03
181	15.84	0.49	16806	4.29	4.29	4.29	4.23
182	15.49	0.51	16806	4.41	4.40	4.39	4.24
183	15.13	0.45	16806	4.44	4.45	4.46	4.36
184	15.34	0.49	16806	4.54	4.55	4.56	4.34
185	15.34	0.49	11107	5.34	5.38	5.40	4.82
186	15.34	0.49	13268	4.91	4.95	4.96	4.58
187	15.34	0.49	15731	4.63	4.65	4.66	4.40
188	15.34	0.49	18521	4.42	4.43	4.44	4.26
189	15.34	0.49	21667	4.27	4.27	4.28	4.16
190	15.38	0.48	16806	4.49	4.51	4.53	4.24
191	14.81	0.48	16806	4.43	4.44	4.45	4.32
192	14.93	0.50	16806	4.45	4.47	4.48	4.25
193	14.93	0.50	11107	5.18	5.22	5.23	4.70
194	14.93	0.50	13268	4.80	4.82	4.84	4.46
195	14.93	0.50	15731	4.54	4.54	4.57	4.30
196	14.93	0.50	18521	4.35	4.36	4.37	4.18
197	14.93	0.50	21667	4.21	4.22	4.22	4.08
198	15.25	0.47	16806	4.60	4.61	4.61	4.29

Testing Dataset

No.	Energy	Multifractality	Spring stiffness	Fatigue life (Base 10 logarithm scale, Blocks to failure)			
				Coffin-Manson	Morrow	SWT	ESD
1	5.19	0.36	16806	4.35	4.35	4.33	4.39
2	5.62	0.42	16806	4.73	4.77	4.79	4.72
3	2.24	0.42	16806	5.42	5.33	5.29	5.21
4	2.19	0.38	16806	5.04	4.98	4.95	4.80
5	4.24	0.54	16806	5.23	5.16	5.13	4.81
6	4.87	0.47	16806	5.09	5.04	5.01	4.82
7	5.69	0.43	16806	4.78	4.70	4.66	4.48
8	5.51	0.42	16806	4.78	4.71	4.68	4.60
9	2.69	0.30	16806	7.75	7.72	7.70	5.69
10	2.92	0.28	16806	6.85	6.64	6.55	5.48
11	4.36	0.33	16806	6.41	6.37	6.35	5.05
12	3.80	0.38	16806	6.12	6.03	5.98	4.65
13	4.14	0.40	16806	5.23	5.25	5.27	4.49
14	4.11	0.40	16806	5.41	5.41	5.41	4.63
15	5.00	0.39	16806	5.49	5.52	5.53	4.74
16	7.76	0.44	16806	4.37	4.36	4.35	4.16
17	8.56	0.48	16806	4.56	4.58	4.60	4.64
18	5.82	0.36	16806	4.38	4.40	4.41	4.58
19	5.68	0.54	16806	4.42	4.44	4.44	4.48
20	14.95	0.49	16806	4.39	4.42	4.43	4.41
21	13.74	0.52	16806	4.49	4.50	4.51	4.44
22	16.60	0.56	16806	4.16	4.17	4.17	4.14

List of Publications

Journal Article

1. **Chin, C.H.**, Abdullah, S., Singh, S. & Ariffin, A.K. 2018. Establishing Energy-Damage Relationship for Fatigue Data Editing of Strain Loading History. *International Review of Mechanical Engineering (IREME)* 12: 612. (SCOPUS indexed journal)

2. **Chin, C.H.**, Abdullah, S., Singh, S.S.K., Ariffin, A.K. & Schramm, D. 2020. Durability assessment of suspension coil spring considering the multifractality of road excitations. *Measurement* 158: 107697. (WoS indexed journal, Q2, IF: 2.791)

3. **Chin, C.H.**, Abdullah, S., Singh, S., Ariffin, A.K. & Schramm, D. 2021. Neuro-fuzzy fatigue life assessment using the wavelet-based multifractality parameters. *Journal of Mechanical Science and Technology* 35(2). (WoS indexed journal, Q3, IF: 1.345)

4. **Chin, C.H.**, Abdullah, S., Singh, S.S.K., Ariffin, A.K. & Schramm, D. 2021. Computing low-frequency vibration energy with Hölder singularities as durability predictive criterion of random road excitation. *Soft Computing* 25: 6469–6487. (WoS indexed journal, Q2, IF: 3.050)

5. **Chin, C.H.**, Abdullah, S., Singh, S.S.K., Schramm, D. & Ariffin, A.K. 2021. Durability prediction of coil spring through multibody-dynamics-based strain generation. *Mechanical Systems and Signal Processing* 154: 107580. (WoS indexed journal, Q1, IF: 6.471)

6. **Chin, C.H.**, Rahim, A.A.A., Abdullah, S., Singh, S.S.K. & Md Nor, N. 2021. Acceptability of the effective strain damage model for fatigue life assessment considering the load sequence effect for automotive coil spring. *Engineering Failure Analysis* 126: 105462. (WoS indexed journal, Q1, IF: 2.897)

7. **Chin, C.H.**, Abdullah, S., Singh, S.S.K., Ariffin, A.K. & Schramm, D. 2022. Probabilistic-based fatigue reliability assessment of carbon steel coil spring from random strain loading excitation. *Journal of Mechanical Science and Technology* 36(1). (WoS indexed journal, Q3, IF: 1.734)

8. **Chin, C.H.**, Abdullah, S., Yin, A.G. & Ariffin, A.K. 2022. Vibration fatigue analysis through frequency response function of variable amplitude loading. *Journal of Mechanical Science and Technology* 36(1): 33–43. (WoS indexed journal, Q, IF: 1.734)

9. Santharaguru, N., Abdullah, S., **Chin, C.H.** & Singh, S.S.K. 2022. Failure behaviour of strain and acceleration signals using various fatigue life models in time and frequency domains. *Engineering Failure Analysis* 139: 106454. (WoS indexed journal, Q2, IF: 3.114)

Book chapter

1. **Chin, C.H.**, Abdullah, S., Singh, S.S.K., Schramm, D., Ariffin, A.K. & Nasir, N.N.M. 2019. Compression of Strain Load History Using Holder Exponents of Continuous Wavelet Transform BT - Proceedings of the 7th International Conference on Fracture Fatigue and Wear. pg. 258–272. Springer Singapore: Singapore.

2. Rahim, A. A. A., **Chin, C. H.**, Abdullah, S., Singh, S. S. K. & Nor, N. M. 2022. Fatigue Life Analysis of Strain Loadings Using Effective Strain Damage Approach with the Consideration of Cycle Sequence Effects BT - Structural Integrity and Fatigue Failure Analysis. In Lesiuk, G., Szata, M., Blazejewski, W., Jesus, A.M.d., Correia, J.A. (eds.). Structural Integrity and Fatigue Failure Analysis. pp. 87–95. Cham: Springer International Publishing.

Conference Proceeding

1. **Chin, C.H.**, Abdullah, S., Ariffin, A.K. & Singh, S.S.K. 2018. Durability Analysis for Coil Spring Suspension Based on Strain Signal Characterisation. International Journal of Engineering & Technology 7(3.17): 104–109. (SCOPUS indexed Proceeding)

2. Rahim, A.A.A., **Chin, C.H.,** Abdullah, S., Singh, S.S.K., Nuawi, M.Z. & Hassan, F.H.A. 2018. Characterization of Wavelet Decomposition Strain Signal Using the K-Mean Clustering Method. International Journal of Engineering & Technology 7(3.17): 158–162. (SCOPUS indexed Proceeding)

3. **Chin, C. H.**, Abdullah, S., Singh, S. S. K., Ariffin, A. K. & Schramm, D. 2019. Multifractal analysis for durability predictive criterion of suspension coil spring signal. In BinAbdollah, M.F. (ed.). *PROCEEDINGS OF MECHANICAL ENGINEERING RESEARCH DAY 2019 (MERD'19)*. pp. 139–141. (WoS indexed Proceeding)

4. **Chin, C.H.**, Abdullah, S., Singh, S.S.K., Ariffin, A.K. & Schramm, D. 2020. Bump Energy for Durability Prediction of Coil Spring Based on Local Regularity Analysis. *International Journal of Integrated Engineering* 12(5): 12–19. (SCOPUS indexed Proceeding)

DOI: 10.17185/duepublico/78359
URN: urn:nbn:de:hbz:465-20230428-145026-7